Imaging and Quantification of Microcirculatory Network within Tissue Beds *in vivo* using Optical Coherence Tomography

Siavash Yousefi

A dissertation

submitted in partial fulfillment of the

requirements for the degree of

Doctor of Philosophy

University of Washington

2014

Reading Committee:

Ruikang K. Wang, Chair

Francesco Curra

Lih Lin

Program Authorized to Offer Degree:

Electrical Engineering

University of Washington

Abstract

Imaging and Quantification of Microcirculatory Network within Tissue Beds *in vivo* using Optical Coherence Tomography

Siavash Yousefi

Chair of the Supervisory Committee:

Professor Ruikang K. Wang

Bioengineering

Optical coherence tomography (OCT) which is an imaging modality based on Michelson interferometry of near-infrared broadband light has become one of the standard imaging modalities in ophthalmology and intravascular cardiology. In this thesis, we have developed tools and techniques to visualize quantify OCT angiography for translational applications. First, a clutter removal is proposed to suppress static and slowly moving tissue structures from moving red blood cells (RBCs) within the tissue. Then, RBC flow and relative flux is estimated using spectral estimation techniques. Then, a segmentation technique is developed to quantify lymphatic vessels within the tissue structures that appear as transparent tubular structures. Similar method based on Hessian filters is generalized to segment blood vessels for further quantification in OCT angiography. Finally, we utilize the developed tools and techniques for translational applications of OCT and OCT angiography for wound healing and studying

complications of microvascular network induced by injection of cosmetic dermal fillers at capillary level. All of the above techniques are non-invasive, label-free, three-dimensional and *in vivo*.

TABLE OF CONTENTS

LIST OF FIGURES

LIST OF TABLES

LIST OF PUBLISHED PAPERS

Part of this thesis has been published in the following papers and patents

[1] Siavash Yousefi, Jia Qin, Suzan Dziennis and Ruikang K. Wang, "Non-invasive assessment of microcirculation dynamics during cutaneous wound healing *in vivo*," Journal of Biomedical Optics, 2014 (Accepted).

[2] Siavash Yousefi, Zhongwei Zhi, Jia Qin and Ruikang K. Wang, "Label-free optical imaging of lymphatic vessel lumen within tissue beds in vivo," IEEE Journal of Selected Topics in Quantom Electronics, vol. 20, No. 2, March/April 2014. *(invited paper)*

[3] Siavash Yousefi, Zhogwei Zhi and Ruikang K. Wang, "Label-free optical lymphangiography: development of an automatic segmentation method applied to optical coherence tomography to visualize lymphatic vessels using Hessian filters," Journal of Biomedical Optics, 18(8), 086004, April 2013 (appeared on octnews.org main page as feature of the week)

[4] Siavash Yousefi, Jia Qin, Suzan Dziennis and Ruikang K. Wang, "Super-Resolution Spectral Estimation of Optical Microangiography for Capillary Flow Quantification", Biomedical Optics Express, Vol. 4, No. 7, July 2013 (doi: 10.1364/BOE.4.001214)

[5] Siavash Yousefi, Jia Qin, Zhongwei Zhi and Ruikang K. Wang, "Uniform Enhancement of Optical Micro-Angiography Images using Rayleigh Contrast-Limited Adaptive Histogram Equalization," Quantitative Imaging in Medicine and Surgery, Vol. 3, No. 1, February, 2013. (Appeared on journal cover page)

[6] Siavash Yousefi, Zhongwei Zhi and Ruikang K. Wang, "Eigendecomposition-Based Clutter Filtering Technique for Optical Micro-Angiography," IEEE Transactions on Biomedical Engineering, Vol. 58, No. 8, Aug. 2011, pp. 2316-2323.

[7] Siavash Yousefi and Ruikang k. Wang, "Methods and systems for determining hemodynamic properties of a tissue," US patent application filed on April 9, 2014 [IP: 46337.01US1].

[8] Siavash Yousefi and Ruikang k. Wang, "Method and device for imaging lymphatic circulations and its applications," disclosed to UW's patent office.

ACKNOWLEDGMENTS

First of all, my parents Ahmad Ali Yousefi and Mina Jamzad, deserve a great appreciation because all of this would not have been possible without their support. They have been great motivation and inspiration and I hope I could have slightly made you happy and proud.

I would like to express my gratitude and appreciations to my PhD mentor and advisor, Professor Ruikang K. Wang (a.k.a Ricky), who has been a constant support since I joined the Biophotonics and Imaging Laboratory (BAIL). I really appreciate his trust in me and being patient with my ups and downs in work and personal life. I'm sure my PhD experience and outcome would have been dramatically different if I have not joined Ricky's lab when he joined the University of Washington (UW). I also would like to thank my colleagues and lab members who taught me a lot and made the rest of this thesis possible. Specifically, Zhongwei Zhi (Tim) who set up most of our OCT systems. Also, Lin An and Lei Shi who modified and maintained our systems on a regular basis. My background was engineering while working in such interdisciplinary fields, and I learned a great deal from a great expert, Dr. Suzan Dziennis, who taught me a lot in the lab about experimental set up, animal handling, lab ethics and etc. Dr. Jia Qin was also one of the key people in our team and helped me out a lot at the beginning for animal studies and contributed directly to most of the papers we published together. I made great friends in the lab and hopefully can continue in the future such as Utku Baran, who came from our neighboring country and we shared a lot of similar culture. I'd also like to thank a great friend, Floyd Karp, who helped me out a lot in the last year and gave me lots of useful advice. Again, I'd like to thank all of the current and former members of BAIL at UW and UW Bioengineering staff and

faculties who were just great. I will always remember and appreciate my former advisor, Professor Yongmin Kim and his lab members who were great friends and mentors. Dr. Kerem Karadyi taught a lot of the things I know about ultrasound and mediaprocessor programming. I enjoyed the company of my great friend Cheoljin Lee, all the good days and challenging time we spent together will never be forgotten and I'm grateful to have such awesome people in my life. I met a great deal of Persian friends in Seattle who always kept my company and made my tough days seem fine. They were and are great friends and wish to have been a good friend for all of them. If I want to mention specific names, this page would be filled with names. Thank you all.

My uncles and aunts and their family in the US and Canada were great support and help. I did not feel very homesick by having such great relatives and cousins.

During my PhD work at BAIL, I've been lucky to get the chance to collaborate with amazing people from different departments and institutes. We had an amazing collaboration with Dr. Shu-Hong Chang (Holly)'s lab from UW ocular plastic surgery. Holly is not only a great surgeon, but also a great person to know and work with. I personally learned a lot from her and her team and enjoyed every moment of the days we spent doing experiments and procedures. Another collaborator was Dr. Junmei Chen from Puget Sound Blood Center (PSBC) and Dr. Jose Lopez's lab. Junmei along with Terri and Jennie were one of our first collaborations and their suggestions and expertise shaped lots of ideas and great results. I'd also like to mention other collaborators that we worked on different projects, Dr. Yak-Nam Wang and Dr. Francesco Curra, who were great to work with.

Last but not the least, I would like to thank my PhD committee members who took the time to review my work and were expert opinions on these results. Professor Ricky Wang who spent a lot of time reading and correctly my writing and sometimes unorganized ideas and shaped them

towards a solid understandable work. Professor Lih Lin and Professor Francesco Curra were my reading committee who had to read and correct all of the two-hundred something pages of my thesis. Also, Professor Larry Crum and Professor Holly Chang who had to make room in their empty schedule to meet me and attend my final exam. Also, Professor Johnathan Posner, while an expert in the topic, was my GSR and made sure everything was in agreement with UW grad school guidelines.

Again, I'd like to thank all people who contributed to my career and success and wish them all the best.

Chapter 1. INTRODUCTION

1.1 Optical coherence tomography

Optical coherence tomography (OCT) is an imaging modality based on Michelson interferometry of near-infrared broadband light using ballistic and near-ballistic photons. OCT has been widely used to non-invasively provide high-resolution, depth-resolved cross-sectional and three-dimensional (3-D) images of highly scattering samples [Huang-1991, Fercher-2003, Tomlins-2005]. More recently, spectral-domain OCT (SD-OCT) and swept-source OCT (SS-OCT) imaging have been developed where these frequency-domain OCT (FD-OCT) methods have advantages over time-domain ones in terms of acquisition speed, sensitivity and signal to noise ratio [Leitgeb-2003, Choma-2003]. In order to compensate for the complex conjugate ambiguity and acquisition speed, which limited the practical applications of FD-OCT, real-time *in vivo* full-range complex FD-OCT has been developed to increase the ranging distance in the sample [An-2010, Wang-2007]. Due to the relative transparent optical properties of human eye, ophthalmology is a perfect application for OCT. OCT has shown promising results in structural and functional imaging of posterior segment of the eye (retina, optic nerve head and choroid) [An-2010, Yi-2009, Regatieri-2012], anterior segment of the eye (cornea, iris and lens) [Li-2011, Johnstone-2011, Lim-2008] as well as their mechanical properties [Li-2012] for diagnosis, monitoring and preventing many eye disease such as glaucoma [Wollstein-2005], diabetic retinopathy [Imai-2001] and age-related macular degeneration [Hee-1996]. Another popular application of OCT is visualization of intravascular structures for patients with coronary

atherosclerotic plaques [Jang-2002] and evaluation of intracoronary stenting [Bouma-2003] using OCT-enabled intravascular catheters [Kubo-2007, Yabushita-2002, Fujimoto-2003].

1.2 Modeling light scattering in OCT

OCT imaging is based on elastic light scattering in the tissue, meaning that the frequency and energy of the scattered light is the same as the light received at the scatterer. The degree of mismatch, the size and shape of the scatter relative to the wavelength and their relative density determines light scattering [Brezinski-2006]. The Rayleigh and the Mie theories are solutions of the Maxwell equations that model the scattering of a plane monochromatic optical wave by a single spherical particle. The Rayleigh theory is applicable only to particles that are much smaller than the optical wavelength, whereas the Mie theory is valid for homogenous isotropic spheres of any size. The Mie theory is an exact solution of the Maxwell equations for a plane monochromatic electromagnetic wave scattered by a homogenous sphere and can reduce to Rayleigh theory when the particle is much smaller than the wavelength [Wang-2012_ Book].

In the Mie theory, the following assumptions are made on the Maxwell equations:

$$\nabla . \vec{E} = 0, \tag{1-1}$$

$$\nabla . \vec{B} = 0, \tag{1-2}$$

$$\nabla \times \vec{E} = -\frac{\partial \vec{B}}{\partial t}, \tag{1-3}$$

$$\nabla \times \vec{B} = \left(\frac{n}{c}\right)^2 \frac{\partial \vec{E}}{\partial t} \tag{1-4}$$

where $\vec{E}$ and $\vec{B}$ are the electric and magnetic fields, respectively, n is the refractive index of the medium and c is the speed of light in the vacuum. By replacing the equations, each vector component satisfies the following vector and scalar wave equations

$$\nabla^2\vec{E} = \left(\frac{n}{c}\right)^2 \frac{\partial^2\vec{E}}{\partial t^2}, \tag{1-5}$$

$$\nabla^2\vec{B} = \left(\frac{n}{c}\right)^2 \frac{\partial^2\vec{B}}{\partial t^2}, \tag{1-6}$$

$$\nabla^2 E = \left(\frac{n}{c}\right)^2 \frac{\partial^2 E}{\partial t^2}, \tag{1-7}$$

and

$$\nabla^2 B = \left(\frac{n}{c}\right)^2 \frac{\partial^2 B}{\partial t^2}. \tag{1-8}$$

The scalar equation can be solved by separation of variables. We can write electric and magnetic fields in the form of $\Psi(\vec{x},t) = X(\vec{x})T(t)$ where $\vec{x}$ represents the spatial coordinates. By substitution, we can obtain the following equations that the left-hand side and the right-hand side equations are independent and equal to a constant

$$\frac{\nabla^2 X}{X} = \left(\frac{n}{c}\right)^2 \frac{1}{T}\left(\frac{\partial^2 T}{\partial t^2}\right) = constant. \tag{1-9}$$

Solving this equation for T yields

$$T \sim \begin{Bmatrix} \cos\omega t \\ \sin\omega t \end{Bmatrix} \tag{1-10}$$

And the spatially dependent part is a scalar Helmholtz equation given by

$$\nabla^2 X + k^2 X = 0 \tag{1-11}$$

which can be solved by representation of X in the spherical coordinates given by

$$X = R(r)\Theta(\theta)\Phi(\phi). \tag{1-12}$$

Solving for each coordinate separately,

$$\Phi \sim \begin{Bmatrix} \cos(m\phi) \\ \sin(m\phi) \end{Bmatrix}, \tag{1-13}$$

$$R \sim \begin{Bmatrix} j_1(kr) \\ y_1(kr) \end{Bmatrix}, \tag{1-14}$$

$$\Theta \sim \begin{Bmatrix} P_{1,m}(cos\theta) \\ Q_{1,m}(cos\theta) \end{Bmatrix} \tag{1-15}$$

where $j_1(x)$ and $y_1(x)$ are the spherical Bessel functions of the first and second kind, respectively, $P_{1,m}(cos\theta)$ and $Q_{1,m}(cos\theta)$ are the associated Legendre polynomials of first and second kind, respectively. By replacing the solutions to $\Psi(\vec{x}, t) = X(\vec{x})T(t)$ we can get

$$\Psi \sim \exp(i\omega t) \begin{Bmatrix} \cos(m\phi) \\ sing(m\phi) \end{Bmatrix} \begin{Bmatrix} j_1(nk_0r) \\ h_l^{(2)}(nk_0r) \end{Bmatrix} P_{l,m}(cos\theta) \tag{1-16}$$

where $h_l^{(2)}(nk_0r) \sim \frac{i^{l+1}}{nk_0r} \exp(-ink_0r)$ is the spherical Hankel function of the second kind chosen because of its asymptotic behavior. If the solution with $\exp(-i\omega t)$ is used, the spherical Hankel function of the first kind $h_l^{(2)}(nk_0r)$ should be used instead for the outgoing spherical wave. It can be shown that the solutions of scalar wave equations can be generalized to vector wave equations [Wang-2012_ Book].

In order to infer information about the refractive index distribution $n(r)$ from measurements on the scattered light, the media is assumed to be a weakly scattering environment. The Helmholtz equation for the scattered field can be written by

$$\nabla^2 U(r, \omega) + k_0^2 U(r, \omega) = -4\pi F(r, \omega).U(r, \omega) \tag{1-17}$$

$$F(r, \omega) = \frac{1}{4\pi} k_0^2 [n^2(r, \omega) - 1] \tag{1-18}$$

where $k_0 = {}^{\omega}/_{c}$, $F(r,\omega)$ is the scattering potential associated with the medium, ω is the angular frequency of light, c is the speed of light and r is the spatial location.

The elementary equation that gives Green's function $g(r,\omega)$ is the solution of

$$\nabla^2 g(r,\omega) + k_0^2 g(r,\omega) = -\delta^{(2)}(r) \tag{1-19}$$

given by $g(r,\omega) = \frac{e^{ik_0 r}}{r}$ and the solution for the scattered filed is a convolution between the source term and the Green function, given by

$$U(r,\omega) = \int F(r',\omega).U(r',\omega).\frac{e^{ik_0|r-r'|}}{|r-r'|}d^3r'. \tag{1-20}$$

This equation can be simplified with the far-zone approximation ($r' \ll r$) thus

$$|r-r'| \approx r - \frac{k_s}{k_0}.r' \tag{1-21}$$

where $\frac{k_s}{k_0}$ is the unit vector associated with the direction of propagation. In the far-zone, the scattered field is given by

$$U(r,\omega) = \frac{e^{ik_0 r}}{r}\int F(r',\omega).U(r',\omega).e^{-ik_s r'}d^3r' \tag{1-22}$$

which indicates that the field behaves as a spherical wave, perturbed by the scattering amplitude defined as

$$f(k_s,\omega) = \int F(r',\omega).U(r',\omega).e^{-ik_s r'}d^3r'. \tag{1-23}$$

If assuming that the scattering is weak and considering the Born approximation [Born-1999] that the field inside the scattering volume is constant and equal to the incident field, $U_i(r',\omega) \cong e^{ik_i r'}$, we can obtain for the scattered field

$$f(k_s,\omega) = \int F(r',\omega).e^{-i(k-k_s)r'}d^3r' \tag{1-24}$$

where the right hand side is a 3D Fourier transform. Due to the Fourier integral properties, scattering potential can be retrieved using inverse scattering problem given by

$$F(r', \omega) \propto \int U(q, \omega). e^{iqr'} d^3q \tag{1-25}$$

where q is the difference between the scattered and initial wavevectors given by $q = k_s - k_i = 2k_0.\frac{sin\theta}{2}$ and θ is the scattering angle. Therefore, measuring U at many scattering angles allows the reconstruction of the scattering potential from its Fourier components.

In general, most measurements are intensity-based. If only the intensity of the scattered light ($|U(q, \omega)|^2$) is available, then the autocorrelation of the scattering potential ($F(r', \omega) \otimes F(r', \omega)$) is retrieved not $F(r', \omega)$ itself, which is the correlation theorem applied to 3D Fourier transforms.

Assuming that the sample is made of identical particles of scattering potential $F_0(r)$, then the ensemble scattering potential under Born approximation can be expressed as

$$F(r) = F_0(r) * \sum_j \delta(r - r_j) \tag{1-26}$$

where δ is Dirac delta function.

The scattering amplitude at $(q = k_s - k_i)$ is the 3D Fourier transform of $F(r)$ given by

$$f(q) = \int F_0(r) * \sum \delta(r - r_j). e^{iqr} dr^3 = f_0(q). \sum e^{iqr_j} = f_0(q). S(q). \tag{1-27}$$

where can define $S(q) = \sum e^{iqr_j}$ as the structure function and $f_0(q)$ as the form function.

1.3 Scattering approximation

Assuming that an object positioned at the beam waist and the object depth at the order of magnitude of the corresponding Rayleigh depth is illuminated by a plane monochromatic wave (wavenumber k) Gaussian laser beam given by

$$E^{(i)}\left(r, k^{(i)}, t\right) = A^{(i)} e^{(ik^{(i)}.r - i\omega t)} \tag{1-28}$$

where $k^{(i)}$ is the wave-vector of the illuminating wave and $|k^{(i)}| = k = 2\pi/\lambda$ is the wave-number. For simplicity, field quantization and polarization effect are ignored. After the incident light interacts with the tissue sample, some part of that will scatter in the form of $E^{(s)}\left(r, k^{(s)}, t\right)$ such that the sum of two waves $E^{(i)}\left(r, k^{(i)}, t\right) + E^{(s)}\left(r, k^{(s)}, t\right)$ satisfies the Helmholtz equation. Under weakly scattering object assumptions, first Born approximation applies and the scattered field can be obtained as a volume integral extended over the illuminated object volume $V(r')$:

$$E^{(s)}\left(r, k^{(s)}, t\right) = -\frac{1}{4\pi}\int_{V(r')} F\left(r', k^{(i)}\right).E^{(i)}\left(r', k^{(i)}, t\right) \times G(|r - r'|)d^3r', \tag{1-29}$$

with the scattering potential $F\left(r, k^{(i)}\right) = -k^2[n^2(r, k^{(i)} - 1]$ and Green's function

$$G(|r - r'|) = \frac{e^{\left(ik^{(s)}|r-r'|\right)}}{|r-r'|}. \tag{1-30}$$

Assuming that the scattering potential is independent of the wavenumber (neglecting dispersion of the refractive index), we can obtain

$$E^{(s)}\left(r, k^{(s)}, t\right) = -\frac{1}{4\pi D}\int\limits_{V(r')} F(r')A^{(i)} e^{\left(ik^{(i)}.r' - i\omega t\right)} \times e^{[ik^{(s)}.(r-r')]}dr'^3$$

$$= -\frac{A^{(i)}}{4\pi D} e^{(ik^{(s)}.r - i\omega t)} \times \int_{V(r')} F(r').e^{(-iK.r')}dr'^3. \tag{1-31}$$

If the Fresnel number $\frac{d^2}{\lambda D}$ of the illuminating beam is smaller than 1, the scattering potential F is constant in the x' and y' spatial locations and the integral can be simplified by replacing a constant factor W chosen proportional to the cross section of the beam waist of the illuminating beam. Hence we can replace the 3D Fourier transform by a one-dimensional Fourier transform,

$$E^{(s)}\left(r, k^{(s)}, t\right) = -\frac{A^{(i)}W}{4\pi D}\, e^{(ik^{(s)}.r - i\omega t)} \times \int_0^T F(z')\, e^{(iKz')}dz', \tag{1-32}$$

where the second term is the one-dimensional Fourier transform of the scattering potential

$$E^{(s)}\left(r, k^{(s)}, t\right) = -\frac{A^{(i)}W}{4\pi D}\, e^{\left(ik^{(s)}.r - i\omega t\right)} \times FT\{F(z)\}. \tag{1-33}$$

Since only the intensity of the scattered light is accessible, a multi-wavelength illumination has to be utilized so that the field scattering potential can be obtained by an inverse Fourier transform of $E^{(s)}$.

Since only the intensity of the scattered light ($I(P,k)$) is available, then the autocorrelation of the scattering potential is retrieved by taking the inverse Fourier transform of $I(P,k)$:

$$FT^{-1}\{I(P,k)\} = C\langle F^*(z)F(z+Z)\rangle \; = C.ACF_F(Z). \tag{1-34}$$

Scattering potential of the object can be obtained if an additional singular light remitting interface such as a reference mirror is positioned at a distance L from the object at $z = z_I$. In this case, the scattering potential can be described as a sum of the actual object $F_0(z)$ and an impulse potential with amplitude reflectivity R given by

$$F(z) = F_0(z) + R\delta(z - z_I). \tag{1-35}$$

Then, the autocorrelation yields

$$\begin{aligned}\langle F_0^*(z)F_0^*(z+Z)\rangle \; + \; \langle F_0^*(z)R\delta(z+Z-z_I)\rangle \; + \; \langle R\delta^*(z-z_I)F_0(z+Z)\rangle \; + \\ \langle R^2\delta^*(z-z_I)\delta(z-z_I+Z)\rangle \; = \\ ACF_F(z) + RF_0^*(z_I - Z) + RF_0(z_I + Z) + R^2\delta(Z).\end{aligned} \tag{1-36}$$

where the third term $RF_0(z_I + Z)$ can account for a true reconstruction of the object structure centered at $Z = -z_I$. Any overlap between the four terms of the ACF above is avoided by choosing the distance between the interference and the object larger than the object depth: $L > T$. If the object is illuminated only with one wavelength and one direction of illumination, only the integrated information (one-dimensional structure) can be acquired. Three-dimensional structural

information can be reconstructed using multi-wavelength and multi-directional illumination [Wolf-1969, Dändliker-1970]. Multi-directional illumination can be realized if a diffraction grating is used in front of the object [Fercher-1979] and multi-wavelength illumination can be achieved with tunable lasers or broadband light sources such as diode lasers and superluminescent diodes. This is the basic concept of SD-OCT.

1.4 SD-OCT

In SD-OCT, a low time-coherence broadband light source such as a superluminiscent diod (SLD) running at near-infrared wavelength is utilized. The light from the laser source is divided into two lines of sample arm and reference arm using an optical beam-splitter. The schematic diagram of SD-OCT imaging system is shown in **Figure 1-1**. In the reference arm of the interferometer, a stationary mirror is utilized after polarization controller (PC). In the sample arm of the interferometer, an objective lens is used to focus the light into the sample and a galvoscanner mirror system is utilized to perform 3-D scanning on the sample. Then, a 2x2 optical fiber coupler is utilized to recombine the backscattered light from the sample and the reflected light from the reference mirror. The recombined light is then routed to a home-built high-speed spectrometer via the optical circulator. The captured spectrum from each A-line is transferred to the processing unit using National Instruments' Frame-grabber via Camera Link™.

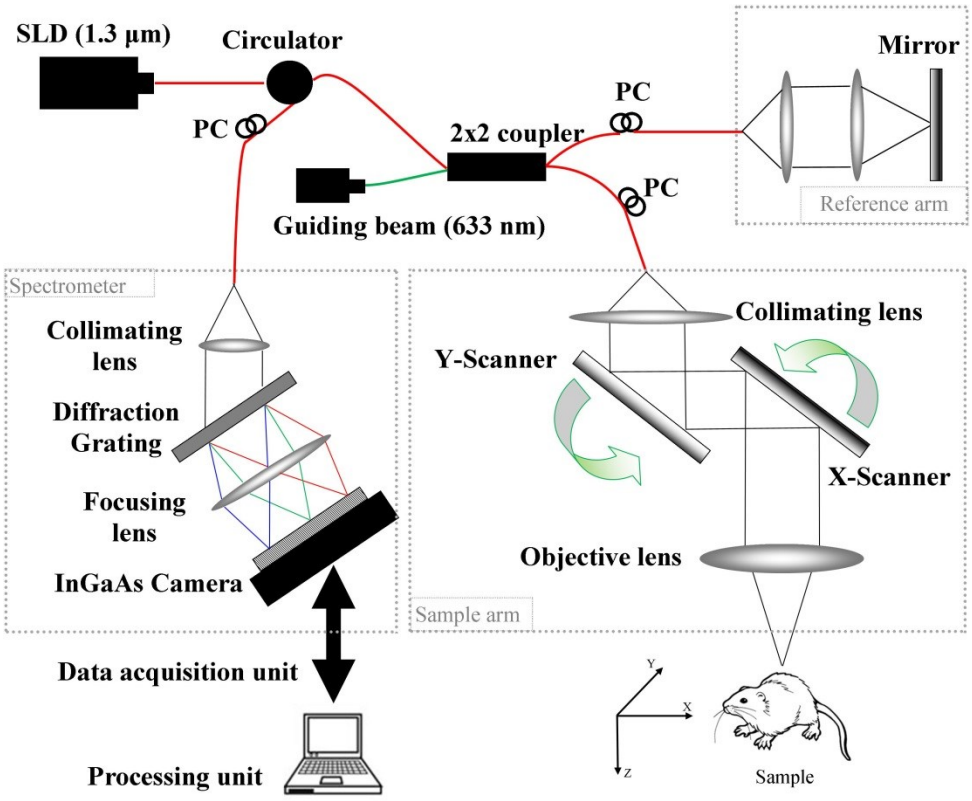

Figure 1-1 Schematic diagram of SD-OCT system set-up.

The spectral intensity at the interferometer is given by

$$I_{SR}(K) = I_S(K) + I_R(K) + 2\sqrt{I_S(K)I_R(K)}\,.\,Re\{\mu(K).\,e^{i[\Phi_S(K)-\Phi_R(K)]}\} \qquad (1\text{-}37)$$

where $I_S(K) = |A_S(K)|^2 = \left|a_s(K).\,e^{i\Phi_S(K)}\right|^2$ is the spectral intensity of the sample beam, $I_R(K)$ is the power spectrum of the reference beam, $\mu(K)$ is the spectral degree of coherence and $\Phi_S(K)$ and $\Phi_R(K)$ are the spectral phase of the sample wave and the reference beam, respectively.

OCT depth field of view (FOV) is limited by the resolution of the spectrometric device. Assuming that $\mu(K) = 1$, $z_{reference} = 0$ and the sample is a point-source δ-like object structure, the interferogram can be written as $2\sqrt{I_s(K)I_R(K)}\cos\{Kz_s\}$ with the spectral interferogram frequency $\omega_K = z_s$ in K-space. It follows from the sampling theorem [Bracewell-2000] that $N =$

$\frac{\Delta K}{\pi} z_s$ equidistant sampling points are required to specify the position z_s of the sample with depth resolution corresponding to ΔK. Therefore, depth FOV is limited by the number of spectrometer element detectors while depth resolution is limited by the spectral width ΔK of the light source.

1.5 OCT system parameters

One of the advantages of OCT is that the axial and the lateral resolutions are decoupled from each other. The axial resolution of the OCT system is determined by the spectral bandwidth of light source and is defined as the half of the coherence length of the light source which can be expressed by

$$R_a = \frac{l_C}{2} \approx \frac{0.44\lambda_0^2}{\Delta\lambda} \tag{1-38}$$

where l_c is the coherence length, λ_0 is the center wavelength and $\Delta\lambda$ is the spectral full-width at half maximum (FWHM) of the light source. The lateral resolution of the OCT system is determined by the objective lens that is used to deliver/focus the light onto the sample and is expressed by

$$R_l = 1.22 \frac{\lambda_0}{2NA_{obj}} \tag{1-39}$$

where NA_{obj} is the numerical aperture (NA) of the objective lens which is inversely proportional to the lateral resolution. On the other hand, the depth-of-focus (DOF) is given by

$$Z_{DOF} = 2 \frac{\lambda_0 n}{NA_{obj}^2} \tag{1-40}$$

where n is the average refractive index of the sample. In general, the lateral resolution can be enhanced by the increase of numerical aperture. The increase of the numerical aperture leads to

the reduction of DOF. Intuitively, increasing the NA of the object lens tends to increase the lateral resolution of the OCT system while at the same time reduces the DOF in the sample. The objective lens is chosen based on the imaging application whether a higher lateral resolution is required or a longer DOF.

The sensitivity of the OCT system is defined by the weakest sample reflectivity that can be measured by the system, which is equivalent to the noise level of the system. The dominating noise sources in the OCT system are shot noise due to photocurrent variance, receiver noise and excess noise due to self-beating of broad-band light waves. The resulting mean square photocurrent noise is given by [Rollins-1999, Podoleanu-1999]

$$\langle \Delta i_p^2 \rangle = \langle \Delta i_{sh}^2 \rangle + \langle \Delta i_{ex}^2 \rangle = 2q_e B\langle i \rangle + (1+\Pi^2)\langle i \rangle^2 \frac{B}{\Delta v_{eff}}, \tag{1-41}$$

where B is the electrical bandwidth, Π is the degree of source polarization, $< i >$ is the mean detector photocurrent and Δv_{eff} is the effective optical line width of the source which is $\Delta v_{eff} = 1.5\Delta v$ where Δv is the full width at half maximum of the power spectrum. Hence, the SNR is the ratio of the mean signal power and the noise power given by

$$SNR = \frac{2\alpha^2 P_S P_R}{\langle i_{sh}^2 \rangle + \langle i_{ex}^2 \rangle + \langle i_{re}^2 \rangle} \tag{1-42}$$

where $\alpha = (\frac{q_e \eta}{h\bar{v}})$, q_e is the electronic bandwidth, P_S is the power at the sample arm and P_R is the power at the reference arm. Intuitively, the OCT system sensitivity is proportional to the source power and inversely proportional to the electronics bandwidth.

1.6 Scanning protocol

3D imaging is achieved by using two galvo-scanners (X-scanner and Y-scanner in Figure 1.1) to raster-scan the focused beam spot across the sample, with one scanner for X-direction (lateral)

scan, and another for Y-direction (elevational) scan. Each B-scan (x-direction scan) is formed by acquiring adjacent A-lines with a spacing of the order of the least sampling distance of based on the system's lateral resolution. Adjacent B-scans on the sample are acquired by shifting the Y-scanner (C-scan direction). The 3D image is formed by placing adjacent B-scan cross-sectional images.

In order to assess OCT functional imaging in addition to tissue structure, scanning pattern on the sample should be manipulated by reducing the scanning frequency (to balance sensitivity and Nyquist rate for Doppler imaging) or repetition of A-scans or B-frames per spatial location (for angiography or speckle tracking). The scanning pattern utilized to assess a specific information is called scanning protocol and is defined by the number of A-scans per location and per B-frame, scanning speed on the scanner, line acquisition rate on the camera and the number of B-frames per 3D data.

1.7 Image reconstruction

Each A-scan is a vector containing k_j, $\mathrm{j} = 1,2,\dots,\mathrm{p}$, where k_j is the wavenumber of the light captured by the jth pixel, j is the pixel number of the line scan CCD camera and p=1024. The interference signal of one A-scan captured by the CCD camera can be expressed by

$$I(k_j) = S(k_j)E_R^2 + 2S(k_j)E_R \int_{-\infty}^{\infty} a(z)cos(2\,k_j nz)dz + 2S(k_j)E_R a(z_l)cos[2k_j nz] \quad (1\text{-}43)$$

where $I(k_j)$ is the light intensity detected by the *jth* detector, k_j is the wavenumber, $j = 1,2,\dots,1024$ is the pixel number of the line scan CCD camera, E_R is the light intensity reflected from the reference mirror, $S(k_j)$ is the spectral density of the light source used at k_j, n is the refractive index of tissue, $a(z)$ is the amplitude of the backscattered light and z is the depth from

which the light back scattered from. In this equation, the self cross-correlation between the light backscattered from different positions within the sample is neglected because the light backscattered from the sample is relatively weaker than the light reflected from the reference mirror. The first term is the DC signal produced the light reflected from the reference mirror and accounts for the background signal. The second term is the spatial frequency component of the static tissue sample which can provide static structural information of the sample. After the A-line is captured, the background signal is subtracted from the spectrum and the interference spectrum is rescaled from the nonlinear wavelength (λ) to frequency domain ($\omega = 2\pi c/\lambda$) by using spline interpolation and resampling, followed by dispersion compensation and Fourier transformation.

In ultrahigh-resolution OCT, dispersion mismatch between the reference and sample arms must be compensated for optimal resolution. Dispersion arises because propagation constants of the tissue $\beta(\omega)$ is frequency dependent and should be compensated to match the dispersion in the reference arm. For any given material, the propagation constant can be expanded by Taylor series expansion near the center frequency of the light source ω_0 given by

$$\beta(\omega) = \beta(\omega_0) + \left.\frac{d\beta}{d\omega}\right|_{\omega_0}(\omega - \omega_0) + \left.\frac{1}{2}\frac{d^2\beta}{d\omega^2}\right|_{\omega_0}(\omega - \omega_0)^2 + \left.\frac{1}{6}\frac{d^3\beta}{d\omega^3}\right|_{\omega_0}(\omega - \omega_0)^3 + \cdots \quad (1\text{-}44)$$

where $\frac{d\beta}{d\omega}$ is the inverse group velocity, $\frac{1}{2}\frac{d^2\beta}{d\omega^2}$ describes the group velocity dispersion that causes broadening of the axial resolution in OCT and $\frac{1}{6}\frac{d^3\beta}{d\omega^3}$ is referred to as third-order dispersion which produces asymmetric distortion of point spread function in OCT [Wojtkowski-2004]. Due to mismatch between reference and sample path lengths, a frequency-dependent phase shift $\phi(\omega)$ is imported to the signal. Therefore if spectrum is multiplied by a nonlinear phase term prior to Fourier transform, the axial resolution is degraded.

Dispersion correction can be performed before applying Fourier transform on the interference signal, after reference background removal and hyperbolic $\omega \sim 1/\lambda$ dependence of the spectrum on wavelength. Since the spectral fringe pattern from the spectrometer is a real function, a Hilbert transform is used to generate the imaginary part of the complex analytic signal of the spectral fringe pattern . Then, the real and imaginary parts of the spectral fringe pattern are used to contruct the complex analytic representation of the spectral fringe pattern $\hat{S}(\omega) = |S(\omega)|e^{(i\phi(\omega))}$. The phase term of $\hat{S}(\omega)$ is modified by adding a phase correction to compensate dispersion:

$$\bar{\phi}(\omega) = -a_2(\omega - \omega_0)^2 - a_3(\omega - \omega_0)^3 \ . \tag{1-45}$$

The coefficient $-a_2$ is adjusted to cancel the group velocity dispersion imbalance and $-a_3$ is adjusted to cancel the third-order dispersion imbalance. Using an iterative approach, these parameters can be automatically estimated to correct the dispersion.

1.8 Optical micro-angiography (OMAG)

Optical micro-angiography (OMAG) is a label-free non-invasive imaging and processing method to obtain 3-D blood perfusion map in microcirculatory tissue beds in vivo using FD-OCT [Wang-2007]. OMAG is based on acquiring very dense B-scan and utilizing the information between adjacent A-lines to assess blood flow perfusion. The sensitivity of the system to blood flow highly depends on the temporal spacing between adjacent A-lines. On the other hand, if the time difference between acquisition of A-lines is long, total scanning time to acquire 3D data will be very long and limits the feasibility for in vivo applications. To overcome the time-spacing limitation and limiting total scanning time, a different scanning protocol is required. Ultrahigh-sensitive OMAG (UHS-OMAG) is a variation of OMAG technique, capable of imaging

microvasculature down to capillary level, in which data acquisition is based on repeated B-scan (frame) acquisition at the same spatial location [An-2010_UHS], and then separating static scatterers (e.g. structure tissue) and dynamic scatterers (e.g. moving red blood cells within patent vessels) by the use of OMAG algorithm. By synergistically utilizing both the amplitude and phase information of complex OCT signals, the OMAG technique is sensitive to both the axial and transverse blood flows, providing blood flow map at small vessels and capillaries as well as larger vessels. UHS-OMAG has been applied to visualize blood perfusion and micro-vasculature map in various living tissue samples such as retina [An-2011], cerebral [Jia-2011], renal microcirculation [Zhi-2011] and skin [Qin-2011]. Hemodynamic quantification can be extremely useful in cancer, stroke and some other disease which involve vasculature.

1.9 Microcirculatory network

The circulatory network in mammals composed of cardiovascular and lymphatic system delivers oxygen, nutrition, immune cells and hormones to tissue via arteries and collects waste materials from cells via veins and lymphatic vessels. These compounds are exchanged with cells via capillary beds. The vessels on the arterial side of the microcirculation are called the arterioles. Arterioles are innervated, surrounded by smooth muscle cells and their diameter is typically 10-100 μm. Nutritious oxygenated blood is delivered by arterioles to the capillaries. Capillaries are the smallest vessels in a body (typically 5-10 μm) and their endothelial linings are only one cell layer thick. The exchange of oxygen, water, carbon dioxide and many other nutrients and waste chemical substances between blood and surrounding tissue is performed by capillary beds. The more metabolically active the cells, the more capillaries they will require to supply nutrients and carry away waste products. The capillary wall is a one-layer endothelium that allows

bidirectional gas and lipophilic molecules to pass through without the need for special transport mechanisms depending on osmotic gradients. Deoxygenated blood flows out of the capillaries into the venules (typically 10-200 μm) which have little smooth muscles. Erythrocytes or red blood cells (RBCs), the most common type of blood cells, are the main career of transferring oxygen and tissue fluid to the cells. RBCs are mainly composed of a protein called hemoglobin that binds to oxygen contained in a flexible plasma membrane. From the top view, their shape appears as a circular disk and from the side view appears as a biconcaved disk. Although their size is typically around 7 μm in diameter, their unique shape allows RBCs to squeeze through capillaries as small as 3 μm while capillaries partially expand as erythrocytes and leukocytes pass through them. In addition to these blood vessels, the microcirculation network also includes lymphatic capillaries and collecting ducts. The lymphatic system usually develops in parallel to the blood vessels in the skin and in most internal organs and is not present in central nervous system, bone marrow and avascular structures such as cartilage, epidermis and cornea. Besides draining lymph fluid from extracellular spaces, other roles of lymphatic system include absorbing lipids from intestinal tract, maintaining fluid hemostasis and transporting antigen-presenting cells and leukocytes to lymphoid organs. Also, lymphatic system plays an important role in the development of several diseases such as cancer, lymphedema, some inflammatory conditions and allergies [Alitalo-2005, Oliver-2004, Zgraggen-2013].

Chapter 2. EIGENDECOMPOSITION-BASED CLUTTER REJECTION FILTERS

2.1 Background and literature review

There are various methods reported in the literature to visualize blood flow in vessels and contrast them from surrounding tissue microstructures using OCT imaging systems. Optical Doppler tomography (ODT) combines Doppler velocimetry with OCT and utilizes the Doppler shift in the frequency of light scattered from a moving particle (such as red blood cells) to measure the velocity both in time-domain [Chen-1997] and frequency-domain [Wang-2004] OCT. In order to detect the Doppler shifts in the frequency spectrum, multiple observations (ensembles) of the interference signal from the same location are acquired. Then, the Doppler center frequency is estimated using spectrogram method based on the short-time Fourier transform (STFT) algorithm. However, the minimum detectable Doppler frequency shift varies inversely with the FFT window time at each pixel, which introduces a trade-off between velocity sensitivity and imaging speed as well as spatial resolution [Ding-2002].

In order to remove the relationship between the velocity sensitivity and spatial resolution while maintaining a high acquisition speed, phase resolved optical Doppler tomography (PRODT) was introduced in time [Ding-2002] and frequency domain [Wang-2004]. PRODT evaluates the phase difference between adjacent A-lines within one B-image to estimate the Doppler frequency shift. Then, the estimated mean frequency is used to measure the blood flow velocity using Kasai autocorrelation technique [Kasai-1985]. Although widely used, the sensitivity of PRODT to blood flow is low and makes it difficult to visualize 3D microcirculations in applications such as

human skin where the blood flow within the capillary vessels is in the order of 0.1 – 0.9 mm/s [Kellman-1996]. Also, it would be advantageous to extract Doppler information using the frequency domain method because the velocity dynamic range of a phase-resolved ODT system is determined by A-line scanning rate.

Vokac et al. [Vakoc-2009] proposed a method to improve the sensitivity of PROCT by utilizing the phase variance between adjacent B-scans. However, their method was sensitive to slow flows within capillary vessels, because, the time interval between the adjacent B-scan images was relatively long (~ few microseconds). Because of the relatively long imaging time (~25 min), their method could not be used for *in vivo* human applications such as human skin or retina where involuntary subject movements are inevitable.

Clutter rejection is one of the most important data processing steps in visualizing blood perfusion and vascular structures. Clutter is the scattered signal from stationary or slowly moving tissues in the coherence sampling volume of the probe beam in the sample arm. Since clutter signal is typically stronger than the Doppler signal, it can reduce the sensitivity and accuracy in estimating the flow. The concept of clutter rejection filtering is similar to medical ultrasonic imaging where mechanical ultrasound waves are used to visualize the blood flow in arteries and veins. Color Doppler imaging (CDI), a tomographic real-time imaging technique, is one of the principal ultrasonic imaging modalities that is similar to optical micro-angiography and has a wide range of clinical applications. In CDI, blood flow of an ROI (region of interest) is color-coded and visualized on top of B-mode (gray-scale coded intensity image of tissue structures) images and displayed in real-time (33 frames per second or higher). In order to estimate the Doppler frequency shift, clutter should be suppressed using a post-processing step commonly known as clutter rejection filtering. Clutter filters can be divided into three main categories:

static filters where an IIR or FIR filter with fixed coefficients is used, adaptive filters where the characteristics of the filter is adapted to the received signal, and a combination of static and adaptive filters. Static filters are widely used and preferred over adaptive ones in commercial products because they can be implemented in real-time. However, static filters cannot efficiently remove clutter due to nonstationary tissue motions from cardiac activities, respiration and the transducer/patient movements. Also, the assumption that clutter is centered around zero frequency is not always met in practice. Several adaptive filters have been proposed among which eigen-regression filters can theoretically provide the maximum clutter suppression due to its best mean square approximation of the clutter [Kruss-2002].

There are several methods proposed in the literature for clutter rejection in OCT-based flow imaging. Ren and Li [Li-2006] developed a delay line filter (DLF) to reject the clutter effect and showed that a first-order phase-shifted DLF could effectively remove the clutter in capillary flow phantom and in mouse ear. Compared to the conventional phase-resolved optical Doppler tomography, DLF was more sensitive to Doppler flow and picking up small blood vessels that were masked by clutter signal in PR-OCT. Also An and Wang [An-2010] applied a static high-pass filter in OMAG to remove the clutter component from the received Doppler signal. However, these static filters were sensitive to tissue movements and their performance in removing the clutter degraded at the presence of unwanted motion. In order to compensate bulk tissue motion, An and Wang [An-2008] proposed a phase compensation method to estimate clutter's center frequency and shift it to zero, and then applied a static filter to remove the clutter component. However, this technique may not be effective when the clutter is broadband or the flow signal is very strong where the estimated center frequency may not be accurate.

2.2 Proposed approach

In this part, we propose eigendecposition-based filtering technique for clutter rejection in optical imaging of blood flow. A series of flow phantom studies are performed where tissue (phantom) motion is externally introduced by tapping over the imaging surface to simulate tissue motion. The performance of ED-based clutter rejection in removing the tissue motion and picking up the flow information is studied and the efficiency of the proposed technique is compared with those of phase-compensation method and static high-pass filtering. Also, *in vivo* experiments are performed for visualizing microcirculations within human skin tissue beds and the performance of different clutter filters is compared with each other. Finally, we show the sensitivity of the ED-based clutter rejection filters in picking up blood flow in the capillaries of mouse ear.

2.3 Methodology and problem formulation

The interference signal of one B-scan captured by the CCD camera can be expressed by

$$I(t,k_j) = S(t,k_j).E_R^2 + 2S(t,k_j).E_R \int_{-\infty}^{\infty} a(z,t).\cos(2\,k_j n(t) z)dz$$
$$+ 2S(t,k_j).E_R a(z_l).\cos[2k_j n(t)(z_l - vt)] \quad (2\text{-}1)$$

where $I(t,k_j)$ is the light intensity detected by the jth detector at time t, k_j is the wavenumber, j=1,2,…,1024 is the pixel number of the line scan CCS camera, E_R is the light reflected from the reference mirror, $S(k_j)$ is the spectral density of the light source used at k_j, n is the refractive index of tissue, z is the depth coordinate, $a(z)$ is the amplitude of the backscattered light and z is the depth from which the light back scattered from, v is the velocity of moving blood cells in a blood vessel which is located at depth z_l. In this equation, the self cross-correlation between the light backscattered from different positions within the sample is neglected because the light

backscattered from the sample is relatively weaker than the light reflected from the reference mirror. The first term in (1) is the DC signal produced the light reflected from the reference mirror. The second term is the spatial frequency component of the static tissue sample which can provide static structural information of the sample. The third term is the Doppler beating signal which is introduced by the moving particles in the tissue sample.

2.3.1 Flow sensitivity

The maximum detectable velocity that is not phase-wrapped is determined by the time spacing (ΔT) between adjacent A scans, $v = \lambda / 2n\Delta T$, where λ is the central wavelength of the light source, *n* is the average refractive index of the sample and factor of two is accounting for the forward and return path. So, detecting the flow in the capillary, in which the typical flow velocity is ≤100 μm/s, requires the time spacing to be larger than ~4.7 ms which corresponds to a scanning speed of ~213 A scans per second. However, such a long imaging time is not practical for 3D *in vivo* imaging of capillary blood flows. In contrast to the conventional OMAG method, current scanning protocol utilizes scanning in the C-scan direction to increase the sensitivity of the system to the minimum detectable flow while keeping the imaging speed high. In our system setup, the imaging rate is 300 fps (t_C~3.3 ms). Therefore, considering that the C scan direction is densely sampled at an oversampling factor of 12, the detectable flow velocity would be ~141 μm/s while the imaging speed is still kept at 47,000 A scans per second. This detectable flow velocity would be sufficient to image the blood flow in capillaries. It should be noted that the maximum detectable velocity by the system is determined by the system imaging speed. In this case, the imaging speed is the A-scan rate which is 47 KHz and the maximum detectable velocity by the system is ~15 mm/s. However, if the velocity is >141 μm/s, the phase wrapping effect will occur and the true velocity may not be measured unless some phase-unwrapping algorithm

be used [Subhash-2010]. On the other hand, the minimum detectable flow velocity is determined by the system phase noise floor, $\sigma_{\Delta\varphi}^2$=1/S where *S* is the intensity signal to noise ratio [Vakoc-2005]. Thus, with the system signal to noise ratio at 105 dB, the minimum detectable flow velocity would be ~4.0 μm/s.

2.3.2 ED-Filtering formulation

In order to retrieve the flow information, multiple A-lines are acquired from the same location. After removing the DC component in Eq. 1, the phase difference at each depth location is utilized to estimate its corresponding average flow velocity. The received backscattered signal at a particular depth along each A-line form a vector defined as

$$X = [x(1),\ x(2), \dots, x(N)]^T \tag{2-2}$$

where *N* is the ensemble size. The observation or ensemble of samples from one particular depth location is modeled as the sum of three independent zero-mean complex Gaussian processes: a clutter component *c*, a blood component *b* and additive white noise *n*. Its vector notation is given by

$$X = c + b + n\ . \tag{2-3}$$

ED-based filtering takes advantage of the characteristics unique to high-frequency blood flow mapping that tissue motion is correlated over the depth of interest and the reasonable tissue motion velocities are small but on the same order of the blood flow velocity [Kruse-2002].

Since *X* is Gaussian, it is completely characterized by its correlation matrix *Rx*, given by

$$R_x = R_c + R_b + \sigma_n^2 I \tag{2-4}$$

where R_C is the clutter correlation matrix, R_b is the blood correlation matrix, σ_n^2 is the noise variance, and I is the identity matrix.

Assuming that clutter is the dominant signal and its characteristics are similar along the depth [Song-2006], spatial average of the correlation of the received signal along the axial direction is an estimate of the clutter correlation matrix R_C given by

$$\widehat{\mathrm{R}}_{\mathrm{c}} = \frac{1}{\mathrm{M}}\sum_{\mathrm{i}=1}^{\mathrm{M}} \widehat{\mathrm{R}}_{\mathrm{c}} = \frac{1}{\mathrm{M}}\sum_{\mathrm{i}=1}^{\mathrm{M}} \mathrm{X_i X_i^H} \tag{2-5}$$

where X_i is the complex Doppler signal from depth i, $(.)^H$ is the Hermitian transpose. The estimated correlation matrix $\hat{R}_c$ is decomposed into its corresponding eigenvalues and eigenvectors given by

$$\hat{R}_c = E\Lambda E^H \tag{2-6}$$

where $E=[e_1, e_2, \ldots, e_N]$ is the $N \times N$ unitary matrix of eigenvectors, $\Lambda=diag\{\lambda_1, \lambda_2, \ldots, \lambda_N\}$ is the $N \times N$ diagonal matrix of eigenvalues and $\lambda_1 \geq \lambda_2 \geq \ldots \lambda_N = \sigma_n^2$ and σ_n^2 is the noise variance. Assuming that the clutter space is spanned by K eigenvectors, eigenregression filter is applied to the received signal by removing the clutter components as follows

$$Y = (I - \sum_i e_i e_i^H).X \tag{2-7}$$

where Y is the Doppler signal after removing the clutter component. Also, the corresponding frequency response of this filter can be represented by

$$H(\omega) = 1 - \frac{1}{N}\sum_i |DTFT\{e_i\}|^2 \tag{2-8}$$

where DTFT is the discrete-time Fourier transform (DTFT).

And finally, the Doppler center frequency of the flow is estimated by

$$\hat{f}_b = \frac{1}{2\pi} atan(\frac{Im\{\hat{R}_y(1)\}}{Re\{\hat{R}_y(1)\}}) \tag{2-9}$$

where $\hat{R}_y(1)$ is the first lag autocorrelation of *Y*.

2.4 Experimental setup

The schematic of the OCT system is previously given in **Figure 1-1**. In the OCT system, we used a superluminiscent diode (SLD) with the center wavelength of 1310 nm and bandwidth of 65 nm was used, delivering an axial resolution of ~12 μm in the air. An optical circulator was used to couple the light from the SLD into fiber-based Michelson interferometer. In the reference arm of the interferometer, a stationary mirror was utilized after polarization controller. In the sample arm of the interferometer, a microscopy objective lens with 18-mm focal length was used to achieve ~5.8 μm lateral resolution. Then, a 2 × 2 optical fiber coupler was utilized to recombine the backscattered light from the sample and the reflected light from the reference mirror. Since the wavelength of the light source is invisible to the human eye, a 633-nm laser diode was used as a guiding beam to locate the imaging position. This reference helps to adjust the sample under the OMAG/OCT system and image the desired location. The recombined light was then routed to a home-built high-speed spectrometer via the optical circulator. In the design of the spectrometer, a collimator with the focal length of 30 mm and a 14-b, 1024-pixels InGaAs linescan camera (SUI, Goodrich Corp) were used. The camera speed was 47 000 lines per second and the measured SNR was ~105 dB with a light power on the sample at ~3 mW. The spectral resolution of the designed spectrometer was ~0.141. The schematic

2.5 Experimental results

We applied the ED-based technique both in phantom and in *in vivo* and compared its quantitative and qualitative performance with that of phase-compensation and high-pass filtering. Then, we

applied ED-based technique to visualize microcirculation in microvascular structures in mouse ear.

2.5.1 Phantom studies

First, we performed a series of experiments on a custom-made flow phantom. The phantom was made from gelatin mixed with 2% milk to simulate the background optical heterogeneity of the tissue in which a capillary tube with an inner diameter of ~200 μm was submerged and v2% TiO2 particle solution was flowing in it. The inclining angle of the tube towards the incident beam (Doppler angle) was set at ~80°. The flow rate of the particle was controlled by a precision syringe pump to a range that falls within the detectable range of the OMAG system. In this experiment, the ensemble size of OMAG data was 9. In order to mimic tissue movements, we intentionally introduced motion to the phantom by tapping over the imaging surface and phantom while increasing the tapping intensity for each experiment.

The performance of each clutter filter was measured by two quantities: clutter suppression level (CSL) and flow suppression level (FSL). CSL and FSL are defined by the ratios of the signal power before and after clutter suppression in the already known flow and stationary areas. The comparison criteria are based on the ability of each filter in suppressing the clutter in the stationary areas and the suppression level in the flow area.

Typical performance of different clutter rejection filters for one cross section of the flow phantom is displayed in **Figure 2-1(A), (B)** and **(C)**, where static high-pass filter, phase compensation and ED-based technique have been applied, respectively. In this figure, the darker intensities correspond to less power suppression. Also, the structure image of the phantom is shown in **Figure 2-1(D)** where the flow pipe is located in the center and is surrounded by the phantom material. The structure image is very blurry which shows some motion in the phantom

tissue and pipe due to the external motion introduced by tapping. It can be observed that the performance of static high-pass filter is inferior compared to the other two methods. Also, ED-based techniques is superior to the phase compensation method where the pipe's surrounding tissues is brighter (higher suppression level in stationary area). Also, the boundaries of the flow pipe and the edges of the phantom are darker in phase compensation (less suppression of the stationary tissue boundaries) where these areas have been more effectively suppressed via ED.

Table 2.1 represents the quantitative comparison between different filters where the average FSL and CSL are measured for all experiments. Compared to the other two methods, ED-based technique was more effective in suppressing clutter while its flow suppression was similar to phase compensation. Although static high-pass filter had lower FSL value, it was not as effective as the other two methods in suppressing clutter.

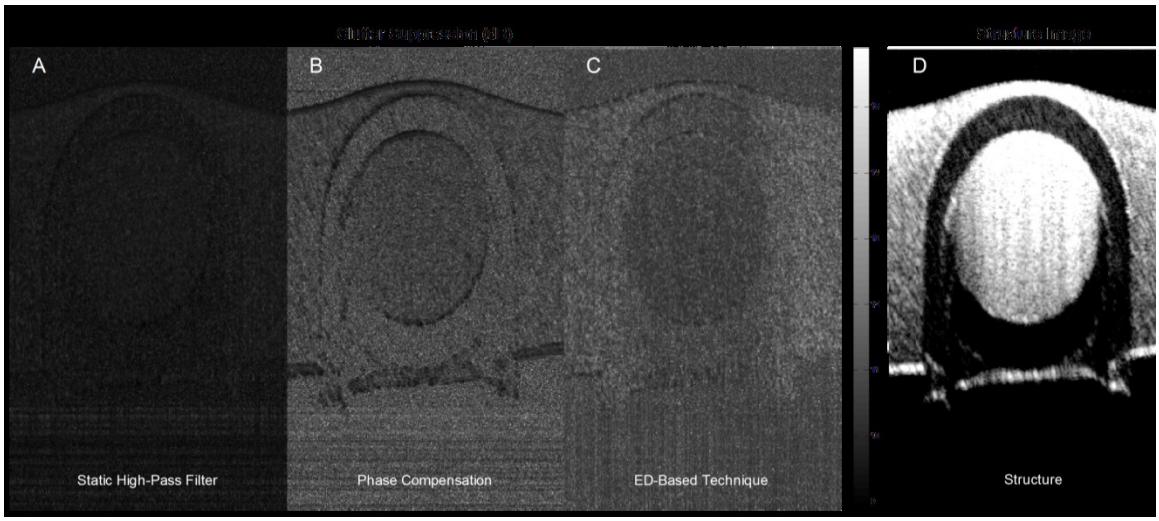

Figure 2-1 Typical performance of clutter rejection filters in flow phantom studies.

(A) static high-pass filter, (B) phase compensation and (C) ED-based technique. The flow pipe is located in the center, surrounded by tissue material. The intensity values correspond to the suppression level after clutter rejection. Higher suppression outside the tube (more bright) and lower suppression inside the tube (less bright) is preferred. (D) Structure image, which is blurry because of the motion introduced by tapping over the imaging surface to simulate tissue motion.

Table 2-1 The quantitative comparison between different filters in phantom studies

	Static High-pass filter	Phase compensation	ED-based clutter rejection
CSL (dB)	10.7	11.9	12.9
FSL (dB)	9.6	10.7	10.7

2.5.2 In vivo human skin

We applied different clutter filtering techniques to OCT images acquired from human skin. The images were acquired from the back of the finger of a healthy volunteer. In this experiment, the ensemble size of OMAG data was 4. **Figure 2-2** shows one slice of the 3D image in the X-Y plane which is visualizing microcirculations in reticular dermis (RD) layer of the skin. The RD is the lower layer of the dermis, found under the papillary dermis (PD), composed of thick, densely packed collagen fibers, and the primary location of dermal elastic fibers [Marks-2006]. **Figures 2-2(A), (B)** and **(C)** correspond to static high-pass filter, phase compensation and ED-based technique, respectively, applied to the same dataset acquired from the RD layer. It can be observed that ED-based technique, compared to the phase compensation and static high-pass filter, reveals more detail in the microcirculation and is less sensitive to unwanted tissue motion during optical scanning. Also, when ED-based technique is used, large vessels appear brighter which means that the flow signal is stronger at that location and the flow map image has a better contrast. Note the arrows pointing to the locations where ED-based technique in particular outperforms the other methods and the micro-vascular structure in the pointed locations are distinctively visible in **Figure 2-2(C)** while such structures were not visible in **Figures 2-2(A)** and **(B)**. The estimated root-mean-square (RMS) contrast values of the cross-sectional images shown in **Figure 2-2 (A), (B)** and **(C)** are 41.76, 42.57 and 46.72, respectively.

Also, **Figure 2-3** shows micro-vascular structures in the papillary dermis (PD) layer of the human skin acquired from another location on the back of the finger of a healthy volunteer. Similar to **Figure 2-3**, different techniques have been applied to the same data location where ED-based technique outperformed the other two. The pointed arrows, specifically pinpoint some locations where qualitative comparison between the en-face images confirms the ability of ED-based technique in removing clutter and better assessment of micro-vascular structures. The estimated RMS contrast values of the cross-sectional images shown in **Figures 2-3 (A), (B)** and **(C)** are 44.98, 45.50 and 52.01, respectively.

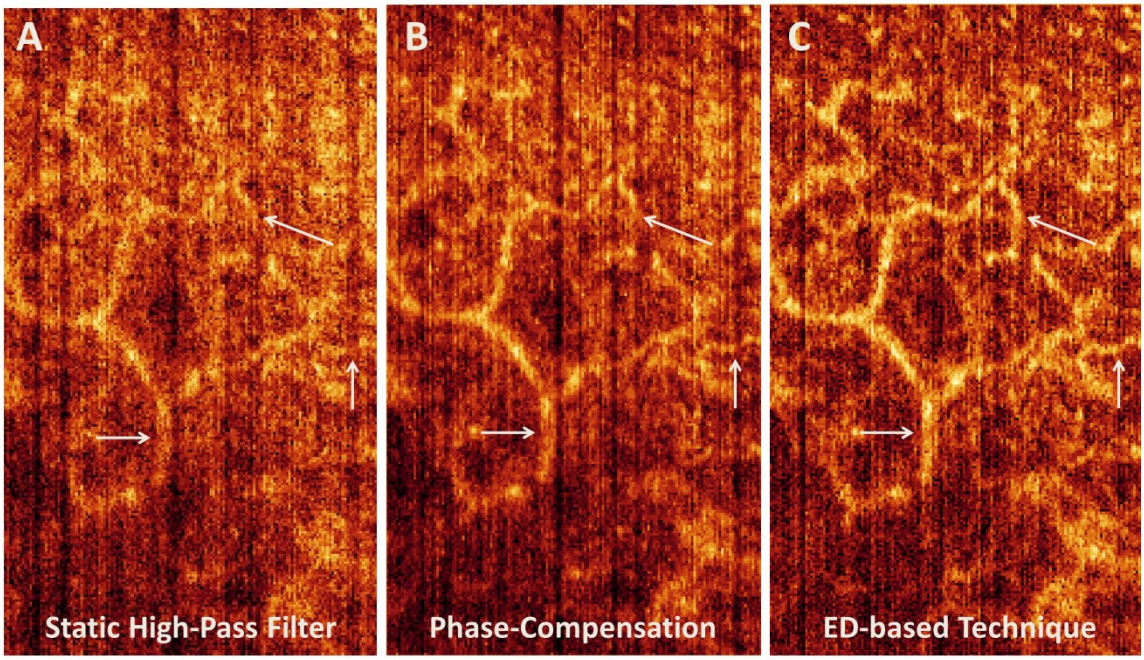

Figure 2-2 Qualitative comparison between static high-pass filter

(A), phase compensation (B) and ED-based technique (C) on one slice of the human skin in the X-Y plane showing vascular perfusion in reticular dermis layer. The estimated root-mean-square contrast value for each image is 41.76, 42.57 and 46.72 for **Figures 2-2 (A), (B)** and **(C)**, respectively.

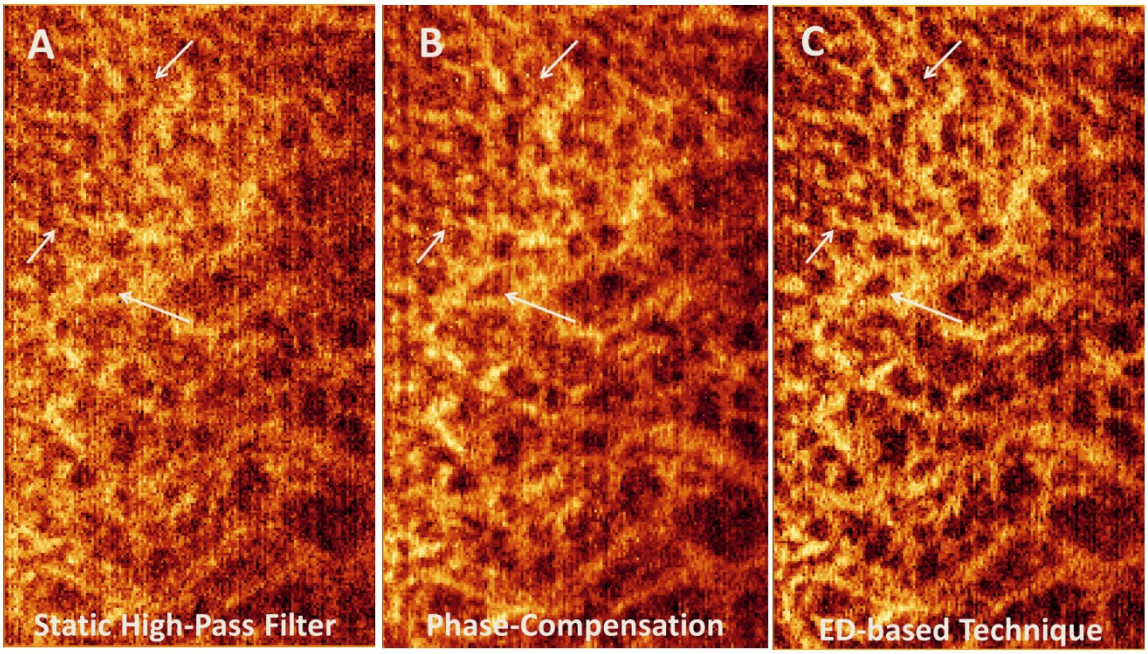

Figure 2-3 Qualitative comparison between static high-pass filter

(A), phase compensation (B) and ED-based technique (C) on one slice of the human skin in the X-Y plane showing vascular perfusion in papillary dermis layer. The estimated root-mean-square contrast values are 44.98, 45.50 and 52.01 for **Figures 2-3 (A),** (B) and **(C)**, respectively.

2.5.3 In vivo mouse ear

The skin of the hairless mouse ear closely resembles human skin, with the exception of sweat glands. Mouse ear is ~300 µm thick and is composed of two full-thickness layers of skin separated by a thin supporting skeleton of elastic cartilage. The vascular network of the hairless mouse ear normally originates from three pairs of arterioles and venules entering the base of the ear. Four subdivisions (or orders) of blood vessels are noted from the three primary pairs of arterioles and venules (first-order vessels) to the precapillary arterioles and postcapillary venules (fourth-order vessels). The inner diameters of arterioles range from 35 µm in the first-order arterioles to 8-9 µm in the precapillary arterioles while ranging from 50-400 µm for first-order to 8-9 µm for the fourth-order venules. Also, arteriovenous anastomoses (AVA) with intermittent

flow (inner diameters ranging from 10- to 12- μm) supply a branching network of capillaries. Most capillary loops are observed around the hair follicle [Eriksson-1980].

We acquired noninvasive 3D optical images from the ear skin of a three months old mouse. A healthy C57 BL/6 mouse weighting around 25 gm was used in this study. The experimental protocol was in compliance with the Federal guidelines for care and handling of small rodents and approved by the Institution Animal Care and Use Committee (IACUC) of University of Washington. **Figure 2-4** shows an *en-face* (x-z) 3D volumetric projection image of the microvascular network in mouse ear where ED-based clutter filter has been applied to the received Doppler data. Detailed organization of the vascular structure of the capillaries, arterioles, venules and arterio-venous anastomosis can be observed.

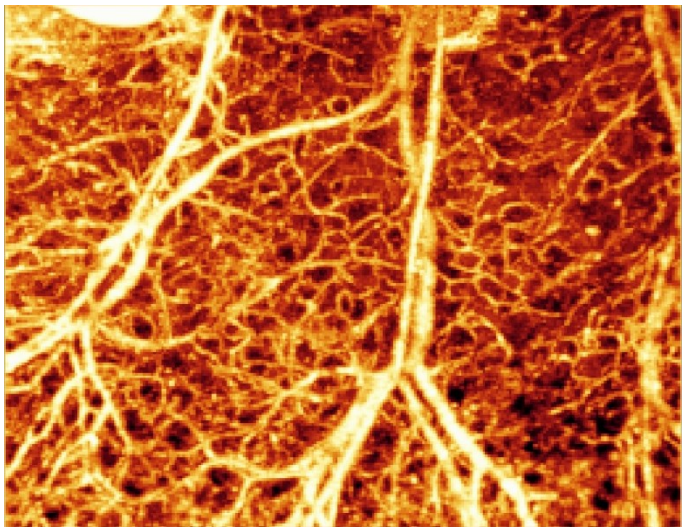

Figure 2-4 En-face projection image of the microvascular network in mouse ear.

2.5.4 Discussions

Compared to the static high-pass filtering and phase-compensation method, ED-based technique was less sensitive to tissue motion and could suppress clutter more efficiently. However, it is computationally more expensive than the other two methods. Although, Lovstakken et al.

[Lovstakken-2006] proposed an algorithm for real-time implementation of adaptive ED-based clutter rejection filtering in ultrasound color Doppler imaging (CDI), static filters are still preferred over adaptive ones in real-time applications.

We implemented static high-pass filter, phase-compensation method and ED-based technique in Matlab® and estimated their performance on a personal computer with a six-core 3.4 Ghz processor and 8 GB of memory. Each frame consisted of 256 A-lines, 512 samples per A-line and 9 ensembles. The average processing time for one frame using static high-pass filter, phase-compensation method and ED-based technique was about 1.775, 5.914 and 2.104 seconds, respectively. Therefore, processing a 3D image which has 200 B-lines using ED-based technique can take ~7 minutes.

ED-based technique assumes that the clutter is the most dominant portion of the received signal. However, when a very strong flow (arteries that are considered very large in the scale of OCT imaging) is present, that assumption is no longer true. In this case, the order of the eigenvalues will change and the largest eigenvalues are no longer corresponding to the clutter.

Also, selecting the appropriate number of eigenvectors to represent clutter space is always a challenge. In most of the *in vivo* experiments, the first two eigenvectors were properly representing the clutter space. However, that was not the case in phantom studies and more than two eigenvectors were removed to better reject clutter components (especially when the tapping intensity and manually introduced motion in the phantom increased). In order to account for this problem, an algorithm can be used to estimate the center frequency of each eigenvector and categorize that as either clutter or flow. Also, the ensemble size can also impact the number of eigenvectors representing each space.

It should also be noted that ensemble size can have an impact on the performance of ED-based technique and increasing the ensemble size will improve the performance of clutter filter in better estimation of the clutter spectrum. However, increasing the ensemble size, linearly reduces the imaging speed and frame rate and there is always a trade-off between ensemble size and imaging speed.

2.6 Conclusions

In this chapter, we proposed ED-based clutter filtering technique for clutter suppression in optical imaging of blood flow. The performance of the proposed filter was compared with two existing methods, static high-pass filtering and phase-compensation method, where ED-based technique outperformed the other two methods, qualitatively and quantitatively. We compared the performance of these filters in a custom-built phantom and *in vivo* human skin. Also, the 3D projection view of *in vivo* imaging of mouse ear using ED-based technique was presented. This technique can be used in flow imaging applications where clutter suppression is required to extract flow information from the stationary or slowly moving tissues and specially when involuntary movements due to cardiac and respiratory cycles are inevitable (such as retina imaging).

Chapter 3. UNIFORM ENHANCEMENT OF OPTICAL MICRO-ANGIOGRAPHY IMAGES

3.1 Introduction

Label-free optical hemodynamic imaging has made possible the visualization of moving red blood cells inside vessels and separating them from surrounding tissues [Wang-2007_OMAG]. Such complementary information to the tissue microstructure can be used to monitor physiological and pathological behaviors of living tissue [Misgeld-2006]. Developmental tissues such as regeneration and maturation, is always accompanied by formation of new vessels (angiogenesis), and monitoring of this progress can be useful in numerous research and clinical applications [McDonald-2003]. Also, some diseases are directly or indirectly related to or influenced by the functional microvasculature, for example stroke and traumatic brain injury [Molina-2005], diabetes [Imai-2001], wound healing [Martin-1997], glaucoma [Wollstein-2005] and age-related macular degeneration [Hee-1996].

When the imaging is performed, the probing light is subject to specular reflection at the tissue surface when it shines onto tissue. Furthermore, the propagation of light within the tissue suffers from attenuation and scattering which makes the backscattering light collected at the detector non-uniform. These physical limitations can result in local imaging contrast degraded, leading to non-uniform appearance of the micro-angiogram images. This situation is more serious when a large area of the tissue is imaged, in which because of the limited field of view of the current scanning mechanism of the probe beam, multiple tile images are needed to acquire and stitch together (mosaicking) to form a final image. In such circumstance, even by fixing the

visualization dynamic range for each of the image tiles, the final vasculature map will still not be homogenous throughout the entire image.

Figure 1A shows the vasculature map in mouse ear which is formed by stitching 22 OMAG images together. Although the dynamic range in all of the images is identical, an obvious difference is observed between their background and contrast. It can be observed that the background on the lower part of the ear is relatively higher than the other areas. Also, some small vessels and capillary loops on the ear edge are with very low contrast. Similarly, Figure 1B shows the vasculature map in another mouse ear, which is the result of stitching 29 OMAG images together. The background inhomogeneity due to specular reflection and low signal at capillary loops is significant, affecting the visualization and eventual quantification. Also, the intensity value at some large vessels is saturated. Due to these problems, OMAG images acquired at different time points or from different animals would not be repeatable, especially when quantifying some vessel parameters such as vessel area density and vessel diameter are required.

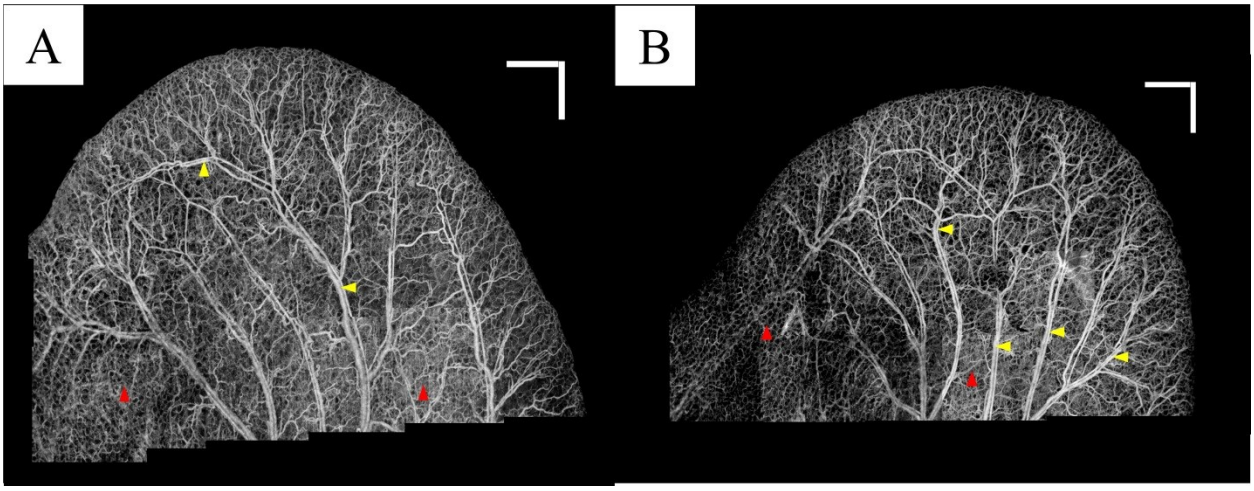

Figure 3-1 Nonuniform perfusion map distribution.

OMAG images of two mouse ear vasculature maps after stitching 22 (A) and 29 (B) mosaics. The background is inhomogeneous and the signal strength and contrast at small vessels and capillary loops is low (red arrows). Also, some larger vessels are saturated (yellow arrows).

In order to solve this problem, a post-processing step is required. Digital contrast enhancement is a post-processing technique applied to digital images to qualitatively improve the contrast of images. This process allows fixed or adaptive manipulation of the dynamic range such that the results are more informative for human eye. Normal human visual system can only distinguish less than ~100 different gray levels. However, current technology allows for capturing digital images at very higher bit information (12-14 bits or higher) which is about a few thousand levels. In order to distinguish an object from its surrounding environment, a good contrast in the image is required. Contrast is defined as the difference in luminance between the object of interest and the other objects at the same field of view. The post-processing algorithms are popular in the field of radiology [Miles-2012], computed tomography [Tan-2012] and digital mammography [Pisano-2000] where the contrast of the images are typically low and requires manual/automatic enhancement for better diagnosis.

In other words, the goal of this post-processing step is to map a given intensity value of one specific pixel (and its surroundings) of the input image, to an output value to form a visually uniform, informative and high-contrast image in the output. The existing contrast enhancing and normalization algorithms can be divided into two categories: static and adaptive. In static algorithms such as intensity windowing, a small range of input intensity dynamic range is stretched to the entire visualization dynamic range and the values below and above the limits are saturated. Histogram of an image is the probability distribution function (PDF) of the occurrence of one specific gray level in that image. Histogram equalization (HE) is a contrast enhancement technique that increases the global contrast of images when the information content is

represented by close contrast values. HE method maps input intensities to an output image where its PDF is uniform and its cumulative distribution function (CDF) histogram is the same as the input image. This allows stretching the contrast of the image to be distributed uniformly in the dynamic range [Gonzalez-2002]. However, HE may produce unrealistic images and amplify background noise while decreasing the usable data. HE has been generalized to local histogram equalization which divides the input image into smaller regions and applies HE algorithm to create a uniform distribution in each region. This method is commonly known as adaptive histogram equalization (AHE) [Pizer-1987]. One of the disadvantages of AHE is noise amplification in homogenous regions. In order to overcome this limitation, contrast limited adaptive histogram equalization (CLAHE) was proposed [Pizer-1990, Zuiderveld-1997]. CLAHE limits amplification of noise by clipping the histogram at a pre-defined value before computing the CDF that limits the slope of the output CDF and eventually the transformation function. High peaks in the histograms are usually caused by uniform regions. The advantage of CLAHE is that it equally redistributes the part of the histogram above a clip limit among all histogram bins. Yet, a uniform PDF distribution is not ideal because it would simultaneously distribute the dynamic range between background and foreground and also amplify the noise effect. In order to improve the contrast of OMAG images while not saturating uniform and high intensity areas, non-uniform distribution functions such as Rayleigh (bell shape) distribution can be used. Intuitively, the Rayleigh distribution of OMAG image imposes this condition in that intensities are distributed evenly between small and large vessels, larger vessels are not saturated and there is a good contrast between vessels and their background. Although some other distributions such as Gaussian and exponential can be used instead, we have experimentally observed better results with Rayleigh distribution.

In this section, we propose using Rayleigh contrast-limited adaptive histogram equalization (RCLAHE) technique to create a high-contrast and visually more homogenous OMAG images and a good background/foreground separation without changing physical OMAG quantitative parameters such as vessel area density, vessel length fraction and fractal dimension [Reif-2012]. We also compare the results with some existing methods from the qualitative and quantitative point of view.

3.2 Methodology

3.2.1 Rayleigh contrast-limited adaptive histogram equalization (RCLAHE)

The RCLAHE algorithm can be divided into the following steps:

Step 1: The input image is divided into non-overlapping contextual regions (tiles).

Step 2: For each tile, the height of the histogram of that tile is clipped by the input clip value. Clipping the height of the histogram is equivalent to limiting the slope of the mapping function. The clipping rule is given by the following statements:

$$\boldsymbol{If}\ H_{tile}(i) > N_{clip-limit}\ \boldsymbol{then}\ H_{tile-clip}(i) = N_{clip-limit} \tag{3-1}$$

$$\boldsymbol{Else\ if}\ (H_{tile}(i) + N_{apd}) > N_{clip-limit}\ \boldsymbol{then}\ H_{tile-clip}(i) = N_{clip-limit} \tag{3-2}$$

$$\boldsymbol{Else}\ H_{tile-clip}(i) = (H_{tile}(i) + N_{apd}) \tag{3-3}$$

where $H_{tile}(i)$ is the histogram of the image tile (contextual region), $H_{tile-clip}(i)$ is the clipped histogram of the tile, $N_{clip-limit}$ is the actual clip limit which is defined by

$$N_{clip-limit} = (Maximum\ multiple\ of\ average\ pixels\ in\ each\ gray\ level\ of\ the\ tile) \times (average\ number\ of\ pixels) \tag{3-4}$$

and N_{apd} is the average number of pixels distributed into each gray level.

Step 3: The intensity values of the tile after histogram clipping is then transformed into the Rayleigh distribution. RCLAHE is based on a monotonic gray-level intensity transformation such that the cumulative output density should equal to the cumulative probability distribution of the input image. Mathematically, the output intensity level y is related to the input intensity level x by Rayleigh function given by

$$y = y_{min} + \left[2\alpha^2 \ln\left\{\frac{1}{1-P_{input}(x)}\right\}\right]^{1/2} \tag{3-5}$$

where y_{min} is the low bound, α is the Rayleigh parameter and $P_{input}(x)$ is the cumulative probability of the input image. Then, the output probability density can then be derived as

$$p(y) = \frac{y-y_{min}}{\alpha^2} \exp\left\{-\frac{(y-y_{min})^2}{2\alpha^2}\right\} \quad for\ y \geq y_{min}. \tag{3-6}$$

A higher Rayleigh parameter (α) value will result in more significant contrast enhancement in the image while at the same time increasing saturation and noise levels.

Step 4: The center point of tile is regarded as the sample point. The resulted mapping at each pixel is interpolated using bilinear interpolation of the neighboring sample points.

We have experimentally found that $\alpha \sim 0.45$ was a good trade-off between contrast and noise in our OMAG images. Another parameter of RCLAHE is the saturation clip level which limits the CDF slope and the value of ~0.001 was experimentally chosen in our experiment.

In order to quantify the performance of our method besides visual validation, we utilized several quantities which can be divided into two categories: image quality measures and OMAG parameters which are explained below.

3.3 Image quality measures and quantities

3.3.1 Entropy

Entropy measures the content of an image, with higher values indicating more detailed images. The first-order entropy corresponds to the global entropy and is defined by

$$H(x) = \sum_{i=1}^{m} P(x_i)I(x_i) = \sum_{i=1}^{m} P(x_i)\log_b \frac{1}{P(x_i)} = -\sum_{i=1}^{m} P(x_i)\log_b P(x_i) \qquad (3\text{-}7)$$

Where x_i is an intensity value, m is the total number of intensity values in the dynamic range and $P(x_i)$ is the probability that a pixel in the image has an intensity value of x_i.

3.3.2 Edge content-based contrast metrics (ECBCM)

Since human contrast sensitivity is highly dependent on spatial frequency, edge content-based contrast metrics (ECBCM) uses the concept of local band-limited contrast to simulate how human visual system processes information contained in an image. ECBCM of an area r is given by

$$EC = \frac{1}{r^2}\int_{x-\frac{r}{2}}^{x+\frac{r}{2}} r dx' \int_{y-\frac{r}{2}}^{y+\frac{r}{2}} dy' |\nabla I(x,y)| \qquad (3\text{-}8)$$

where $\nabla I(x,y)$ is the gradient (first-order derivative) of the image $I(x,y)$. The formulation can be discretized in the form of

$$EC_r = \frac{1}{m\times n}\sum_x \sum_y |\nabla I(x,y)| \qquad (3\text{-}9)$$

where $m \times n$ is the total number of pixels inside an area r [Saleem-2012].

3.3.3 Saturation evaluation

Saturation is defined as the percentage of saturated pixels (pure black or pure white) in an image.

3.3.4 Root-mean-square (RMS) contrast

Contrast is the difference in luminance that makes an object distinguishable from its background. It has many definitions but one of the most commonly used forms of contrast is root-mean square (RMS) contrast which is defined as

$$Contrast_{rms} = \sqrt{\frac{1}{M*N}\sum_{i=0}^{N-1}\sum_{j=0}^{M-1}(I_{ij} - \bar{I})} \tag{3-10}$$

where I_{ij} is the intensity of the image at pixel location (i, j), $\bar{I}$ is the average intensity of all intensity values in the image and $M * N$ is the size of the image. Also, it is assumed that the intensity is normalized to the range $[0, 1]$.

3.3.5 Vessel area density, vessel length fraction and fractal dimension

Most of the quantities defined above were common in any kind of image analysis and may not directly show any meaningful physiological parameter of vasculature map. Reif et al. [Reif-2012] defined measurable parameters which could quantify OMAG images and were related to the physiological structure and location of the vessels. First, OMAG images are binarized using a threshold value. The vessel area density (VAD) is defined as the ratio of the number of white pixels (vessel) to the total number of pixels in the binary image. Then, the binary image is skeletonized [Gonzalez-2002] and the vessel length fraction (VLF) is defined as the ratio of white pixels to the total number of pixels in the skeleton image. Finally, the fractal dimension is calculated using a box counting technique [Masters-2004] in the skeleton image. The box counting method divides the skeletonized image into equal-sized square tiles and counts the number of boxes containing a vessel segment. Through varying the box size, the process is repeated until the box size is equal to the image size. Then, the fractal dimension is defined using

$$FD = -\frac{\log_{10}(N(l))}{\log_{10}(l)} \tag{3-11}$$

where l is the box length and $N(l)$ is the number of boxes needed to cover the image. Both VAD and VLF have values in the range of $[0, 1]$ while FD has a value in the range of $[0, 2]$.

3.4 Experimental setup

To demonstrate the effectiveness of the proposed RCLAHE method in enhancing the imaging contrast while not affecting the metrics in terms of the microvasculature quantification, we used an OMAG imaging system to acquire the microvasculatural images within tissue beds in vivo, on which the algorithm is tested. The schematic of our OCT system setup is given in **Figure 1-1** and the detail of the system was explained in the section 2.4 (experimental setup). The typical field of view and scanning range for our OCT system was 2.2x2.2 mm^2 in the current setup. In order to scan a larger field on the ear, we used a mechanical translating stage to move the tissue sample to the desired location and after acquisition and processing, the mosaics were stitched together to form a larger image.

Non-invasive *in vivo* images were acquired from the pinna of a healthy ~6 weeks old male hairless mouse (Crl:SKH1-Hr^{hr}) weighting approximately 26g. During the experiment, the mouse was anesthetized using 2% isoflurance (0.2 L/min O_2, 0.8 L/min air). The ear was kept flat on a microscope glass using a removable double-sided tape. The experimental protocol was in compliance with the Federal guidelines for care and handling of small rodents and approved by the Institution Animal Care and Use Committee (IACUC) of the University of Washington, Seattle.

The scanning protocol was based on three-dimensional ultrahigh-sensitive optical micriangiography (UHS-OMAG) technique [An-2010_UHS]. The x-scanner (fast B-scan) was driven with a saw tooth waveform and the y-scanner (slow C-scan) was driven with a step

function waveform. The fast and slow scanners covered a rectangular area of ~ 2.2x2.2 mm^2 on the sample. Each B-scan consisted of 400 A-lines covering a range of ~ 2.2 mm on the sample. The duty cycle of the saw tooth waveform rising edge was set at ~80% per cycle, which provided a B-scan frame rate of ~ 94 frames per second. The C-scan consisted of 400 scan locations with B-scan repetition of 8 frames per location for flow imaging and quantification. The total size of the data set was $1.28x10^6$ A-lines. In order to cover a large field of view, multiple 3-D scan were acquired and the sample was translated using a mechanical stage. This allowed imaging an area of ~1.5x1.5 cm^2 on the mouse ear pinna. The captured data was processed off-line using MATLAB© (MathWorks) which processed repeated B-scans at the same spatial location and generated cross-sectional vessel map using eigendecomposition-based (ED) filtering technique [Yousefi-2011]. Then, the adjacent cross-sections were visualized in a volumetric formation to show 3-D information and vessel map.

3.5 Results and discussions

Figure 3-2(A) shows a typical cross-section (B-scan) of the mouse ear pinna structure (near the edge). **Figure 3-2(B)** shows the processed ED-OMAG cross-section at the same location. Total 3-D data can be visualized in **Figure 3-2(C)** where vessels (labeled red) are overlaid on the structure (yellow), where the location of structure and vessel cross section of **Figure 3-2(A)** are marked as the dark line. After 3-D Gaussian filtering followed by median filtering, maximum intensity projection (MIP) map of the vessels are given in **Figure 3-2(D)**, showing the detailed microvascular network, including capillary vessels, that perfuses the scanned tissue volume. With the multiple titles of such MIP images acquired, the vasculature map of the entire mouse ear pinna is obtained by simply manually stitching them together. Two such stitched images are

shown in **Figure 3-1**. All of the contrast enhancement, equalization methods and quantifications explained in this paper were performed on individual MIP images (titles).

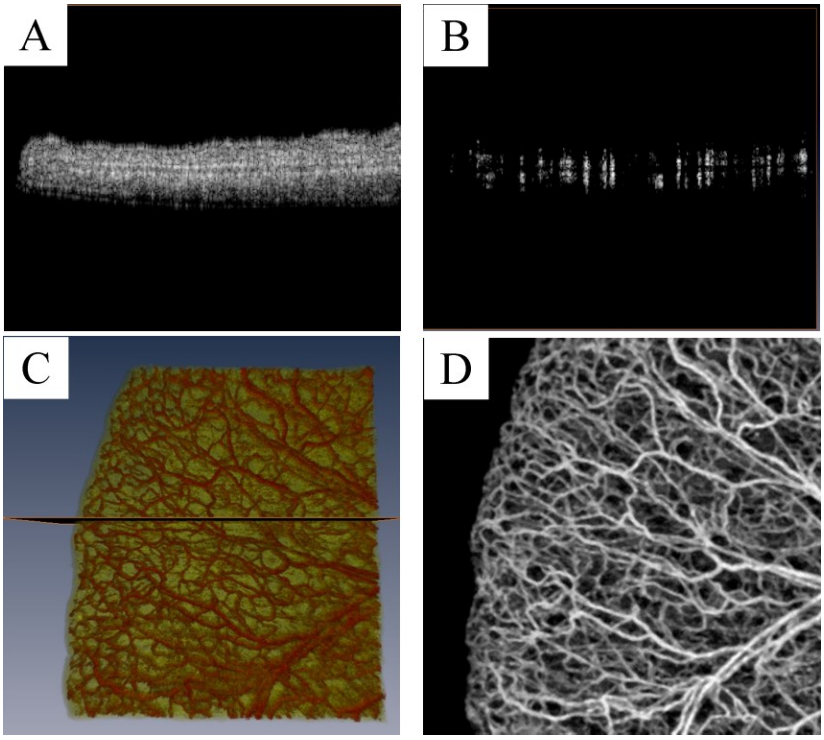

Figure 3-2 OCT/OMAG mouse ear pinna sample.

(A) A cross section tomogram of the mouse ear pinna at the edge where different layers such as stratum corneum, epidermis and auricular cartilage can be distinguished. (B) OMAG processing of the same cross-section tomogram using eigen-decomposition filter. (C) Simultaneous 3-D visualization of structure (color-coded as yellow) and vessels (color-coded as red). The location of tomogram cross-sections shown in (A and B) can also be seen as the black plane crossing. (D) Maximum intensity projection map color-coded in gray-scale image of the vessels. Total image size is about 2.2x2.2 mm^2.

Figure 3-3(A) shows OMAG microvasculature map of mouse ear pinna after stitching 22 projection map images (mosaics) without applying any post-processing to this image. It can be observed that the vessel signal background noise is not homogenous all over the ear due to imaging conditions, surface refraction and variations of light scattering properties. RCLAHE was applied to every single mosaic and then the mosaics were stitched together to form **Figure 3-3(B)**. It is obvious that the OMAG image is now homogenous everywhere, and signals from

vessels has been improved while not saturated. **Figure 3-3(C)** shows one of the mosaics of **Figure 3-3(A)** where the vessel map and background is not homogenous, and **Figure 3-3(D)** shows RCLAHE enhanced mosaic. It can be observed that the contrast of the capillary loops on the ear edge has been improved. Also, the background has been suppressed while foreground has been amplified.

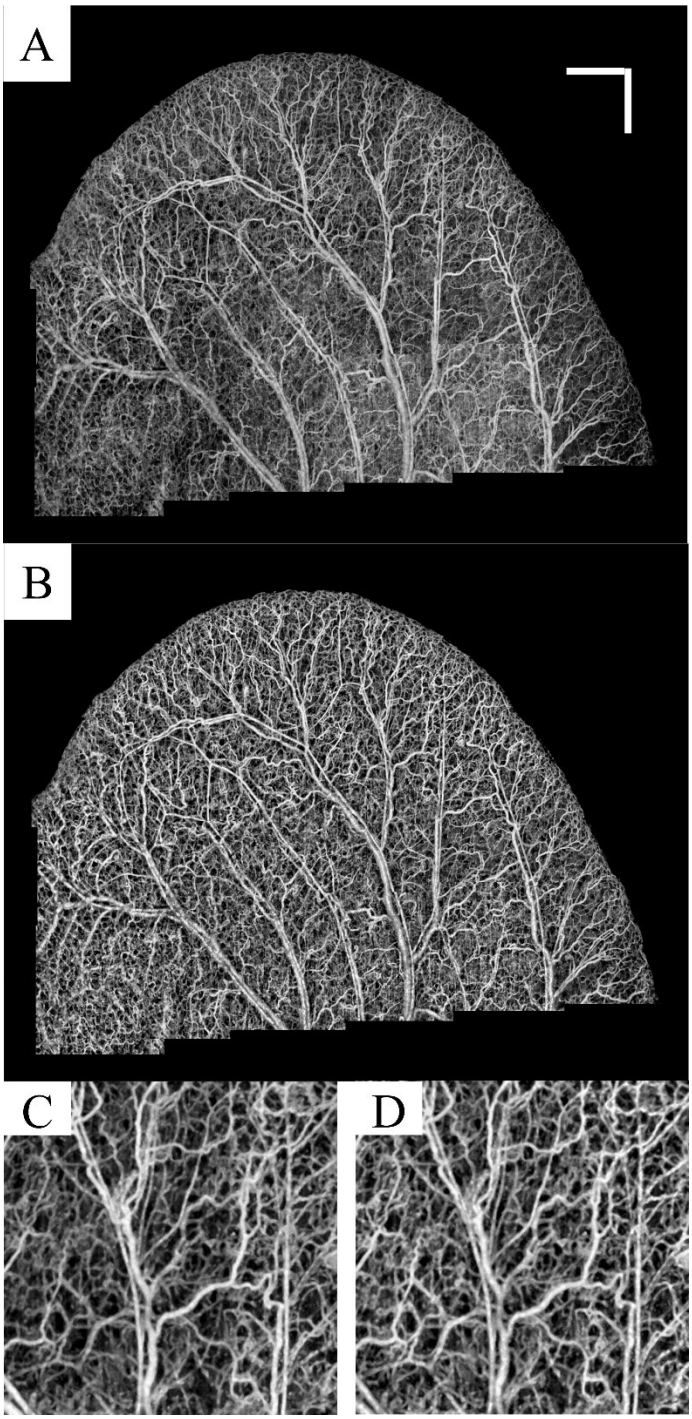

Figure 3-3 Uniform enhancement using RCLAHE

(A) OMAG microvasculature map of mouse ear pinna after stitching 22 projection map images (mosaics) without applying any post-processing to this image. (B) After performing RCLAHE on each mosaic and stitching the images together. (C) One of the mosaics of Figure 3-3(A) where the vessel map and background is not homogenous (D) RCLAHE enhanced mosaic. Scale bar = 1mm and each mosaic is 2.2x2.2 mm^2.

Similarly, **Figure 3-4(A)** shows OMAG microvasculature map of another mouse ear pinna after stitching 25 mosaics without any post-processing and after applying RCLAHE (**Figure 3-4(B)**). Also, **Figure 3-4(C)** shows one of the mosaics which had a high background due to high surface refraction which has been corrected in **Figure 3-4(D)**. It can be observed that the signal at the lower left corner of the ear pinna is poor, and the capillary loops have low contrast. These defects have been corrected using RCLAHE (**Figure 3-4(D)**).

In order to compare the performance of RCLAHE with other standard contrast enhancement and equalization methods, we applied contrast stretching algorithm (CSA), local histogram equalization (LHE), global histogram equalization (GHE) and uniform contrast limited adaptive histogram equalization (UCLAHE), respectively, to the mouse ear pinna mosaics and compared the results with RCLAHE both qualitatively and quantitatively. The parameters discussed earlier were used to quantify the performance of each method. Note that GHE is identical to LHE but the algorithm is applied to all of the mosaics at the same time. This procedure improves the general appearance of the image because it considers the histogram in all of the mosaics. Also, the ear edge mosaics that have a high background after LHE was corrected using GHE.

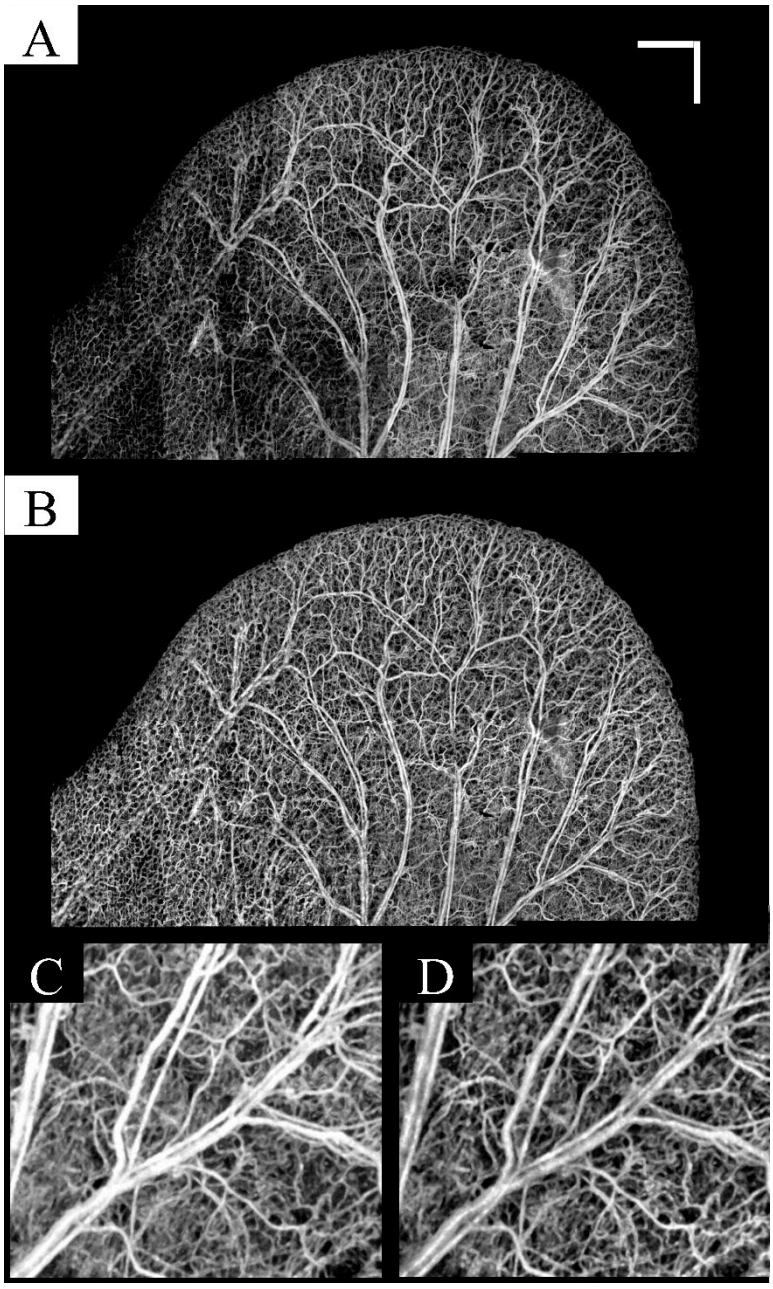

Figure 3-4 Uniform enhancement using RCLAHE.

(A) OMAG microvasculature map of mouse ear pinna after stitching 25 projection map images (mosaics) without applying any post-processing to this image. (B) After performing RCLAHE on each mosaic and stitching the images together. (C) One of the mosaics of Figure 3A where the vessel map and background is not homogenous (D) RCLAHE enhanced mosaic. Scale bar = 1 mm and each mosaic is 2.2x2.2 mm^2.

In order to compare the performance of RCLAHE with other standard contrast enhancement and equalization methods, we applied contrast stretching algorithm (CSA), local histogram equalization (LHE), global histogram equalization (GHE) and uniform contrast limited adaptive histogram equalization (UCLAHE), respectively, to the mouse ear pinna mosaics and compared the results with RCLAHE both qualitatively and quantitatively. The parameters discussed earlier were used to quantify the performance of each method. Note that GHE is identical to LHE but the algorithm is applied to all of the mosaics at the same time. This procedure improves the general appearance of the image because it considers the histogram in all of the mosaics. Also, the ear edge mosaics that have a high background after LHE was corrected using GHE.

Figure 3-5(A) shows the original ear pinna image without any equalization, and **Figures 3-5(B-H)** show the performance of CSA, LHE, GHE, UCLAHE and RCLAHE methods on **Figure 3-5(A)**, respectively. The performance of each method on a selected mosaic can be observed where the mosaics are the result of no enhancement (**Figure 3-5(G)**), CSA (**Figure 3-5(H)**), LHE (**Figure 3-5(I)**), GHE (**Figure 3-6(J)**), UCLAHE (**Figure 3-5(K)**) and RCLAHE (**Figure 3-5(L)**) methods, respectively. Compared to the original image before enhancement (**Figure 3-5(A)**), CSA (**Figure 3-5(B)**) improves the contrast of the vessels but does not improve the signal strength at the vessel locations and some weak capillary loops are not improved. Also, the background at high surface refraction areas of ear was not improved. Although LHE (**Figure 3-5(C)**) improves and amplifies the vessels and capillary loops at the areas with weak signals, but has an artifact at the ear edge where the background noise has also been amplified. GHE (**Figure 3-5(D)**) does not have ear edge artifact but the vessels have been saturated and some weak vessels are still not obvious. Also, the heterogeneous background at high surface refraction areas is still obvious. Although UCLAHE (**Figure 3-5(E)**) overcame most of the limitations of its

previous methods but the signal is still very weak at capillary loops and small vessels and the image contrast is very low. Also, the high surface refraction is not compensated either. RCLAHE (**Figure 3-5(F)**) creates a homogenous vasculature map all over the ear and improves the weak signal at capillary loops and small vessels as well as high surface refraction areas. Also, RCLAHE is less saturated than UCLAHE and better intensity distribution at larger vessels can be observed.

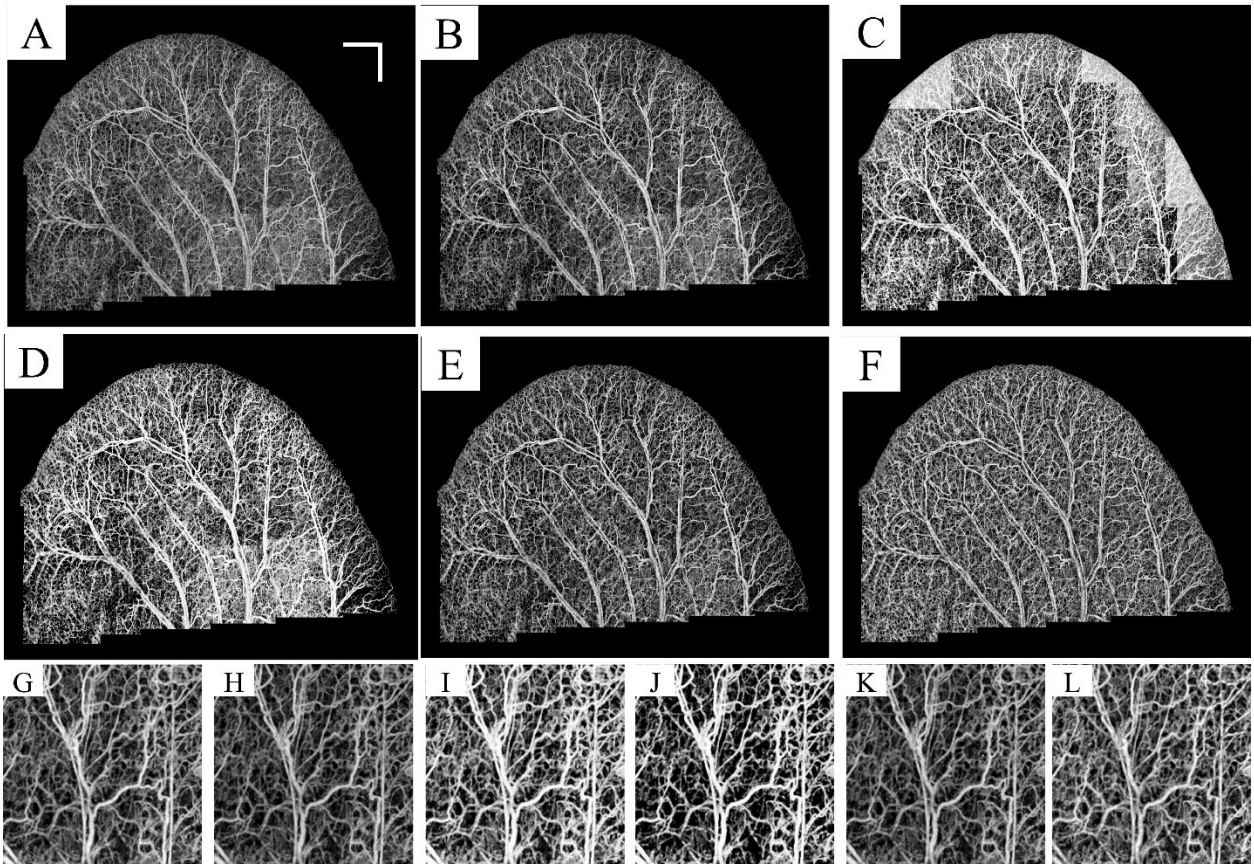

Figure 3-5 Equalization enhancement comparison

(A) The original ear pinna image without any equalization. The performance of CSA (B), LHE (C), GHE (D), UCLAHE (E) and RCLAHE (F) methods on Figure 5A, respectively. The performance of each method on a selected mosaic where the mosaics are the result of no enhancement (G), CSA (H), LHE (I), GHE (J), UCLAHE (K) and RCLAHE (L) methods, respectively. Scale bar = 1 mm and each mosaic is 2.2x2.2 mm^2.

Table 3-1 shows the quantitative comparison of OMAG and image parameters in **Figures 3-5(A-F)**. It can be observed that LHE and GHE increased the mean intensity, RMS contrast and ECBCM of the original image while at the same time increased the saturation level especially at larger vessels. Although CSA method improved saturation level, other image parameters such as mean intensity, RMS contrast, ECBCM and entropy were reduced. UCLAHE improved mean intensity and RMS, RMS contrast and saturation level while the entropy and ECBCM were decreased. RCLAHE improved the image parameters. The entropy and RMS contrast of LHE and GHE were higher than RCLAHE, because the ear edge background was amplified and the vessel boundaries were saturated. More importantly, the OMAG parameters were very similar between different methods and most of methods slightly increase these parameters which was because of increasing the mean intensity of the images which allowed some weak vessel signal be also included in the quantification. UCLAHE had similar mean intensity value which made its OMAG parameters identical to the original image. Basically, the our analysis show that these contrast enhancement methods did not change physical appearance of the vessels and therefore OMAG parameters were similar in all cases.

Table 3-1 Image parameter comparison after equalization.

The comparison of OMAG and image parameters after applying different methods on mosaic images of Figures 6 (A-F). The values are shown as mean value ± standard deviation of all mosaics.

	OMAG parameters				Image parameters				
	Fractal Dimension	Density Skeleton	Density Vessel	Mean Intensity	Intensity standard deviation	Saturation (%)	RMS contrast1	ENROPY	Edge Content
No Equalization	0.97±0.09	0.05±0.01	0.28±0.09	0.22±0.12	0.39±0.09	0.07±0.16	0.21±0.02	0.69±0.22	0.05±0.01

Contrast Stretch	0.95±0.09	0.05±0.01	0.28±0.09	0.15±0.09	0.33±0.09	0.01±0.00	0.18±0.02	0.57±0.23	0.05±0.01
Local Histogram Equalization	1.09±0.05	0.07±0.02	0.39±0.10	0.57±0.17	0.43±0.17	1.08±0.06	0.26±0.06	0.86±0.35	0.07±0.03
Global Histogram Equalization	1.03±0.10	0.06±0.01	0.34±0.06	0.47±0.21	0.42±0.16	0.94±0.06	0.29±0.06	0.83±0.33	0.08±0.03
UCLAHE	0.96±0.09	0.06±0.01	0.28±0.09	0.18±0.09	0.35±0.09	0.01±0.0	0.19±0.02	0.62±0.22	0.05±0.01
RCLAHE	1.03±0.07	0.06±0.01	0.32±0.08	0.29±0.09	0.44±0.06	0.04±0.03	0.23±0.02	0.85±0.16	0.07±0.02

In order to show the performance of the implemented methods on only one mosaic image, the OMAG and image parameters of **Figures 3-5(G-L)** were compared in **Table 3-2**. In this mosaic (**Figure 3-5(G)**), the background of the image was and vessel intensities were not homogenous. Also, larger vessels were saturated and their distribution was flat. Except for LHE, other methods did not dramatically change the OMAG parameters. Although CSA method improved the saturation problem, its RMS contrast, entropy and ECBCM were lower than the original image. GHE obviously saturated the larger vessels image. Although UCLAHE solved saturation, it could not improve the heterogeneous background artifact and its entropy, ECBMC and RMS contrast were low. RCLAHE not only reduced the background artifact, it also increased RMS contrast, entropy and ECBCM without oversaturating the image.

Table 3-2 Image parameter comparison after equalization.

The comparison of OMAG and image parameters after applying different methods on one mosaic image. The values are mean values of each parameter in the mosaic (**Figures 3-5 (G-L)**).

	OMAG parameters				Image parameters				
	Fractal Dimension	Density Skeleton	Density Vessel	Mean Intensity	Intensity Standard deviation	Saturation (%)	RMS contrast	ENROPY	Edge Content
No Equalization	0.98	0.07	0.33	0.29	0.45	0.04	0.22	0.87	0.07

Contrast Stretch	0.98	0.07	0.33	0.21	0.41	0	0.20	0.75	0.07
Local Histogram Equalization	1.12	0.09	0.49	0.48	0.50	1.11	0.29	1.00	0.09
Global Histogram Equalization	1.00	0.07	0.38	0.39	0.49	1.01	0.33	0.96	0.10
UCLAHE	0.97	0.07	0.33	0.24	0.43	0	0.21	0.78	0.07
RCLAHE	1.04	0.08	0.38	0.37	0.49	0.09	0.24	0.95	0.09

Similarly, **Figures 3-6(A-F)** show the qualitative comparison between different methods and their image and OMAG parameters are compared in **Table 3-3**. Also, the performance of different methods on a selected mosaic in **Figure 3-6(G)** are shown in **Figures 3-6 (F-L)** and their quantities were compared in Table 4. The original image (**Figure 3-6(A)**) had some areas with weak signals and low contrast at capillary loops near the ear edge. Although CSA improved the local appearance and contrast of the image at some areas, the overall picture was heterogeneous and some week signal vessels were not amplified because they were in the same mosaic of some stronger signals. LHE and GHE improved the contrast and mean intensity while both methods saturated the image and LHE had similar artifacts at ear edges and GHE could not compensate the high surface refraction. UCLAHE could not improve the background artifact at low intensity capillary loops near the ear edge and its overall appearance was not homogeneous. RCLAHE solved the low artifact at low intensity capillary loops and edges while preserving the saturation level. It also improved other parameters such as RMS contrast, ECBCM and entropy. OMAG parameters were larger than the original image because weak signal capillary loops fell below segmentation threshold and after RCLAHE processing; these loops were also included in OMAG parameter analysis.

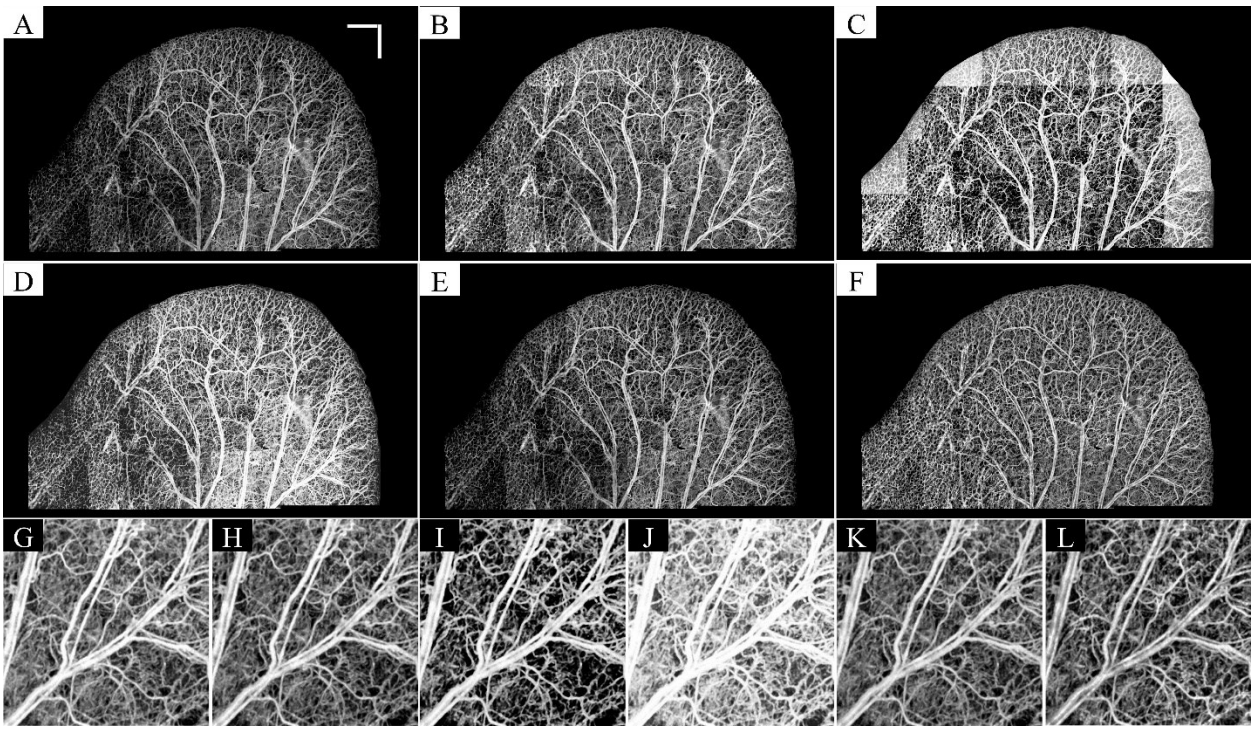

Figure 3-6 Equalization comparison.

(A) The original ear pinna image without any equalization. The performance of CSA (B), LHE (C), GHE (D), UCLAHE (E) and RCLAHE (F) methods on (A), respectively. The performance of each method on a selected mosaic where the mosaics are the result of no enhancement (G), CSA (H), LHE (I), GHE (J), UCLAHE (K) and RCLAHE (L) methods, respectively. Scale bar = 1 mm and each mosaic is 2.2x2.2 mm^2.

Table 3-3 Image parameter comparison after equalization.

The comparison of OMAG and image parameters after applying different methods on mosaic images of **Figures 3-6(A-F)**. The values are shown as mean value ± standard deviation of all mosaics.

	OMAG parameters				Image parameters				
	Fractal Dimension	Density Skeleton	Density Vessel	Mean Intensity	Intensity standard deviation	Saturation (%)	RMS contrast	ENROPY	Edge Content

No Equalization	0.94± 0.09	0.05±0.02	0.25±0.11	0.15±0.13	0.30±0.14	0.05±0.25	0.18±0.04	0.52±0.31	0.04±0.02
Contrast Stretch	1.00±0.08	0.05±0.02	0.29±0.11	0.30±0.12	0.44±0.08	0.64±0.06	0.25±0.03	0.83±0.20	0.05±0.02
Local Histogram Equalization	1.06±0.05	0.06±0.02	0.34±0.11	0.53±0.19	0.43±0.17	1.01±0.07	0.25±0.09	0.86±0.35	0.06±0.03
Global Histogram Equalization	1.01±0.11	0.06±0.03	0.31±0.15	0.38±0.23	0.42±0.11	0.40±1.14	0.22±0.05	0.79±0.27	0.05±0.02
UCLAHE	0.95±0.09	0.05±0.02	0.25±0.11	0.17±0.12	0.33±0.13	0.01±0.00	0.19±0.05	0.57±0.30	0.05±0.02
RCLAHE	1.04±0.05	0.06±0.02	0.32±0.12	0.28±0.12	0.42±0.09	0.05±0.04	0.23±0.04	0.79±0.24	0.06±0.02

Table 3-4 Image parameter comparison after equalization.

The comparison of OMAG and image parameters after applying different methods on one mosaic image. The values are mean values of each parameter in the mosaics (**Figures 3-6(G-L)**).

	OMAG parameters			Image parameters					
	Fractal Dimension	Density Skeleton	Density Vessel	Mean Intensity	Intensity standard deviation	Saturation (%)	RMS contrast	ENROPY	Edge Content
No Equalization	0.96	0.06	0.33	0.42	0.49	1.16	0.25	0.98	0.07
Contrast Stretch	0.95	0.06	0.32	0.39	0.48	0.77	0.25	0.97	0.07
Local Histogram Equalization	1.01	0.07	0.36	0.46	0.49	1.01	0.31	0.99	0.09
Global Histogram Equalization	1.14	0.08	0.47	0.75	0.43	5.32	0.24	0.81	0.07
UCLAHE	0.94	0.06	0.33	0.34	0.47	0	0.23	0.92	0.07

RCLAHE	1.02	0.07	0.41	0.39	0.49	0.11	0.23	0.97	0.08

3.6 Conclusion

In this chapter, we proposed using RCLAHE to improve the contrast and overall appearance of OMAG without saturating the vessels. The qualitative and quantitative performance of the proposed method was compared with those of CSA, LHE, GHE and UCLAHE. It has been demonstrated that RCLAHE outperformed LHE and GHE while at some local areas it was similar to CSA and UCLAHE. However, the overall performance was relatively better, and RCLAHE was the only method to overcome the heterogeneous background artifact. This post-processing can be applied in applications which require imaging a larger than the system field of view area or when inhomogeneous background surface refraction variations exist. OMAG parameters such as vessel density and fractal dimension were similar in most of the methods which confirmed that contrast enhancement methods did not change physical meaning of the image and only the overall appearance was different which an observer can decide which methods works best for a particular application. This method is not limited to optical microangiography and can be used in other image modalities such as photo-acoustic tomography and scanning laser confocal microscopy.

Chapter 4. SIMULTANEOUS BLOOD FLOW/FLUX MEASUREMENTS USING MUSIC

4.1 Introduction

The main role of microcirculatory system (including cardiovascular and lymphatic) is to transport oxygen, nutrition, fluid and necessary signaling molecules to the living cells via arteries/arterioles and collecting carbon dioxide and waste materials from the tissue cells. The exchange of oxygen and nutrition happens at capillary beds and then waste and carbon dioxide produced by the cells is diffused back into the capillaries and venules and sent back to the heart and respiratory system. Part of the waste in the interstitial fluid is also collected in the form of a protein-rich interstitial fluid (lymph) by lymphatic vessels [Martínez-Corral-2012]. Erythrocytes or red blood cells (RBCs), the most common type of blood cells, are the main carrier of oxygen and tissue fluid to the cells. RBCs are mainly composed of a protein called hemoglobin that binds to oxygen contained in a flexible plasma membrane. From the top view, their shape appears as a circular disk and from the side view appears as a biconcaved disk. Although their size is typically around 7 μm in diameter, their unique shape allows RBCs to squeeze through capillaries as small as 3 μm in diameter while capillaries partially expand as erythrocytes and leukocytes pass through them.

There are multiple sources in the literature that define blood flow, flux and flow rate interchangeably that sometimes causes ambiguity and confusion. In physics, flux is defined as a vector that has a direction and quantifies the flow rate of a property per unit area. In the neurovascular community, RBC flux is commonly referred to as the number of RBCs that pass

through a single capillary vessel per unit time [Kleinfeld-1998]. RBC flux measurement in the microcirculatory system allows for estimating the blood perfusion within tissue beds surrounding capillary beds, necessary for estimating metabolic activity of the tissue. Consequently, non-invasive measurement of RBC flux has an impact on studying and evaluating clinical applications related to vasculitis [Hagen-1998, Jennette-1997], angioneurosis [Donaldson-1963], diabetes [Horstmann-1951], cancer [Seyfried-2010], cardiovascular [Wang-2011], neurovascular [Lee-1999] and retinal disease [Gariano-2005].

The most common non-invasive and label-free methods reported in the literature for measuring and imaging RBC flux within capillaries and small vessels are Laser Doppler Fluxmetry (LDF), laser Doppler imaging (LDI), photoacoustic microscopy (PAM) and optical microangiography (OMAG). LDF is based on Doppler shift and broadening of monochromatic light due to moving particles (such as moving RBCs in the capillaries and small vessels) within the tissue [Stern-1975]. LDF has been widely used both in research and clinic to monitor subcutaneous microcirculatory flow in some disease such as Raynaud's phenomenon [Herrick-1998]. In LDF, blood flux is defined as the product of the mean velocity and number (concentration) of RBCs, expressed in terms of arbitrary perfusion units and is a relative measure rather than an absolute value [Herrick-1998, Murray-2004]. Usually, LDF in a subcutaneous site is measured in response to an external stimulus such as pressure or temperature [Murray-2004, Bornmyr-2001]. Laser Doppler imaging (LDI) is an expansion of LDF to provide perfusion map by scanning laser over a large area via a moving scanner mirror and analyzing the backscattered light signal, giving a two-dimensional image of blood flow perfusion. LDI has shown promising applications in dermatology such as assessment of burns [Niazi-1993, Jeng-2006, Kloppenberg-2001], dermal inflammation [Harrison-1993, Clough-1999] and cutaneous ulceration [Newton-2002] and in

rheumatology such as Raynaud's phenomenon [Clark-2003, Seifalian-1995] and inflammatory joint disease [Ferrell-2001]. Although widely used, the main disadvantages of LDF techniques are: (1) low spatial resolution (difficult to resolve single capillaries), (2) limited imaging depth (less than 0.5 mm) and (3) depth-integrated signal (cannot provide depth-resolved information).

Photoacoustic imaging (PAI) is performed by transmitting a sequence of short laser pulses into the sample tissue and ultrasound detection of the resulted thermo-elastic expansions of tissue cells [Maslov-2008]. Since hemoglobin is the main absorbing chromophore in the blood, high-resolution PAM has been demonstrated in imaging vascular structures from macro vessels down to individual capillaries [LHWang-2008]. Using absorption properties of oxygenated-hemoglobin and high-frequency (25-Mhz) ultrasound microscopy, Jiang et al. [Jiang-2012] proposed a Doppler ultrasound and photoacoustic method of imaging blood oxygen flux in a single vessel where oxygen saturation and total hemoglobin concentration were estimated using PAM and mean flow velocity was estimated by ultrasound. Then, the blood oxygen flux (ml/min) was calculated as the volume of oxygen content transported from an area cross-section per unit time. The major limitations of PAM are its sophisticated system set-up and the requirement of sample-detector coupling medium.

In contrast to PAI that is based on light absorption properties of the tissue, optical coherence tomography (OCT) is a non-contact technique based on light backscattering properties of the tissue structures [Tomlins-2005, Fercher-2003]. OCT is analogous to ultrasound tomography and similar to ultrasound Doppler modes, OCT hemodynamic information can be acquired in addition to structure information. Compared to ultrasound imaging, OCT resolution is higher while the penetration and imaging depth is limited. Optical microangiography (OMAG) is a label-free non-invasive imaging and processing method to obtain 3-D blood perfusion map in

microcirculatory tissue beds in vivo using Fourier-domain OCT [Wang-2007_OMAG, Wang-2007_cerebro]. Conventional Doppler OCT (DOCT) or phase-resolved Doppler OCT (PRDOCT) utilizes the difference between phase information of adjacent A-lines acquired at the same spatial location to measure particle velocity within each voxel from the Doppler (phase) shift [Izatt-1997, Zhao-2000]. It is commonly known and accepted that PRDOCT is mainly sensitive to the axial component of the flow (parallel to the beam). Due to the slow velocity of particles within capillary network (0.1-8 mm/s) and total imaging time limitation, PRDOCT is only practical for imaging blood flow perfusion within larger vessels (>30 μm diameter). Using PRDOCT, volumetric blood flow can be extracted by integrating the velocity profile over a vessel cross-section and taking other factors such as Doppler angle, tissue bulk motion and pulsation [Wang-2008_retina]. However, the limitation on this approach for measuring total blood flow is its sensitivity to the estimated Doppler angle as well as accurate estimation of vessel cross-section where some OCT image artifacts such as forward-scattering and phase-ambiguities below vessels can affect the accuracy of this approach [Zhao-2000, Wang-2002]. In order to compensate for these artifacts, Srinivasan et al. suggested to use an en-face imaging technique that was originally developed in Doppler Ultrasound [Szabo-2004], in which the total blood flow is evaluated by integrating Doppler velocity profile over the en-face plane (xy plane) at each depth position instead of xz or yz planes [Srinivasan-2010]. Similar approach has been utilized to measure total volumetric blood flow in rodents [Zhi-2011_volumetric, Zhi-2012_retina] and human retina [Makita-2011, Choi-2012].

However, PRDOCT only measures the velocity of the particles passing through the probe beam and cannot quantify the number of particles or RBC flux. PRDOCT is analogous to color-Doppler ultrasound mode in which directional blood velocity (axial component) is quantified by

measuring the center frequency of the Doppler shift. Due to its sensitivity to noise and tissue motion, color-Doppler mode is mainly used to measure large vessels and fast flow velocities and cannot measure blood velocity when ultrasound beam is perpendicular to the flow direction. Power-Doppler ultrasound can overcome some of the color-Doppler mode limitations by quantifying the amplitude peak in the shifted/broadened Doppler spectrum and is particularly useful for imaging small vessels and low-velocity flow [Rubin-1993, Babcock-1996]. It is known that under constant concentration condition, the Doppler spectrum is proportional to the number of RBCs while the Doppler peak value is sensitive to changes in concentration, shear rate and turbulence [Shung-1992]. Also, some studies suggest that erythrocyte aggregation affects ultrasonic backscatter from RBCs and therefore shear-rate-dependent attenuation coefficient should be compensated for higher shear rates [Huang-2011].

Given the similarities between ultrasound imaging and OCT, since color Doppler ultrasound is analogous to PRDOCT, we propose that there exists a similarity between ultrasound power Doppler and peak amplitude of the Doppler signal from moving particles such as RBCs. Therefore, we can infer that quantification of Doppler peak amplitude leads to measuring the number of RBCs moving through the probe beam (RBC flux), assuming constant blood concentration within capillaries beds.

Previously, some methods have been proposed in the OCT community based on signal decorrelation time [Srinivasan-2012, Wang_2010] and amplitude peaks at capillary locations [Lee-2013] to quantify RBC velocity and flux in single capillaries. The amplitude peak method only works in small capillaries with single RBC flowing through the vessel. In order to reproduce a high-resolution frequency estimate, the method based on signal decorrelation time required to capture a large amount of data set that made this method sensitive to possible tissue

motion and vessel wall artifacts. Conventional spectral estimation techniques utilize fast Fourier transform (FFT) to estimate spectral information and the estimation resolution is very sensitive to the number of FFT points. However, collecting large amount of FFT points (i. e. 1024) for each voxel makes such conventional methods extremely challenging for in vivo experiments because of motion artifacts and total imaging time. In order to mitigate these limitations, model-based spectral estimation techniques can be more favorable because the latter requires very fewer data points to estimate signal spectrum.

In this chapter, we utilize the super-resolution technique to simultaneously quantify bidirectional RBC flow and flux by spectral estimation of the received OCT signal from moving particles within capillaries and microvessels. We show the efficiency and performance of the proposed method in simulation and tissue-mimicking flow phantom. Compared to the existing methods that can either quantify flow direction or power, our proposed method allows simultaneous flow (velocity) direction and power (flux) estimation. Since, a super-resolution estimation technique is utilized, our method does not need a large data set to reconstruct power spectrum of the OCT signal. This method may be utilized to facilitate the evaluation of tissue oxygen/nutrition exchange and consumption by microstructures in biological tissues such as human/animal retina, skin and rodent brain.

We define RBC flux as the rate of moving RBCs per unit area. Flux measurement requires knowledge about the velocity and concentration (number) of RBCs in the whole blood. We propose utilizing a super-resolution estimation technique to simultaneously measure velocity and concentration of the scattering particles within the flowing solution. Accurate flux measurement can be achieved after correcting for axial and lateral broadening of the field to correct for cross-sectional area units and calibrating the concentration/velocity curves.

4.2 Proposed method

Multiple signal classification (MUSIC) is a super-resolution spectral estimation method based on the principle of orthogonality [Schmidt-1986]. The MUSIC estimation is based on the orthogonality property of noise and signal eigenvector subspaces. In contrast to the classical spectral estimation methods such as periodogram and correlogram [Maple-1987] that use FFT, the frequency resolution of MUSIC is independent of the number of FFT points, which makes it a super-resolution method.

We can model OCT signal measurement at each voxel as superposition of three independent components: tissue signal (stationary and slowly moving tissue structures), hemodynamic signal (mostly contribution from moving red blood cells) and noise (system noise and shot noise). Given the assumption that these components are independent, MUSIC has the capability to decompose the received OCT signal into orthogonal basis functions and therefore contributions from moving RBCs can be estimated and quantified.

The 3D OCT signal at each voxel given by a complex value $x[n]$ where n corresponds to the temporal sampling at the voxel location, can be decomposed in terms of its exponential eigenfunctions given by

$$x[n] = \sum_{i=1}^{P} a_i e^{j(n\omega_i + \varphi_i)} + b_a[n] \tag{4-1}$$

where $b_a[n]$ is a centered complex white noise of variance $E\{|b_a[n]|^2\} = \sigma^2$ independent from a_i, a_i are random and independent variables of variance $\sigma_{a_i}^2$ that model field reflectivity, P is the total number of orthogonal components in the signal and a_i, φ_i and ω_i are the amplitude, phase and angular frequency of each component, respectively. Then, we can write the autocorrelation function of the observations as [Castanié-2013]:

$$r_{xx}[k,m,m'] = \sum_{i=1}^{P}\sum_{l=1}^{P} E\{\alpha_i \alpha_l^*\}\, e^{(\omega_i-\omega_l)k}.\, e^{j(m\omega_i - m'\omega_l)} + \sigma^2\delta_{m-m'} \qquad (4\text{-}2)$$

where $\delta_{m-m'}$ is the Kronecker symbol and $k = m - m'$. If a_i are non-correlated, then $x[n]$ is stationary and its correlation coefficients are:

$$r_{xx}[m-m'] = r_{xx}[k] = \sum_{i=1}^{P} A_i e^{jk\omega_i} + \sigma^2\delta_k \qquad (4\text{-}3)$$

where $A_i = a_i^2$ and $(|k| = 1,2,\dots,M)$ are autocorrelation lag values for M number of temporal samples. The M order correlation matrix is then given by

$$R_{xx} = \begin{bmatrix} r_{xx}[0] & r_{xx}[-1] & \cdots & r_{xx}[-(M-1)] \\ r_{xx}[1] & r_{xx}[0] & \cdots & r_{xx}[-(M-2)] \\ \vdots & \vdots & \ddots & \vdots \\ r_{xx}[M-1] & r_{xx}[M-2] & \cdots & r_{xx}[0] \end{bmatrix}. \qquad (4\text{-}4)$$

If the temporal samples are larger than the number of orthogonal components $(M > P)$, then $Rank\{R_{xx}\} = \min\{M,P\} = P$. The eigendecomposition of R_{xx} is given by

$$R_{xx} = \sum_{i=1}^{M} \lambda_i u_i u_i^H \qquad (4\text{-}5)$$

where $\lambda_1 \geq \lambda_2 \geq \lambda_3 \geq \cdots \geq \lambda_M$ are eigenvalues and $u_1, u_2, u_3, \dots, u_M$ are their corresponding normalized eigenvectors. Since $Rank\{R_{xx}\} = P$, then R_{xx} can be represented by its first P eigenvalues/eigenvectors and $\lambda_{p+1} = \lambda_{p+2} = \cdots = \lambda_M = 0$. Therefore

$$R_{xx} = \sum_{i=1}^{P} \lambda_i u_i u_i^H \qquad (4\text{-}6)$$

and the eigenvectors $\{u_1, u_2, \dots, u_P\}$ are the principal eigenvectors of the autocorrelation matrix R_{xx} that spans the signal subspace. The autocorrelation matrix can also be written in the form of eigenfunctions

$$R_{xx} = \sum_{k=1}^{P} A_k S_k S_K^H = SAS^H \qquad (4\text{-}7)$$

where ω_i is one of the input's principal frequency components, $S_{M\times P} = [S_1\, S_2 \dots S_P]$, $S_i = [1\ e^{j\omega_i}\ e^{j2\omega_i}\ e^{j3\omega_i} \dots e^{j(M-1)\omega_i}]'$ and $A = diag([A_1, A_2, \dots, A_P])$. Here H is the matrix

Hermitian (complex conjugate transpose) and $diag([.])$ is a diagonal matrix. The vector space $S_{M\times P} = \{S_1, S_2, \dots, S_P\}$ is called the signal subspace of $\{x[n]\}$.

Since we assume that the noise and signal subspaces are orthogonal to each other [Maple-1987], a frequency estimator function can be developed to exhibit pseudo-spectrum plots with sharp peaks at signal frequency locations. In theory, the $M - P$ noise subspace eigenvectors $\{u_{P+1}, u_{P+2}, \dots, u_M\}$ of the autocorrelation matrix or any linear combination of them with an arbitrary weighting α_k given by

$$\sum_{k=P+1}^{M} \alpha_k |S^H(\omega) u_k|^2 = S^H(\omega).\left(\sum_{k=P+1}^{M} \alpha_k u_k u_k^H\right).S(\omega) \tag{4-8}$$

would be zero if evaluated at $S(\omega_i) = [1\ e^{j\omega_i}\ e^{j2\omega_i}\ \dots e^{j(M-1)\omega_i}]$, where ω_i is the frequency component of the input signal.

The MUSIC spectral estimator is defined by the function

$$P(\omega) = \frac{1}{\sum_{k=P+1}^{M} (|S^H(\omega) u_k|)^2} \tag{4-9}$$

and theoretically have an infinite value if evaluated at one of the signal's frequency components ($\omega = \omega_i$). In practice, the MUSIC frequency estimation function is finite due to estimation error, but exhibits local maxima (peak) at those frequencies. Locating the peak value and its corresponding frequency will be an indicator of the blood flux and flow, respectively, at the voxel of interest. Accurate estimation of the blood velocity (ω_i) requires temporal sampling above the Nyquist rate [Shannon-1949]. However, the estimate peak value ($P(\omega_i)$ or flux) is less sensitive to that condition and frequency aliasing.

In practice, correlation matrix is not available and therefore an estimate of the correlation matrix is considered

$$\hat{R}_{xx} = \begin{bmatrix} \hat{r}_{xx}[0] & \dots & \hat{r}_{xx}[-(M-1)] \\ \vdots & \ddots & \vdots \\ \hat{r}_{xx}[M-1] & \cdots & \hat{r}_{xx}[0] \end{bmatrix} \tag{4-10}$$

where

$$\hat{r}_{xx}[m] = \frac{1}{N}\sum_{n=-\frac{N-1}{2}}^{\frac{N-1}{2}} x(n+m)x^*(n) \tag{4-11}$$

and N is supposed to be odd. This estimation of R_{xx} relies on the assumption that $x[n]$ is ergodic. A spectral estimation method is called super-resolution when its asymptotic resolution is theoretically infinite in the sense that two signals with closely spaced frequency components can be separated regardless of the signal-to-noise ratio (SNR), provided that the number of samples used for the estimation of the correlation matrix tends to infinity and the correlation estimate approaches the actual correlation matrix. To illustrate the concept of super-resolution in comparison to the classical Fourier analysis, we can rewrite the spectral estimators of the periodogram and correlogram, making the same sizes of observations M and N. Assuming N observations of $x(k)$ partitioned in L adjacent sequences of M successive observations of $x(k)$ partitioned in L adjacent sequences of M successive observations of $x(k)$, the super-resolution periodogram is given by

$$\hat{S}_{xx}^{per}(f) = \frac{1}{L}\sum_{l=0}^{L-1} \hat{S}_{xx}^{(l)}(f) = \frac{1}{L}\sum_{l=0}^{L-1}\left(\frac{1}{M}\left|\sum_{m=0}^{M-1} x(lM+m)e^{-jm\omega}\right|^2\right) \tag{4-12}$$

and the correlogram is given by

$$\hat{S}_{xx}^{corr}(f) = \sum_{m=-\frac{M-1}{2}}^{\frac{M-1}{2}} \hat{r}_{xx}(m).e^{-jm\omega} \tag{4-13}$$

where $\hat{r}_{xx}$ is given in (11). The super-resolution property of the sub-space based methods (periodogram) is based on the fact that at fixed M, it is enough to increase N so large that the method can distinguish two signals whose frequency components are closely-spaced. However, this is not the case for the periodogram (classical estimation techniques) methods because both M and N should increase at the same time to have this result.

The concept of Doppler frequency and its corresponding power peak is very similar to ultrasound Doppler modes where ultrasound color Doppler mode estimates the Doppler frequency shift and ultrasound power Doppler estimates the peak of the Doppler frequency spectrum. Power Doppler has higher sensitivity to slow flow and is related to the number of RBCs flowing through the beam [Cobbold-2007, Rubin-1993]. The backscattered OCT signal has relatively higher signal-to-noise ratio (SNR) at stationary and non-moving tissue boundaries because the structure pattern is repeatable. However, the backscattered signal from moving scatters such as moving red blood cells inside patent vessels is typically weaker and temporally varying. Since the tissue component is always stronger than the hemodynamic component, their corresponding MUSIC eigenvalues will be in order so that the larger eigenvalue belongs to tissue signal subspace while smaller eigenvalue belongs to the hemodynamic signal subspace. Therefore, their corresponding subspaces can be separately estimated. In MUSIC estimation, the number of input signal components (P) is a user-defined input variable. By defining the number of input signal components to be $P = 2$, the largest peak in the MSUIC pseudo-spectrum of OMAG data corresponds to the stationary and non-moving tissue and the second largest peak corresponds to the moving RBCs. We can also approach this problem by first removing the stationary and non-moving tissue structural components (also known as clutter) from the input data, and then characterizing the remaining component which corresponds to the RBCs. This can be done using eigendecomposition-based clutter rejection filtering technique [Yousefi-2011] or by simply subtracting A-lines acquired at the same location [Devor-2012, Wang_2010]. The advantage of this approach is that after removing the clutter, a mask image based on the remaining flow information can be created and MUSIC is performed only on the voxels with high flow value, which would dramatically reduce the total processing time.

4.3 Simulation studies

An OCT backscattered signal from a single RBC based on Gaussian-shaped light source assumptions can be approximated by [Srinivasan-2012, Lee-2012]

$$R_1(t) = R_0 e^{-\alpha z_1(t)^2} e^{j\beta z_1(t)} \tag{4-14}$$

where R_0 is proportional to the field reflectivity of the particle, $z_1(t)$ is the depth location of the scatterrer at time t and α and β are constants modeling beam parameters and axial length of the coherence gating. Assuming that the particle is moving at a constant velocity in the axial direction (**Figure 4-1(A)**) $z_1(t) = v.t$, we can write the OCT backscattered signal from a moving RBC within capillary network by

$$R_1(t) = R_0 e^{-\alpha(v.t)^2} e^{j\beta v.t}. \tag{4-15}$$

In order to model the RBC velocity in the capillary network with a requirement of Nyquist rate to avoid aliasing, we make the following assumptions. RBC particles travel around 10μm within the probe beam, therefore the Nyquist rate is defined as

$$Nyquist\ rate = 2 \times \frac{Maximum\ Particle\ Velocity}{Traveling\ Distance}. \tag{4-16}$$

Since typical RBC velocity is around 0.8 to 8 mm/s in rodent brain [Unekawa-2010], a sampling rate required to avoid estimation aliasing would be

$$Sampling\ rate \geq Nyquist\ rate \tag{4-17}$$

that in this case, sampling rate should be above 3.2 kHz. For other applications such as human retina, the RBC velocity is around $[1\ to\ 45]\ mm/s$ [Nagahara-2011] and traveling distance inside the beam is around 20 μm, the sampling rate to avoid aliasing would be above 9 kHz.

Assuming that N is the number of RBCs passing through the beam, we can generalize equation (10) as superposition of N number of RBCs plus noise

$$R_1(t) = \sum_{i=1}^{N} R_{0,i} e^{-\alpha\left(v_z(t-\tau_i)\right)^2} e^{j\beta.v_z.(t-\tau_i)} + n(t) \quad (4\text{-}18)$$

where $R_{0,i}$ is proportional to the field reflectivity of the i^{th} RBC particle, $n(t)$ is additive white Gaussian noise and τ_i is its corresponding delay time of arrival (**Figure 4-1(B)**). In our simulations, sampling rate was $f_s = 10\ kHz$. Also, $R_{0,i}$ and τ_i where random variables for each particle with uniform distributions between [0,1] and a white Gaussian noise distribution $\frac{2}{f_s} \times N(0,1)$, respectively. Given the measurement samples of $R_1(t)$ at $t = \left[\frac{0}{f_s}, \frac{100}{f_s}\right]$, we want to estimate v_z and its corresponding peak (related to N) using MUSIC algorithm. For instance, given the simulation parameters ($N = 1000$, $f_s = 10\ kHz$ and $f_{rbc} = 2\ kHz$), a typical MUSIC estimation plot is given in **Figure 4-1(B)**.

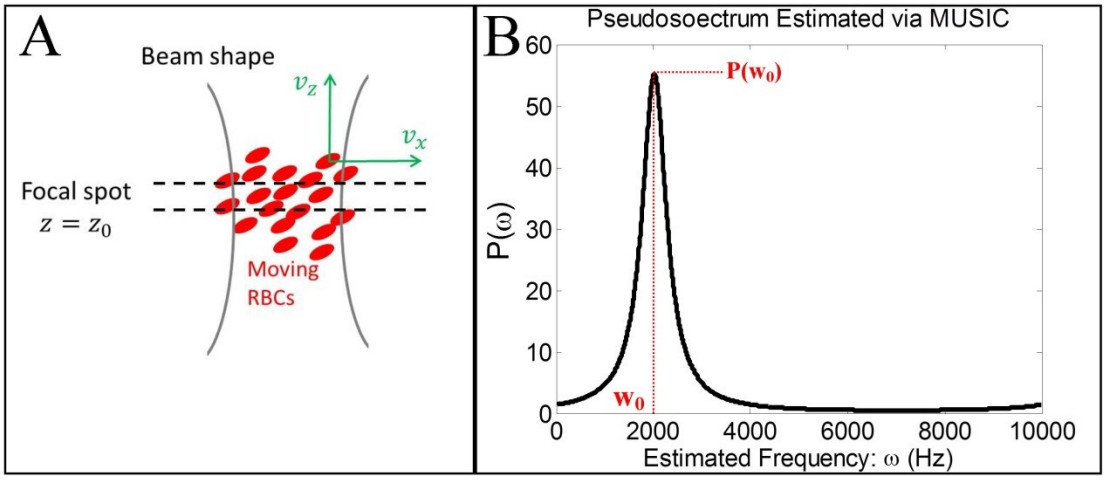

Figure 4-1 MUSIC estimation of moving RBCs.

(A) Moving red blood cells within microcirculatory at the focal spot of OCT beam. (B) A typical MUSIC spectral estimation of a simulated moving particle. The center frequency indicates the particle velocity and its corresponding peak indicates concentration and number of particles moving within that voxel.

In order to show the sensitivity of MUSIC estimator to the signal frequency (f_{rbc}) and number of RBCs (N), we performed a series of simulations. It should be noted that the number of RBCs should depend on the volume RBC concentration (C) and RBC velocity. Therefore, by increasing the signal input frequency f_{rbc}, the number of particles that pass through the beam would also increase. We assumed a linear relationship between RBC frequency and total number of moving particles ($N = f_{rbc} \times C$). Also, RBC frequency f_{rbc} in equation (4-13) is squared ($e^{-\alpha(v_z(t-\tau_i))^2}$) and appropriate sampling rate should be considered to avoid estimation aliasing. We performed our simulations for three levels of concentrations: low, medium and high ($C = [30, 40, 50]\%$) that resembles the blood hematocrit. For each parameter set, the simulation was repeated multiple times and the mean values of estimate peak ($P(\omega_0)$), estimated frequency (ω_0) and root-mean-square (RMS) error in frequency estimations were calculated. **Figure 4-2(A)** shows the frequency estimation as a function of the input frequency and the RMS errors were plotted in **Figure 4-2(B)**. The estimated MUSIC peaks were also shown in **Figure 4-2(C)**. It can be observed that the estimated frequency is independent of the concentration level and number of particles, as expected. Also, RMS error increases for higher frequencies and RMS error is higher for low concentration level. The explanation for this difference is that for lower concentration, fewer particles contribute to the received OCT signal and therefore estimation error is higher. On the other hand, MUSIC peak can clearly distinguish the difference between the numbers of scattering particles and therefore is an indication of RBC flux. It should be noted that estimated flux is a relative value and under fixed experimental conditions, changes in the flux can be related to variation of physiological conditions such increase or decrease in blood flux in specific areas. This is similar to the applications of laser Doppler perfusion measurement techniques that a baseline is collected and then changes relative to the baseline are measured. However,

measurements of different subjects/sites may not be comparable in an absolute value and only relative values should be considered. That is the reason why most laser Doppler perfusions and flux measurements are given in auxiliary units. Therefore, the measured MUSIC peak is in auxiliary units. Also, most of the techniques in the OCT literature measure only the RBC velocity and total blood volume by integrating over a vessel cross-section. It can be observed in **Figure 4-2(A)** that our assumption is not sensitive to concentration variations and RBC flux.

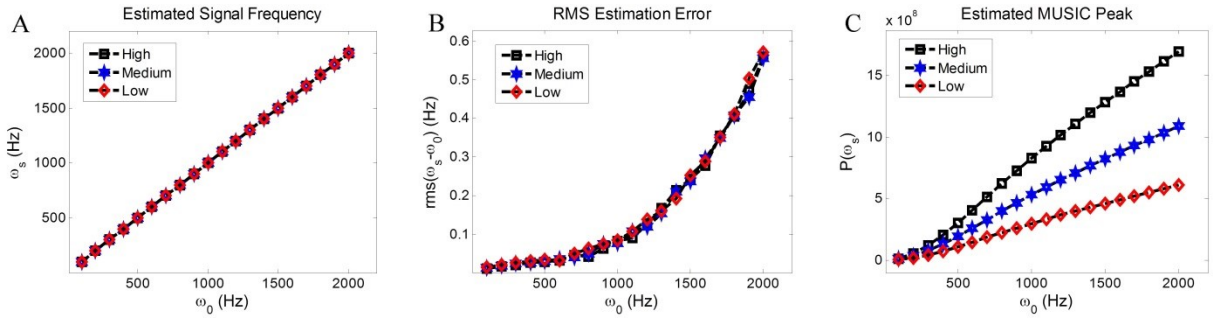

Figure 4-2 MUSIC simulation results.

(A) Estimated signal velocity (flow) in simulation. (B) RMS error of velocity estimation. (C) Flux estimated based on the peal value of the MUSIC spectrum for three different levels of concentration/number of particles (R-sqaure fitting goodness of r2≥0.99).

4.4 System set up and experimental preparation

4.4.1 3.1 OCT system set up

The schematic of our OCT system setup is given in **Figure 1-1** and the detail of the system was explained in the section 2.4 (experimental setup). The typical field of view and scanning range for our OCT system was 2.2x2.2 mm^2 in the current setup.

4.4.2 Scanning protocol

The scanning protocol utilized in this experiment is based on wide velocity range Doppler microangiography [Shi-2013]. In this protocol, the beam is shifted to each spatial location and after the scanner is stabilized, multiple repeated A-scans per location are captured at a defined scan frequency (defined by Nyquist rate). Then, the probe beam is shifted to the adjacent spatial location and the same procedure continues until all the locations in the field of view on the tissue are covered. The advantage of this method is that temporal power spectral density broadening due to the moving scanner speed is minimized because the scanner is fully stabilized [Srinivasan-2010]. In this experiment, we acquired 25 A-lines repetition per location, 200 A-lines per B-frame and 200 frames for each 3D scan. Since the camera was triggered at 7 kHz (due to Nyquist rate), total scanning time for a 3D data set was ~140 seconds.

4.5 Phantom studies

In order to show the performance of MUSIC method to estimate RBC velocity and flux, we made a series of experiments on a custom-made flow phantom. The phantom was made from 1% agar solution and 10% of low-fat milk (2% fat) to mimic heterogeneous tissue environment. A capillary tube with an inner diameter of ~400 μm was submerged and a diluted solution of milk (2% fat) and water was mixed to flow through the tube. A syringe pump (Fusion 100, Chemyx Inc.) was utilized to move the flowing particles from a syringe (5ml, Luer-Slip plastic, National Scientific, Germany) through the tube at a constant flow rate controlled by the pump. In order to simulate variable concentrations, three different diluted solutions of milk and water were utilized to model low, medium and high levels of concentration. The dilution portions of milk-to-water ratios were 0.5, 1 and 2 for low, medium and high concentration levels, respectively. For each

solution, the syringe was pumped at controlled volumetric flow rates of [25, 50, 75, 100, 125, 150, 175, 200] µl/min. The OCT system and scanning protocol explained earlier were utilized to capture cross-sectional images. Instead of 3D data acquisition, 200 repeated B-frames consisting of 200 adjacent A-lines per B-frame and 25 A-line repetitions at each spatial location when scanner was stable were captured and the estimated values were averaged. In order to minimize processing time, first the location of flow/tissue pixels was masked based on Eigen-decomposition clutter rejection filter [Yousefi-2011]. Then, for each flowing voxel, MUSIC frequency (ω_s) and peak (P(ω_s)) were calculated. Total blood flow and flux within the tube were calculated by integrating estimated velocity and flux over all pixels within the tube.

Figure 4-3(A) shows a cross-section of the phantom structure at the site of measurement. **Figure 4-3(B)** is the flow locations extracted using eigendecomposition clutter rejection and used as a mask to reduce processing time. **Figures 4-3(C,D)** show the estimated velocities and spectrum peaks, respectively, using MUSIC algorithm shown in the red-dotted square delineated in **Figure 4-3(B)**. It can be observed that the estimated MUSIC frequency (ω_s) is distributed based on laminar flow profile over the tube cross-section area and does not depend on the signal amplitude. On the other hand, MUSIC power peak ($P(\omega_s)$) depends on the amplitude of the received signal and signal attenuation can influence the estimated peak. It should be noted that the inner diameter of the flow phantom utilized in this experiment was 400 µm which is relatively larger than most of the capillaries and small vessels in vivo. For instance, the diameter of arterioles in a young healthy wild-type mouse range between 10 µm to 50 µm and the diameter of venules are typically between 15 µm to 80 µm. Therefore, when estimating flow and

flux *in vivo*, OCT signal attenuation within an arteriole/venule will be significantly less obvious, hence the MUSIC power estimate can demonstrate a laminar-like profile.

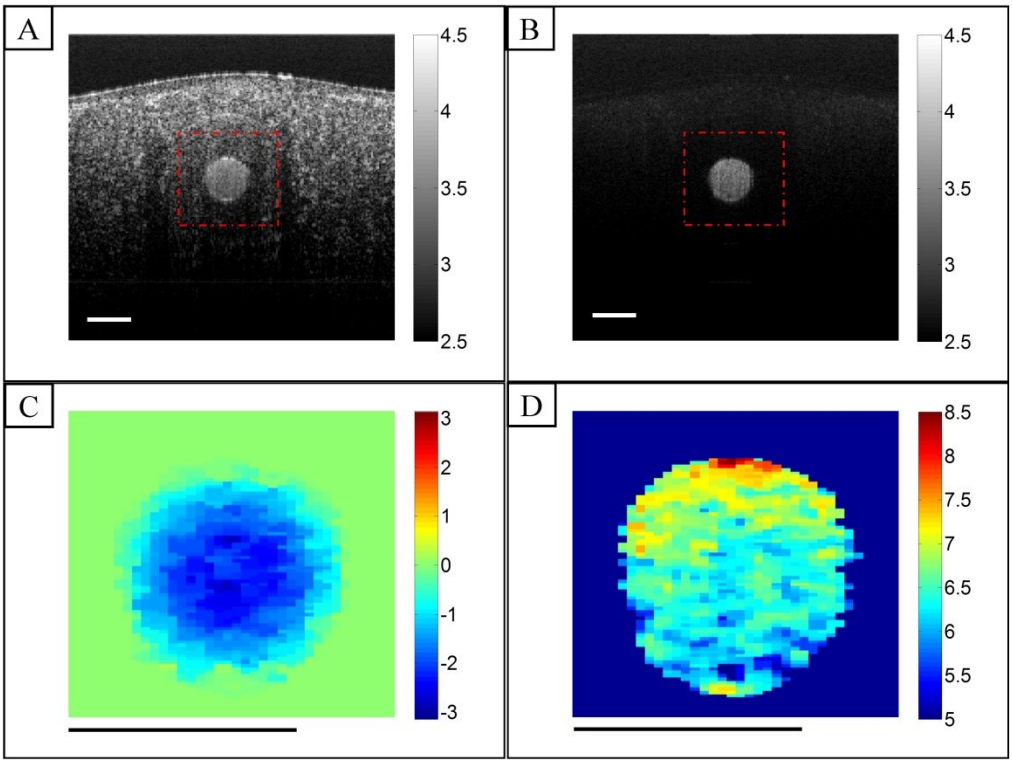

Figure 4-3 MUSIC estimation in a phantom cross-section.

(A) A cross-section of the flow phantom structure. (B) Clutter rejected from structure measurements showing flowing particles (dB). (C) Estimated particle velocities (flow) based on MUSIC center frequency of the spectrum peak (shown from [-π π] in the rectangle area of Fig. 4(A). (D) Estimated moving particle flux based on MUSIC peak (dB). Scale bar = 400 μm.

Total blood flow and flux within the phantom tube were calculated by integrating estimated MUSIC frequency (ω_s) and MUSIC power peak ($P(\omega_s)$ over the flowing tube area using the following equations, respectively:

$$Total\ flow = \int_{S\,(i,j)} \omega_s(i,j) \tag{4-19}$$

$$Total\ flux = \int_{S\,(i,j)} P_{MUSIC}(i,j) \tag{4-20}$$

where $S\ (i,j)$ is the area cross-section of the tube. This method was utilized because we acquired only 2D scans and repeated the 2D scans for better statistics of the data and proof concept. Since the tube angle and imaging location were kept constant in between all measurements, the estimated total flow and flux can be comparable among these experimental conditions. When a 3D scan is acquired, the integration can be performed on the xy cross-section of the tube or vessel wall to avoid ambiguity about Doppler angle.

Figure 4-4(A) shows the total velocity (flow) that is the integration of estimated MUSIC velocities inside the tube. It can be observed that by increasing the flow rate in the syringe pump, total flow has increased linearly. As expected, changes in the number and concentration of flowing particles (flux) were not observed in the velocity map. Therefore, measuring total blood flow using integration of velocity map over a vessel cross-section (in any cross-section) cannot resolve flux information. However, blood flux can be assessed by estimating the peak of the MUSIC power spectrum, as shown in **Figure 4-4(B)**. For each concentration level, by increasing the flow rate of syringe pump, total MUSIC flux increased in an almost linear way. By increasing the concentration of flowing particles inside the tube, total MUSIC flux value significantly increased that was in agreement with the simulations. The only difference is that by increasing the flow rate on the syringe pump, total MUSIC flux leans towards a non-linear behavior that can be explained by photon multiple scattering effect and attenuation. This nonlinear effect of flux has been reported in the laser Doppler literature and similar measurements on flux (perfusion) as a function of particle velocity and concentration of moving particles has been presented [Serov-2001, Serov-2005]. Also, OCT signal attenuation and absorption should increase as particle concentration and velocity increases. Therefore, the

detected signal SNR from deeper backscatterers was lower and the estimated MUSIC peak was lower than expected.

In order to validate the results with actual flux values, exact measurement of particle concentration and size is required. However, in our case, we validated sensitivity of MUSIC flux estimation based on the linearity of total blood flux with respect to the density. Since all of the experimental conditions remain the same and only the solution concentration was altered, and total flux is linearly related to the solution concentration, we expect that by doubling the solution concentration, total flux would also double. Since the particle concentration of the low, medium and high conditions in **Figure 4-4** are linearly related, the slope of the fitted line to each curve can be a good measure to asses sensitivity of the MUSIC estimator to flux variations. A 1st order polynomial was fitted to the total flux of each solution concentration data points as a function of syringe pump's flow rate using the minimum least square error method with 95% confidence bounds and the fitting results are summarized in **Table 4-1**. Since R-square (goodness of the fit) for all of the cases is larger than 0.93, the data is fitted well to a linear first order polynomial model.

It can be observed that the first coefficient of the fitted curves (P1) that shows the slope of the line is linearly related to the variations of the concentration. For instance the ratio of the coefficients can be calculated by

$$\frac{P1(4\%)}{P1(2\%)} = 2.06 \pm \varepsilon_1 \text{ and } \frac{P1(2\%)}{P1(1\%)} = 1.85 \pm \varepsilon_2 \quad (4\text{-}21)$$

which are nearly a factor of two when the concentration is doubled. One reason that the ratios are not perfectly twice might be due to the impurities of the solution or other experimental and measurement errors.

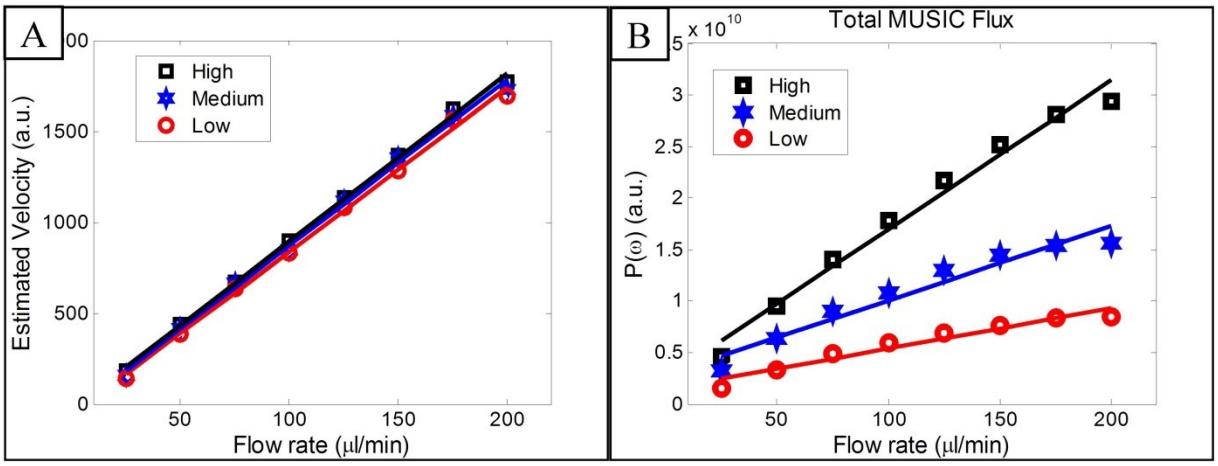

Figure 4-4 Velocity and flux estimation of phantom flux using MUSIC.

(A) Estimated flow rate by integrating total velocity of particles from the tube cross-section. The estimated flow follows a linear line as a function of syringe pump flow rate ($r \geq 0.99$). (B) Estimated flux by integrating total MUSIC peak at the tube-cross section. The estimated flux is almost linear as a function of syringe pump flow rate ($r \geq 0.93$).

Table 4-1 Parameter fitting to the estimation plots.

Fitted parameters to the measured total blood flux using a minimum least square error fitting to a first-order polynomial for different concentration of flowing particles. R-sqaure is a measure of linearity in the data fitting algorithm

Concentration	Fitted to a 1st order polynomial : f(x) = P1*x+P2		
	P1/10^7	P2/10^8	R-square
High (4%)	11.62 ± 1.75	19.36 ± 22.14	0.97
Medium (2%)	5.64 ± 1.44	2.08 ± 18.19	0.94
Low (1%)	3.05 ± 0.81	8.46 ± 10.23	0.93

Flow and flux profiles within the tube are plotted in **Figure 4-5(A)** and **(B)**, respectively where x-axis is the spatial location at the tube cross-section. For each concentration, the syringe pump is driven by 125, 150, 175 and 200 μL/min flow rate. The velocity profile resembles parabolic

shape. And regardless of the particle concentration, velocity profile remains the same. On the other hand, flux profile does not have a very smooth parabolic profile as explained earlier. Since MUSIC peak is sensitive to the amplitude of the received signal, surface reflection from the phantom and tube structures that were perpendicular to the beam can cause signal saturation or attenuation. Therefore, the flux profile does not follow a typical parabolic shape. However, changing in the concentration of moving particles can be differentiated on the flux profile and by increasing the concentration, flux profile appears larger.

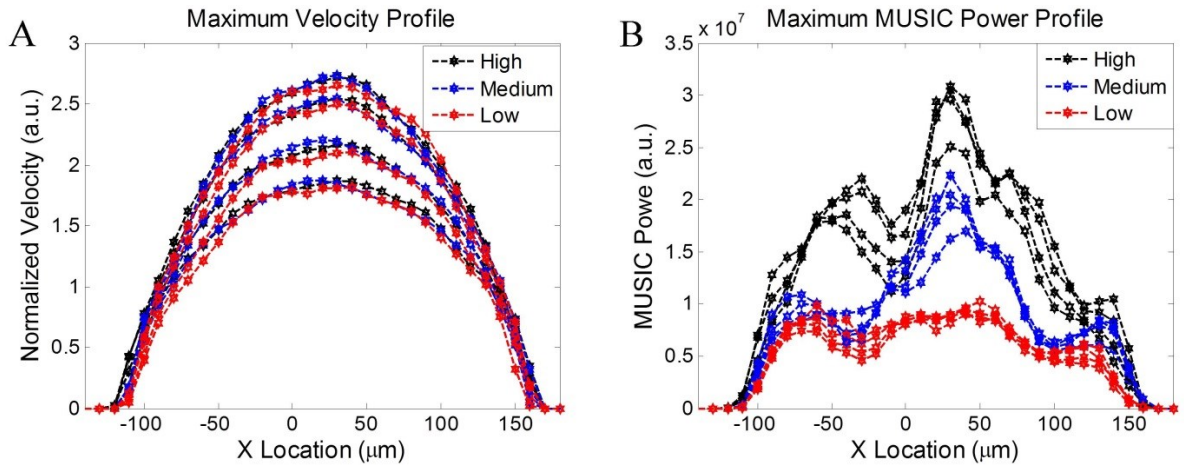

Figure 4-5 Flow and flux profile in phantom cross section.

(A) Estimated velocity. Flow profiles of four syringe flow velocities (125, 150, 175 and 200 μL/min)along the tube with various concentration of particles. (B) Estimated MUSIC power peak for the profiles shown in (A).

We compared the performance of MUSIC method in estimating total blood flow and flux with some of the existing techniques in the literature including phase-resolved color Doppler (PRCD) [Makita-2006, Zhao-2000], speckle variance (SV) [Mariampillai-2008] and phase difference variance (PDV) [Yang-2008, Kim-2011]. We calculated total blood flow using each algorithm and presented the results similar to the approach explained in **Figure 4-4** and equations (4-19-4-

20). The comparison between PRCD, PDV and SV for total flow measurements is shown in **Figure 4-6**. It can be observed that PRCD is only sensitive to the velocity information, and the concentration of the flowing particles has a slight change in the estimated total blood flow. On the other hand, PDV and SV can encode the concentration information. However, the slopes of the fitted line for SV and PDV are not linearly dependent on the flowing particles' concentration and the estimate is very biased. The ratio of the slopes of high to medium and medium to low concentrations are 1.06 and 1.10, respectively, which indicates that PDV cannot linearly encode the changes in the flowing particle concentrations and flux. The R-square measures of fitting a polynomial to the PDV data indicated that a second-order polynomial was a better fit to the data set, suggesting that PDV estimation of total blood flow may be linearly dependent on the square of the particle velocity. For the SV method, we noticed that the overall value of the estimated total blood flow was relatively larger for higher concentrations, while there was no linear relationship to the syringe pump's increase of flow rate. Also, the ratios of the high/medium and medium/low slopes were 5.39 and 1.68, respectively, which deviates significantly from the ratio of the original concentration values. Similar to the PDV method, the R-square measures of goodness showed that SV data set is better fit with the second-order polynomial rather than a first-order. The fitting measures and quantities of PRCD, PDV and SV are given in **Table 4-2**.

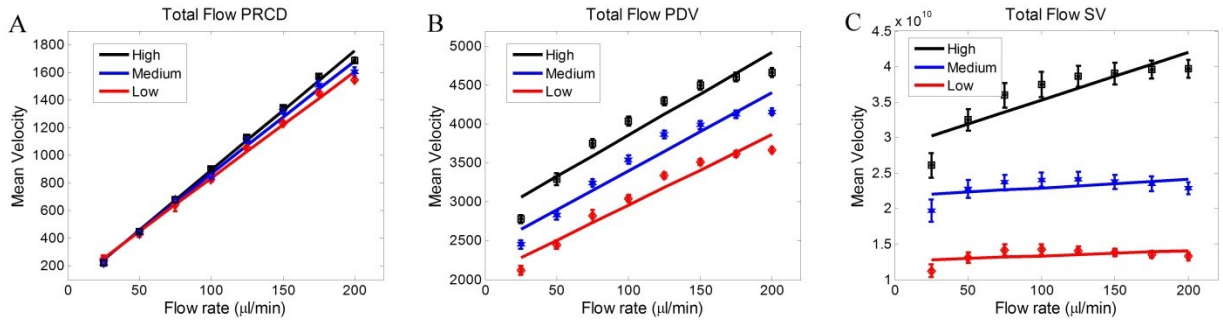

Figure 4-6 Comparison of flow estimating techniques.

Comparison between PRCD(A), PDV(B) and SV(C) methods of measuring total flow

Table 4-2 Linearity of SV, PDV and PRCD methods to measure total flow.

Method	Concentration	R-square (1^{st} order)	$\frac{P1(high)}{P1(medium)}$	$\frac{P1(medium)}{P1(low)}$
SV	High	0.76	5.39	1.68
	Medium	0.28		
	Low	0.21		
PDV	High	0.92	1.06	1.10
	Medium	0.93		
	Low	0.95		
PRCD	High	0.99	1.05	1.06
	Medium	0.99		
	Low	0.99		
MUSIC	High	0.97	2.06	1.85
	Medium	0.94		
	Low	0.93		

Notwithstanding, MUSIC estimation also has some limitations. The computational complexity of the MUSIC method is in the order of M^3 which is mainly because of searching the eigen-elements of the covariance matrix. Also, MUSIC is based on a precise modeling of the noise and assumes that the covariance matrix of the noise is known which may not be true for array processing. And other periodogram methods such as minimum variance should be utilized

instead. One of the major limitations is that MUSIC method requires the knowledge about the number of complex sine waves before estimating their frequencies and the performance of the MUSIC estimation highly depends on accurate determination of the number of estimated complex sine waves. There are some techniques based on the likelihood function of the observation to determine the order of a model. Akaike information criterion (AIC) [Akaike-1973] consists of minimizing the quantity below in relation to the supposed number P of complex sine waves to determine the order of an autoregressive model:

$$AIC(P) = -Nlog(\frac{\prod_{i=p+1}^{M}\hat{\lambda}_i}{\left(\frac{1}{M-P}\sum_{i=p+1}^{M}\hat{\lambda}_i\right)^{M-p}}) + p(2M-p) \tag{4-21}$$

where p is an estimate of P, N is the number of observations and $\hat{\lambda}_i$ are the eigenvalues of the covariance matrix $\hat{R}_{xx}$ arranged in descending order. The estimation of the noise variance is then given by the average of $(M-p)$ smallest eigenvalues of the covariance matrix, that is

$$\hat{\sigma}^2(p) = \frac{1}{M-p}\sum_{i=p+1}^{M}\hat{\lambda}_i. \tag{4-22}$$

Another criterion widely used to determine the order of a model is minimum description length (MDL) [Rissanen-1978. Schwarz-1978] which is slightly different from AIC:

$$MDL(p) = -Nlog(\frac{\prod_{i=p+1}^{M}\hat{\lambda}_i}{\left(\frac{1}{M-P}\sum_{i=p+1}^{M}\hat{\lambda}_i\right)^{M-p}}) + \frac{1}{2}p(2M-p)\log(N). \tag{4-23}$$

The MDL criterion is consistent and converges to the true value of P when $N \to \infty$. It is commonly known that the AIC criterion tends to overestimate while the MDL criterion underestimates the number of complex sine waves. Therefore, a hybrid technique based on both criterions may be utilized to determine the order of MUSIC.

Although widely used to measure Doppler velocity in Doppler OCT, it has recently been demonstrated that Kasai estimator [Kasai-1985] is statistically suboptimal as determined by the

standard performance metrics of estimator bias, variance and efficiency [Chan-2013]. The Kasai estimator is computationally simple and can be implemented for real-time applications. However, no prior knowledge or assumption is required about the noise statistics, meaning that the estimator is not optimal. It was suggested that maximum likelihood estimator (MLE) which is a parametric estimation technique based on the peak location of the power spectral density, can provide a consistent, asymptotically unbiased and asymptotically efficient estimation. In theory, the performance of an estimator is compared with Cramer-Rao lower bound (CRLB), which indicates the theoretical best performance of an unbiased estimator. It was shown that MLE estimator can achieve CRLB when SNR is higher than 36 dB and length of data is larger than 8. On the other hand, MUSIC algorithm estimates the spectral density of the received signal and finds peaks and their corresponding frequency locations on the spectrum which is similar to MLE and requires less knowledge of the model, except for the number of components in the signal. Stoica et al. [Stoica-1989] have shown that MUSIC estimator should asymptotically achieve CRB for uncorrelated signals and its error variance monotonically decreases by increasing samples. It was proved that MUSIC estimator is a large sample realization of the MLE if and only if the signal covariance matrix is diagonal (uncorrelated signal). In the correlated signal case, MUSIC error variance may occasionally increase. Therefore, MUSIC estimation can provide a promising estimate of the Doppler frequency (flow) and its corresponding peak (flux) and can asymptotically reach CRLB.

The proposed technique is directly applicable to *in vivo* studies that require to monitor relative changes of blood flux with respect to physiological changes such as stroke models where a baseline and post-operation data are available for relative comparison [Zhang-2009]. Also, by making some assumptions about hematocrit level of the blood sample (assuming constant

concentration), total blood flux can be measured similar to PAI [Jiang-2012]. Although we have shown flux measurement within a flow phantom with known flowing conditions, we would like to measure the flux within capillaries *in vivo* where a prior knowledge of the hematocrit condition is not available. However, absolute measurement of blood flux *in vivo* requires calibration of parameters to precisely indicate how the measured total blood flow, flux and particle concentration are inter-related. In future, we would like to perform more experiments using whole blood samples and generate flow and flux curves to be able to provide calibrations based on the variation of RBC concentration, blood velocity and oxygen saturation. Given the calibration plots, we would be able to precisely measure total flow and flux within capillaries.

4.6 *In vivo* studies

4.6.1 Animal preparation

Non-invasive in vivo images were acquired from pinna of healthy ~8 weeks old male hairless mice weighing approximately 28g. During experiments, the mouse was anesthetized using 2% isoflurance (0.2 L/min O2, 0.8 L/min air). The ear was kept flat on a microscope glass. The animal was placed in supine position on a heating blanket (Harvard Apparatus). The animal internal body temperature was constantly monitored using an intra-rectal temperature monitoring system which was used to actively maintain the animal body temperature by the use of temperature feedback provided by the heating blanket. The experimental protocol was in compliance with the Federal guidelines for care and handling of small rodents and approved by the Institution Animal Care and Use Committee (IACUC) of the University of Washington, WA.

4.6.2 Scanning protocol

The scanning protocol was based on three-dimensional UHS-OMAG technique. The x-scanner (fast B-scan) was driven with a saw tooth waveform and the y-scanner (slow C-scan) was driven with a step function waveform. The fast and slow scanners covered a rectangular area of ~ 2.2x2.2 mm^2 on the sample. Each B-scan consisted of 400 A-lines covering a range of ~ 2.2 mm on the sample. The duty cycle of the saw tooth waveform rising edge was set at ~80% per cycle, which provided a B-scan frame rate of ~ 94 frames per second. The C-scan consisted of 400 scan locations with B-scan repetition of 8 frames per location for flow imaging and quantification. The total size of the data set was $1.28x10^6$ A-lines and total acquisition time was 32 seconds. The captured data was processed off-line using MATLAB© (MathWorks).

4.6.3 *MUSIC-OMAG visualization*

For better visualization of MUSIC-OMAG quantification, we divided the dynamic range of MUSIC power ($P(\omega)$) into two bands: the lower-band and the upper-band power, which were separated using a threshold value. The threshold was manually set to a value such that blood flow in small vessels and capillary loops were separated from that of larger vessels. This threshold value can be variable depending on the sampling rate and the structure to be imaged and the user can arbitrarily choose it based on the characteristics to be emphasized. We should note that this threshold value is only for visualization purposes and does not have any impact on the quantification itself. The upper-band was color coded and overlaid on the gray-coded lower band. **Figures 4-7 (A-C)** show the lower-band power (gray), upper-band power (color-coded) and combined power, respectively. We set the threshold such that the lower-band power corresponded to the slower flow inside small vessels and capillary loops. Due to the parabolic flow profile inside vessel lumen, the lower-band power is also expected near vessel wall in larger

vessels while the upper-band power is expected towards the large vessel center line. **Figure 4-7(D)** shows the corresponding UHS-OMAG processing of the same data set. By comparing UHS-OMAG and MUSIC-OMAG, it can be observed that they are almost identical and all of the small vessels and capillaries observed on UHS-OMAG can also be found in MUSIC-OMAG which confirms the sensitivity of MUSIC-OMAG quantification.

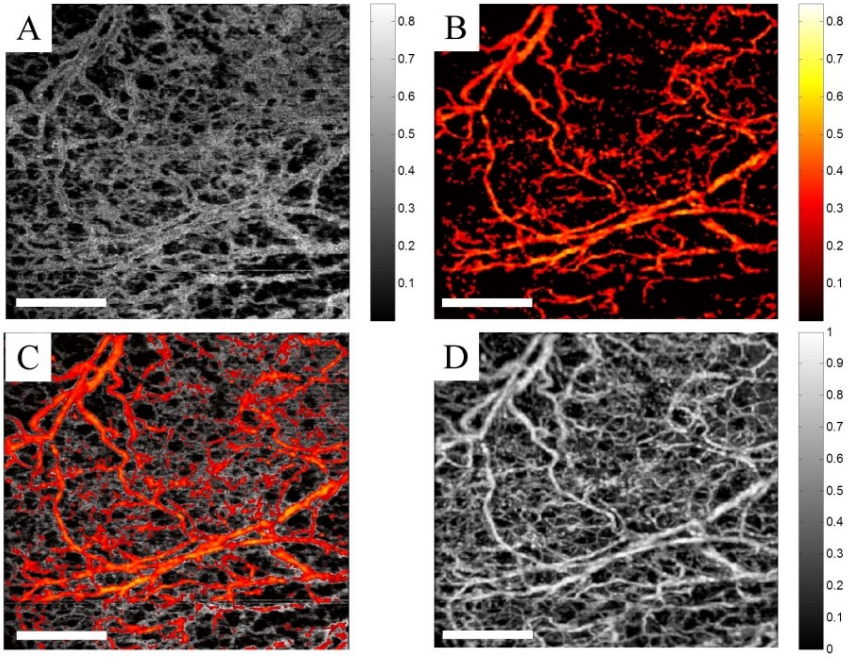

Figure 4-7 MUSIC-OMAG visualization.

(A) Lower-band power, gray-coded. (B) Upper-band power, color-coded. (C) Combined MUSIC-OMAG power, where upper-band power is overlaid on the lower-band power. (D) UHS-OMAG of the corresponding data set processing using ED method. (The scale bar = 500 μm)

The entire mouse ear pinna was divided into 2.2x2.2 mm^2 overlapping mosaics and each mosaic was scanned using UHS-OMAG scanning protocol. Then, the mosaics were processed separately using ED-OMAG and MUSIC (for quantification) and their corresponding maximum intensity projection maps were stitched together to form the entire ear pinna en-face angiogram. **Figures 4-8(A and B)** show the UHS-OMAG and MUSIC-OMAG images of the mouse pinna,

respectively. It can be observed in MUSIC-OMAG image that the larger arteries and veins are dominated by upper-band power and color-coded while smaller vessels and capillary loops toward the pinna edge are mainly dominated by lower-band power and gray-coded. This quantification and visualization technique allows observing certain response in capillary loops while the change in larger vasculature is not significant. **Figure 4-8(A)** and **Figure 4-8(B)** are resulted by using two different algorithms: ED-UHS-OMAG (for visualization of blood flow perfusion) and MUSIC-OMAG (for quantification of blood flow perfusion or flux rate). We should emphasize that these algorithms are different in nature. ED-UHS-OMAG is based on processing A-line by A-line, whereas MUSIC-OMAG is based on voxel-processing by the use of the proposed algorithm. Assuming that the signal is divided into tissue, blood and noise contributions, tissue and blood flow contributions are estimated by orthogonality principle (equation 9). The estimated contributions will have a center frequency (ω, i) and a corresponding spectral power [P(ω_i)] estimated using equation 10. For better visualization of capillaries and large vessels using different color-maps, these results are visualized using the method explained in **Figure 4-7**. Again, we have to emphasize that the data acquisition protocol and scanning pattern is similar to the ones previously used for UHS-OMAG visualization, and we propose to quantify blood flow perfusion within capillary beds using the proposed MUSIC-OMAG algorithm.

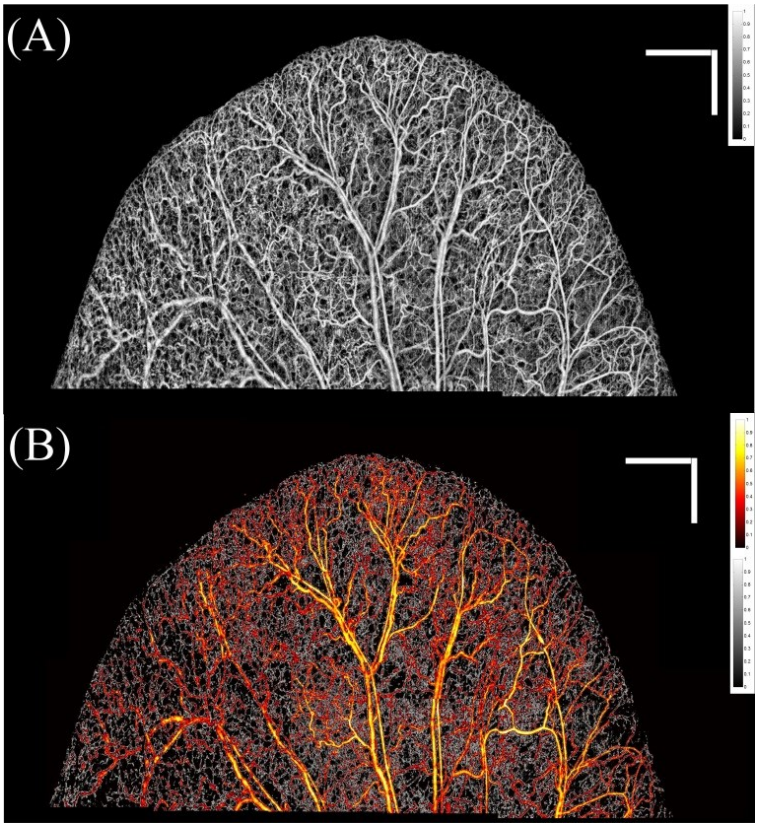

Figure 4-8 Complete mouse ear pinna quantification.

(A) UHS-OMAG image of the entire mouse ear processing using ED method, stitched together. (B) MUSIC-OMAG processing of the same data set of (A). Large vessels and faster flow are color-coded while slower flow and capillary loops are gray-coded. The bar size is 1x1 mm.

4.6.4 Thermoregulatory response

During the experiments, the animal's body temperature was actively maintained by the feedback loop provided by the heating blanket, while the OCT system was continuously capturing the UHS-OMAG dataset over the time. Over the time period of 60 minutes, due to the active control of body temperature by the feedback loop, the temperature was changed from 37 ºC, gradually raised to 39.5ºC followed by a gradual drop to 32 ºC, and then returned back to the 37.6 ºC which was the target temperature for normal physiological condition. Accidently, this feedback control process gave us an opportunity to monitor the microcirculation response to the changes of body temperature, asserting the sensitivity of MUSIC-OMAG to capillary hemodynamic

variations. On the other hand, this process also simulated the process of a thermoregulatory experiment in terms of physiological process. At the body temperature of 39.5 ºC, the animal experienced hyperthermia, while a body temperature of 32 ºC leaded to hypothermia for the animal. Because we continuously captured the UHS-OMAG data at the same location over the whole process, we processed the dataset to obtain the response of microcirculation within the tissue beds to the changes of the body temperature. Compared to normothermia (37.6 ºC), we expect that the capillary flow activity should increase (vasodilation) during hyperthermia, while it should decrease (vasoconstriction) during hypothermia. Although, transient vasodilation, vasoconstriction and blood flow response to temperature challenge is a multi-factorial phenomenon and can be very complicated in nature [Kellogg-2006], we expect that hemodynamic should follow a hysteresis-like curve in response to thermoregulatory challenge in the current study.

Figure 4-9 shows a series of the dynamic MUSIC-OMAG images captured during active feedback control of the heating blanket to the body temperature of the animal used, where the response of the capillary flow to the temperature change can be observed. The increase of the body temperature towards hyperthermia (39.5 ºC) leads to the increase of the density of capillary network in the areas in between larger vessels; and in the meantime, some new capillaries appeared (e.g., green pointer in **Figure 4-9(C)),** demonstrating the increase of blood flow within microcirculatory tissue beds during hyperthermia. These changes were mostly observed at capillary level where the density of gray-coded areas corresponding to small vessels and capillaries was increased. During the feedback control of the body temperature towards hypothermia (32.0 C), it was observed that most of the small capillaries disappeared and blood flow in some larger vessels also decreased (e.g. green pointer in **Figure 4-9(H)**). However, these

changes were more obvious at capillary level shown by gray map which corresponds to lower-band power. By the increase of the body temperature towards normothermia (37.6 ºC), the functional capillaries which were missing in hyperthermia appeared again. At this point, the appearance of the blood vessel network was very similar to the baseline image at 37.5 ºC (e.g. green pointer in **Figure 4-9(L)**).

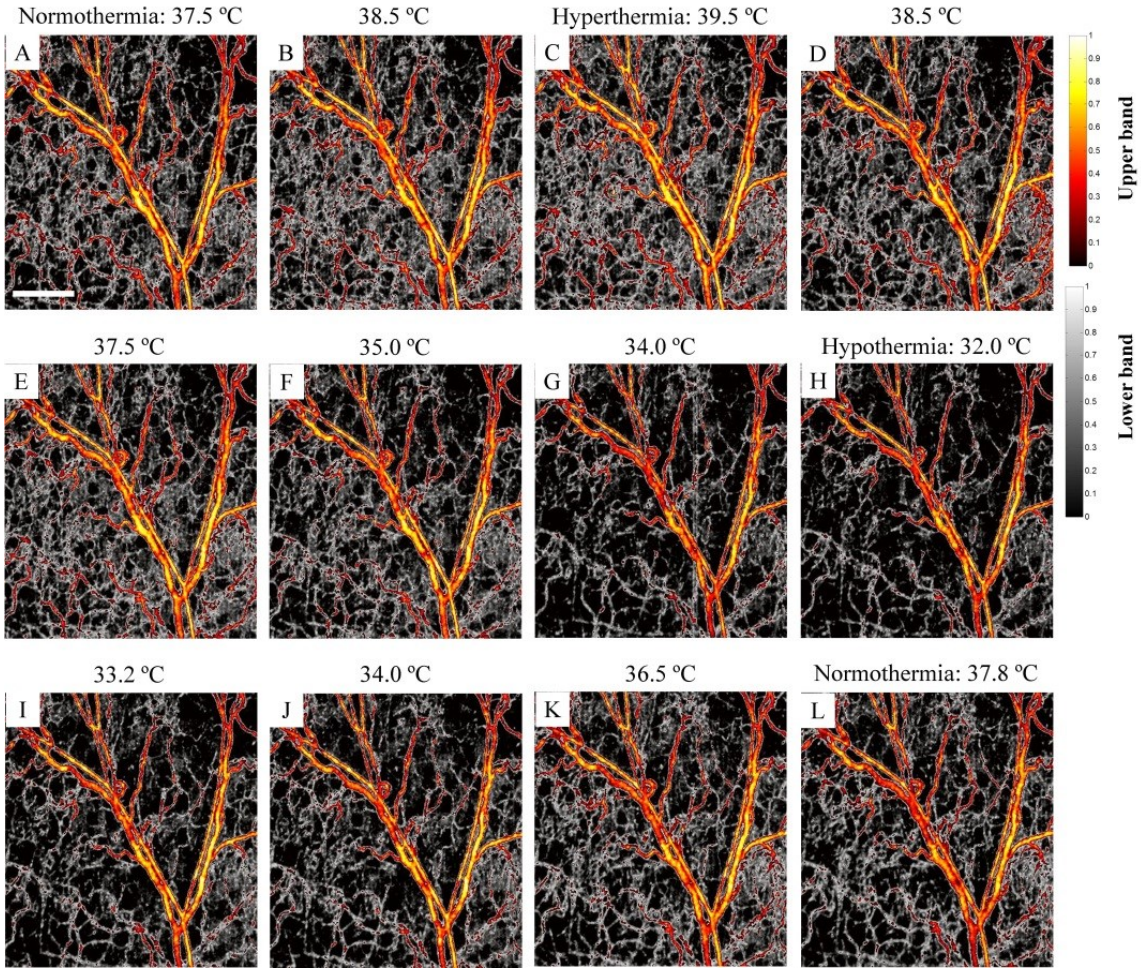

Figure 4-9 Micricirculation quantification during yhermoregulatory.

MUSIC-OMAG monitoring the vasculature response to the thermoregulatory challenge. During the hyperthermia (39.5 ºC), new capillaries appear while most of the small vessels and capillaries disappear during hypothermia (32.0 ºC), and they go back to the baseline image when returning to normothermia (37.8 ºC). (The scale bar = 500 μm)

Total blood flow rate at capillaries is related to blood flux which is the rate of red blood cells passing through a unit area cross-section. Assuming that the MUSIC power estimates blood flux, we can estimate total blood flux by integrating these values in a given region of interest. We measured mean and standard deviation of total blood flux in **Figures 4-9 (A-L)**. Then, we normalized the mean value by the total blood flow in the beginning of normothermia and plot it as a function of temperature in **Figure 4-10(A)**. As we expected, total blood flow increased during the hyperthermia, decreased during hypothermia and almost went back to the baseline. We also measured the normalized vessel area density [Reif-2012] of the ear and plot it over the temperature values in **Figure 4-10(B)**. As we already observed from the vessel map, the vessel area density increased during hypothermia which means that more capillaries appeared. During hypothermia, the vessel area density decreased which was observed in **Figure 4-9(H)** that small capillaries disappeared. By increasing the temperature and moving towards normothermia, more capillaries appeared again, therefore vessel area density increased. Measuring total blood flow requires some assumptions and calibration. What we're measuring here is a function of number of particles passing through the beam at a vessel cross-section and their velocity. In order to measure total blood flow, more parameters would be required.

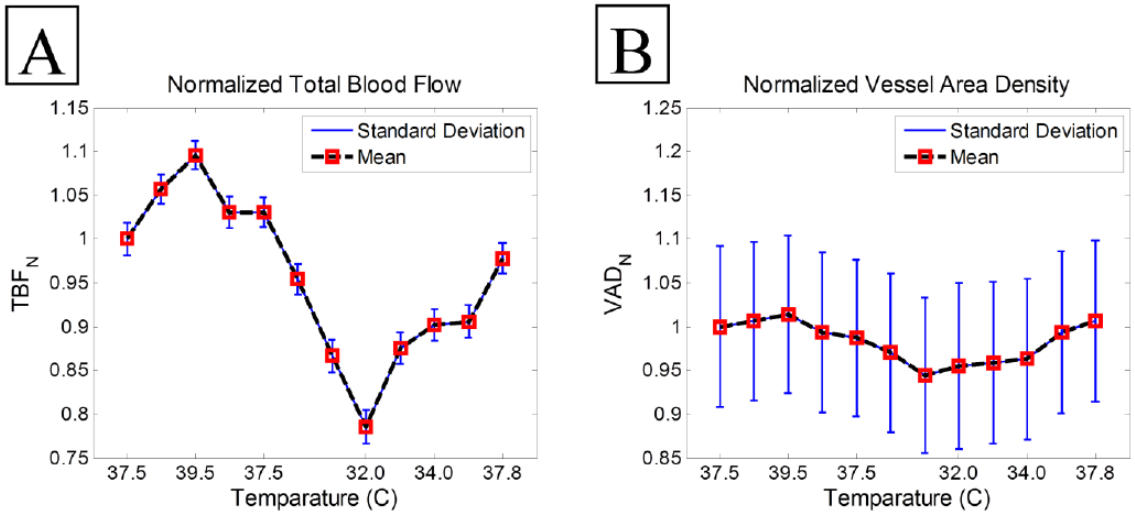

Figure 4-10 Normalized total blood flow

(A) and normalized vessel area density (B) average in response to the thermoregulatory challenge.

4.6.5 Flow profile measurement

Normal blood flow inside relatively large blood vessels is not uniform at the vessel cross section and has a parabolic distribution with the maximum value at the center of the vessel and slower towards the vessel wall. Parabolic or laminar flow allows minimum loss kinetic energy and fluid pressure transfer and reduces friction by allowing the blood layers to slide smoothly over each other in concentric layers or laminae [Baun-2012]. Therefore, we expect a parabolic quantity across the vessel cross-section after quantifying the flow using MUSIC-OMAG. **Figure 4-11(A)** shows the en-face view of maximum-intensity projection map of MUSIC-OMAG quantification of micro-vasculature in the mouse ear pinna in a 2.2x2.2 mm^2 area color-coded with the thresholding visualization technique. **Figure 4-11(B)** is the zoomed area of the designated white rectangle in **Figure 4-11(A)** visualized with a different color map for simplification. Three flow profiles at two vessel locations marked by solid lines (I and II) are shown in **Figures 4-11(C and D)**, respectively. We plotted the flow profile of each horizontal line of **Figure 4-11(B)** such that X-axis is given by horizontal line in μm and Y-axis is the estimated MUSIC-OMAG power

$P(\omega)$ (normalized units) and each color (red, green and blue) corresponds to one plot. Three consecutive locations were plotted to confirm their similarities along the vessels and repeatability of MUSIC-OMAG. It can be observed that the flow profile meets a typical laminar flow profile inside vessels where the flow value is largest in the middle of the vessel and decreases towards the vessel wall. Also, the flow goes to nearly zero outside vessels where no flow exists. In the areas that other capillaries are present at a different depth plane above or below the vessel of interest, the flow profile may not completely go below the noise level. This phenomenon is more obvious in **Figure 4-11(D)**. Since there are two vessel branches in the **Figures 4-11 (C and D)**, two parabolic flow shapes are observed. Based on our knowledge of anatomy, the thinner vessel corresponds to an arteriole and the larger vessel is a venule. Therefore, blood flow direction in these pairs should be opposite of each other.

4.6.6 Comparison

We compared MUSIC-OMAG with CAC method over four data sets from thermoregulatory experiments: normothermia (37.8 ºC), hyperthermia (39.5 ºC), hypothermia (32.0 ºC) and return to normothermia (37.5 ºC). **Figures 4-11(A-D)** show the performance of MUSIC-OMAG on these data points, respectively. Similarly, Figs. E-H show the performance of CAC method and **Figures 4-11(I-L)** show the corresponding UHS-OMAG processing of those data points. It can be observed that CAC was capable of picking up changes in the capillary blood flow. However, it was very sensitive to respiratory-induced motion, which showed up as vertical stripes on the image. Besides the observed artifacts on the vessel wall, the signal inside the large vessels was aliased, mainly due to the fast flow (fast relative to the Nyquist rate) and the received signal at that location was completely decorrelated. Although the background of UHS-OMAG images

shown in **Figures 4-11(I-L)** was obviously lower during hypothermia, the variations between different data points were not as apparent as MUSIC-OMAG.

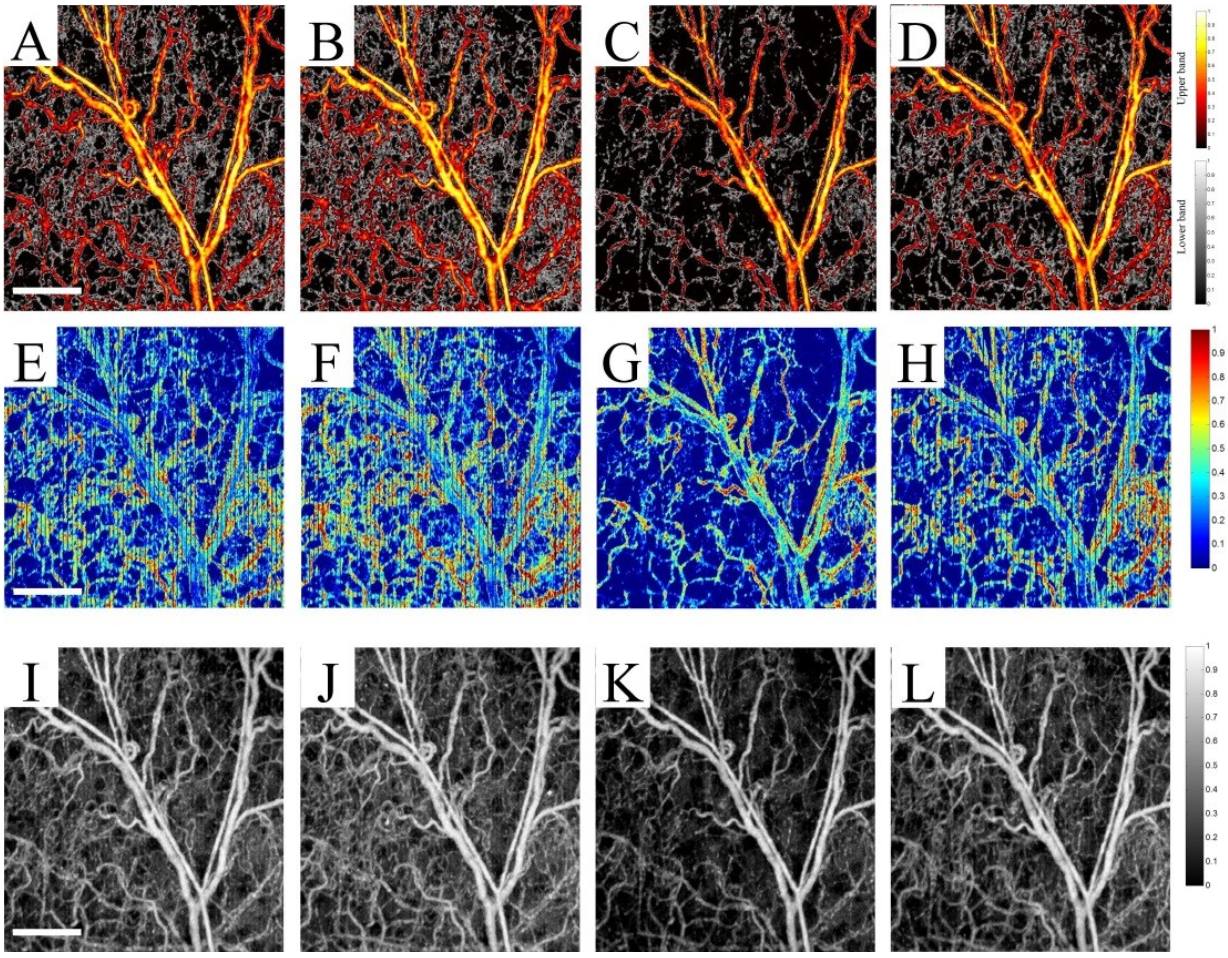

Figure 4-11 Estimation comparison.

A comparison between MUSIC-OMAG (A-D), autocorrelation method (E-H) and UHS-OMAG (I-L) processing of the mouse ear capillary response to thermoregulatory challenge, where the first column (A, E and I) is the normothermia condition (37.5 ºC), the second column (B, F and J) is hyperthermia condition (39.5 ºC), the third column (C, G and K) is hypothermia (32. ºC) and the last column (D, H and L) is return to the normothermia condition (37.8 ºC). (The scale bar = 500 μm)

The performance of CAC method highly depends on the sampling rate (to avoid aliasing) and the number of data points (frequency resolution). Since the signal at each voxel decorrelates within few samples, the dynamic range of the CAC method is relatively small. Compared to UHS-

OMAG and MUSIC-OMAG, the CAC method was sensitive to tissue motion which eventually caused vertical dark stripes on the image. Also, there were some artifacts on vessel walls and aliasing inside larger vessels which were not observed in MUSIC-OMAG.

While MUSIC-OMAG overcame these artifacts as well as the frequency resolution, it came with the price of computational power which was relatively longer than CAC. Processing time per frame on a 6-core processor (AMD Phenom(tm) II X6 1090T, 3.21 Ghz) desktop computer based on Matlab code implementation was 0.19, 2.78 and 12.15 seconds/frame for ED-based UHS-OMAG, CAC and MUSIC-OMAG, respectively. Another major advantage of MUSIC-OMAG over CAC is the data acquisition time and volume. Due to sensitivity of the frequency estimation technique to the frequency resolution, at least 128 samples per location were required to get a reasonably good estimate using CAC method. However, MUSIC-OMAG is performed on data acquired using UHS-OMAG scanning protocol which requires a significantly smaller data volume and time.

One way to increase the processing time is to mask the input data before MUSIC processing by UHS-OMAG. This allows processing only the voxels which are supposedly inside the vessels. We should emphasize that the characteristics of all of the quantification techniques such as CAC and MUSIC-OMAG highly depends on the received signal and the local conditions such as surface and specular reflection and absorption, which eventually may influence the repeatability of capillary flow quantification.

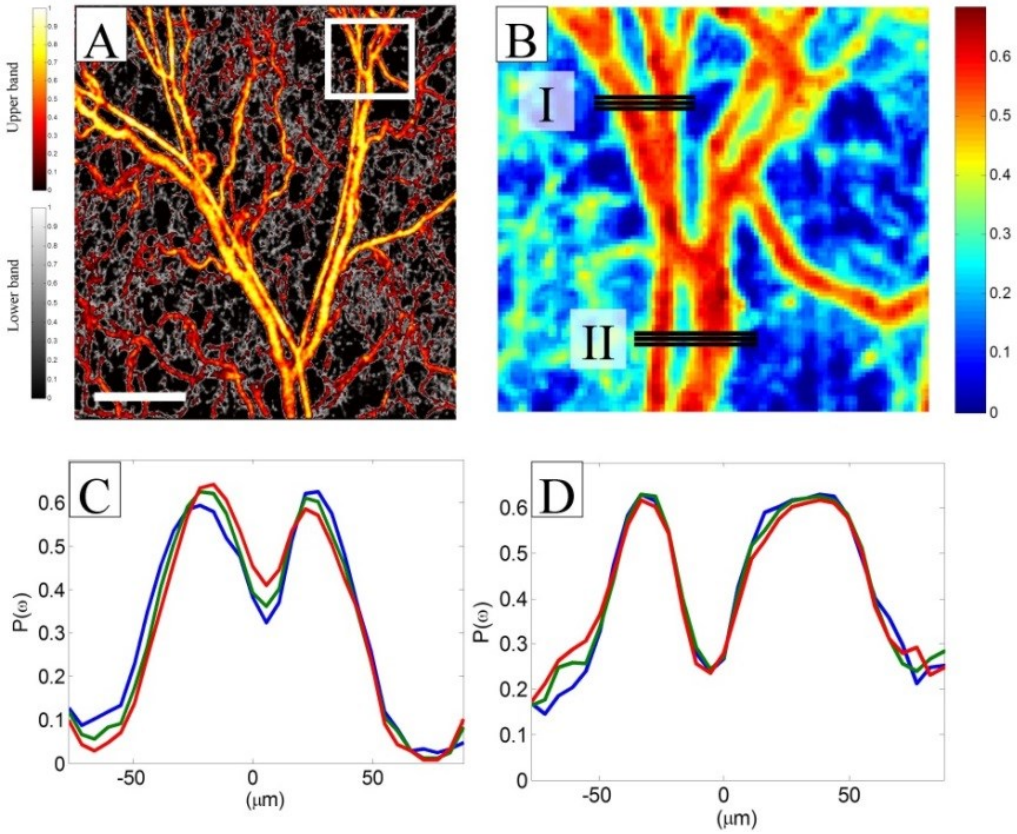

Figure 4-12 Flow profile characteristics of vessels using MUSIC-OMAG method.

(A) MUSIC-OMAG processing. (B) Zoomed in version of (A) color-coded for better visualization. (C and D) Flow profile of the vessels marked in box (I) and (II) in (B), respectively. (The scale bar = 500 μm)

4.7 Conclusions

In this chapter, we proposed a super-resolution technique to quantify simultaneous RBC flow and flux, based on the velocity and number of particles passing through the beam, respectively. Most of the existing methods in the literature only quantify RBC flow by assessing velocity profile in microevssels. Also, the proposed method of quantifying RBC flux can only quantify flux of single RBCs in small capillaries that only one cell at the time passes through the vessel cross-section. The MUSIC method of simultaneous flow and flux measurement is similar to those in the laser Doppler techniques of blood perfusion assessment and ultrasound power Doppler ultrasound. MUSIC estimation can asymptotically reach CRLB which is the best

possible estimator given that model. Compared to the existing methods of PRDCD, PDV and SV, MUSIC is capable of linearly quantifying RBC velocity and concentration whereas other techniques are biased and not sensitive to particle concentration.

In the *in vivo* experiments, the total scanning time for 3-D application is identical to three-dimensional ultrahigh sensitive optical micro-angiography and it does not have aliasing at large vessels. Therefore, this method can efficiently quantify blood flow in capillary beds as well as large vessels. In order to test the sensitivity of MUSIC-OMAG to capillary hemodynamic variations, we utilized the experimental dataset of UHS-OMAG, which were continuously acquired during active control of the body temperature of the animal, giving an opportunity to observe capillary flow response in the mouse ear pinna. We observed that the capillary network became denser in areas between larger vessels and some new capillaries appeared during hyperthermia, demonstrating the increase of blood flow within the microcirculatory tissue beds. During hypothermia, most of the small capillaries disappeared and blood flow in some larger vessels also decreased. When the body temperature returned to normothermia status, the capillaries appeared again. We also compared MUSIC-OMAG with CAC method over four data points during the change of the body temperature in the animal. We showed that the performance of MUSIC-OMAG was superior to CAC; and furthermore no apparent motion artifacts were observed at vessel walls and inside large vessels. Also, MUSIC-OMAG method was sensitive to small capillary response to the change of the body temperature. The flow profile at large vessels evaluated by the MUSIC-OMAG was in agreement with typical flow characteristics.

The flux measurement units are auxiliary values. Given fixed experimental conditions such as measurement site and angel, physiological variations due to changes in the blood flux perfusion

can be utilized. However, flow (velocity) measurement units are absolute and dependent on the sampling rate and Doppler angel. Simultaneous RBC flow and flux measurement in the microcirculatory system allows estimating the blood perfusion within the tissue beds surrounding capillary beds and therefore estimating metabolic activity of the tissue. Thus, we expect that the non-invasive and label-free measurement of RBC flow/flux can be utilized in clinical applications related to vascular disease, diabetes, cancer and retinal diseases.

4.8 Appendix

Principle of orthogonality of the signal and noise subspaces [Castanié-2013]

Theorem: Let $V = [V_s, V_b]$, $\Lambda_s = diag[\lambda_1, \dots, \lambda_P]$, $\Lambda_b = diag[\lambda_{P+1}, \dots, \lambda_M]$ where $P < M$ and the dimensions of V_s and V_b are $M \times P$ and $M \times (M - P)$, respectively. If we hypothesize that the covariance matrix Γ_{xx} of the amplitude of the complex sine waves is of full rank P, the minimum eigenvalue of Γ_{xx} is $\sigma^2$and the columns of V_s span the same subspace as S (signal subspace) given by $S_{M\times P} = [S_1\, S_2 \dots S_P]$ where $S_i = [1 \;\; e^{j\omega_i} \;\; e^{j2\omega_i} \;\; e^{j3\omega_i} \dots e^{j(M-1)\omega_i}]'$.

Proof: In the absence of noise ($\sigma^2 = 0$), the covariance matrix Γ_{xx} is written

$$\Gamma_{xx} = S\Gamma_{ss}S^H. \tag{4A-1}$$

Since the dimension of full-rank matrices S and Γ_{ss} are $M \times P$ and $P \times P$ with $P < M$, respectively, Γ_{xx} of dimension $M \times M$ is of full rank at most equal to P. On the other hand, since Γ_{xx} is a covariance matrix, it is Hermitian, non-negative, definite and its eigenvalues are real and positive or null. The hypothesis ($P < M$) implies that Γ_{xx} has P positive eigenvalues and ($M - P$) eigenvalues equal to zero.

Let v be an eigenvector associated with the null eigenvalue of Γ_{xx}, then

$$\Gamma_{xx} v = S \Gamma_{ss} S^H v = 0 \, . \tag{4A-2}$$

Since S and $\Gamma_{ss}$are full rank, we obtain

$$S^H v = 0 \tag{4A-3}$$

which implies that v belongs to the subspace orthogonal to the subspace spanned by the columns of S

$$v \in esp\{S\}^{\perp}. \tag{4A-4}$$

The set of eigenvectors $esp\{V_b\}$ associated with the zero eigenvalue belongs to the $esp\{S\}^{\perp}$ subspace. On the other hand, any vector of $esp\{S\}^{\perp}$ is an eigenvector of Γ_{xx} associated with the zero eigenvalue. Therefore

$$esp\{V_s\} = esp\{S\}^{\perp} \tag{4A-5}$$

that implies that the other eigenvectors of Γ_{xx} associated with strictly positive eigenvalues and spanning $esp\{V_s\}$ are in $esp\{S\}$. Then we have

$$esp\{V_s\} \subset esp(S). \tag{4A-6}$$

Since Γ_{xx} is Hermitian, there exist an onrthogonal basis of eigenvectors, which implies that

$$dimension(esp\{V_s\}) = P, \tag{4A-7}$$

Consequently implies that

$$esp\{V_s\} = esp(S). \tag{4A-8}$$

In the presence of white noise, the eigenvalues of

$$\Gamma_{xx} = S \Gamma_{ss} S^H + \sigma^2 I \tag{4A-9}$$

are those of $S\Gamma_{ss}S^H$ increased by σ^2 and the eigenvectors are unchanged. Therefore, the subspace $esp\{V_s\}$ spanned by the eigenvectors associated with the P largest eigenvalues of Γ_{xx} is the signal subspace and that the subspace $esp\{V_b\}$ spanned by the $(M - P)$ eigenvectors associated

with the smallest eigenvalue σ^2 is the noise subspace. Consequently, the complex sinusoid vectors of the signal subspace are orthogonal to the noise subspace.

Chapter 5. SEGMENTATION OF LYMPHATIC VESSELS

5.1 Introduction

The vascular system in vertebrates consists of cardiovascular and lymphatic sub-systems, both of which are highly branched tree-like tubular structures. The main role of cardiovascular system is to deliver oxygen, nutrition, fluid and signaling molecules required by living tissue via arteries and arterioles, for which the exchange usually happens at capillary beds. Venules and veins then collect deoxygenated blood from the tissues back to the heart. Due to blood pressure and osmotic gradients, some part of plasma leaks from the capillaries into the interstitial space. The protein-rich interstitial fluid (lymph) is collected back by lymphatic capillaries to maintain tissue fluid homoeostasis.

The lymphatic system consists of unidirectional, thin-walled capillaries and larger vessel network that drains lymph fluid from extracellular space within organs into larger collecting ducts. Lymph fluid moves from lymphatic capillary bed into a larger vessels covered by smooth muscle cells, called precollector vessels. Then, precollector vessels fuse with collecting lymphatic vessels, which have a basement membrane, continuous interendothelial junctions and bileaflet valves, in addition to a layer of smooth muscle cell. Contraction of smooth muscle cell layer and surrounding skeletal muscles as well as arterial pulsations are necessary for lymph movement, while valves prevent lymph backflow [Tammela-2010]. Finally, lymph is returned to venous circulation through thoracic duct. The lymphatic system also includes lymphoid organs such as sentinel lymph nodes (SNL), tonsils, Peyer's patches, spleen and thymus. The lymph nodes (LNs) are glands that collect lymph from vessels and their role is to entrap potentially

harmful substances such as bacteria and cancer cells in the body. SLNs are the primary nodes that drain waste from developing tumors.

The lymphatic system usually develops in parallel to the blood vessels in the skin and in most internal organs and is not present in central nervous system, bone marrow and avascular structures such as cartilage, epidermis and cornea. Besides draining lymph fluid from extracellular spaces, other roles of lymphatic system include absorbing lipids from intestinal tract, maintaining fluid hemostasis and transporting antigen-presenting cells and leukocytes to lymphoid organs. Also, lymphatic system plays an important role in the development of several diseases such as cancer, lymphedema, some inflammatory conditions and allergies [Alitalo-2005, Oliver-2004, Zgraggen-2013].

5.2 Imaging and visualization of lymphatic vessels

Due to the lack of detection and monitoring methods, lymphatic vessels are called "the forgotten circulation" and their role was mostly ignored [Rockson-2008]. Although lymphatic vessels were first described in the 17th century, the first reported detection method was not until mid-20th century and the first lymph-specific molecular marker was introduced only a decade ago. The field of imaging and visualization of lymphatic vessels can be divided into three main categories: lymph-drainage tracing, active cell targeting biomarkers and label-free. In lymph-drainage tracing methods, a contrast agent is required for injection into the tissue, and its uptake pathway by lymphatic vessels and SLNs are then become apparent. Active cell targeting methods involve identification and development of proteins and antibodies that bind to lymphatic-specific cells. Label-free methods involve no tracers or markers and use assumptions about certain characteristics of lymph fluid and their appearance/vessel lumen to image the lymphatic vessels.

5.2.1 Lymph drainage tracing methods

Since one of the roles of lymphatic system is to collect toxic and waste material from interstitial fluid, most of the developed clinical lymphatic imaging techniques was based on injection of contrast agents or dyes in the tissue or direct injection into the lymphatic vessels, which can provide contrast for uptake path by lymph vessels and nodes. Kimmonth pioneered direct visualization of lymphatic vessels (lymphangiography) by injecting radiopaque materials into small lymphatic vessels. He then used X-ray imaging to visualize the uptake path [Kinmonth-1952]. Later on, several contrast-enhanced and labeled lymphangiography agents were developed for standard imaging modalities such as X-ray, computed tomography (CT), magnetic resonance imaging (MRI), ultrasound and optical imaging. In contrast-enhanced lymphangiography, an iodinated contrast agent such as blue dye [Kinmonth-1955], Iotasul (Sshering AG, Berlin, Germany) [PARTSCH-1984] or Iopamidol (Nihon Schering, Osaka, Japan) [SUGA-2003] is either injected directly into a lymph vessel or indirectly into intradermal area for X-ray or computed tomography (CT). Although CT scans differentiated iodine concentration and LN morphology in normal and malignant LN, their application was limited due to the fast drainage of contrast agents from blood vessels that limited the imaging time in clinic. More recent development of bismuth sulfide nanoparticle CT agents with longer circulating half-life addressed some of the problems while their long-term toxicity is a major concern [Rabin-2006].

Positron emission tomography (PET) with beta-emitting isotopes (18-F-fluro-2-deoxy-D-glucose, FDG) provided higher sensitivity specifically when combined with CT for better spatial resolution [Lardinois-2003]. Lymphoscintigraphy with subcutaneous or intradermal injection of 99m-technetium (TC-99m) is currently the “gold standard” for lymphatic imaging in clinic and the most common nuclear method of imaging the lymphatics that enables visualization of the

lymphatic network using single-photon emission computer tomography (SPECT) [YUAN-2006, MCNEILL-1989, SZUBA-2003]. The injected compounds are taken up by lymphatic vessels and transported to draining LNs where they are phagocytosed by nodal macrophages. In lymphoscintigraphy, serial images are acquired using a gamma scintigraphic-camera and quantified by analyzing the clearance rate from the injection site [Modi-2007]. However, this technique requires rejection of scattered gamma photons and a large number of photons remain undetected and the scanning times can be long [Lardinois]. Another major disadvantage of this technique is poor temporal and spatial resolution, which limits direct visualization of detailed lymphatic anatomy and function [Proulx-2013].

MRI, unlike nuclear imaging techniques, does not require ionizing radiation exposure. MR lymphangiography is performed by intravenous or interstitial injection of gadolinium-labeled diethylene-triaminepentaacetic acid (Gd-DTPA), Gd dendrimetrs or liposomes and iron oxide particles [CL´EMENT-2004, MISSELWITZ-2006, BARRETT-2006]. However, besides high costs and low sensitivity of MRI for lymphangiography, MR lymphatic specific contrast agents are not clinically approved and some concerns regarding safety issues remain. Also, most CT and MRI lymphatic imaging is limited to enlarged LNs and vessels and normal LNs are below system sensitivity, despite the large lymph flow [BARRETT-2006].

Ultrasound has been used to investigate lymphadenopathy, enlargement and LNs [Vassallo-1992]. Also, color Doppler ultrasound (CDUS) provided functional imaging of the LNs which can be used to classify nodes as being reactive, metastatic, tuberculous, cystic or enlarged secondary to lymphoma [Tregnaghi-1997]. Intravenous injection of ultrasound micro-bubbles allowed the measurement of flow within a LN [Yang-2001]. Using this technique, benign and malignant lymphadenopathy was distinguished such that the degree and duration of contrast

enhancement as well as the number of vessels recorded was higher within the malignant nodes [Choi]. The main disadvantages of ultrasound are its operator dependent, poor spatial resolution and its limited use in the thorax and deep retroperitoneum [BARRETT-2006].

Photoacoustic tomography (PAT) is an image modality that is based on thermal expansion induced by pulsed laser and subsequent detection using ultrasound transducers. Based on unique absorption coefficients of oxygenated and deoxygenated hemoglobin, PAT allows high resolution imaging red blood cells. However, lymph is optically transparent and cannot be imaged using label-free PAT, therefore dye injection is required. Since Evan's blue has an absorption peak at ~610-nm, its injection into the tissue provides contrast for PAT using a 640-nm laser source. Therefore, PAT using two lasers at 523-nm and 610-nm for blood vasculature and lymphatic vessels, respectively, along with injection of Evan's blue allowed simultaneous imaging blood and lymphatic vessels in mouse cologne [Yang-2012]. Other nanoparticle-based PAT contrast agents such as carbon nanotubes [De La Zerda-2008], gold nanobeacons [Pan-2010] and gold nanocages [Kim-2009] allowed imaging SLNs about 2-3 cm deep in rats and mice.

Optical imaging of lymphatic vessel drainage is gaining increased interests because it does not involve any radiation and can achieve very high resolution [Lucarelli-2009]. Indocyanine green (ICG) is an unconjugated free emissive fluorophore which has a significant Stoke's shift that allows fluorescence measurement at 830 nm if excited at 780 nm. ICG is one of the popular dyes fon non-invasive near-infrared (NIR) detections of tumors in both research and clinic (approved in humans for assessing cardiac and hepatic function as well as lymphatic flow and SLN imaging [Landsman-1976]). Alexa 705, IRDye780, Cy7 and Cy5.5 are among other NIR organic fluorophores used for detecting lymphatic drainage which can also be conjugated with bioactive

molecules to effectively enter and remain in the lymphatic system [Ghoroghchian-2009, Hama-2007]. Although most of the organic NIR fluorophores suffer from weak fluorescent signal through deep tissue sections, research in designing high-emission dipole strength fluorophores still continues. Quantum dots (Qdots) are the result of the recent advances in the field of nanotechnology in fabricating nano-sized semiconductor crystals [Gao-2004]. The size of Qdots can be fine-tuned ranging between 5-20 nm to control the emission wavelengths. The main advantage of Qdots over organic fluorophores is their strong brightness which allows for deeper penetration in the tissue [Zhang-2011]. Using NIR Qdots, *in vivo* lymphatic flow draining and SLNs have been successfully demonstrated in superficial tissues [Kosaka-2009, Kim-2003, Knapp-2007].

5.2.2 Active targeting and molecular imaging using targeting biomarkers

Immunohistochemistry (IHC) is the process of detecting antigens (e. g. proteins) in cells within a tissue section using specific antibodies. IHC, also known as a bridge between immunology, histology and chemistry, is a valuable tool in the diagnosis and research of infectious and neoplastic diseases. The antigen-antibody (Ag-Ab) is demonstrated with a colored histochemical reaction visible by light microscopy or flurochromes with ultraviolet light [Ramos-Vara-2005]. Since lymphatic endothelial cells are different from blood vascular endothelial cells, lymphatic vascular-specific molecules have been discovered and developed for identification of lymphatic vessels in tissues. These molecules include vascular endothelial growth factor receptor-3 (VEGFR-3) [Mäkinen-2001], Prospero-related homeodomain transcription factor Prox1 [Hong-2002], the membrane glycoprotein podoplanin [Breiteneder-Geleff-1999], and lymphatic vessel hyaluronan receptor-1 (LYVE-1) [Jackson-2003]. The receptor tyrosine kinase (RTK) VEGFR-3, one of the first discovered lymphatic endothelial markers [Alitalo-2005], is activated by

VEGF-C and VEGF-D of the VEGF family of growth factors [Adams-2007]. LYVE-1 is one of the most specific and widely used lymphatic endothelial markers that are expressed in a subset of endothelial cells in the large central veins [Maby-El Hajjami-2008]. In adults, LYVE-1 expression decreases in collecting lymphatic vessels and remains high only in lymphatic capillaries [Mäkinen-2005].

Protein-binding detection techniques are not limited to *ex vivo* samples. *In vivo* imaging of lymphatic vessels in development, wound healing, inflammation and tumor metastasis were made possible by expression of enhanced green fluorescent protein- (EGFP-) luciferase fusion protein under the endogenous transcriptional control of VEGFR3 gene. This technique allowed whole-body imaging and monitoring of physiological and pathological lymphangiogenesis *in vivo* [Martínez-Corral-2012]. The active targeting strategies can also be applied to other imaging modalities such as ultrasound and PET. In ultrasound active targeting contrast imaging, antibodies, peptides or other molecules are attached to micro-bubble shell. Some examples include lipid shell microbubbles attached anti-OCAM-1 monocolonal antibody for imaging acute cardiac allogragt transplant rejection in rats, microbubbles targeted to vascular endothelial growth factor receptor type 2 (VEGFR2) for imaging tumor angiogenesis in murine tumor models and microbubbles with RGD peptide for thrombosis and angiogenesis targeting [Weller-2003, Korpanty-2007, Willmann-2008]. Also, feasibility of using recombinant human adenoviral vectors to detect nodal metastases of prostate cancer was demonstrated with adenovirus-mediated gene expression PET imaging [Burton-2008].

5.2.3 Label-free imaging of lymphatic system

Although most of the existing lymphatic imaging techniques require contrast agents, their toxicity and side effects can limit their applications. To the best of our knowledge, the only label-

free methods for imaging lymphatic vessels *in vivo* are optical coherence tomography (OCT) and laser speckle imaging (LSI). However, LSI is not depth-resolved and the resolution is not as high as OCT [Kalchenko-2012]. OCT has been widely used to non-invasively provide high-resolution, depth-resolved cross-sectional and three-dimensional (3-D) images of highly scattering samples [Huang-2011, Fercher-2003, Tomlins-2005]. OCT functional and hemodynamic information can be acquired in addition to the structure. Optical micro-angiography (OMAG) is a label-free non-invasive imaging and processing method to obtain 3D blood perfusion map in microcirculatory tissue beds *in vivo* using FD-OCT [Wang-2007_FR, Wang-2007_OMAG]. Ultrahigh-sensitive OMAG (UHS-OMAG) is an variation of OMAG technique, capable of imaging microvasculature down to capillary level, in which data acquisition is based on repeated B-scan (frame) acquisition at the same spatial location [An-2011, Wang-2010], and then separating static scatterers (e.g. structure tissue) and dynamic scatterers (e.g. moving red blood cells within patent vessels) by the use of OMAG algorithm [Yousefi-2011]. By synergistically utilizing both the amplitude and phase information of complex OCT signals, the OMAG technique is sensitive to both the axial and transverse blood flows, providing blood flow map at small vessels and capillaries as well as larger vessels. UHS-OMAG has been applied to visualize blood perfusion and micro-vasculature map in various living tissue samples such as retina [An-2011], cerebral [Jia-2011], renal microcirculation [Zhi-2011] and skin [Qin-2011]. Hemodynamic quantification can be extremely useful in cancer, stroke and some other disease which involve vasculature.

Although contrast-based imaging LNs has been demonstrated using gold nanoparticles uptake [Jung-2011], label-free imaging of intact SLNs [Jung-2010] and lymph vessels [Zhi-2012] have been demonstrated *in vivo*. Since the lymph fluid is clear and transparent, lymphatic vessels

appear as reduced scattering (system noise level) vessel-like areas in OCT structure cross-section images. The origin of these reduced-scattering connected tubular structures in the skin has been already confirmed by intra-dermal injection of Evan's blue dye and monitoring the uptake path by surrounding lymph vessels into the SLN. Therefore, these lymph vessels can be visualized by applying a lower threshold on the OCT intensity image [Zhi-2012, Vakoc-2009]. However, the intensity-threshold technique does not take the physical shape of the vessels into account, therefore not robust to intensity variations and noise caused by speckle and light absorption in the structure. These limitations increase the chances of segmentation error and false alarms in identifying lymphatic vessels. We have developed an automatic method for segmenting lymphatic vessel in OCT structure images using filtering technique and vesselness models based on Hessian multi-scale filters [Frangi-1998, Yousefi-2013_LymphJBO]. Hessian filters estimate tubular and vessel-like structures and the multi-scale approach allowed segmenting vessels with different size. In this chapter, we demonstrate the capability of OCT for non-invasive label-free imaging of lymphatic vessels along with blood flow perfusion within tissue beds and a segmentation method to extract lymphatic vessel lumen. Simultaneous imaging and visualization of blood and lymphatic vessels will be useful for better understanding and observing tissue structures and microcirculatory response to some pathological cases such as wound healing, infection and cancer angiogenesis.

5.3 Materials and methods

5.3.1 System setup

The scanning protocol was based on three-dimensional ultrahigh-sensitive optical micriangiography (UHS-OMAG) technique [58]. The x-scanner (fast B-scan) was driven with a

saw tooth waveform and the y-scanner (slow C-scan) was driven with a step function waveform. The fast and slow scanners covered a rectangular area of ~ 2.2x2.2 mm^2 on the sample. Each B-scan consisted of 400 A-lines covering a range of ~ 2.2 mm on the sample. The duty cycle of the saw tooth waveform rising edge was set at ~80% per cycle, which provided a B-scan frame rate of ~ 94 frames per second. The C-scan consisted of 400 scan locations with B-scan repetition of 8 frames per location for flow imaging and quantification. The total size of the data set was $1.28x10^6$ A-lines. In order to cover a large field of view, multiple 3-D scan were acquired and the sample was translated using a mechanical stage. This allowed imaging an area of ~1.5x1.5 cm^2 on the mouse ear pinna.

5.3.2 Segmentation of lymphatic vessels from OCT structure images

The local behavior of the 2nd order gradient image (Hessian matrix) is used to identify the boundaries of tubular low-scattering lymphatic vessels and contrasting them from background and other scattering tissue. The multi-scale nature of the method allows identifying vessels of different size. Based on linear space theory, the 2nd order derivative of a discrete matrix (digital image) can be estimated by convolving (filtering) the original image with the 2nd derivative of a Gaussian kernel. The advantage of this substitutions is that the derivative operation reduces to linear filtering and simplifies the implementations on hardware and real-time systems.

The second order derivative can be expressed as

$$\delta x^T H(I)_s \delta x = \left(\frac{\partial}{\partial x}\right)\left(\frac{\partial}{\partial x}\right) I(x,s) = s^{2\gamma} I(x,s) * \frac{\partial^2}{\partial x^2} G(x,s) \qquad (5\text{-}1)$$

where $I(x,s)$ is the original image at scale s and location x, $H(.)_s$ is the gradient vector of the image at scale s, γ is the derivative normalization parameter and $G(x,s) = \frac{1}{\sqrt{2\pi s^2}} e^{-\frac{||x||^2}{2s^2}}$. By analyzing the eigenvalues and eigenvectors of the Hessian matrix, the principal direction of the local structure can be extracted which is the direction of the smallest curvature (along the vessel). By definition, the eigenvalues and vectors of the Hessian matrix are given by solving the following equations

$$H_S e_{s,i} = \lambda_{s,i}\, e_{s,i} \tag{5-2}$$

where $\lambda_{s,i}$ is the $i\text{-}th$ eigenvalue at scale s corresponding to normalized eigenvector $e_{s,i}$ and ($|\lambda_3| \leq |\lambda_2| \leq |\lambda_1|$) for a three-dimensional structure. For an ideal tubular structure $|\lambda_3| \approx 0$, $|\lambda_3| \ll |\lambda_2|$ and $\lambda_2 \approx \lambda_1$. Based on the second order ellipsoid, two geometric ratios are defined

$$R_B = \frac{|\lambda_1|}{\sqrt{\lambda_2 \lambda_3}} \tag{5-3}$$

and

$$R_A = \frac{|\lambda_2|}{|\lambda_3|}. \tag{5-4}$$

The first ratio (R_B) accounts for the deviation from a blob-like structure but cannot distinguish between a line-like and a plate-like pattern. The second ratio refers to the largest cross-section area of the ellipsoid that can distinguish between plate-like and line-like structures since it is zero in the latter case. In order to distinguish background noise where no structure is present, Frobenius matrix norm is utilized. This measure is derived from eigenvalues of Hessian matrix by

$$R_C = \left|\left|H\right|\right|_F = \sqrt{\sum_{j \leq D} \lambda_j^2} \tag{5-5}$$

where D is the dimension of the image. This measure will be low in the background where no structure is present and the eigenvalues are small for the lack of contrast. In regions with high contrast compared to the background, the norm will become larger since at least one of the eigenvalues will be large.

The vesselness function at scale s is defined as

$$v_0(s) = \begin{cases} 0 & if\ \lambda_2 > 0\ or\ \lambda_3 > 0 \\ \left(1 - e^{-\frac{R_A^2}{2\alpha^2}}\right) * e^{-\frac{R_B^2}{2\beta^2}} * \left(1 - e^{-\frac{R_C^2}{2\theta^2}}\right) \end{cases} \quad (5\text{-}6)$$

where α, β and θ are thresholds which control the sensitivity of the line filter to the measures R_A, R_B and R_C. The idea behind this expression is to map the features into probability-like estimates of vesselness according to different criteria.

The vesselness measure is analyzed at different scales. The response of the line filter will be maximum at a scale that approximately matches the vessel size.

$$V_0(\gamma) = \arg max_{\ s}\ \ v_0(s, \gamma),\ s_{min}\ < s < s_{max} \quad (5\text{-}7)$$

where s_{min} and s_{max} are lower and upper bound in the range of scale (vessel sizes).

By utilizing matrix properties of eigenvalues, the computational complexity of this approach is reduced to simple 2-D filtering with already-known Gaussian derivative kernels at multiple scales. Since all of the operations are performed on matrices, the computation can be parallelized on the processing unit and real-time segmentation can be performed on the structure images.

5.3.3 Implementation of 2-D Hessian vesselness filters

We briefly describe our implementation approach which is partially taken from open source codes shared on Matlab Central file exchange center by Marc Schrijver and Drik-Jan Kroon and modified to our specific application.

The Gaussian function at different scales suppresses the noise before using Laplacian on the edges. From linear system theory, we can derive the following equation

$$\frac{d}{dt}[G(t) * I(t)] = \frac{d}{dt}\int I(\tau).G(t-\tau)d\tau = \int I(\tau)\frac{d}{dt}G(t-\tau)d\tau = I(t) * \frac{d}{dt}G(t) \quad (5\text{-}8)$$

and similarly

$$\frac{d^2}{dt^2}[G(t) * I(t)] = I(t) * \frac{d}{dt^2}G(t) \quad (5\text{-}9)$$

If the intensity values of the input image is given by $I(x,y)_s$ where (x,y) is the spatial location and s is the filter scale value, the Hessian matrix can be represented by

$$H(x,y)_s = I(x,y) * \begin{bmatrix} \frac{\partial^2 G(x,y)_s}{\partial x^2} & \frac{\partial^2 G(x,y)_s}{\partial x \partial y} \\ \frac{\partial^2 G(x,y)_s}{\partial y \partial x} & \frac{\partial^2 G(x,y)_s}{\partial y^2} \end{bmatrix} = I(x,y) * \begin{bmatrix} G_{xx} & G_{xy} \\ G_{yx} & G_{yy} \end{bmatrix} = \begin{bmatrix} D_{xx} & D_{xy} \\ D_{yx} & D_{yy} \end{bmatrix} \quad (5\text{-}10)$$

where $G(x,y)_s$ is the Gaussian function at scale s given by $G(x,y)_s = e^{-\frac{x^2+y^2}{2s^2}}$ (for simplicity we omitted the normalizing factor $\frac{1}{s\sqrt{2\pi}}$).

Therefore,

$$\frac{\partial^2 G(x,y)_s}{\partial x^2} = G_{xx} = \left(\frac{x^2-s^2}{s^4}\right).e^{-\frac{x^2+y^2}{2s^2}} \quad (5\text{-}11)$$

$$\frac{\partial^2 G(x,y)_s}{\partial y^2} = G_{yy} = \left(\frac{y^2-s^2}{s^4}\right).e^{-\frac{x^2+y^2}{2s^2}} \quad (5\text{-}12)$$

$$\frac{\partial^2 G(x,y)_s}{\partial x \partial y} = \frac{\partial^2 G(x,y)_s}{\partial y \partial x} = G_{xy} = \frac{xy}{s^4}.e^{-\frac{x^2+y^2}{2s^2}} \quad (5\text{-}13)$$

and the eigenvalues of the Hessian matrix can be derived by

$$\lambda_{1,2} = \frac{1}{2}(D_{xx} + D_{yy} \pm \sqrt{\left(D_{XX} - D_{yy}\right)^2 + 4\,D_{xy}^2}\,) \quad (5\text{-}14)$$

And their corresponding eigenvectors are

$$v_1 = \frac{2D_{xy}}{\sqrt{(D_{XX}-D_{yy})^2+4\,D_{xy}^2}} \tag{5-15}$$

$$v_2 = \frac{D_{xx}-D_{yy}}{\sqrt{(D_{XX}-D_{yy})^2+4\,D_{xy}^2}} \tag{5-16}$$

When implementing on Matlab (The Mathworks) or any programming language, it is not necessary to calculate eigenvalues and eigenvectors at each pixel, and the process can be parallelized by calculating the eigenvalues of the 2-D image matrix using the equation (5-14).

Since one of the vesselness parameters ($R_B = \frac{\lambda_1}{\lambda_2}$) require division by λ_2, the corresponding matrix has to be replaced with a small epsilon value to avoid division by zero. We typically utilized scale values ranging $s = [0.5\colon 0.5\colon 10]$ and masked out the segmented vessels with $s < 1$. However, depending on the vessel sizes of interest, these parameters can be modified. Also, the normalization factors of equation (5-6) were experimentally tested to work best when set to $\beta = 12\ and\ \theta = 0.45$.

5.3.4 Cylindrical circular model with Gaussian cross-section

For better demonstration of the model, we calculated the eigenvalues of the Hessian matrix for an ideal vessel structure shown in Figure 5-1 which is a circular cylinder model with Gaussian-like intensity profile at the cross-section. Basically, the model is a cylinder-shaped vessel with a Gaussian intensity profile at its cross-section given by

$$I_0(x,y,z) = \frac{C}{2\sigma_0^2} e^{-\frac{x^2+y^2}{2\sigma_0^2}} \tag{5-17}$$

where x, y and z are Cartesian coordinates, σ_0 is Gaussian parameter and C is a normalization factor. Therefore, the Hessian matrix of the shape structure is given by

$$H = \begin{bmatrix} d^2I_0/d_x^2 & d^2I_0/d_xd_y & d^2I_0/d_xd_z \\ d^2I_0/d_yd\_x & d^2I_0/d_y^2 & d^2I_0/d_yd_z \\ d^2I_0/d_zd_x & d^2I_0/d_zd_y & d^2I_0/d_z^2 \end{bmatrix} = \frac{I_0}{\sigma_0^4}\begin{bmatrix} x^2-\sigma_0^2 & xy & 0 \\ xy & y^2-\sigma_0^2 & 0 \\ 0 & 0 & 0 \end{bmatrix}. \quad (5\text{-}18)$$

Eigenvalues and eigenvectors of the Hessian matrix are

$$\lambda_1 = -\frac{I_0}{\sigma_0^2},\ \lambda_2 = -\frac{I_0}{\sigma_0^2}\left(\frac{\sigma_0^2-(x^2+y^2)}{\sigma_0^2}\right)\ and\ \lambda_3 = 0 \quad (5\text{-}19)$$

$$\overrightarrow{v_1} = (-y, x, 0),\ \overrightarrow{v_2} = (x, y, 0)\ and\ \overrightarrow{v_3} = (0,0,1) \quad (5\text{-}20)$$

that can be generalized for an ideal tubular structure.

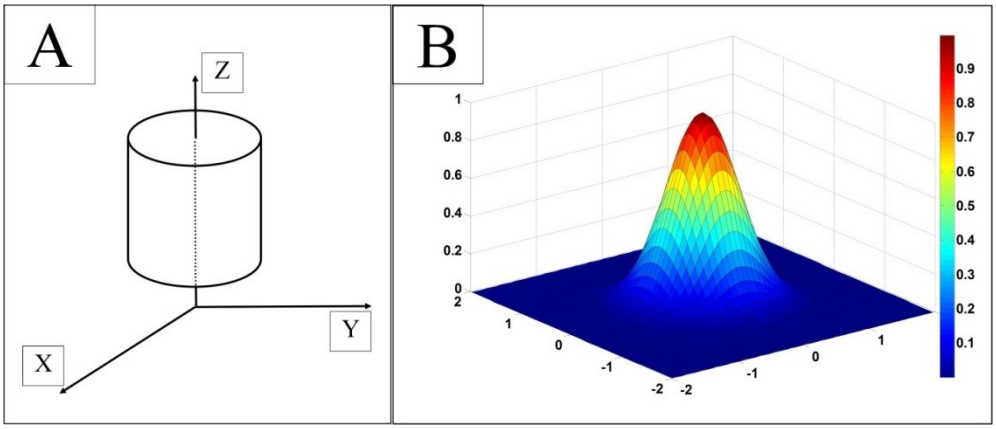

Figure 5-1 Cylindrical circular vessel model.

A. Cylindrical circular vessel model with Gaussian intensity profile at cross-section (B).

5.4 System set up and experimental preparation

The schematic of our OCT system setup is given in **Figure 1-1** and the detail of the system was explained in the section 2.4 (experimental setup). The typical field of view and scanning range for our OCT system was 2.2x2.2 mm^2 in the current setup.

Non-invasive *in vivo* images were acquired from the pinna of a healthy ~6 weeks old male hairless mouse (Crl:SKH1-Hr^{hr}) weighting approximately 25g. During the experiment, the mouse was anesthetized using 2% isoflurance (0.2 L/min O_2, 0.8 L/min air). The ear was kept flat on a microscope glass using a removable double-sided tape. The experimental protocol was in compliance with the Federal guidelines for care and handling of small rodents and approved by the Institution Animal Care and Use Committee (IACUC) of the University of Washington, Seattle. In order to scan a larger field on the ear, we used a mechanical translating stage to move the tissue sample to the desired location and after acquisition and processing, the mosaics were stitched together to form a larger image.

5.5 Experimental Results

The ear pinna is consisted of two layers of skin and a layer of cartilage in the middle which holds the skins together. We used this model because it was a convenient *in vivo* model given the penetration depth limitations of optical imaging, we were able to thoroughly image the structures within tissue, including blood and lymphatic vessels. Using this model allowed studying and monitoring some phenomena such as vasculature remodeling and response to injuries. Under normal conditions, majority of the lymphatic vessels and capillaries are very small and fall below the sensitivity of our system. However, immediately after we created a biopsy punch, we observed that the size of lymphatic vessels enlarged. Perhaps this enlargement was due to the inflammatory and immune response at the injury site. The biopsy punch model was very similar to the one previously reported by Jung et al. [Jung-2013] where they created a biopsy punch and complete removal of tissue on the ear skin flap and monitored the vascular remodeling and healing process along the time. In this paper, we also monitor the response of lymphatic vessels

along with blood vessels to that injury model. Using our OCT system, we studied simultaneous response of blood and lymphatic vessels to the biopsy punch injury. 3-D images were acquired at each location covering 2x2 mm^2 and a large field of view was covered by mechanically shifting the sample under the system. The 3-D images at each location were processed separately and the lymphatic vessels were segmented using Hessian vesselness filters. Figure 5-2**(A-C)** show blood vessels, lymphatic vessels and structure cross-section images of a selected location on the ear, respectively. Figure 5-2**(D-F)** show the volumetric blood vessels and lymphatic vessels map, respectively, and the cross-section shown in Figure 5-2**(C)** is also located. The lymphatic vessels are coded by green color and blood flow perfusion is coded with orange. By combining blood flow perfusion and lymphatic vessels from Figure 5-2**(D)** and Figure 5-2**(E)**, Figure 5-2**(F**) was generated that shows three-dimensional complications of circulatory system. For better visualization and quantification, maximum intensity projection (MIP) maps of the vasculature were created. Figure 5-2**(G-H)** show the MIP of blood flow perfusion, lymphatic vessels and their combinations. For Figure 5-2**(H)**, lymphatic MIP was color-coded based on the vessel diameter. The vessel diameter was estimated using distance transform.

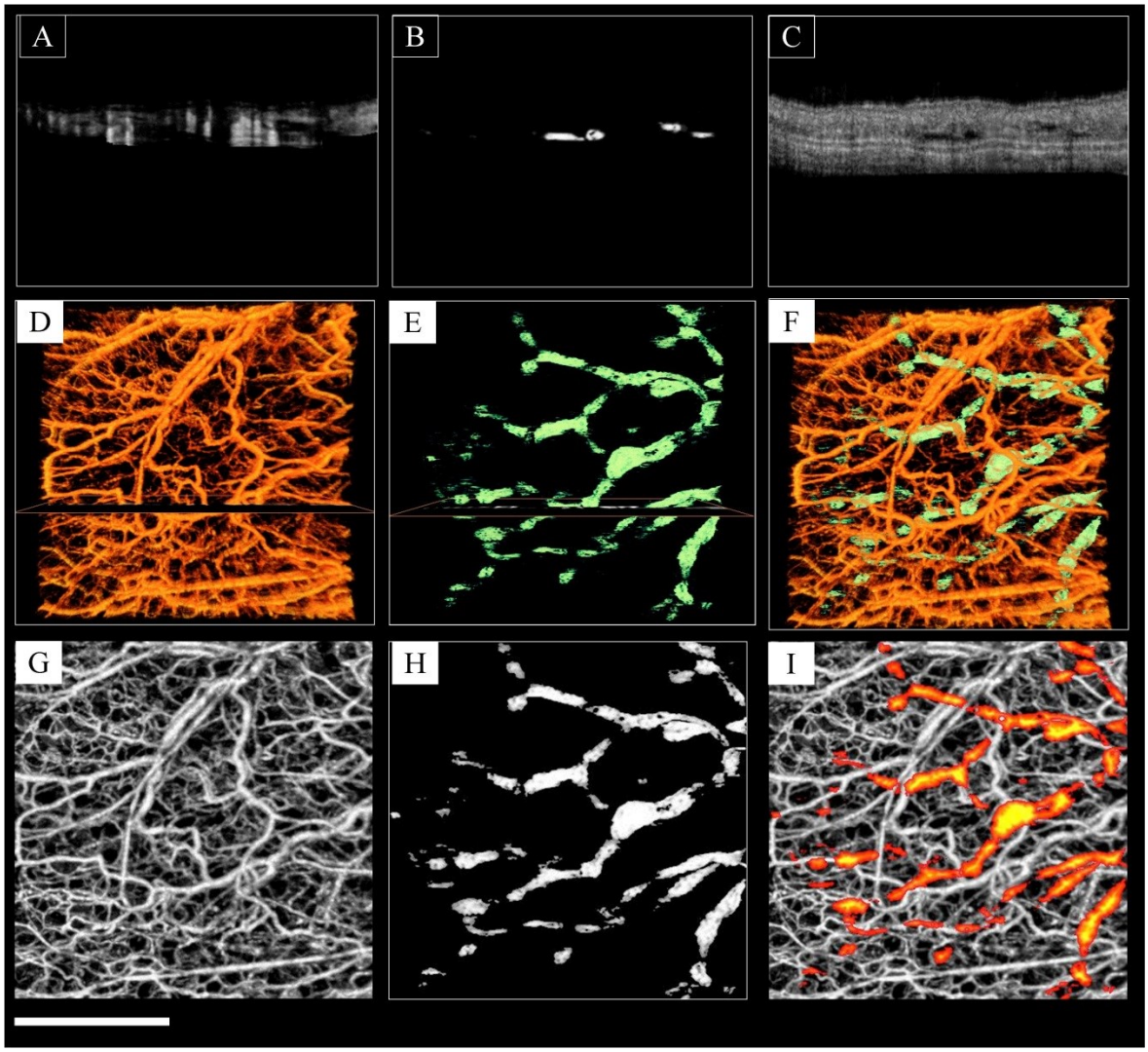

Figure 5-2 Blood flow perfusion and lymphatics *in vivo*.

Cross-section images of processed blood vessels (A), segmented lymphatic vessels (B) and OCT structure B-mode (C) and their corresponding 3-D volume rendering of blood vessels (D) and lymphatic vessels (E). The cross-section location is also marked. (F) Combined blood vessels (orange color) and lymphatic vessels (green color) in volume rendering. (G) Maximum intensity projection map of blood vessels. (H) Maximum intensity projection map of lymphatic vessels. (I) Combined blood vessels (gray-scale) and lymphatic vessels (color-coded) maximum intensity projection map. The lymphatic vessels color map is a function of vessel diameter and maximum intensity value from (H). (Scale bar = 1mm)

Figure 5-3**(A-D)** show the process of vasculature remodeling and lymphatic vessel response to the wound. Each image is combination of 9 OCT-OMAG mosaics acquired around the wound

area. Blood vessels are gray-coded and lymphatic vessels were color-coded with diameter-dependent orange color map. The peak activity of lymphatic vessel enlargement was observed around ~1 week after inducing the wound. This observation is in agreement with the wound healing phases during the inflammatory phase [Martínez-Corral-2012, Shaw-2009, Baum-2006]. The immediate response of lymphatic vessels after inducing the punch (Figure 5-3**(A)**) was mainly concentrated around the wound, collaterals and downstream of the injured vessels. However, the size of the lymphatic vessels had significantly increased after one week (Figure 5-3**(B)**) and it was not only around the wound, but also at farther locations on the ear. Then, the size and distribution of lymphatic vessels reduced on Day15 and Day22 (Figure 5-3 **(C) and (D)**, respectively) and was mainly around the wound area, maybe due to inflammation. Wound healing and tissue regeneration is associated with angiogenesis. Angiogenesis can be observed starting on Day8, where new capillary network is formed around the wound area in the form of granulation tissue and eventually mature in the form of new vessels inside the wound.

5.5.1 Lymphatic vessel quantification

In order to quantify the lymphatic vessel response to biopsy punch, two parameters were measured.

Lymphatic vessel area density (LVAD) was defined as the area of the segmented lymphatic vessels in the projection view divided by the area of the ear given by

$$LVAD = \frac{Total\ area\ of\ the\ lymphatic\ vessels}{Total\ area\ of\ the\ ear} \quad (8).$$

Lymphatic vessel diameter (LVD) was quantified using Euclidean distance transform (EDT) of the binarized lymphatic vessel en-face projection map.

The EDT of each pixel in a binary image measures the Euclidean distance between that pixel and the nearest nonzero pixel element of that image. First, the lymphatic vessel map was binarized above a threshold. Then, the vessel center-line was extracted by skeletonizing the binary vessel map. Finally, the distance transform of the intensity-inverted lymphatic vessel map was estimated at each vessel centerline pixel. EDT at the vessel centerline is an estimate of the vessel diameter. For each imaging time-point after inducing the biopsy punch, LVAD, mean value and standard deviation of LVD were calculated. The lymphatic vessel response was observed immediately after creating the wound. Peak LVAD and LVD were observed on Day8 and eventually at Day22 they decreased below values of Day1. The quantification values are plotted in Figure 5-3**(E)** and Figure 5-3**(F)** for LVAD and LVD, respectively.

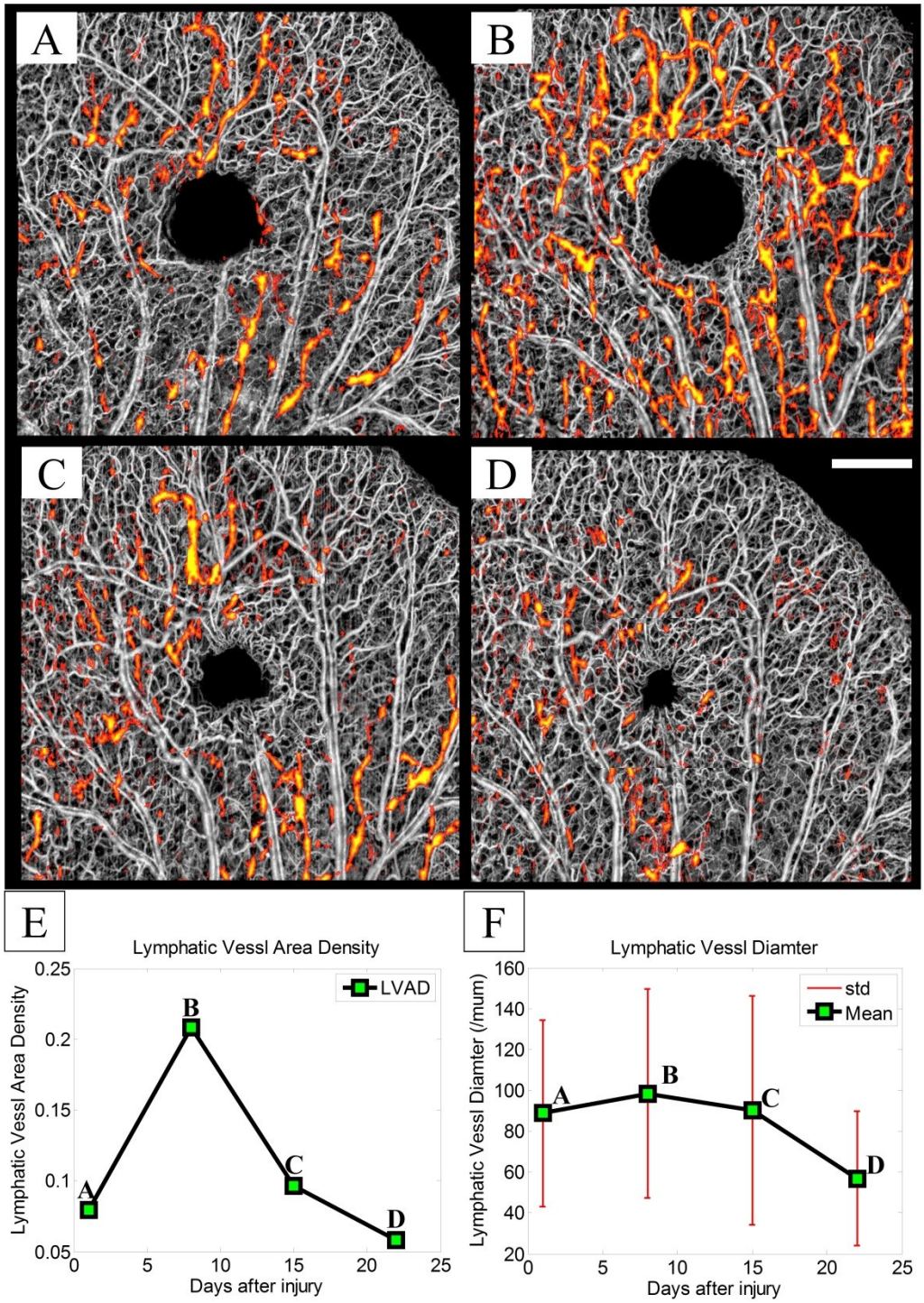

Figure 5-3 Microcirculation response during wound healing.

(A-D) Simultaneous imaging blood and lymphatic vessels in the healing process. (E) Lymphatic vessel area density and [F] lymphatic vessel diameter quantification of wound healing in the mouse ear pinna model. The labels A-D on figures (E) and (F) are corresponding to their microvasculature maps of figures (A-D).

5.5.2 Imaging sentinel lymph node

Current gold standard for assessing the stage of breast cancer is SLN biopsy [Veronesi-1997]. The biopsy requires complete removal of SLN with the help of an invasive dye injection. However, it may not be necessary to completely remove SLN if they could be non-invasively imaged [Krag-1998]. Removal of SLNs may lead to post-operative complications such as lymphedema and sensory nerve injury [Purushotham-2005]. Since light penetration limits OCT imaging depth to ~1.5mm, imaging intact LNs required surgical exposure of the node. Although OCT probes can be mounted in a medical needle [Li-2000] for deeper tissue imaging, exact location and desired microstructures and blood flow perfusion can be better assessed by surgical exposure. A three-month-old C57 BL/6 mice (~25 g) was immobilized in a stereotaxic stage and was anesthetized with vaporized isoflurane (0.2L/min oxygen and 0.8 L/min air) while the body temperature was kept constant at normothermia using a heating pad. The auxiliary lymph node was surgically exposed by pulling aside the skin and surrounding tissue. Then the sample was placed under the probe beam and we performed OCT/OMAG imaging on the exposed SLN *in vivo*. Figure 5-4**(A)** shows a structure cross-section where lymph vessels appear as transparent vessel-like structures. Figure 5-4**(B)** shows the blood flow perfusion cross-section processed using OMAG algorithm. The vessel lumen segmentation is shown in Figure 5-4**(C)**. The volume rendering of blood flow perfusion (color-coded in orange) and lymphatic vessels (color-coded with green) are shown separately in Figure 5-4**(D)** and Figure 5-4**(E)** and overlaid onto Figure 5-4**(F)**. Figure 5-4**(G)** shows an X-Z cross-section view overlaying blood and lymphatic vessels on the structure image that the boundaries of the lymphoid lobule are visible (red marker). These vasculatures show an artery/vein pair and a lymphatic vessel around the node and branch of these vessels enter the node.

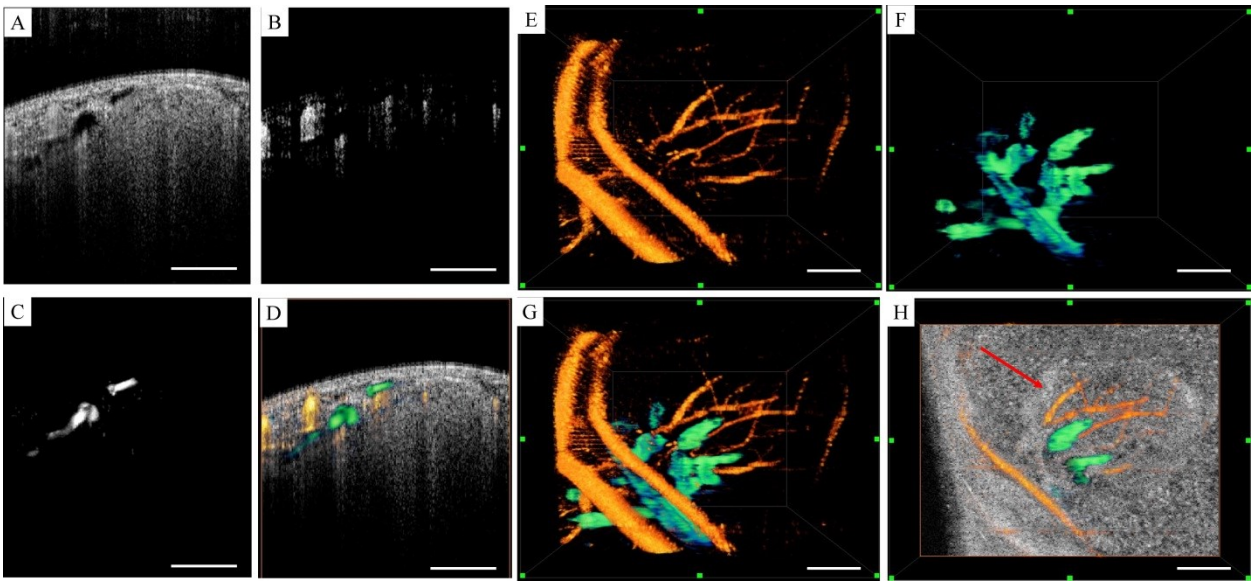

Figure 5-4 Sentinel lymph node

(A) Structure cross-section. (B) Blood flow perfusion. (C) Lymph vessels. (D) Overlaying blood and lymphatic vessels on a structure cross-section. (E) Volume rendering of blood vessels. (F) Volume rendering of lymphatic vessels. (G) Overlaying blood and lymphatic vessels. (H) Location of lymph node with the blood and lymph capillaries. (Scale bar = 300μm)

5.5.3 Comparison with intensity-threshold method

In comparison to the intensity-threshold method, Hessian filters are more robust to the noise and intensity variations in the OCT structure image. Also, Hessian filters take the physical appearance of the structure and quantify the closeness to a tubular structure. Figure 5 shows the comparison between the Hessian vesselness filter and the intensity-threshold method. Figure 5-5**(A) and (D)** show structure cross-sections with visible lymphatic vessels. Figure 5-5**(B) and (E)** show lymphatic vessel segmented based on Hessian vesselness filters on the structure images and Figure 5-5**(C) and (F)** show the segmentation results using the intensity threshold on the structure images of Figure 5-5**(A) and (D)**, respectively. Due to their segmentation nature, Hessian vesselness method produced smoother vessel lumens and was more sensitive to vessel shape while intensity-threshold method had no sensitivity to the vessel shape and size (red pointers). It can be observed that the intensity-threshold method is less robust to

noise and the threshold parameters and gray-level values at the vessel lumen and can significantly influence the shape of the segmented vessels. Also, the shadows bellow the blood vessels can produce false alarms (yellow and cyan pointers). Therefore, segmenting lymphatic vessels using intensity-threshold segmentation requires extra step to manually remove noisy areas while Hessian-based method can be used as an automated step without the need of manual segmentation.

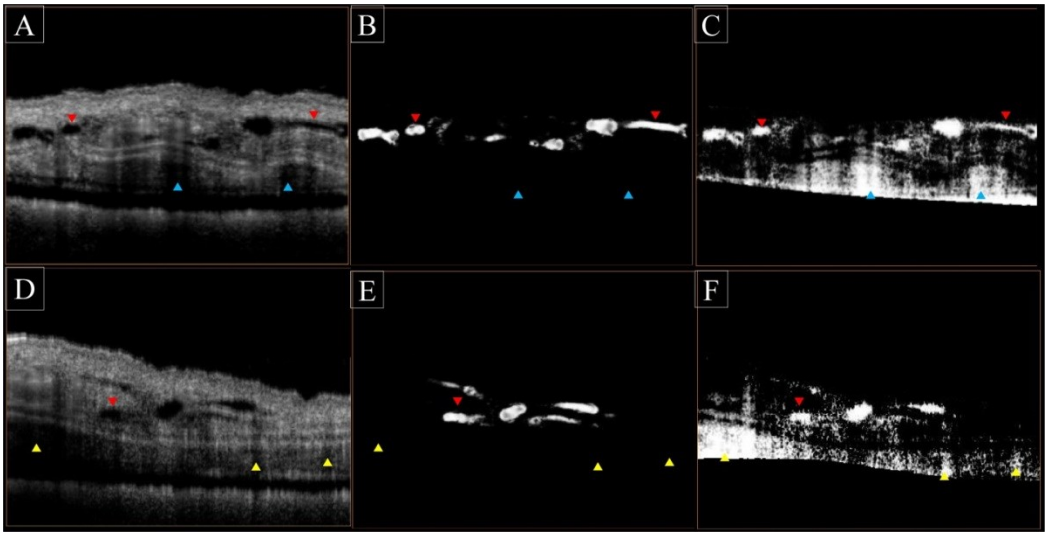

Figure 5-5 Lymphatic vessel segmentation method comparison.

Comparison between the Hessian vesselness filter and the intensity-threshold method. (A, D) OCT structure cross-section of mouse ear, (B,E) lymphatic vessels segmented using Hessian vesselness filters and (C,F) corresponding lymphatic vessels segmented using intensity-thresholding method. Blue and yellow arrows indicate the sensitivity of intensity-thresholding method to noise and intensity variations. Red arrows indicate that intensity-thresholding method is not sensitive to vessel shape.

5.6 Validation of lymphatic system

In order to validate the structure and location of lymphatic system in the mouse ear pinna, we injected Evan's blue dye using a 30G needle into the soft tissue. The injected dye is collected by

lymphatic vessels that shows location of large lymphatic vessels in the ear. Figure 5-6 shows the progress of dye injection into the lymphatic system. The photos were taken with a simple camera on smartphone. Figure 5-6(A) shows *in vivo* mouse ear pinna sample before dye injection. Immediately after injecting the Evan's Blue dye into the soft tissue, the dye was collected by the existing lymphatic vessels (Figure 5-6(B)). Due to spreading of the dye within the interstitial fluid, more lymphatic vessels were involved and their diameter appeared enlarged (Figure 5-6(C)). We repeated the injection a few times at different sites to observe the pattern of lymphatic system in the ear (Figure 5-6(D)). The lymphatic network in the mouse ear pinna is very dense and similar to blood vessels, expands all over the ear. Their activity is however different and they become more apparent when an external material is injected into the interstitial fluid.

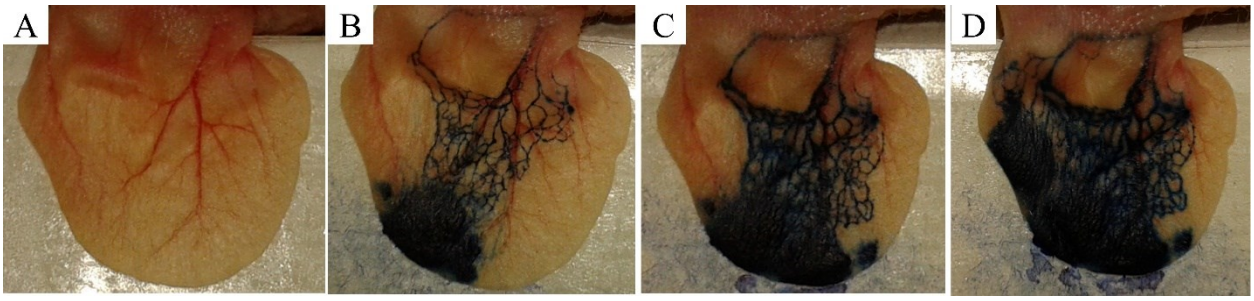

Figure 5-6 Evan's Blue collected by lymphatic vessels.
The lymphatic system response to the injection of Evan's blue dye into the mouse ear pinna *in vivo*.

We also performed OCT imaging after dye injection and observed the behavior of lymphatic uptake after dye injection. Figure 5-7 shows cross-section images from the same mouse ear pinna after dye injection. It can be observed that lymphatic vessels are enlarged and collect the dye from the interstitial fluid. Figure 5-7 (A-C) show the structure cross-sections and Figure 5-7 (D-F) show their corresponding depth en-face structure sections. Red arrows indicate location of

selected lymphatic vessels that resemble lymphatic system response during wound healing. Green arrows indicate location of selected larger blood vessels and blue arrows are labeled as dye injected into the interstitial fluid that has not been fully collected by lymphatic system yet. Since the amount of the injected dye is above the capability of the lymphatic system to immediately collect the dye from interstitial fluid, some part of the dye remains within the tissue for a longer period of time. Even after a couple of weeks, the color ear was slightly blue.

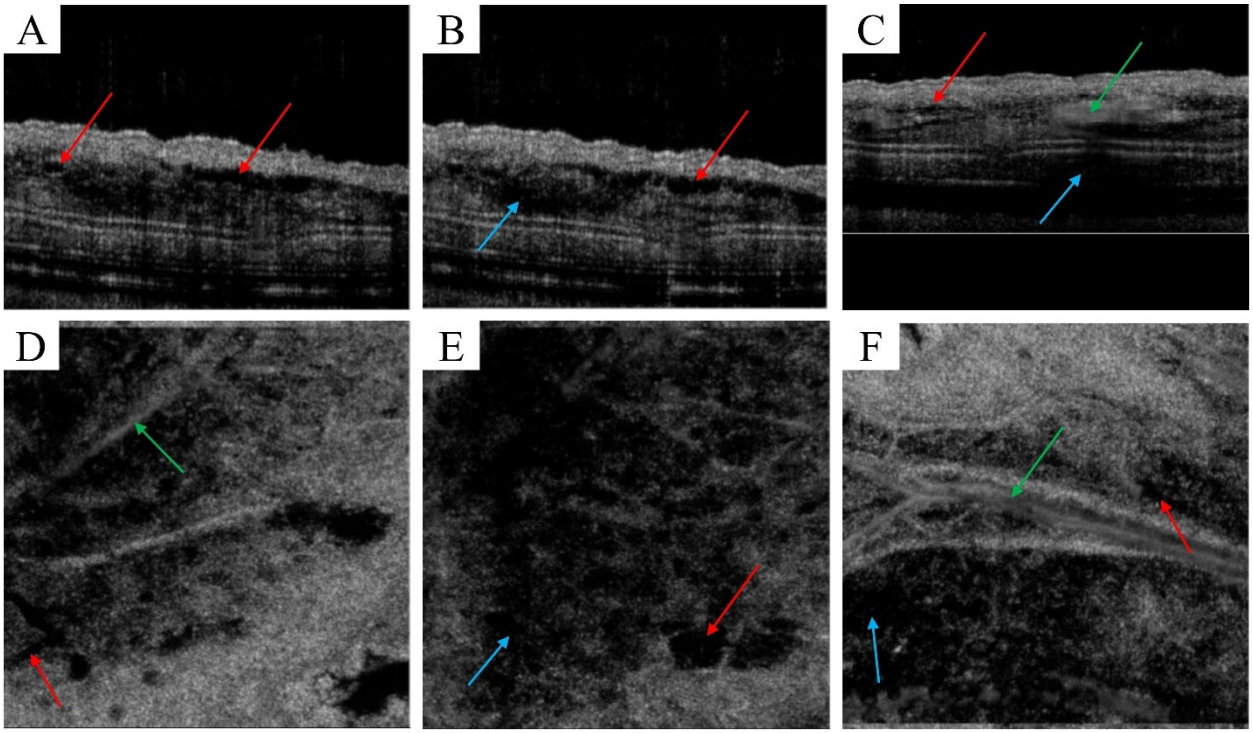

Figure 5-7 OCT scan after Evan's Blue injection.

OCT cross-sections (A-C) and their corresponding depth en-face structure sections (D-F). Red arrows: lymphatic vessels. Green arrows: blood vessels. Blue arrows: Evan's blue dye at interstitial fluid.

5.7 Conclusions

In this chapter, we reviewed the capability of using OCT for label-free imaging blood flow perfusion and lymphatic vessels and developed an automatic filtering technique and vesselness

model based on Hessian multi-scale vesselness filters for segmenting lymphatic vessel in OCT structure images. Hessian filters estimate tubular and vessel-like structures and the multi-scale approach allowed segmenting vessels with different size. Using this segmentation technique along with optical micro-angiography (OMAG) allows for label-free non-invasive simultaneous visualization of blood and lymphatic vessels *in vivo*.

In order to observe the capability of our system, we created a biopsy punch wound on the mouse ear and monitored the dynamics and healing process of lymphatic and blood vessels around the wound. Although no significant lymph was detected on the baseline image, immediately after inducing the punch the lymphatic vessels were significantly enlarged around the wound and in the downstream tissue. In order to quantify the lymphatic vessel response to biopsy punch, two parameters were measured: lymphatic vessel area density and lymphatic vessel diameter. The lymphatic vessel response was observed immediately after creating the wound. Peak LVAD and LVD were observed on Day8 and eventually at Day22 they decreased below values of Day1.

Lymphatic system plays an important role in cancer, immune system response, inflammatory disease, wound healing and tissue regeneration. Development of imaging techniques and visualization tools for lymphatic system is valuable in understanding the mechanisms and studying therapeutic methods in related disease and tissue response. Due to lack of label-free non-invasive imaging techniques, lymphatic vessels have been ignored and their behavior in the disease and their response to treatment methods is not very well known. Label-free non-invasive imaging and segmentation of SLNs and lymphatic vessels can be used in different applications such as dermatology, cosmetic and beauty, cancer, wound healing and infectious disease where lymphatic system plays an important role in delivering immune response and draining waste. The observed lymphatic vessels on the OCT structure images are directly related to the resolution of

the system. By increasing the system resolution, smaller lymphatic vessels and capillaries can also be observed and eventually segmented using our proposed method.

Chapter 6. SEGMENTATION OF BLOOD VESSELS

6.1 Introduction

In the previous chapters, we have demonstrated techniques for non-invasive imaging and visualization of micro-circulations within tissue beds *in vivo*. In this chapter, we propose methods and techniques to segment and quantify shape and diameter of the capillary beds. Such information can be very useful for quantitative studies of microcirculation research.

Since the primary clinical application of OCT has been in the field of ophthalmology, numerous methods have been proposed in the literature to segment blood vessels from OCT intensity and angiogram images. Some techniques in the literature utilize structural and cross-section information of the OCT B-scan and locate the blood vessels. Goldenberg et al. [Goldenberg-2013] proposed a method to measure the diameters of large retinal blood vessels using spectral domain OCT (Spectralis; Heidelberg Engineering, Heidelberg, Germany) structure cross-sections. Since they combined OCT with the infrared images, it made it possible to identify each of the large arteries and veins on the OCT raster scan that appeared as reduced scattering high-contrast vessel-like shapes in the infrared image. Similarly, Pilch et al. [Pilch-2012] and Srivastava et al. [Srivastava-2013] have proposed model-based techniques that utilized machine learning algorithm to train for the circular shape of blood vessels when OCT data is correlated with infrared camera image.

Besides adaptive thresholding on OCT angiograms, other techniques based on Hessian filters have also been proposed in the animal studies [Lee-2014, Poole-2014, Kowalski-2014]. Although widely used to segment tubular structures, multi-scale Hessian filters tend to blur the

vasculature map. Multi-scale Hessian filters require a known scale to maximize the vesselness function over that range and find the maximum range. However, if the upper limit of the scales are chosen large enough to account for measuring the large vessels, smaller vessels appear blurred. Figure 6-1 shows segmentation results on mouse ear pinna vasculature using multi-scale Hessian filters where the sensitivity of the method to the maximum scale can be clearly observed. Figure 6-1 (A-C) show the binary vessel map after segmentation using maximum scales of 2, 5 and 10, respectively, and Figure 6-1 (D-F) show the vessel radius estimated using distance transform of the inverted binary image after segmentation. It can be observed that the estimated vessel radius is very sensitive to the pre-selected value of the maximum scale. The distance transform results are the minimum number of pixels in between each foreground pixel to the boundary of the object (vessel). The distance transform of a blood vessel should have a maxima in the vessel centerline. The exact vessel diameter/radius can be measured after correcting for the beam broadening and measuring the spatial size of each voxel. That calibration would be identical for each system when the object is given at a specific depth of focus and therefore calibration can be performed before imaging. In order to minimize the sensitivity of microvasculature segmentation technique to the maximum scale parameter of Hessian filters, another segmentation technique based on intensity value can be utilized in parallel to the Hessian technique and the final segmentation can be achieved by compounding these results.

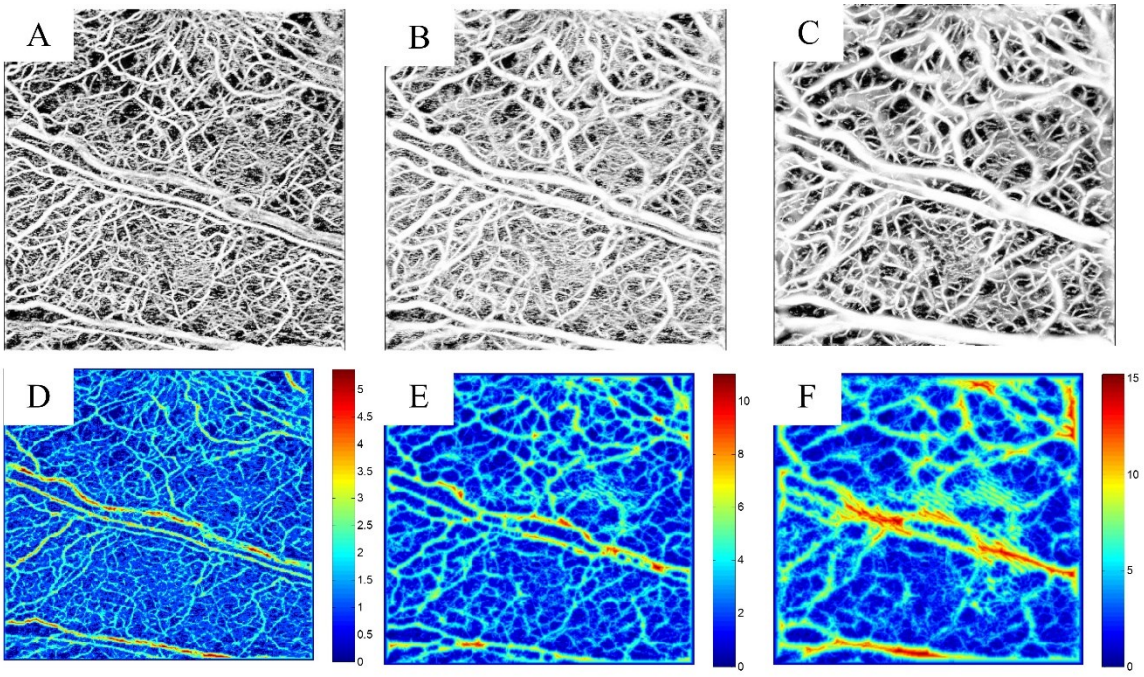

Figure 6-1 Sensitivity of the Hessian-based filters to the maximum scale.

(A-C) Segmented binary vessels using the maximum scales of 2, 5 and 10, respectively. (D-F) Corresponding vessel radius using distance transform.

6.2 Methodology

After acquiring and processing OCT/OMAG cross-section images, a 3D matrix is formed that contains the volumetric information data. Then, the volumetric data is resampled along the depth such that each frame corresponds to the microcirculation map at one specific depth, called orthoslice. In other words, the volumetric 3D data is re-arranged from Z-X-Y coordinates into X-Y-Z coordinates. For each depth-specific orthoslice, segmentation algorithm is performed and the segmented images are stacked into a new 3D volumetric data set. Finally, the segmented volumetric data is re-arranged from X-Y-Z back to Z-X-Y coordinates to be equivalent to the input data set. The segmentation procedure is utilized by compounding two independent segmentation schemes, one based on shape of blood vessels and the other one based on intensity

values of foreground/background. Multi-scale Hessian filters (already explained in chapter 5) and morphological binary segmentation techniques were utilized as our shape-based and intensity-based methods, respectively.

6.2.1 Morphological image segmentation

First, image pre-processing (Gaussian smoothing filters) and histogram equalization is performed on the original image. Then, foreground and background objects are detected where foreground accounts for the desired objects (vessels) we are interested in segmenting. Foreground markers which are connected blobs of pixels inside of each foreground object and background markers can be detected using opening-by-reconstruction and closing-by-reconstruction morphological techniques that clean up the original image [Vincent-1993]. These cleaning up operations create flat maxima inside each object in the foreground image. Then, the foreground object (binary) and markers can be detected by performing adaptive thresholding and local maxima detection on the cleaned up image, respectively. The background image can also be calculated by inverting the foreground binary image. Since original images are slightly noisy and non-uniform, a lot of local minima is produced and this leads to an oversegmentation. Oversegmentation means that instead of one large area representing an object in the image, a lot of smaller areas that each one covers a tiny portion of the object in the image are produced. In order to minimize the effect of noise and inhomogeneity, a pre-processing step can be utilized such as histogram equalization explained in chapter 3.

Figure 6-2 shows the performance of the morphological segmentation technique on the image of Figure 6-1. Figure 6-2 (A) shows the maximum intensity of the original microcirculation map and Figure 6-1(B) shows the segmentation results using morphological segmentation. The binary map can be overlaid on the original image to suppress the background and increase the contrast.

The high-contrast background suppressed image is shown in Figure 6-2 (C) and Figure 6-2 (D) shows and the estimate of the vessel radius using distance transform.

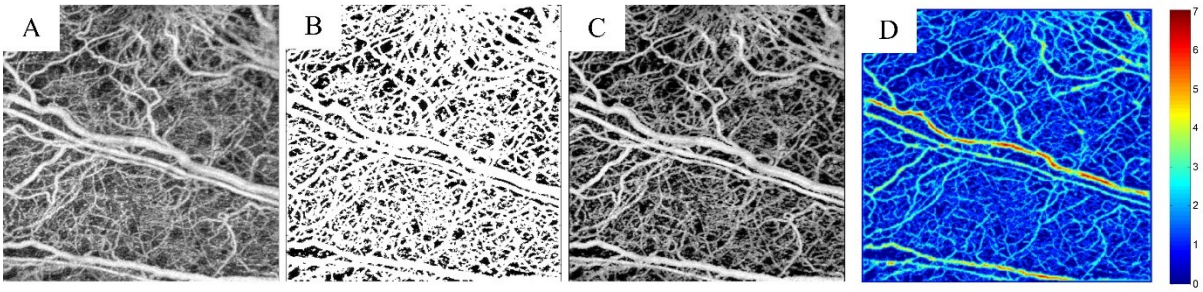

Figure 6-2 Morphological image segmentation.

(A) MIP of the original image. (B) MIP of the segmented image using morphological segmentation. (C) Overlaid the segmented binary image on top of the original image to suppress the background. (D) MIP of the estimated vessel radius using distance transform on the binary segmented vessels.

However, morphological segmentation is only sensitive to the intensity values and does not take the shape of the vessel into account. These limitations can produce false positive segmentation in the image. Also, the vessel boundaries are not clearly defined and all pixels within a vessel are treated equally. By combining the shape-based (Hessian filters) and intensity-based (morphological segmentation) techniques, we can achieve a segmentation technique which is both sensitive to the shape and intensity of the objects. These two techniques can be compounded using a weighted average scheme where the coefficients are chosen by the user to achieve the best performance. The combination of shape-based and intensity-based techniques allows efficient segmentation of blood vessels where the algorithm is sensitive to both shape and intensity of the vessels. Also, Hessian vesselness function does not treat all pixels within the vessels the same and the vessel centerlines always have higher vesselness function. The intensity-based technique corrects for the blurring artifact and unwanted vessel boundary

enlargement due to inaccurate choice of maximum scale value. Figure 6-3 shows the performance of the combined segmentation technique on the image of Figure 6-1. Figure 6-3(A) shows the maximum intensity of the original microcirculation map and Figure 6-3(B) shows the segmentation results using morphological segmentation. The binary map can be overlaid on the original image to suppress the background and increase the contrast. The high-contrast background suppressed image is shown in Figure 6-3(C) and Figure 6-3(D) shows and the estimate of the vessel radius using distance transform. By visual comparison with Figure 6-1 and Figure 6-2, it can be observed that the segmented blood perfusion maps are less sensitive to intensity variations, choice of maximum scales and the vessel shapes are preserved.

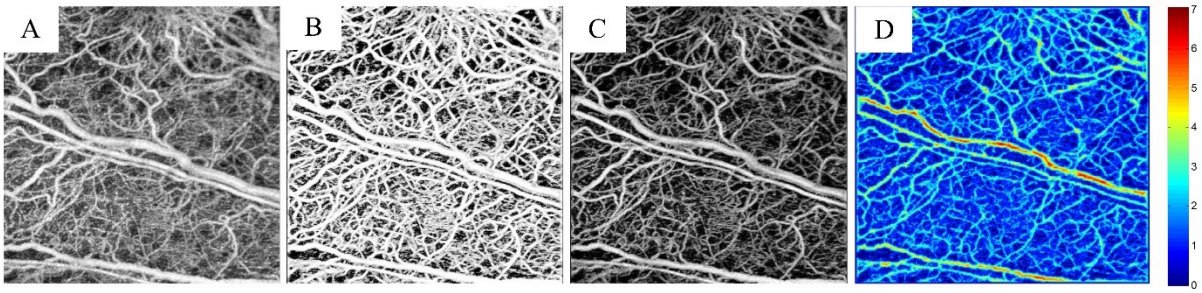

Figure 6-3 Combined shape-based and intensity-based segmentation techniques.

(A) MIP of the original image. (B) MIP of the segmented image using the combined segmentation technique. (C) Overlaid the segmented binary image on top of the original image to suppress the background. (D) MIP of the estimated vessel radius using distance transform on the binary segmented vessels.

Besides the vesselness function, other information of the microvasculature can be acquired from the Hessian filters. The maximum scale at which the Hessian vesselness function is maximum is an indication of the diameter of the vessel. Also, the direction of the segmented blood vessels can be estimated using the corresponding eigenvectors estimated in chapter 5.3. Basically, the direction of the segmented blood vessel using multi-scale Hessian filters can be estimated by

$$Direction_{Vessel} = \tan^{-1}\left(\frac{e_{s,1}}{e_{s,2}}\right) \quad (6\text{-}1)$$

where $e_{s,i}$ is the *i-th* normalized eigenvector at scale s corresponding to the eigenvalue $\lambda_{s,i}$ of the Hessian matrix (equation 5-2). Figure 6-4 (A) shows the Hessian vesselness function and Figure 6-4 (B) shows the scale at which the vesselness function is maximum. Figure 6-4 (C) shows the direction of the vessels estimated from ratio of the eigenvectors. It can be observed that the vessels with positive direction are lined upward whereas the vessels with negative directions are those vessels whose angels are downwards. It should be noted that some vessels may change their directions at different locations and these changes are incorporated in the vessel direction function. Therefore, the combination of shape-based and intensity-based segmentation techniques provides complementary information about vessel diameter, size and orientation that could be used for quantification purposes.

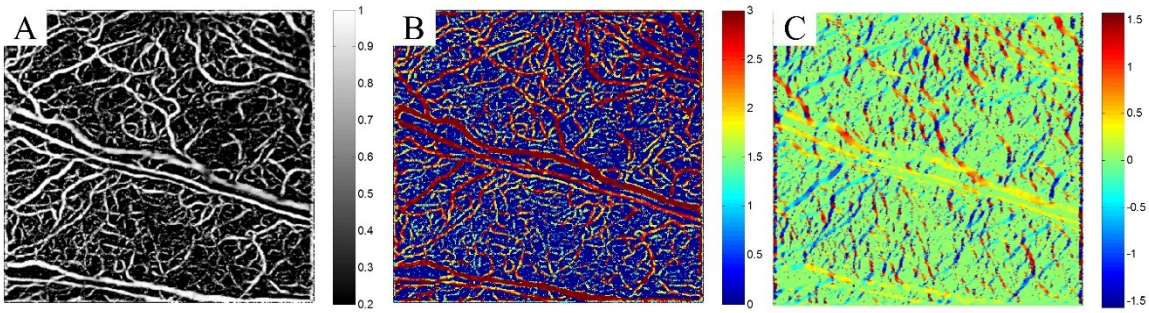

Figure 6-4 Hessian vesselness function.

(A) Hessian vesselness function. (B) The scale which Hessian vesselness has a maximum. (C) Direction of the segmented vessels.

6.3 Experimental results and discussions

6.3.1 Angiogenesis model

We utilized the proposed segmentation scheme to monitor changes in the vasculature and their diameter during the mouse ear pinna wound healing model previously presented in chapter 5.5. A 1 mm biopsy punch was performed on the ear pinna of a hairless mouse and the injured area was monitored on weekly basis. After OMAG processing using the method of eigendecomposition (Chapter 2), the 3D perfusion maps were resampled along the depth and each depth cross section was segmented using the combined method. For each frame, the distance transform and binary maps were calculated. Also, to enhance the microvasculature contrast and improve the visualization of microcirculations, we masked the original image with the binary maps and generated high-contrast high-resolution microcirculation maps within the tissue beds.

Figure 6-5 (A-F) show the maximum intensity projection of the microcirculation activity during the healing process after inducing the 1 mm biopsy punch. Figure 6-5 (A) was captured a few seconds after the injury. At this moment, the blood has coagulated on the damaged blood vessels and microcirculation has been rewired from collateral vessels to support the downstream injured tissue. Figure 6-5 (B-F) were captured on weeks 1, 3, 4, 9 and 18 after inducing the biopsy punch. Figure 6-5 (G-L) show the high-contrast masked microcirculation map after segmenting the blood vessels and removing the background. It can be clearly observed that the contrast of the masked image is much higher than the original data and individual capillaries can be visually resolved. The segmented binary images are shown in Figure 6-5 (M-R). The vessel diameters were estimated using the distance transform and their value was calibrated using the system

parameters and the maximum distance projections of the corresponding angiogenesis maps are shown in Figure 6-5 (S-X).

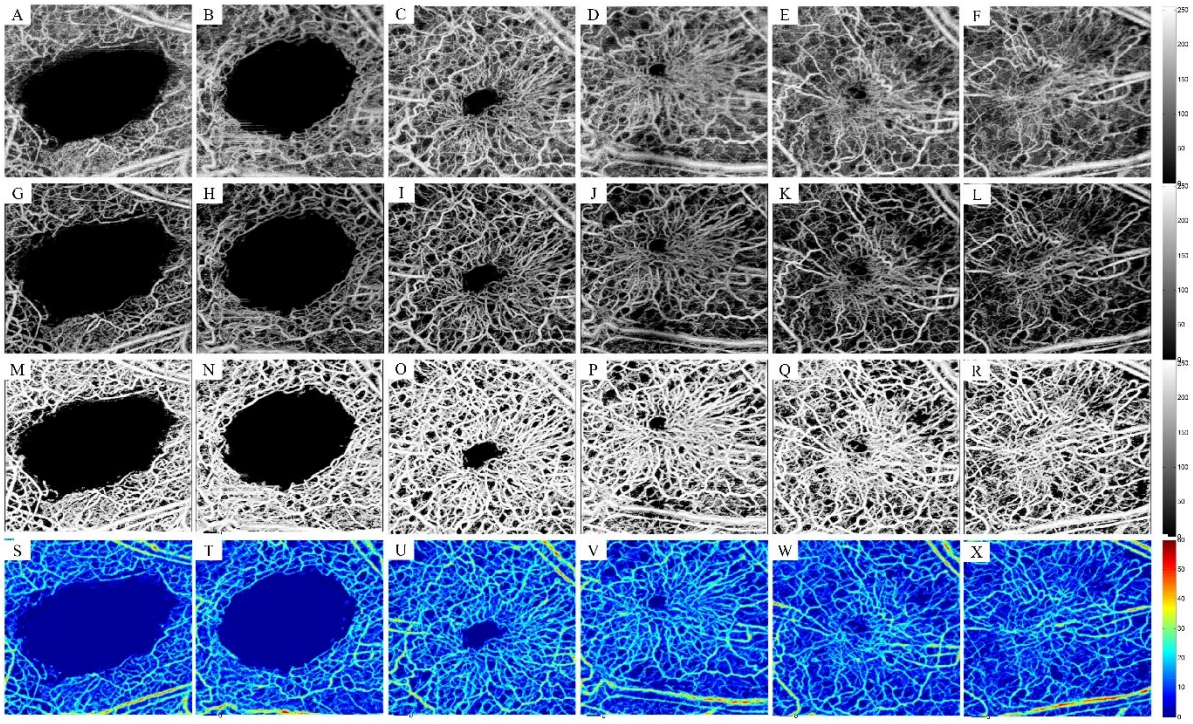

Figure 6-5 Segmentation of the wound healing model using the combined scheme.

(A) Remaining microcirculation in the wound area a few seconds after inducing the punch (B-F) Angiogenesis and natural healing process on week 1, 3, 4, 9 and 18. (G-L) Corresponding high-contrast microcirculation after masking the segmented binary mask on the original data. (M-R) Binary segmented microcirculation using the combined segmentation technique. (S-X) Maximum distance transform projection map corrected for beam broadening and voxel size corresponding to the first row.

We quantified the diameter of newly formed vessels in the wound area as well as vessel area density in the region of interest. The region of interest was defined a circular shape around the wound location. We manually located the center of the circle to be roughly at the center of the wound. The radius of the circle was selected large enough to cover the wound and was kept fixed in between all samples. The vessel diameter values were calculated by finding the vessel centerline using binary skeletonizing algorithm [Gonzalez-2002] and the values of the distance

transform on the skeleton map were used as an estimate of the vessel diameter. Figure 6-6 (A) shows the binary overlaid vasculature on the 3rd week after the injury and its skeletonized map is shown in Figure 6-6 (B). The skeleton map is an estimate of the centerline location of blood vessels. Figure 6-6 (C) shows the distance transform corresponding to the binary image of Figure 6-6 (A) and the corresponding distance transform on the vessel centerlines are shown in Figure 6-6 (D). The vessel diameter estimates are given in auxiliary units and the exact value can be found after correcting for system parameters and beam broadening for each voxel. For our purpose, the relative values of the estimated vessel diameter along the time is valid. The diameter of the new vessels in the wound area can be quantified by forming the histogram distribution of Figure 6-6 (A).

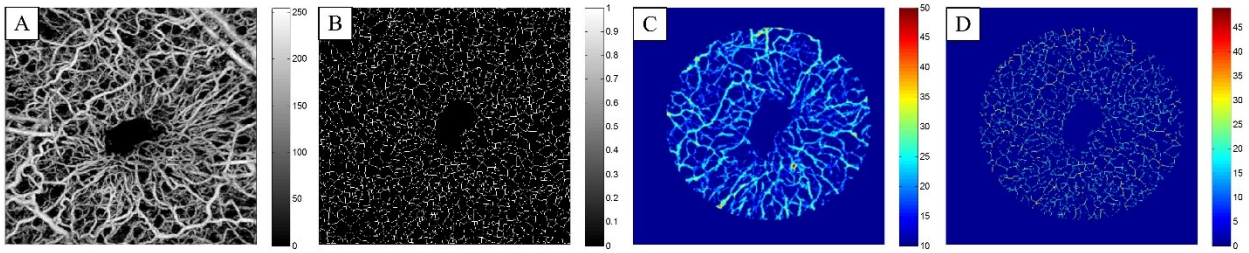

Figure 6-6 Quantification of wound healing.
(A) Segmented blood vessels on 3rd week. (B) Skeletonized vessel map. (C) Distance transform in the ROI. (D) Distance transform on the skeleton map of (B).

Similar procedure was performed on all other images and the distribution of vessel diameter was estimated for each experiment. It can be observed in Figure 6-7 (A) that during the healing process, vessel diameters increase for a couple of weeks until the wound area closes (3rd week) and then decreases and stabilizes as the tissue matures and wound heals. Figure 6-7 (B) shows the changes in the vessel area density in the wound area during the healing process. The vessel area density was estimated by finding the ratio of the vessel area (nonzero maps on the binary

image) divided by the total imaging area within the region of interest around the initial wound injury. Similar to the diameter changes, first the vessel area density monotonically increased until the wound area was fully closed. Then, the area density reduced due to tissue maturation and apoptosis of some vessels within the granulation tissue.

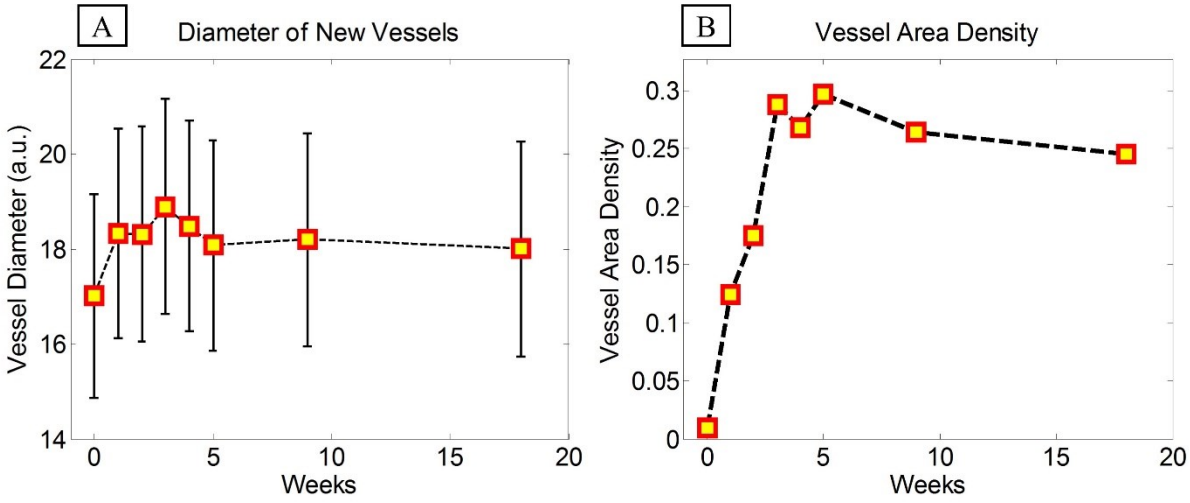

Figure 6-7 Wound healing quantification.

(A) Diameter of new vessels in the wound area shown in the form of mean ± standard deviation (B) Average vessel area density in the wound area during the healing process.

6.3.2 Fundus camera vasculature segmentation

Besides visual and qualitative validation of segmentation results, segmentation algorithms can be quantitatively assessed by comparing the results with gold standard methods of segmentation. Since no gold standard technique exist in digital segmentation, one way is to compare the results with those from manual segmentation done by trained experts. Although manual segmentation from one expert can be erroneous, combination of manual segmentations done by multiple users can reduce the error and therefore can be utilized as a gold standard. To the best of our knowledge, there is no standard OCT microangiography database. Therefore, we tested our

algorithm on the Utrecht University's digital retinal images for vessel extraction (DRIVE) database [Staal-2004, Niemeijer-2004]. The DRIVE database consists of 40 fundus camera retina images and many researchers have been testing their segmentation algorithms to extract blood vessel information. The photographs for the DRIVE database were obtained from a diabetic retinopathy screening program in The Netherlands. The screening population consisted of 400 diabetic subjects between 25-90 years of age. 40 photographs have been randomly selected, 33 do not show any sign of diabetic retinopathy and 7 show signs of mild early diabetic retinopathy. The images were acquired using a Canon CR5 non-mydriatic 3CCD camera with a 45 degree field of view (FOV). Each image was captured using 8 bits per color plane at 768 by 584 pixels. The FOV of each image is circular with a diameter of approximately 540 pixels. For this database, the images have been cropped around the FOV. For each image, a mask image is provided that delineates the FOV. For the set of 40 images, manual segmentations are available that can be used as gold standard. All human observers that manually segmented the vasculature were instructed and trained by an experienced ophthalmologist. They were asked to mark all pixels for which they were for at least 70% certain that they were vessel. All of the images contained in the database were actually used for making clinical diagnoses.

We should note that our segmentation technique is originally developed for OCT microangiography but we can generalize the algorithm to other modalities such as retinal fundus images. Since the main characteristic of retinal vessels in fundus camera is their contrast from surrounding tissue background and their low intensity due to light absorption, our segmentation technique is sensitive to the pre-processing stage that converts the fundus image to an image similar to those generated by optical microangiography.

In our pre-processing algorithm, the green channel of the fundus images were utilized and a 3*3 Gaussian smoothing filter followed by adaptive histogram equalization were performed to generate a uniform distribution of pixels. Because of absorption properties of red blood cells and retina tissue, the green channel of color fundus images usually generates the highest contrast between blood vessels and background [Hoover-2000]. Finally the image was inverted to make blood vessels appear brighter than the adjacent tissue. Figure 6-8 (A-B) show the color and the corresponding green channel of a retinal fundus image from the DRIVE dataset, respectively. The corresponding contrast-enhanced inverted image after intensity inversion and masking is shown in Figure 6-8. It can be observed that the retina vessels have been enhanced while other features in the image such as the low-intensity fovea region also appear bright. In this case, we expect that sensitivity of our segmentation technique may drop while specificity should be acceptable.

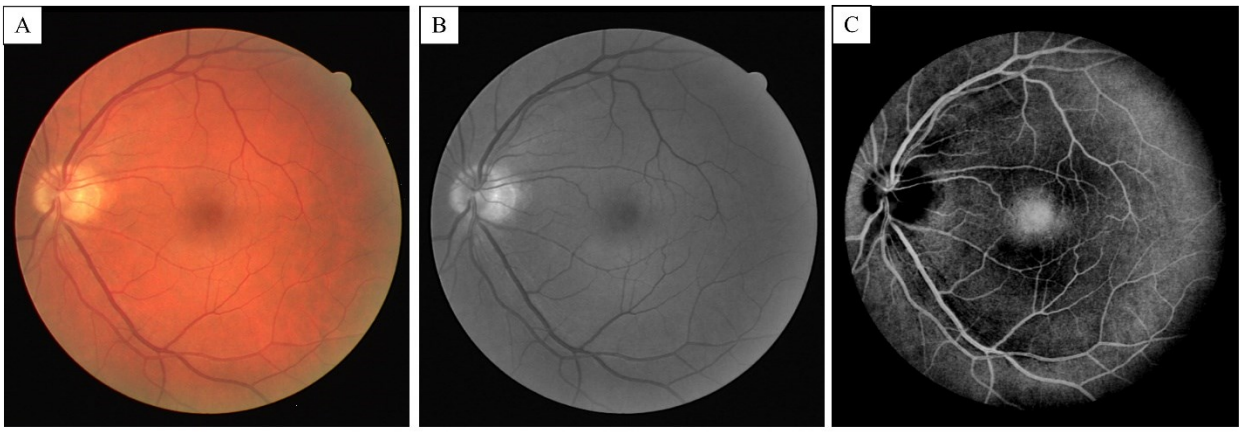

Figure 6-8 Sample fundus camera image from dataset.

(A) Fundus color image of retina from the DRIVE data set (B) The green channel of the color image. (C) Contras-enhanced and inverted fundus image from the green channel after the pre-processing filtering.

Figure 6-9 shows segmentation results on the enhanced image shown in Figure 6-8 (C). Figure 6-9 (A-C) show segmentation results using Hessian vesselness filters, intensity-based filter and combined methods, respectively. The manual segmentation (gold standard) is also shown in Figure 6-9 (D) for comparison. It can be observed that intensity-based technique has some error around the low-intensity fovea region as well as small and low-contrast vessels. On the other hand, Hessian vesselness filters show better results on fovea and smaller vessels while they have error near the optic nerve head that the intensity variations are high. The combination method takes these limitations in to account and minimizes the error generated by both algorithms.

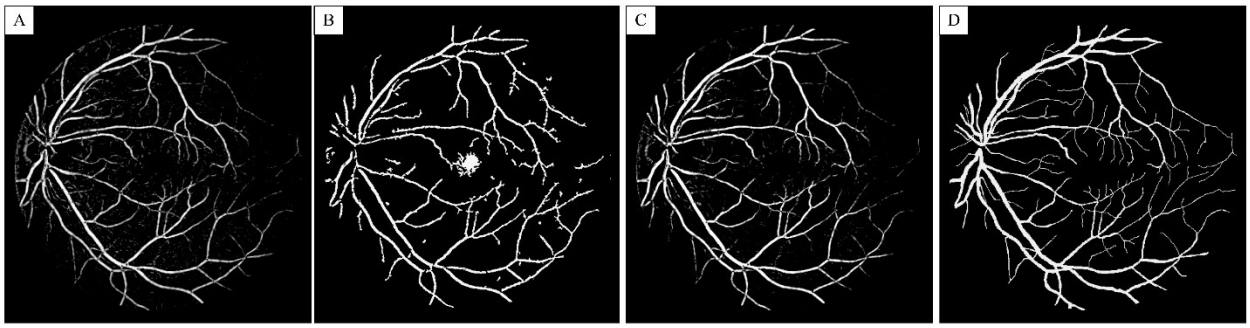

Figure 6-9 Segmentation results on DRIVE dataset.
(A) Hessian filter. (B) Intensity segmentation. (C) Combined Hessian and intensity filter. (D) Manual segmentation.

We tested our algorithm on all 40 images in the DRIVE dataset and measured sensitivity, specificity and accuracy of our algorithm with respect to the manual segmentations. Table 6-1 summarizes the results that indicates true and false segmentation rates given the manual segmentation results. The following parameters are defined as following. The sensitivity or true positive rate is defined as the rate of pixels that were segmented by both manual and automatic segmentation techniques (true positive) divided by total number pixels segmented by the gold

standard. Higher sensitivity indicates how similar manual and automatic techniques are in segmenting the blood vessels. The specificity or true negative rate is defined as the rate of pixels that were correctly not segmented by both techniques (true negative) divided by the total number of non-vessel pixels. Finally, the accuracy is defined as the rate of pixels correctly segmented and not segmented by the algorithm (true positive + true negative) divided by the total number of pixels in the image.

We can see from Table 6-1**Error! Reference source not found.** that the sensitivity of our proposed method is relatively low, as we predicted. This is mainly due to the assumptions we made on the fundus images regarding the intensity of retina vessels. On the other hand, some tiny vessels that were represented by only one pixel in the manual segmentation images were not detected because of their relatively low contrast from background and morphological opening operations performed on the images. However, the specificity and accuracy of our proposed method are relatively high which indicates that most of the large and high contrast vessels were accurately segmented.

Table 6-1 Segmentation results using the proposed segmentation technique.

	Manual Segmentation 1	Manual Segmentation 2
Sensitivity	0.77 ± 0.05	0.79 ± 0.04
Specificity	0.95 ± 0.02	0.95 ± 0.01
Accuracy	0.93 ± 0.02	0.94 ± 0.01

Although our technique is not meant for vessel segmentation from fundus camera images, we compared our results with a few techniques in the literature that worked on the same data set to get a better sense on how existing methods perform on the DRIVE dataset. The first column in

Table 6-2 indicates the method used for retinal vessel segmentation from DRIVE fundus camera image database and the second column indicates the accuracy results of its corresponding technique. We borrowed these results for comparison from the Image Sciences Institute's website.

Table 6-2 Performance accuracy comparison.

Method	Accuracy
Staal [Staal-2004]	0.944
Niemeijer [Niemeijer-2004]	0.941
Zana [Zana-2001]	0.937
Jiang [Jiang-2003]	0.921
Martínez-Pérez [Martínez-Pérez-1999]	0.918
Chaudhuri [Chaudhuri-1989]	0.877
Al-Diri [Al-Diri-2009]	0.925
Modified Hessian	0.933

Figure 6-10 shows the performance of our segmentation technique compared with manual segmentation (gold standard) and possible cases that our technique can fail. The first column shows fundus camera images (Figure 6-10 (A), (E), (I) and (M)). The second column shows the segmentation results using our combined technique overlaid on top of the equalized green channel where red color indicates segmented vessel and gray areas show non-segmented background (Figure 6-10 (B), (F), (J) and (N)). The third column shows the result of manual segmentation (gold standard) coded with yellow color overlaid on the green channel of fundus

image (Figure 6-10 (C), (G), (K) and (O)). The last column shows the corresponding segmentation comparison where the yellow color indicates true positive, red color indicates true negative and green value indicates false positive segmentation results (Figure 6-10 (D), (H), (L) and (P)). For the cases that retina layer was very thin (second and third row), the choroid vasculature have also been segmented into the image that increased the rate of false positives. It can be observed that our segmentation technique performed very well on main and large retinal vessels. However, our technique deviated from the manual segmentation results on small vessels with a very low contrast on the actual images. When retina layer was thin due to macular degeneration, choroid vasculature were more obvious in the green channel and they were segmented by our algorithm. However, the users who performed the manual segmentation could avoid doing so by having a prior knowledge about those vessels. Other cases that manual and automatic segmentation techniques did not match were location on the optic disk head where the intensity was a lot higher than normal due to nerve loss and low contrast vessels on the disk head were sacrificed during our pre-processing step.

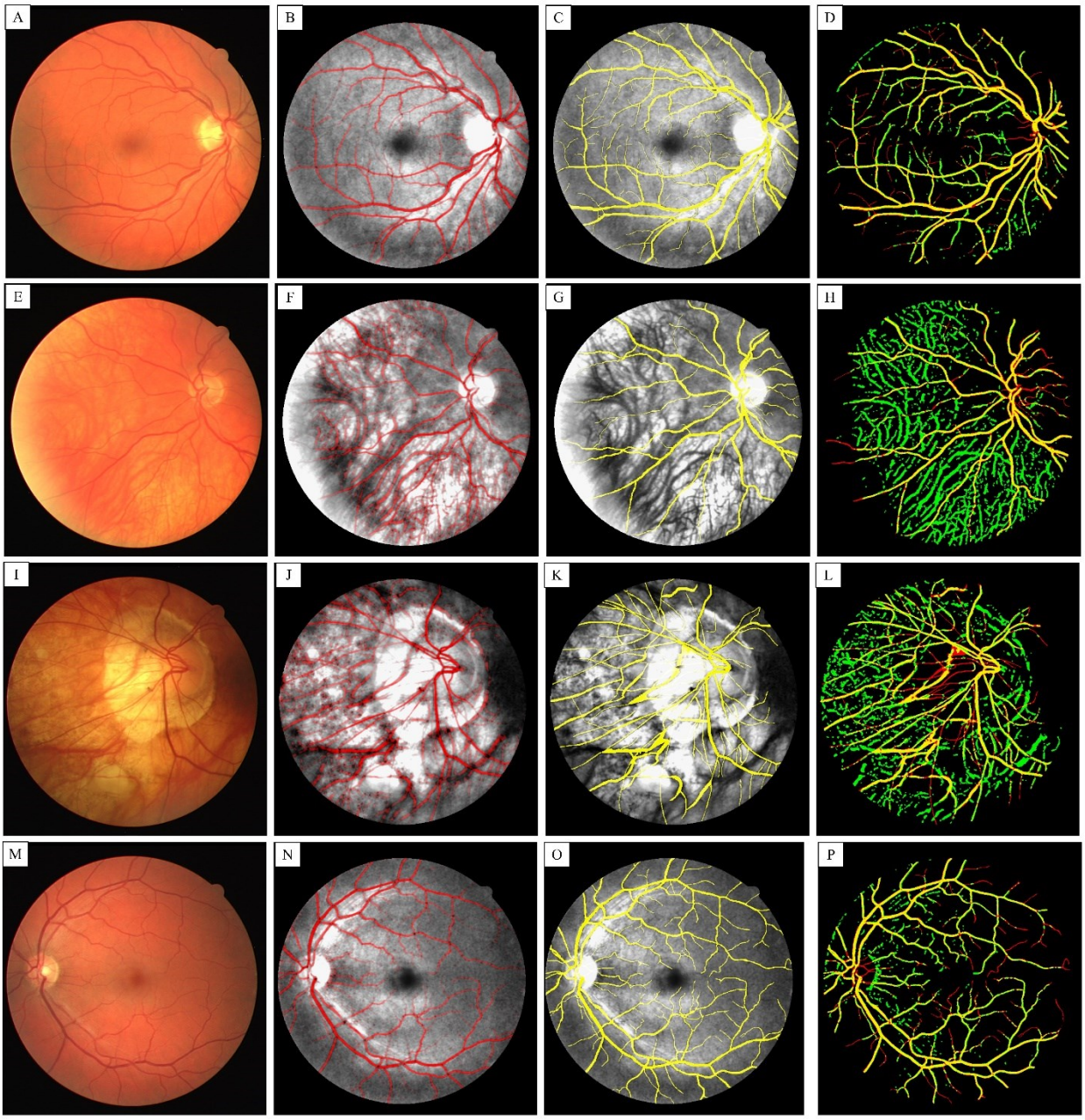

Figure 6-10 Sample segmentation results on retinal fundus camera images.

First column (A, E, I and M) shows fundus camera of four different retina images from the DRIVE dataset. The second column (B, F, J and N) shows the corresponding segmentation results using our combined technique overlaid on top of the equalized green channel where red color shows segmented vessel and gray areas show non-segmented background. The third column (C, G, K and O) shows the result of manual segmentation (gold standard) coded with yellow color overlaid on the green channel of fundus image. The last column (D, H, L and P) shows the corresponding segmentation comparison where the yellow color indicates true positive, red color indicates true negative and green value indicates false positive segmentation

results. For the cases that retina layer was thinned (second and third row), the choroid vasculature have also been segmented into the image.

In general, the segmentation results are highly correlated with our pre-processing step. The point of this chapter was not proposing a pre-processing technique for vessel extraction and segmentation from fundus camera images. However, if the vessels are clearly contrasted from their surrounding tissue, our proposed technique can be utilized to efficiently segment those vessels. Since the DRIVE is a standard dataset and manual segmentation results are available as gold standard, we performed our method on that dataset to challenge the efficiency and compare the results with the existing techniques.

6.4 Conclusions

In this chapter, we modified the Hessian-based vesselness model to segment blood vessels within the tissue beds. Since the estimated vessel diameter and other geometrical parameters highly depend on the maximum scale parameter in the Hessian vesselness model, we proposed a correction segmentation technique to correct the Hessian results. We tested the efficiency of our algorithm on angiogenesis wound healing model and quantified the healing process after a biopsy punch. To quantify the accuracy of our segmentation technique, standard dataset with manual segmentation technique from retina fundus images were selected. The segmentation algorithm was compared with the manual segmentation provided by the experts and achieved a reasonably good results compared to the results of other techniques reported on that dataset. Our segmentation technique is not limited to OCT angiograms and can be applied to other imaging techniques with similar vasculature pattern.

Chapter 7. TRANSLATIONAL APPLICATION 1– IMAGING AND QUANTIFICATION OF MICROCIRCULATION IN A WOUND HEALING MODEL

7.1 Introduction

Cutaneous wounds are usually created as a result of damage to the skin due to injury that can lead to disability or death in some cases such as burns, chronic skin ulcers and diabetes mellitus [Singer-1999]. Natural wound healing consists of overlapping multi-phase processes including hemostasis, inflammation, tissue formation and tissue remodeling. If the skin is not perfectly healed as it was before the injury, scar tissue is formed. The hairless mouse ear pinna model has been extensively used for *in vivo* studies of the skin microcirculation [Barker-1989]. Mouse ear pinna is composed of two layers of skin separated by a layer of cartilage. Because of its relatively thin structure (~500 μm), optical imaging techniques can be utilized to non-invasively image microcirculation within the pinna tissue. These skin layers are almost identical to human skin structure except for sweet ducts and glands [Eriksson-1980].

Wound healing models in mice are very popular among researchers because mice are inexpensive, easy to handle, available in large numbers, and have low risk of death under anesthesia [Peplow-2010]. Most of the existing models of wound healing studies are performed in mice with specific gene-knocked out, followed by immunohistochemistry and histology [Werner-2003]. Development of non-invasive methods for the monitoring of wound healing can help researchers better understand the mechanisms and effect of therapeutic treatment on healing process in chronic and diabetic wound disease. Wound healing and micro-vasculature

remodeling in the mouse ear pinna model has been previously studied using OMAG [Jung-2013] and laser speckle imaging [Rege-2012]. Briefly, a biopsy punch is performed on one of the major artery/vein pairs of the ear. The initial tissue response to the wound is triggered immediately after the punch by blood coagulation, recruiting peripheral capillaries and redirection of main arterial/venous blood flow. During the healing process, the wound size is gradually reduced along the time and the wound surface is fully closed within four weeks. However, microcirculation and capillary maturation continues for months. In this paper, we demonstrate the capability of OMAG to describe in detail the microcirculation response including capillaries, large vessels and lymphatic vessels during wound healing phases.

7.2 System setup and experimental preparation

7.2.1 3.1 OCT system set up

The schematic of our OCT system setup is given in **Figure 1-1** and the detail of the system was explained in the section 2.4 (experimental setup). The typical field of view and scanning range for our OCT system was 2.2x2.2 mm^2 in the current setup. The x-scanner (fast B-scan) was driven with a saw tooth waveform and the y-scanner (slow C-scan) was driven with a step function waveform. The fast and slow scanners covered a rectangular area of ~ 2.2x2.2 mm^2 on the sample. Each B-scan consisted of 400 A-lines covering a range of ~ 2.2 mm on the sample. The duty cycle of the saw tooth waveform rising edge was set at ~80% per cycle, which provided a B-scan frame rate of ~ 94 frames per second. The C-scan consisted of 400 scan locations with B-scan repetition of 8 frames per location for flow imaging and quantification. The total size of the data set was $1.28x10^6$ A-lines. In order to cover a large field of view, multiple 3-D scan were

acquired and the sample was translated using a mechanical stage. This allowed imaging an area of ~1.5x1.5 cm^2 on the mouse ear pinna.

The acquired data was transferred to a personal computer (PC) and processed off-line using an m-file code developed on Matlab© (The Mathworks Inc.). The processing consists of removing interference signal from reference arm, dispersion correction, resampling each A-line from non-linear wavelength space to the linear K-space and applying fast Fourier transform (FFT) [Wang-2007_3D_OMAG]. The FFT amplitude of the repeated B-scans at the same spatial location was averaged temporally to generate structure cross-section images. The procedures to map blood flow perfusion and lymphatic vessels are explained in chapters 2 and 5 of the thesis, respectively.

7.3 Experimental results and discussions

First, non-invasive baseline OCT/OMAG images were acquired from mouse ear pinna. Then, a 1-mm biopsy punch (Integra® Miltex®, Japan) was performed to remove tissue structures along one of the major artery/vein pairs of the ear. Then, OCT/OMAG images of the wound area were acquired immediately after punch. The wound area was monitored weekly for a few months until tissue was visually fully matured. Since the field of view of each OCT scan was limited to ~2.2x2.2 mm^2 (limited because of the numerical aperture of OCT objective lens), total of 9 images (3x3 overlapping scans) were acquired from the wound and its surrounding tissue structures to increase the field of view to ~ 7x7 mm^2. The imaging site was manually shifted using the mechanical stage and we allowed some overlap between adjacent scans for better stitching of individual images. Final image was generated by manually stitching individual images together to form a large field of view detailed image of blood flow perfusion and

lymphatic vessels during healing process. During different phases of healing process, the following interesting observations were made:

7.3.1 Phase I: Hemostasis and collateral recruitment

After inducing the biopsy injury, small amount of bleeding occurs at the injured site that immediately coagulates and fibrin blood clot is formed on the wound edge. The fibrin clot is formed due to aggregation and activation of platelets at the injury site. This is the first phase of wound healing process. Just before the inflammatory phase, fibrin and fibronectin link together and form a net that prevents further blood loss by trapping proteins and particles [Mallett-1992]. The ear pinna in mice consists of very dense and interconnected vascular network and most of the adjacent arteries/veins are connected via anastomosis and collateral vessels. Immediately after cutting major artery/vein, blood flow circulation within the vascular network rewires due to formation of clot that blocks the vessel, variations of blood flow pressure within the vessels and signaling pathways of cellular structures. Such rewiring of blood flow circulation allows the downstream tissues to survive. Figure 7-1 shows the blood flow perfusion maps before and immediately after the injury, respectively. The circle shows the location of biopsy punch and arrows indicate the collateral vessels that take over the blood circulation in the downstream tissue. It can be observed that microcirculation rewiring happened immediately by utilizing the pre-existing vessels in the microvascular network. The green arrows indicate the collateral vessels that will support the damaged tissue immediately after inducing the injury. Also, the red arrows indicate the location of major shunts and bridges between the collaterals and the downstream microvessels. The blood supply is redirected through these channels immediately after the upstream major vessels are damaged. The vertical stripes on the baseline image are

mainly due to animal motion artifact caused by involuntary respiratory and cardiac motion artifacts.

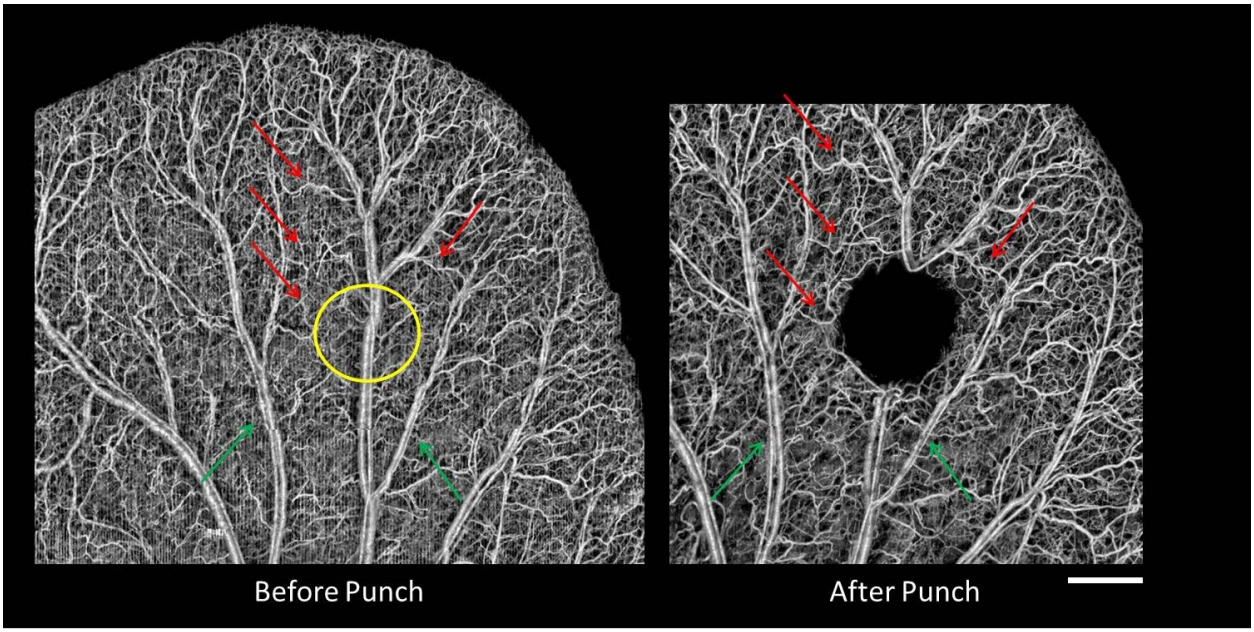

Figure 7-1 Collateral recruitment immediately after inducing the punch.
Collateral vessels indicated by arrows contribute to blood flow perfusion in the downstream to support blood flow. Green arrows: Collateral microvessels. Red arrows: shunts and bridges between the collaterals and downstream of the damaged tissue. Scale bar = 500 μm.

7.3.2 Phase II: Inflammation

Inflammation plays an important role in fighting infection, clearing debris and inducing the proliferation phase in wound healing. Within few hours, the second phase of wound healing (inflammation) starts when platelets release extra-cellular matrix (ECM) proteins, cytokines and other pro-inflammatory factors into the blood. These factors increase cell proliferation and migration to the wound area and make blood vessels dilate [Raghow-1994]. Histamine is the factor that makes blood vessels dilate and become more porous. Increased vessel diameter and porosity facilitates the entry of inflammatory cells such as leukocytes into the wound site from the bloodstream [Boyd-1959]. Growth factors and fibronectin attract neutrophils to the wound site within few hours of wounding to kill bacteria and cleanse the wound by secreting proteases

that decompose damaged tissue. After completing their tasks, neutrophils undergo apoptosis and then are degraded by macrophages. Other leukocytes such as helper T-cells enter the wound site and secrete cytokines that increase inflammation and activity of macrophages [Gillitzer-2001]. Macrophages promote wound healing and regeneration by releasing factors that induce angiogenesis, re-epithelialization, formation of granulation tissue and creation of new ECM and hence pushing the healing process into the next phase [Rappolee-1988].

7.3.2.1 Dilation of the collateral bridges

Although pre-existing collateral and anastomosis vessels help the downstream tissue to survive in the short term, a hypoxic tissue is generated at the injury site and its downstream. We observed that the recruited collateral bridges significantly enlarged along the time. Figure 7-2 show the enlargement of these bridges along the time and arrows indicate the major bridges after injury. These changes mediate the increase of blood flow to support hypoxic tissue that requires increased blood supply to continue healing and surviving. During this phase, platelets at the wound site have released ECM proteins, growth and pro-inflammatory factors such as histamine to the wound area and increased the diameter and porosity of collateral bridges [Boyd-1959, Gillitzer-2001].

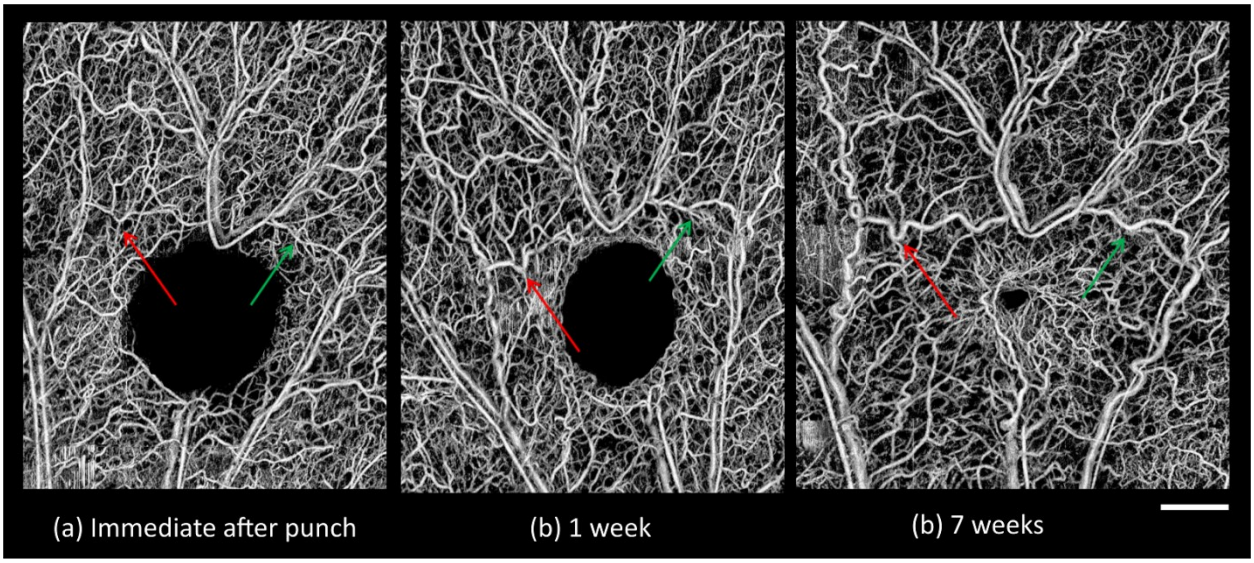

Figure 7-2 Vasodilation in anastomosis shunt vessels.
Red and green arrows indicate two shunt bridges from nearest collaterals. Scale bar = 500 μm.

Enlargement of vessels near hypoxic tissue was not limited to anastomosis bridges and their upstream collateral vessels also enlarged significantly. Figure 7-3 shows dilation of the parallel collaterals that connect anastomosis bridges to the upstream blood supply. It was also observed that the enlargement of collateral vessels was accompanied by increase of their tortuosity, specifically for veins. Similar observations have been reported when vascular endothelial growth factor (VEGF) is utilized to trigger hypoxia-inducible factor-1 (HIF-1) mediated neovascularization in gene knockout mice that lack VEGF [Oladipupo-2011]. We can explain our observation as follows: creating a biopsy punch can induce a hypoxic condition that triggers increase of growth factors including VEGF to the hypoxic area for wound healing and neovascularization. The increase in the VEGF mediates enlargement of collateral and bridge vessels. At the same time, these vessels need to deliver more oxygen and nutrition supply via red blood cells to the damaged and hypoxic tissue and their enlargement mediates that process.

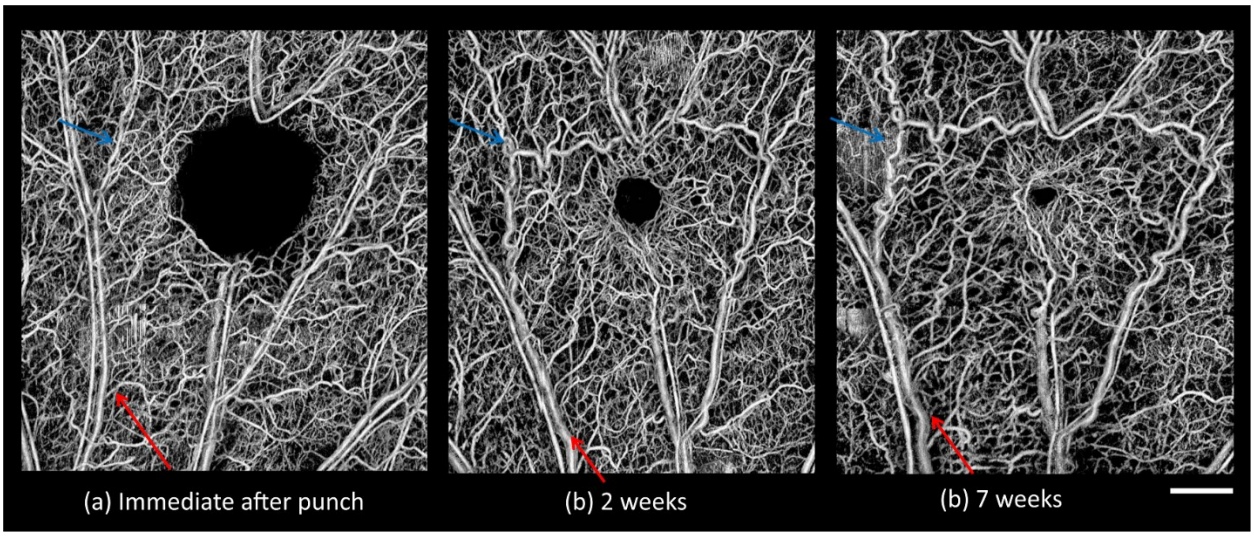

Figure 7-3 Vasodilation in collateral vessels.

The arrows indicate the collateral vessels that enlarge along the time to support the wound site. Scale bar = 500 μm.

7.3.2.2 The response of lymphatic vessels

The lymphatic system usually develops in parallel to the blood vessels in most internal organs or skin and is not present in central nervous system, bone marrow and avascular structures such as cartilage, epidermis and cornea. Besides draining lymph fluid from extracellular spaces, other roles of lymphatic system include absorbing lipids from intestinal tract, maintaining fluid hemostasis and transporting antigen-presenting cells and leukocytes to lymphoid organs. Also, lymphatic system plays an important role in the development of several diseases such as cancer, lymphedema, some inflammatory conditions and allergies [Alitalo-2005, Oliver-2004, Zgraggen-2013].

Although no significant lymph was detected on the baseline image due to the limitation of the axial/spatial resolution, immediately after inducing the punch the lymphatic vessels were significantly enlarged around the wound and in the downstream tissue. Figure 7-4 shows the process of vasculature remodeling and lymphatic vessel response to the wound. Each image is

composed of 9 OCT-OMAG mosaics acquired around the wound area. Discontinuity of the blood and lymphatic vessel maps can be an artifact due to changes in optical angle and properties after shifting the stage. Blood vessels are orange-coded and lymphatic vessels were color-coded with green. The peak activity of lymphatic vessel enlargement was observed within ~1 week after inducing the wound. This observation is in agreement with the wound healing phases during the inflammatory phase. The immediate response of lymphatic vessels after inducing the punch (Day-1) was mainly concentrated around the wound, collaterals and downstream of the injured vessels. However, the size of the lymphatic vessels had significantly increased after one week (Day-8) and it was not only around the wound, but also at farther locations on the ear. Then, the size and distribution of lymphatic vessels reduced after Day-22 and was mainly around the wound area due to inflammation.

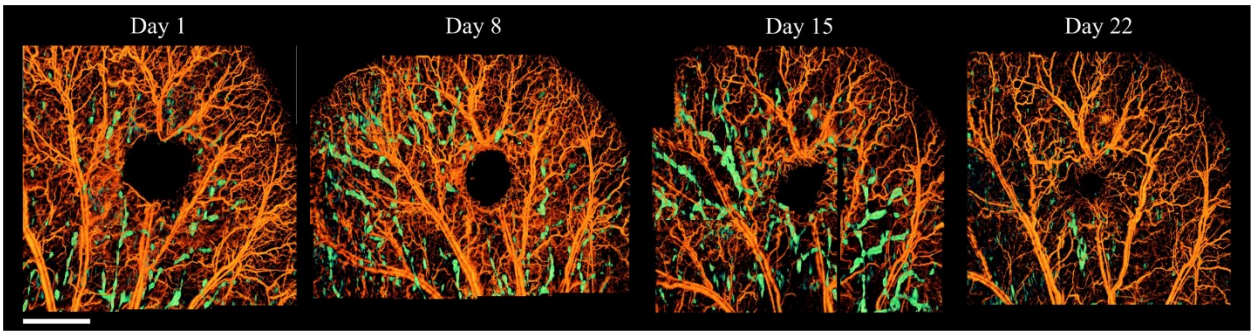

Figure 7-4 Microcirculatory response during wound healing.
Activity of lymphatic vessels during healing process along with blood flow perfusion map. Scale bar = 1mm.

7.3.3 Phase III: Proliferation

At the end of inflammatory phase, fewer inflammatory factors are secreted and number of neutrophils and macrophages are reduced in the wound site [Werner-2003]. Inflammatory phase lasts as long as there is debris in the wound. Proliferation phase begins when endothelial cells migrate to the wound area and fibroblasts accumulate in the wound site, proliferate and lay down

collagen matrix as the inflammatory phase is ending. Fibroblasts are the main cells in the wound area by the end of first week and their number usually peaks at one to two weeks after injury. They usually originate from adjacent uninjured tissue and circulating stem cells in the blood [Song-2010]. Fibroblasts utilize the fibrin cross-linking fibers to migrate across the wound and then deposit ground substance and collagen into the wound bed [Werner-2003]. Since the activity of fibroblasts and epithelial cells requires oxygen and nutrients, angiogenesis is necessary to support healing process [Tonnesen-2000]. The fibronectin found in the fibrin scab attracts endothelial cells to the wound area. Stem cells of endothelial cells originating from parts of uninjured blood vessels develop pseudopodia and push through the ECM to the wound area and establish neovascularization [Greenhalgh-1998]. Hypoxia and lactic acid in the wound area can directly stimulate endothelial growth and proliferation [Falanga-2005]. Figure 7-5 shows proliferation and angiogenesis in the wound area following the injury. Immediately after punch, injured capillaries and blood vessels coagulate and prevent tissue from bleeding. After one week, neovasculature within granulation tissue can be clearly observed that take the form of a “pile of woven wool”. At the second week, wound contraction has already started pulling the neovasculature within the granulation tissue together and the “pile of wool” starts to open up. As the wound healing process continues towards the center of the wound, more granulation tissue is formed at the wound edges followed by neovascularization and angiogenesis. At maturation phase (around week-18), some new vessels have grown larger while others have disappeared due to apoptosis.

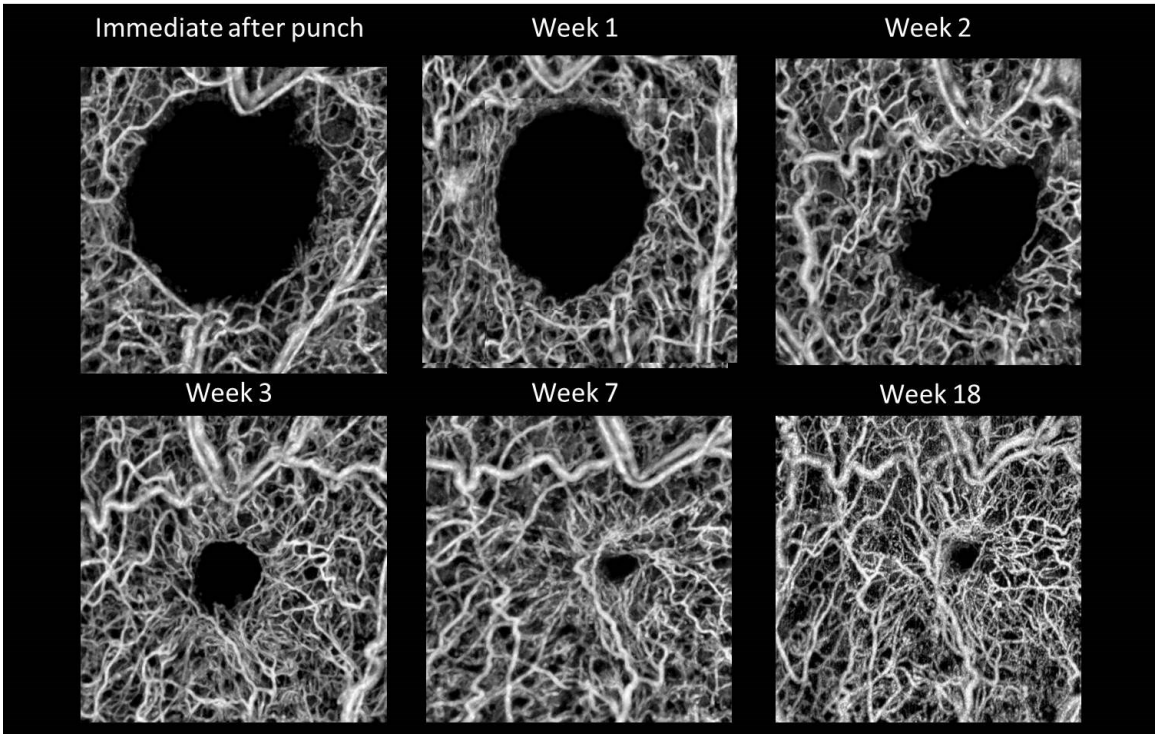

Figure 7-5 Proliferation and neovascularization

7.3.3.1 Re-epithelialization

Granulation tissue is a temporary structure consisting of neovasculature, inflammatory cells, endothelial cells, fibroblasts, myofibroblasts and the components of a new provisional ECM that appears in the wound area during inflammatory phase [Werner-2003]. Fibroblasts produce collagen to increases the wound strength in addition to fibrin-fibronectin clot. Later on, cells involved in inflammation, angiogenesis and connective tissue construction attach to, grow and differentiate on the collagen matrix laid down by fibroblasts [Ruszczak-2003]. Re-epithelialization phase takes place when granulation tissue is formed in the wound area and epithelial cells migrate across the new tissue and form a barrier between the wound and the external environment [Larjava-2012]. Basal keratinocytes at the wound edges and dermal appendages such as hair follicles and sweet glands are the main cells responsible for the

epithelialization phase of wound healing [DiPietro-1995]. Epithelialization advance across the wound edges and stop proliferation and movement when the wound edges meet each other in the middle. Epithelial cells grow like a sheet by climbing over each other to migrate (often called epithelial tongue) [Bartkova-2003]. The first cells that attach to the basement membrane form the stratum basale that continue to migrate across the wound bed. Scar formation depends on how quick the epithelial cells migrate [Son-2005]. Figure 7-6 shows the depth-encoded blood flow perfusion depth map around the wound and their corresponding tissue cross-section B-mode image. Epithelialization can be observed that advances across the wound edges and proliferation stops when wound edges meet each other in the middle. Since epithelial cells grow by climbing over each other, wound edges always seem elevated compared to their distal structures and a scar tissue is formed around week-7. Although the wound edges seem closed within five weeks and punch area is no longer see-through with naked eye, we can observe that healing process inside the wound area continues for several months until tissue is fully matured.

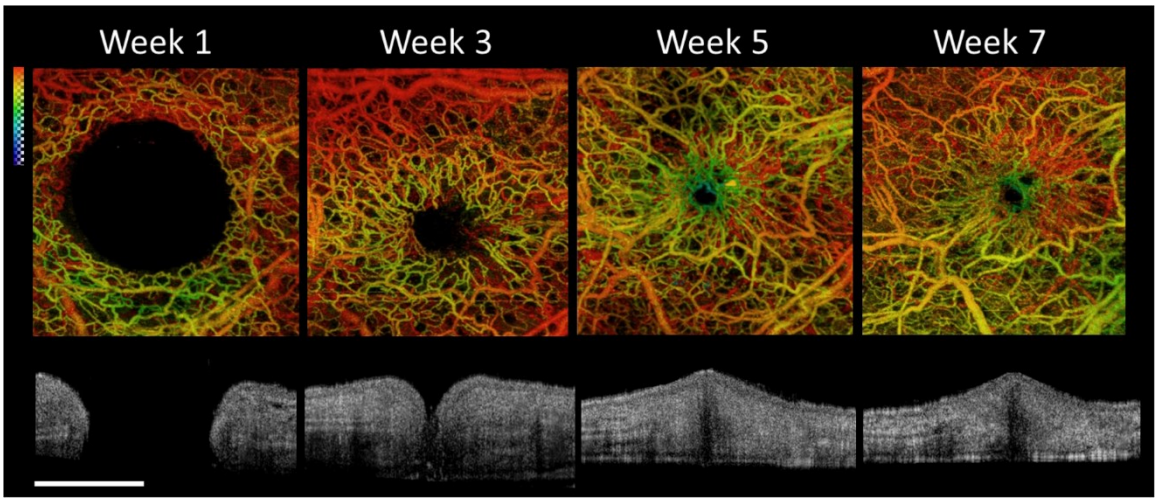

Figure 7-6 Epithelialization.

Depth-encoded en-face maximum intensity projection of blood flow perfusion around wound around and their corresponding structure cross-section images during epitheliazation phase. Red color indicates deeper and blue color indicates more shallow vessels and green color is in between. Initial wound diameter on Week-1 is around 1mm.

7.3.3.2 Wound contraction

Wound contraction is defined as the movement of wound edges towards the center to close it. During wound contraction, fibrous tissue starts to form inside the wound and pulls the boundaries of the injury together [Singer-1999]. The closure of the wound protects underlying tissues and prepares for maturation phase. In cutaneous wound healing, signs of wound contraction are changes in color, itchiness and obvious reduction in wound size. If the wound shape is circular, healing process seem irregular because the skin is pulled together irregularly due to contraction. In most cases, contraction occurs asymmetrically around an axis of contraction that allows better alignment of cells with collagen [Eichler-2006]. Myofibroblasts which contain the same kind of actin found in smooth muscle cells are responsible for wound contraction. Although contraction starts without myofibroblast involvement at first, myofibroblasts are differentiated from growth factor stimulated fibroblasts. Then, myofibroblasts are attracted by fibronectin and growth factors in the ECM to reach and attach to the wound

edges and collagen by desmosomes that allows them to pull the ECM when they contract [Mirastschijski-2004]. As provisional matrix breaks down, hyaluronic acid decreases while chondroitin sulfate increases and gradually trigger fibroblasts to stop proliferating. These events signal the end of contraction stage and beginning of maturation phase [Hinz-2006]. In hospital settings, the wound is kept clean and dry during this phase of healing to prevent severe injuries such as infection, contracture and a failure to fully close. Contraction is considered a good sign that indicates wound healing is moving towards maturation and the patients will be sent home soon.

Figure 7-7 shows wound contraction during healing after biopsy punch. It can be observed that contraction around the third week is pulling the edges at an irregular shape and wound size is reduced by the fourth week due to wound contraction and angiogenesis. As the healing process enters the maturation phase, contraction decreases and blood vessels within ECM separate and become more distinct.

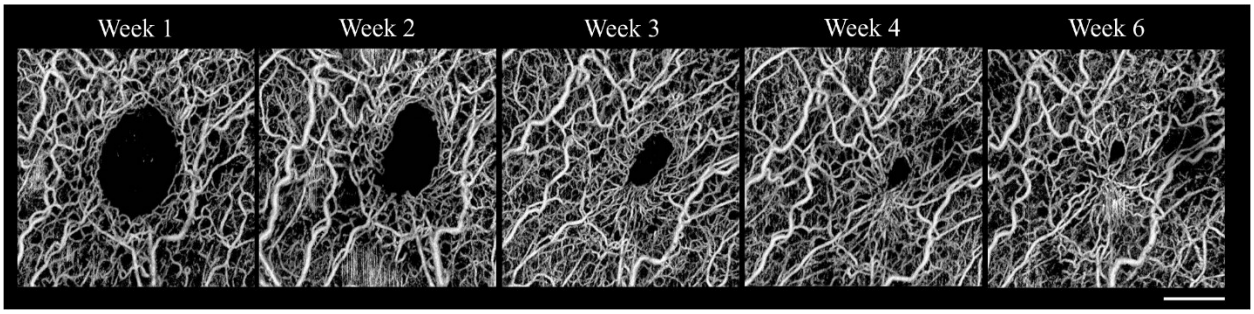

Figure 7-7 Wound contraction.
Scale bar = 500 μm.

7.3.4 Maturation and remodeling after wound closure

Maturation phase of wound healing begins when the levels of collagen production and degradation have equalized[1]. During maturation, disorganized collagen fibers are rearranged and

aligned along tension lines and type III collagen is replaced by type-I collagen [Vanderwee-2007]. Depending on the wound type, maturation phase can last for a year or more, leading to a permanent scar left behind. Since activity of the wound site is reduced and the blood vessels that are no longer needed are removed by apoptosis, the scar redness is reduced and the tensile strength of the wound gradually increases [Greenhalgh-1998]. Figure 7-8 shows the maturation process and remodeling in the wound model. Although by the 36th day the wound site has fully closed, maturation and remodeling continues for a long time and might take several months.

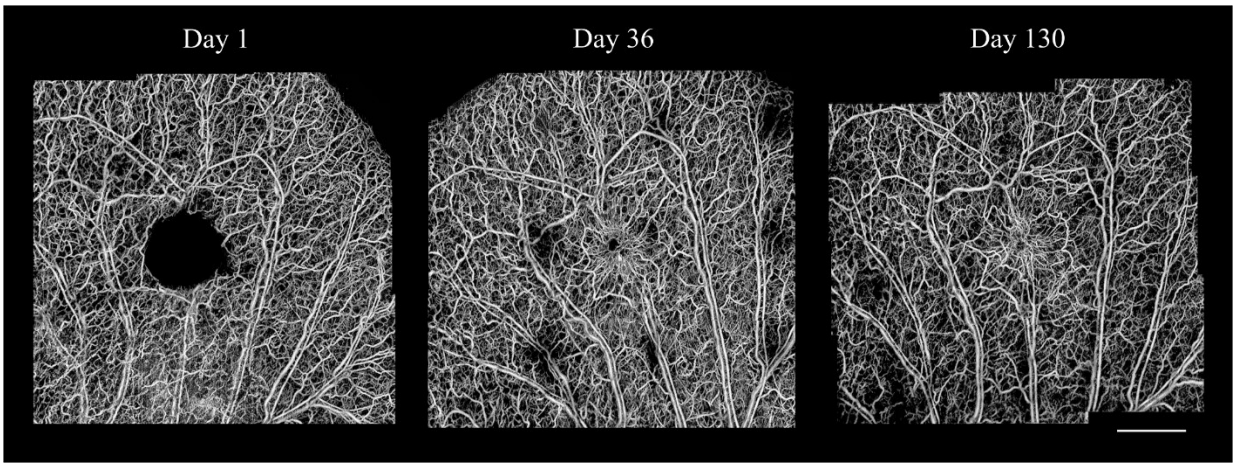

Figure 7-8 Maturation and remodeling.
Scale bar = 1mm.

7.4 Discussions

Although wound healing models in rodents are very attractive because of their availability, ease of handling and low cost, they are criticized for not mimicking the healing mechanism in human wounds. In humans, the major mechanisms of wound closure are re-epithelialization and granulation tissue formation while in rodents is contraction. In order to minimize wound contraction, accurate wound splitting can be performed [Galiano-2004]. Due to the differences

between human and rodent skin, pig skin can be a better model of wound healing because of its similarity to the human [Sullivan-2001]. Both human and pig skin have a thick epidermis (~50-100 μm) [Meyer-1978], show well-developed rete-ridges and dermal papillary bodies and abundant subdermal adipose tissue [Morris-1990, Montagna-1966, Marcarian-1966], similar elasticity [Forbes-1969], similar dermis microvasculature pattern [Rothenberger-2013, Schwarz-2013, Mortite-1947] and sparse body hair that unlike many animals, professes through the hair cycle independently of neighboring follicles [Winter-1966].

Although we have shown qualitative assessment of out wound healing model, multiple parameters can be quantified such as diameter of the blood vessels, lymphatic vessels and the connection of microcirculatory system. However, accurate estimation of angiogram diameter requires similar experimental conditions. Since we monitor and image our model for ~8 weeks or more, in every experiment, we have to make sure that the placement is identical from one experiment session to another. For instance, the objective lens that we utilized is considered a high numerical aperture (10X) and therefore depth of focus (DOF) is limited to a few hundred microns in the tissue. In order to keep the experimental placements similar, we have to make sure that each imaging is performed from the exact depth of focus in the ear while the ear tissue is very flexible and such claim can never be true. The ear tissue is not entirely flat and its thickness and shape varies from location to location. In order to quantify the exact diameter of the blood/lymphatic vessels, one has to make sure to take all of these limitations into account. If the ear tissue is placed ~100 μm above or below the previous location of its placement in the previous experiment, the quantified vessel diameter encodes an error and this error may not be consistent from time to time. Unless consistent and repeatable variations happen, no one can

hypothesize and relate any conclusions based on the estimated parameters on OMAG images in the wound healing model.

Another limiting factor of quantification of blood vessels is the signal ambiguity below the blood vessels because of multiple and forward scattering of photons by red blood cells. In that case, a shadow is cast below the blood vessels and angiograms appear as blood vessels with a long tail. The shadow and tail artifact can cause confusion and error when quantifying blood vessels and therefore a shadow-correction should be utilized [Girard-2011]. Also, attenuation coefficient in the ear tissue can change in between the healing phases and tissue swelling and inflammation changes the optical properties of the tissue. Accurate quantification of healing process requires an estimate of the variations based on tissue properties and a correction factor should be applied [Vermeer-2014].

Wound size can be quantified to compare the healing process in different samples. However, our wound model is not supported by muscle substrates below them and therefore wound contraction can cause error in the quantification of healing process. Also, the closure itself cannot be a very good way to relate to the healing process because as we have shown in the paper, maturation phase can take a very long time and better healing is followed by better vascularization and angiogenesis, as well as the quality of the neovascularization within the granulation tissue.

OCT modality is based on scanning laser and cannot be considered as a true real-time imaging modality. If a phenomena is of interest to be monitored/quantified, other modalities such as laser speckle imaging (LSI) can be utilized to monitor wound healing in the whole ear tissue [Rege-2012]. The trade-off is that LSI cannot reveal depth information and structural cross-section and

the resolution of LSI is above the size of single capillary. While OCT is almost-real time, it provides depth-resolved and capillary-resolution information and therefore a combination of OCT and LSI can be a powerful tool to assess wound healing in tissue samples [Reif-2012_cochlear].

Recently, OCT imaging has been utilized to demonstrate the capability of this technology to characterize and monitor cutaneous wound-healing phases in human leg ulcers [Kuck-2014] and volunteers [Greaves-2013]. The results were in agreement with histological staining of the same tissue structure and therefore, OCT structural and microcirculatory information can be utilized as a non-invasive tool to assess and monitor wound healing in animal models and human.

7.5 Quantification of vessel diameters during healing

Microvessels can be segmented and their diameter be estimated using the method explained in chapter6. One of the major challenges of long-term studies such as the ones we demonstrated in this chapter is repeatability and maintaining similar quality between different imaging time-points. Also, since our objective lens is a high numerical aperture and the depth of focus is relatively small, slight displacement of the sample under the beam (~100 μm) can alter the appearance and shape of the microvessels in the tissue. Therefore, these factors have to be taken into account when quantification is required. If the physiological changes are very obvious and repeatable along the time, we can observe and quantify them. For instance, we have segmented and quantified the vessel diameter in Figure 7-2 and Figure 7-3. Figure 7-9 shows the distance transform after segmentation during wound healing where the collateral vessels have enlarged during the time to support the downstream and damaged tissue.

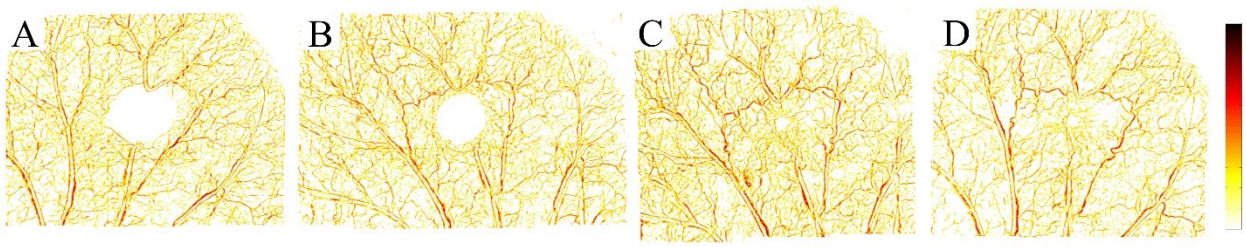

Figure 7-9 Quantification of vessel diameters during wound healing.
Distance transform of the segmented vessels during the healing process on the injury day (A), week 1 (B), week 4 (C) and week 7 (D).

Other parameters such as the diameter of newly formed vessels in the wound area as well collateral vessels can be quantified as already explained in chapter 6. A more systematic analysis of vasculature map can be developed in the future to reconstruct a 3D model based on segmented microvessels. Then, multiple parameters of the vessels such as their diameter, tortuosity and connective network can be analyzed. However, such development requires more effort in the field and is out of the discussion of our thesis.

7.6 Conclusions

Cutaneous wound healing consists of several overlapping phases including hemostasis, inflammation, tissue formation and tissue remodeling. In this chapter, we utilized OCT/OMAG to non-invasively monitor wound healing dynamic process in mouse ear pinna model *in vivo*. The high-resolution OMAG allows tracking microvascular details up to capillary level. Our results are in agreement with expected behavior of tissue during wound healing stages and we can conclude that OCT/OMAG proves to be a practical tool for tracking wound healing in mouse model. In the future, we would like to generalize our results to human studies to design treatment strategies for burns, chronic skin ulcers and diabetes mellitus.

Chapter 8. TRANSLATIONAL APPLICATION 2- STUDYING COMPLICATIONS ASSOCIATED WITH INJECTION OF COSMETIC FACELIFT FILLERS

8.1 Introduction

Skin wrinkles are an indicator of age and for centuries entrepreneurs have been trying to come up with methods to remove or minimize imperfections of their skin by nutrition, facial massage, topical serum solutions and masks. People with more public appearance and visibility were always the pioneers in seeking solutions for their skin wrinkles. In the past century, mainly due to expansion of multimedia network and a change of trend in the culture, most people have been concerned about their look and always wanted to look like actors/models in TV or magazines.

Since the FDA clearance of bovine collagen in 1981, injectable dermal fillers have become an increasingly popular procedures of the cosmetic surgery practice to remove skin wrinkles. A variety of permanent, semi-permanent and dissolvable dermal fillers have been introduced to modify the appearance of soft tissue rhytids and contour deformities. Based on the American Society of Plastic Surgery report in 2012, nearly 2 million cosmetic filler injections were performed in the United States, with the majority of these injections (1.4 million) being hyaluronic acid (HA) gel fillers.

HA is a hydrophobic polysaccharide that naturally exists in the extracellular matrix of all animal tissues and consists of regularly repeating units of B-acetyl-D-glucosamine and D-glucuronic acid [Bowman-2005]. The major differences between currently available HA fillers include their concentration in each syringe, crosslinking agent, degree of modification, source of HA, amount

of free unmodified HA present, and whether the product is monophasic (cohesive gel) or biphasic (particulate) [Allemann-2008]. Products with a higher concentration of crosslinked HA or larger particle sizes are typically utilized for deeper injection in the dermis and subcutaneous tissues to correct deep folds and last longer in the tissue compared to products with lower concentration of crosslinked HA or smaller particle sizes [Shiffman-2013].

With increased use of injectable fillers, growing reports of filler-induced complications have been reported all around the world. Some complications appear immediately after injections (0-2 days) that include under/overcorrection, implant visibility or Tyndall effect, sensitivity to the injected material, and ischemia with or without necrosis. Other complications such as infection, tissue discoloration, inflammation, nodularity, and angioedema may occur in the early post-procedure period (3-14 days). Also long term complications (>14 days) such as persistent erythema, telangiectasia, migration, scarring, and granuloma formation have also been reported formation [Hachach-Haram-2013, Sclafani-2009, Bachmann-2009, Cohen-2008]. Some of these complications are minor and transient, while others may lead to long-term detrimental outcomes.

Although safety studies of dermal fillers have reported that complications from the dermal injections are very rare, different definitions of complication make the assumptions fall apart [Grunebaum-2009]. The rate of any complication from a filler injection including pain and redness has been reported to occur in up to 5% of patients [McCracken-2006]. More relevant to patients and clinicians is the frequency of severe complications such as infection, granuloma formation, ischemia, and necrosis. The incidence of these severe adverse events is somewhere in the range of 0.04% to 0.001% [Daines-2013, Friedman-2002, Hanke-1991, Narins-2006]. Although the chance of such complications is very small, they can be devastating in people who are extremely concerned about their look at first place.

The most devastating complication stemming from cosmetic filler injections is ischemia with subsequent soft tissue necrosis. Filler-induced tissue ischemia has been reported to occur with all types of fillers and in all areas of the face, although it is most commonly seen following glabellar injections [Narins-2006, Salles-2008, Schanz-2002, Gladstone-2007]. Glabellar necrosis usually happens because the vascular supply to this region is derived from a limited number of larger vessels in the supratrochlear and supraorbital arcades, with less collateral circulation than is present in other areas of the face [Bachmann-2009, Hanke-1991, Schanz-2002, Gladstone-2007, Cox-2011, Glaich-2006]. Although delayed presentations have been reported, ischemia is typically accompanied with immediate blanching of the tissues adjacent to the site of injection [Grunebaum-2009, Glaich-2006, Hirsch-2007]. However, ischemic tissue is not always associated with any pain. Over the subsequent 2-3 days, the skin begins to appear dusky or black. Once this occurs, there is little chance of tissue survival. Ultimately, a necrotic ulcer develops and is often crusted by a black eschar of dead skin [Glaich-2006].

There are multiple hypothesis about causes of post-injection tissue necrosis, but the exact mechanism for tissue death is not fully understood. Current theories include arterial or venous compression or obstruction, trauma to the vessel wall, and intravascular (intra-arterial) injection with embolization of the filler material into the capillary bed where oxygen exchange normally occurs [Bailey-2011, Kim-2011_filler, Kim_DW-2011, Lazzeri-2012, Silva-2004, Kassir-2011]. Most clinicians believe that a combination of factors is likely at play leading to ischemia. Proponents of the vascular compression theory state that a large volume of filler injected into a tight space, scar, or area of intradermal bleeding or edema may result in occlusion of the vasculature and subsequent ischemia [Kassir-2011, Narins-2006]. This theory, as well as the direct vessel trauma theory, may clarify why the necrosis is seen in some cases of glabellar

necrosis (lack of collateral blood flow) or in patients who have undergone previous surgery and have an altered blood supply. However, it is not clear why necrosis can also occur in other areas of the face endowed with rich collateral perfusion [Kleydman-2012]. Blood vessels in the face and periocular region are frequently cauterized, ligated, or damaged during surgery or from trauma, but ischemia and necrosis rarely ensue. An *in vivo* model of filler induced tissue ischemia and necrosis is necessary to better understand what is occurring at the microvascular level.

Clinical observations support the theory that intra-arterial injection and embolization of filler material is the mechanism by which ischemia and necrosis occur. Multiple reports of vision loss and ophthalmoplegia from facial filler injections have been published [Kim-2011_filler, Lazzeri-2012, Silva-2004, Kwon-2012]. The proposed mechanism for these ophthalmic problems is that, following inadvertent intravascular injection, filler particles travel in retrograde fashion from peripheral arterial anastomoses to the central retinal artery and short and long posterior retinal arteries. Once in these vessels, the filler material obstructs the normal blood flow to the ocular tissues and unfortunately vision recovery is rare. Conversely, vascular occlusion by direct compression or vascular injury would not cause ischemia of the deeper orbital blood vessels and the subsequent vision loss.

There is also experimental evidence demonstrated by histopathology that intra-arterial injection and embolization of filler material result in tissue ischemia and necrosis. Kim et al. [Kim_DW-2011] injected HA gel into the anterior branch of the posterior auricular artery in rabbits to induce tissue necrosis. Interestingly, the researchers could not provoke necrosis unless they cauterized the adjacent posterior branch of the posterior auricular artery, which provides collateral blood supply. They also failed to induce necrosis with injection of the filler material

directly into the soft tissues of the rabbit ears or with injection into the veins. In a case report by Inoue and colleagues [Inoue-2008], a histopathologic specimen of a necrotic area of alar and nasolabial skin obtained from a 50-year-old woman who had injections of filler into her nasal tip and nasolabial fold showed particles of filler material trapped within arterioles. Similarly, Hanke and colleagues showed intravascular collagen particles in patients with post-injection facial ischemia [Hanke-1991].

In this chapter, we utilized OCT and OMAG technologies in the mouse ear pinna model to study the mechanisms of filler-induced tissue necrosis at the capillary level. Two experiments were designed to test mechanisms proposed for tissue necrosis post filler injection. In the first experiment, we directly injected the filler into the soft tissue. This experiment was designed to test the hypothesis whether filler can compress the tissue and hence damage the microvasculature supply. In the second experiment, we directly injected the filler into an artery and observed the changes in the downstream microvasculature.

8.2 Materials and methods

We chose to use mice as our experimental model because the mouse pinna is thin enough to allow gross visualization of the vasculature and also thin enough for optical imaging. Non-invasive *in vivo* images were acquired from pinna of healthy 8-week old male hairless mice (Cr:SKH1 Hrhr) weighing approximately 28g. During experiments, the mouse was anesthetized using 2% isoflurane (0.2 L/min O2, 0.8 L/min air), and the animal temperature was monitored and maintained with a heating blanket (Harvard Apparatus, Holliston, MA). Baseline OMAG images were obtained for each mouse ear. Experiments were performed to test various theories of filler-induced tissue ischemia. Each ear was then reimaged with the OMAG technology for

comparison with the baseline. The experimental protocol was in compliance with the federal guidelines for care and handling of small rodents and approved by the Institution Animal Care and Use Committee (IACUC) of the University of Washington, Seattle, WA.

8.2.1 Experiment 1 – Soft tissue filler injection

One hypothesis for the mechanism by which dermal filler injections cause tissue ischemia and necrosis is the vascular compression theory. Kassir and colleagues [Kassir-2011] described a 52-year-old man who developed necrosis of his right cheek after injection of HA gel (Perlane®) into an atrophic acne scar. They discussed how this necrosis was caused by vascular compression from the injection of large volumes of filler material into the tight tissues adjacent to the scar. Other authors have postulated that intradermal bleeding or local tissue edema related to injection trauma may compromise the blood flow to the tissues, subsequently causing venous congestion and necrosis [Sclafani-2009, Daines-2013, Narins-2006]. While the vascular compression theory may play a prominent role in areas of the face with decreased collateral circulation or abnormal perfusion due to scarring, an alternate mechanism must account for filler-induced ischemia in normal areas of the face.

Direct subcutaneous injection of filler material was performed to attempt compressive vascular occlusion. A large bolus of undiluted HA gel filler directly injected adjacent to a major vascular bundle. The endpoint of injection was reached when tissue distension pressure caused filler material to extrude through the injection site. OCT/OMAG imaging was performed immediately post-injection and one week later to determine the effect on the pinna microvasculature. Figure 8-1 (A) shows an injection sample into the soft tissue. Since filler is transparent, it appears as dark regions inside the tissue after injection Figure 8-1 (B). After injection, filler

pushes the tissue boundaries and holds a firm substrate in between tissue structure (Figure 8-1 (C)). For this experiment, the dorsal section of the ear was imaged.

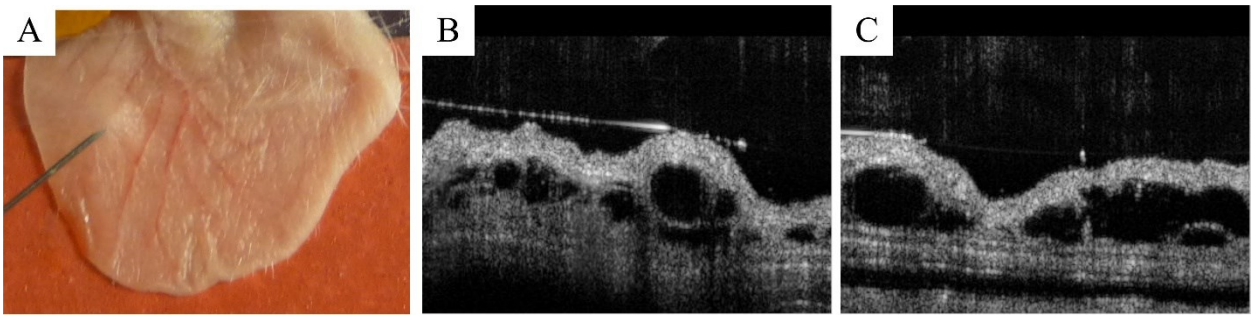

Figure 8-1 Soft tissue filler injection.

(A) A bolus of filler injected into the tissue. (B) OCT cross-section image of filler inside the tissue. (C) Another OCT cross section of filler inside the tissue.

8.2.2 Experiment 2 – Intra-arterial filler injection

In our mouse model, we were not able to demonstrate any arterial occlusion with direct injection of the filler material into the pinna tissues, no matter the amount or location of the filler injected. Transient venous occlusion was noted, including one inadvertent injection into a venule, but this did not result in any significant downstream or peripheral vascular occlusion, and decrease in oxygenation, ischemia, or necrosis. Note that even with definitive arteriole and venous occlusion using suture ligation, no ischemic sequelae were noted because the ear tissue is very-well vascularized and contains numerous anastomosis and pre-existing collateral vessels.

In order to observe the behavior of the filler material in the arteries and larger vessels, we designed an experiment to directly inject the filler material inside an artery. Since, the size of arteries in the mouse ear does not exceed 80 μm and filler injection using a 32G needle or larger was not feasible. Therefore, we reached the ear pinna's upstream vessels that feed from external carotid artery and directed the filler into a branch of external carotid artery (Figure 8-2 (A)). In

order to verify that the branch of external carotid artery supplies the ear vasculature, Evans Blue dye was injected first and we observed that ear immediately turned blue (Figure 8-2 (C)). Since we could not move the mice after the surgery due to post-injection complications, we imaged the ventral section of the mouse ear pinna. In this case, the typical vasculature pattern observed on the ear was slightly different from the dorsal view. However, we were able to image the microvessels before and after the injections.

Figure 8-2 Intravascular injection into external carotid artery.
(A) External carotid artery branch isolated with suture. (B) Mouse ear pinna tissue. (C) Ear tissue after injecting Evans Blue dye into the external carotid artery.

It was then determined that 34-gauge needles (outer diameter 135 μm, inner diameter 50 μm) were suitable for these injections because larger needles caused exsanguination upon withdrawal from the external carotid artery. Undiluted filler material could not smoothly transit through such a small caliber needle, so serial dilutions of HA gel fillers were performed with sterile water to determine the maximum viscosity to effectively transit through a 34-gauge needle. After injection, OCT/OMAG were performed. Based on observations of hemiparesis post injection, we suspect that some of the filler particles accessed the intracranial circulation and caused cerebral vascular compromise. Due to severity of the surgery and possible stroke and damage to the brain

tissue, the mice were euthanized after the intra-arterial injection experiments, so no follow up imaging was obtained.

We performed a series of experiments on mice using different types of HA-based fillers. For each filler type, intra-arterial and soft tissue injections were performed to monitor the behavior of the microvessels around the injection site. For soft tissue injections, follow up imaging was performed to study the long term effect of HA-based fillers in the tissue. Table 8-1 summarizes the fillers we utilized in this chapter and their physical and mechanical properties. Note that the measurements for Belotero® were recorded at a different frequency. These measurements were directly taken from literature references not by us [Sundaram-2010, Santoro-2011].

Table 8-1 Summary of filler properties.

	HA concentration (mg/mL)	Particle size (μm)	Degree of cross-linking (%)	Elasticity (Pa) (Frequency)	Viscosity (cPa) (Frequency)
Restylane®	20	300	1.2	513 (0.7 Hz)	119,180 (0.7 Hz)
Perlane®	20	650	1.4	541 (0.7 Hz)	124,950 (0.7 Hz)
Juvederm®	24	50-500	2	75 (0.7 Hz)	17,699 (0.7 Hz)
Belotero®	20-25	Variable	12	44 (0.1 Hz)	532 (0.1 Hz)
Juvederm	24	Viscous gel	Higher	274	62,902

Voluma®			degree	(0.7 Hz)	(0.7 Hz)
Radiesse®	NA	25-45	NA	1,407 (0.7 Hz)	349,830 (0.7 Hz)

8.3 Experimental results and discussions

8.3.1 Restylane® and Perlane®

Restylane® and Perlane® are HA gels generated by Streptococcus species of bacteria, chemically crosslinked (1.2%) with butanediol diglycidyl ether (BDDE), stabilized and suspended in phosphate buffered saline at $pH = 7$ and concentration of 20 mg/mL. They are a transparent, viscous, and sterile gel that are supplied in a sterile disposable glass syringe equipped with a plunger stopper, finger grip and plunger rod, co-packed in a blister together with sterile 29G or 30G needles. The average particle size for Restylane® and Perlane® are 300 μm and 600 μm, respectively. The products are approved in fill sizes containing 0.4, 0.7, 1 or 2 mL of gel [FDA_Restylane]. The Restylane® family is specifically formulated to act like body's own HA, adding volume and fullness to the skin. It was first launched by Q-Med in 1996 and estimated that over 15 million treatments have been carried out worldwide (as of 2013). Based on the company's description, common side effects such as swelling, redness, pain, bruising and tenderness at the injection site can be observed. Compared to the Restylane®, the average size of the particles are larger in Perlane® and injection can be performed into deeper layers of skin to enhance more severe facial wrinkles.

Direct subcutaneous injection of nondiluted Perlane® filler was performed to attempt compressive vascular occlusion. A 32-gauge needle was utilized to inject a large bolus of undiluted HA gel filler (Perlane®) directly adjacent to a major vascular bundle. Figure 8-3 shows

the microvasculature response of the ear tissue to injection of Perlane® filler into the soft tissue. It can be observed that after injection, some artifacts were observed near the injection area due to changes of the optical properties of the tissue (Figure 8-3 (B)). Within one week after injection, a follow up imaging session was performed (Figure 8-3 (C)) where microvasculature map was very similar to the baseline image (Figure 8-3 (A)). Based on our observations, no obvious tissue necrosis or redness was observed after the injection.

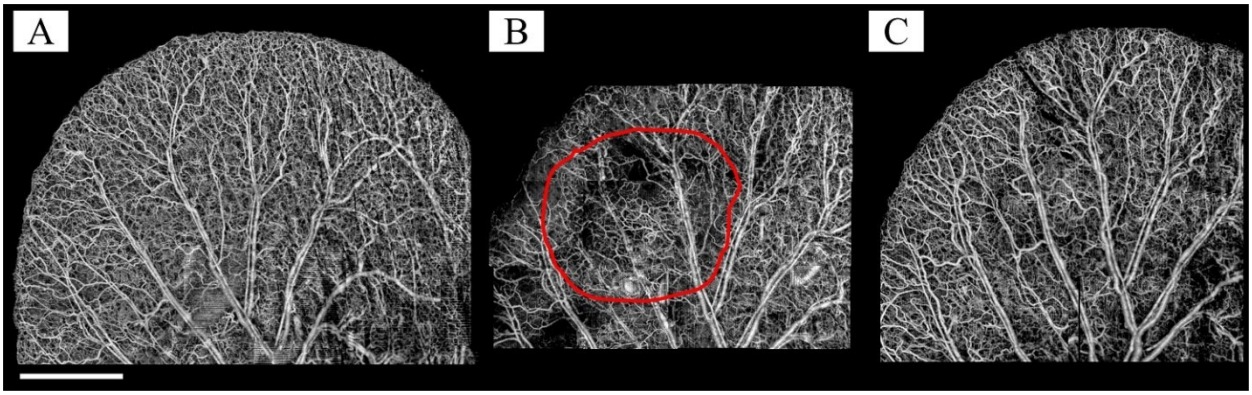

Figure 8-3 Injection of Perlane® into the soft tissue.

(A) Baseline maximum intensity projection map of the microvasculature in the mouse ear model. (B) Vasculature map post-injection. The red line indicates an approximate location of filler bolus (C) One-week follow up imaging after filler injection. Scale bar = 1 mm.

Also, localized cross-section images from two injection sites are shown in Figure 8-4. It can be observed that the filler stays in between the tissue layers and slightly pushes the skin upwards. In this case, vascular compression and tissue necrosis was not observed and we could not locate any damage to the microvessels because of the filler injection.

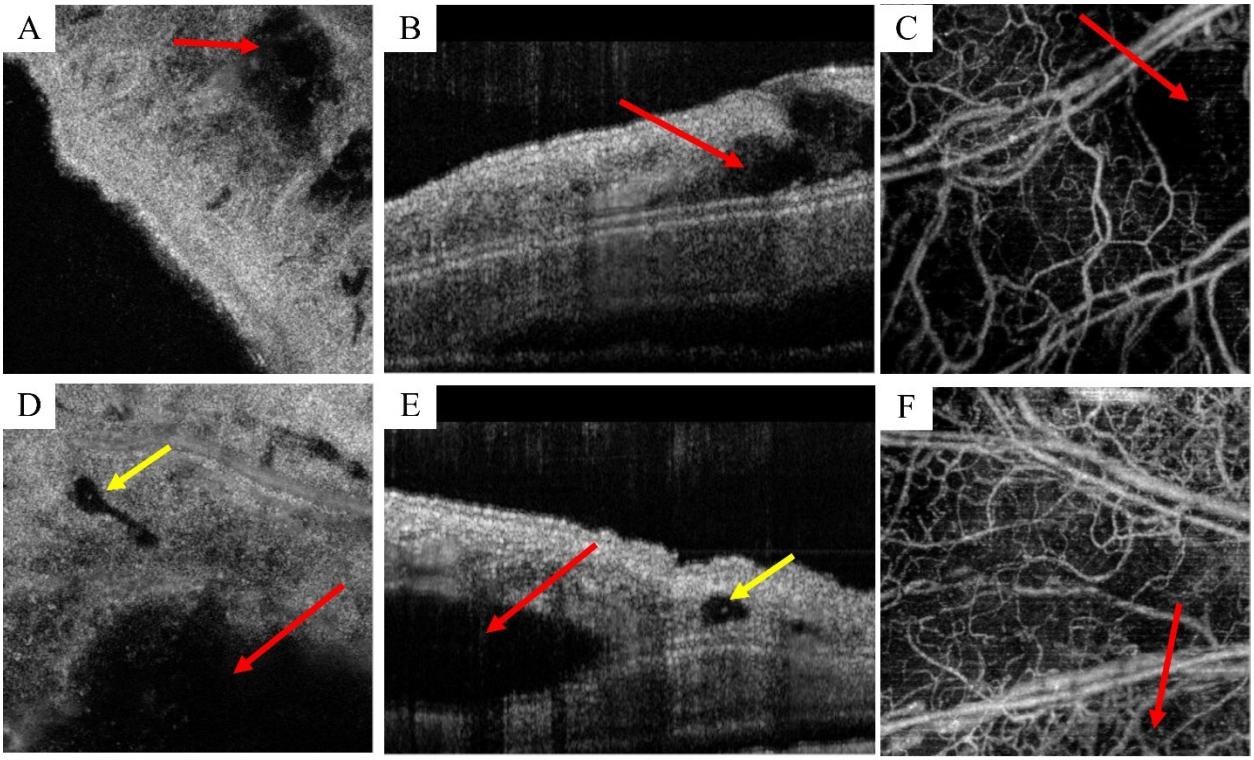

Figure 8-4 Cross-sectional images from filler injected areas.

The red arrows indicate location of filler. The yellow arrows indicate enlarged lymphatic vessels. (A) Top view of structure cross-section (X-Y). (B) Structure cross-section corresponding to (A) at (X-Z) axis. (C) Corresponding maximum intensity projection maps of the microvessels in that area. (D, E and F) similar to the top row, images acquired from a different location on the ear showing depth-map structure cross-section, X-Z cross section and maximum intensity projection map of microvasculature, respectively.

For better visualization of injection and follow-up sessions, we digitally segmented the filler inside the tissue and color-coded the filler area by green and visualized that along the orange color-coded microvessels in Figure 8-5. It can be observed that the filler is well-localized after one week and no damage/change to the microcirculation could be observed at this stage.

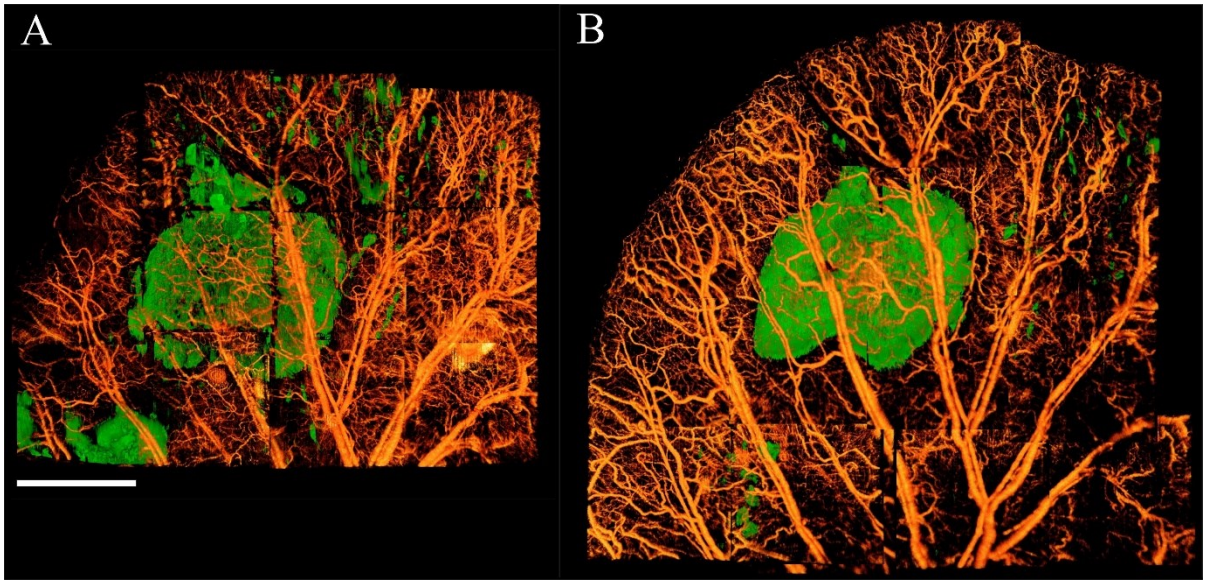

Figure 8-5 The location of injected fillers and microvessels.

Fillers are color coded with green (they are transparent in OCT cross-section images) and vessels are coded with orange color. (A) Immediate after injection. (B) 1-week follow-up image. Scale bar = 1 mm.

Despite multiple injections of Perlane® filler in different locations in the mouse pinna, no significant vascular occlusion was observed in any specimen when imaged with OCT/OMAG. In some specimens, areas of decreased perfusion adjacent to the filler bolus were detected immediately post injection. However, no significant peripheral vascular dropout or ischemia was ever noted. We suspect that some of the areas with apparent vascular dropout are artifacts from tissue thickening and displacement of the vasculature outside of the range of the focus for the imaging techniques. In one pinna specimen, inadvertent intravenous injection of filler was noted (Figure 8-6). Even with this venous occlusion, the peripheral vascular bed did not appear to be compromised due to collateral support. Importantly, the mice that underwent soft tissue injection showed no external signs of ischemia and necrosis at up to one week after the intervention.

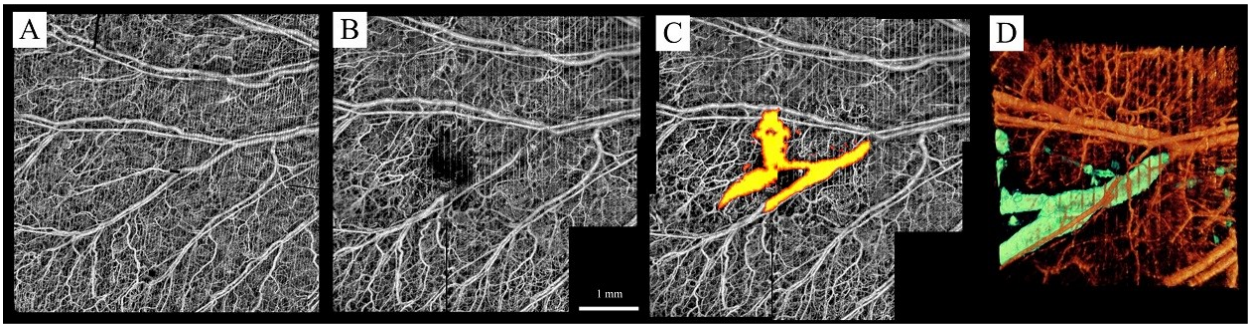

Figure 8-6 Perlane® major vein blockage.

(A) Baseline microvasculature MIP. (B) Post-injection microvasculature MIP. (C) Low-intensity areas segmented on the structure map and overlaid on the microvasculature MIP, clearly showing the trace of the blocked vein. (D) A close view of the occluded vein area visualized via volume rendering the microvessels (red) and segmented filler locations (green).

In another ear pinna sample, 20 µL of Restylane® filler was directly injected into the soft tissue with 30G needle. Due to changes in optical properties of the tissue after the injection, microvasculature looked like they might have been blocked (Figure 8-7 (B)). However, the follow up studies (Figure 8-7 (C)) indicated that the microvasculature pattern was very similar to the baseline image (Figure 8-7 (A)) and therefore external compression hypothesis for Restylane® was not happening.

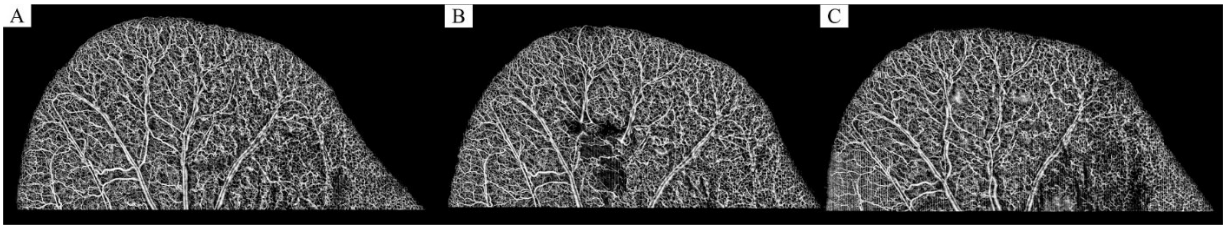

Figure 8-7 Soft tissue Restylane® injection.

(A) Baseline. (B) Immediate after injection. (C) One week follow up.

OCT structure and angiography cross-sections also confirms that the filler only pushes the microvessels and does not cause any compression damage. Figure 8-8 (A,B) show OCT cross-

sections overlaid with microvessels same day of injection. Figure 8-8 (C) shows their corresponding depth-encoded microvasculature map. It can be observed that microvessels partially seem damaged, however, most of the vessels are detected at superficial layers. Since the optical properties of tissue have changed and the amount of filler in the tissue is already pushing the surface, OCT angiograms on the injection day were not enough evidence to judge whether any damage has been done or not. A follow-up imaging session after one week was performed and results are given in Figure 8-8. It can be observed from the structure cross-sections overlaid with micro-vessels that the HA filler has stayed inside the tissue while the microvessels that we thought to have been damaged are very visible in Figure 8-8 (F). At this stage, both superficial and deeper vessels could be identified. Since the pattern of the vessels looks very similar to the baseline images, we don't think that soft tissue injection of Restylane® might have damaged any microvessels.

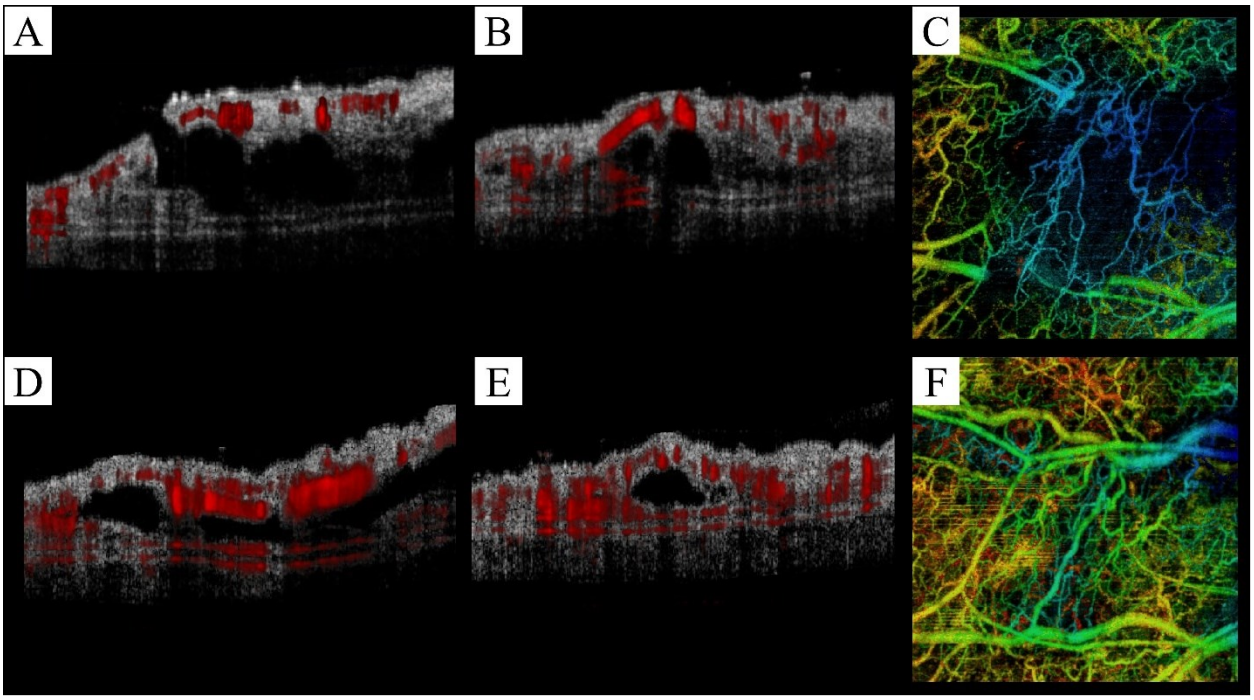

Figure 8-8 Restylane® soft tissue injection.

(A, B) Structure cross-sections overlaid with surrounding microvessels after soft-tissue Restylane® injection. (C) Depth-encoded microvessels corresponding to the cross-sections. (D, E) Structure cross-sections overlaid with surrounding microvessels one week follow up. (F) Depth-encoded microvessels corresponding to the cross-sections.

In another experiment, a 30 μL diluted (12.5%) Restylane® HA gel was directly injected into the external carotid artery and significant peripheral nonperfusion of the mouse pinna was observed with OCT/OMAG (Figure 8-9). There was substantial dropout of large sections of the microvasculature, particularly at the capillary level where oxygen exchange occurs. In a side-by-side comparison of sections before and after intra-arterial injection, these changes become very apparent (Figure 8-9). These results confirmed that Restylane® could potentially block larger arteries/veins if directly injected into the vessels.

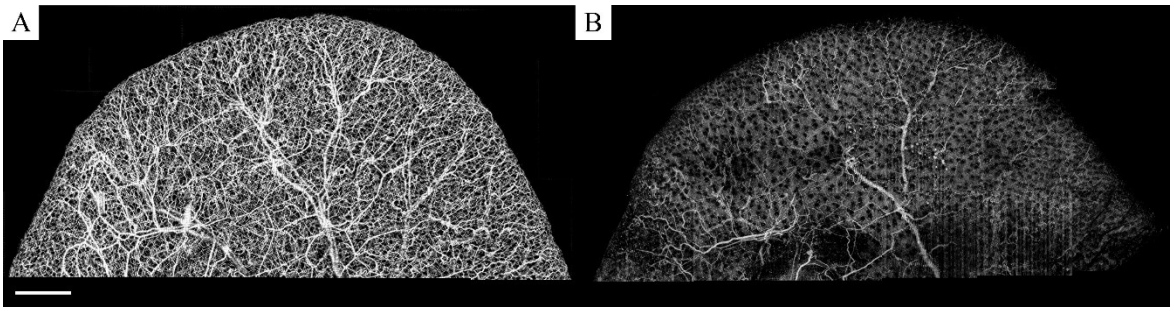

Figure 8-9 Intravascular occlusion after Restylane® injection.

(A) Baseline microvasculature MIP. (B) After intra-arterial injection of Restylane® into the external carotid artery.

Note that particle size in Restylane® is relatively smaller than Perlane®. Therefore, if Restylane® filler can significantly block the arteries, intra-arterial injection of Perlane® would definitely cause more arterial blockage in our model.

8.3.2 Juvéderm ®

Juvéderm is distributed under three labels in the U.S. market: Juvéderm Ultra, Juvéderm Ultra Plus and Juvéderm Voluma of which Juvéderm Ultra is the softest and Juvéderm Voluma has the best lift and is the longest lasting. Juvéderm Voluma is utilized for lifting the cheeks and improving the contours of the face, whereas Juvéderm Ultra and Ultra Plus are better for nasolabial folds (smile lines) and other wrinkles such as marionette lines. Juvéderm Voluma is not recommended for lips, while Juvéderm Ultra and Ultra Plus are popular lip enhancement fillers. Juvéderm Voluma is the first and only HA filer that received FDA-approval for instant volume enhancement to the cheek area.

Juvéderm® is a registered trademark for a family of non-animal hyaluronate gel implants, first introduced by a French company named Corneal in Europe and got their CE marking in the year 2000. In 2004, Corneal and Inamed (distributor in North America) formed a partnership for the clinical development and commercial distribution of Juvéderm® hyaluronate gel implants in Canada, Australia, the United States and Europe under the trade name Hydrafill. In comparison to the crosslinking process of Restylane® family, more BDDE is added to a higher HA concentration (24 mg/mL) and a greater degree of crosslinking (8%) occurs resulting in a gel that has about a 20% thicker viscosity [Allemann-2008]. A typical particle size for Juvéderm® Ultra is around 300 μm [Shiffman-2013].

In the clinical studies for FDA pre-market approval, they compared common side effects such as redness, pain, firmness, swelling, lump, bruising, itching and discoloration with a commercially available skin injection implant (Zyplast®, composed of purified bovine dermal collagen cross linked with glutaraldehyde, dispersed in phosphate buffered saline and 0.3% lidocaine), to show safety and efficacy of their medical device. The results were very comparable and similar to the control study. Their premarket safety report did not include any serious adverse events related to

Juvéderm® treatment, however, one clinically significant event (injection site abscess) was believed to be related to control treatment. Their efficacy report indicated that based on expert reviewer's opinion, they had improved the severity of skin wrinkles compared to the control group [Juvederm_FDA].

We injected 30 μL of Juvéderm® into the soft tissue above the cartilage and observed the microvasculature response same day and one week after the injection. Based on the large image (Figure 8-10), no obvious change was observed in the microvasculature response.

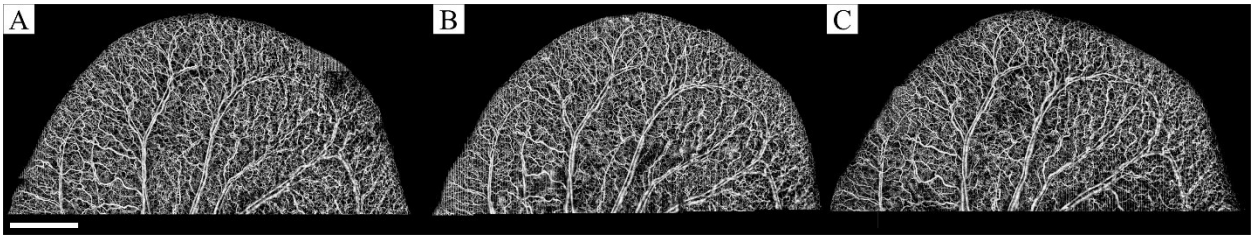

Figure 8-10 Juvéderm® soft tissue injection and microvasculature response.
(A) Baseline vasculature image. (B) Post-injection. (C) One week follow up. Scale bar = 1mm.

OCT structure and microvessel cross-sections after Juvéderm® injections are shown in Figure 8-11. It can be observed that the filler as transparent material in between the tissue structure that pushes the tissue upwards. However, no apparent blockage of microvessels were observed on the day of injection (Figure 8-11 (A,B)) and one week follow up imaging (Figure 8-11 (C,D)). Therefore we concluded that tissue compression and microvasculature blockage did not happen in our model when subcutaneously injecting Juvéderm® directly into the soft tissue.

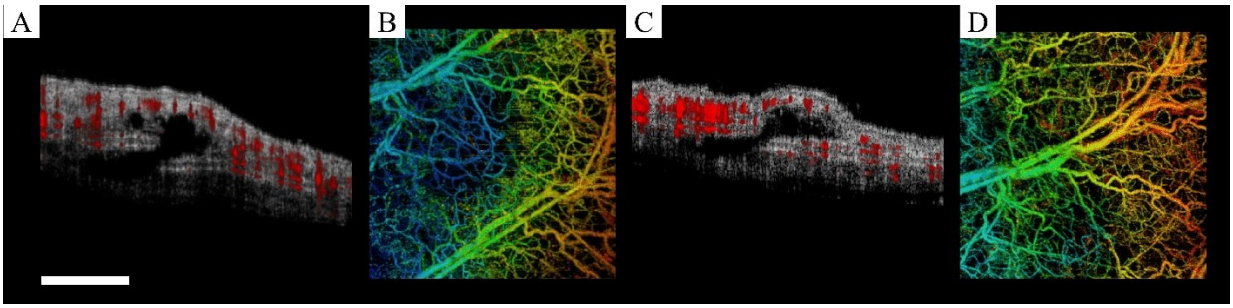

Figure 8-11 Juvederm® soft tissue injection.

(A) Structure cross-section overlaid with microvasculature on the first day post injection and (B) corresponding depth-encoded MIP vessel map. (C) Follow up one week after injection. Structure cross-section overlaid with microvasculature and (D) Depth-encoded microvessels. Scale bar = 500 μm.

In another experiment, a 30 μL diluted (12.5%) Juvéderm® HA gel was directly injected into the external carotid artery and significant peripheral nonperfusion of the mouse pinna was observed with OCT/OMAG (Figure 8-12). Some of the larger vessels remained patent, but there was substantial dropout of large sections of the microvasculature, particularly at the capillary level where oxygen exchange occurs. In a side-by-side comparison of sections before and after intra-arterial injection, these changes become very apparent. The vessels that remained the same were artery-to-artery anastomosis shunts that their primary role is controlling the thermoregulatory conditions. Perhaps their upstream is controlled by other branches of external carotid artery that have not been blocked by Juvéderm® filler. These results confirmed that Juvéderm® could potentially block larger arteries/veins if directly injected into the vessels.

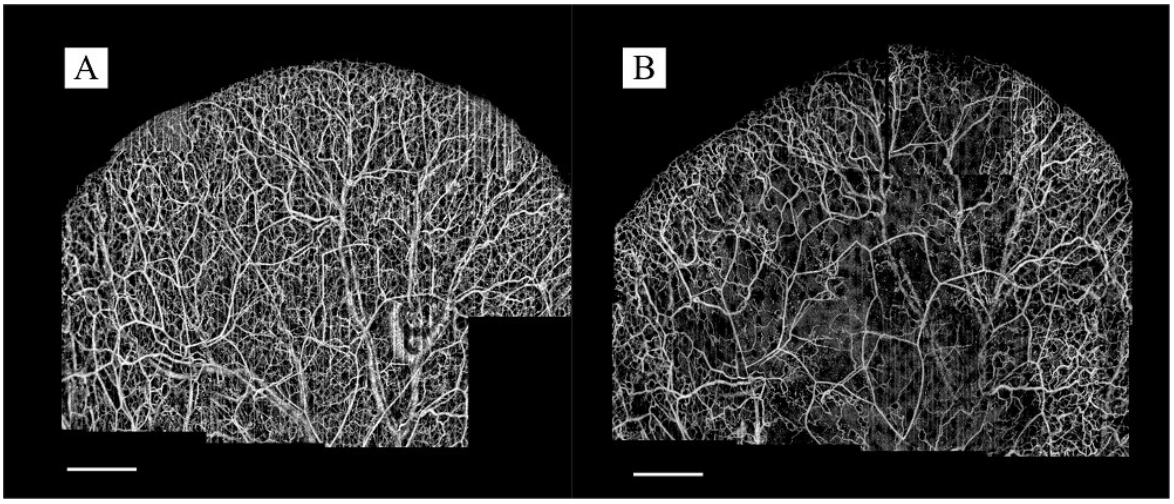

Figure 8-12 Intravascular occlusion after Juvéderm® injection.

(A) Baseline microvasculature MIP. (B) After intra-arterial injection of Juvéderm® into the external carotid artery.

8.3.3 Juvéderm Voluma®

Juvéderm Voluma™ XC which is indicated for deep (subcutaneous and/or supraperiosteal) injection for cheek augmentation is a sterile, biodegradable, non-pyrogenic, viscoelastic, clear, colorless, homogenized gel implant. The gel consists of crosslinked HA produced by *Streptococcus equi* bacteria, formulated to a concentration of 20 mg/mL and 0.3% w/w lidocaine in a physiologic buffer. The HA gel is made primarily of crosslinked HA with some remaining lightly crosslinked and uncrosslinked HA. The 2 mL glass syringe received the CE Mark in December 2009 and the formulation, branded as Juvéderm Voluma™ with lidocaine in foreign markets, is commercially available in multiple countries including the European Union, Australia, Canada, Brazil, Russia, Ukraine, Mexico, Hong Kong, Korea, Taiwan and Singapore [Voluma_FDA]. It was recently announced that Voluma has been approved by the FDA for the US market.

We directly injected ~30 μL of Voluma™ into the mouse ear pinna tissue and observed the changes and dynamics of surrounding microvasculature on the day of injection (Figure 8-13 (B))

and one week after injection (Figure 8-13(C)). Compared to the baseline image (Figure 8-13 (A)), no obvious change in the microvessels could be observed and tissue was back to normal conditions after the injection.

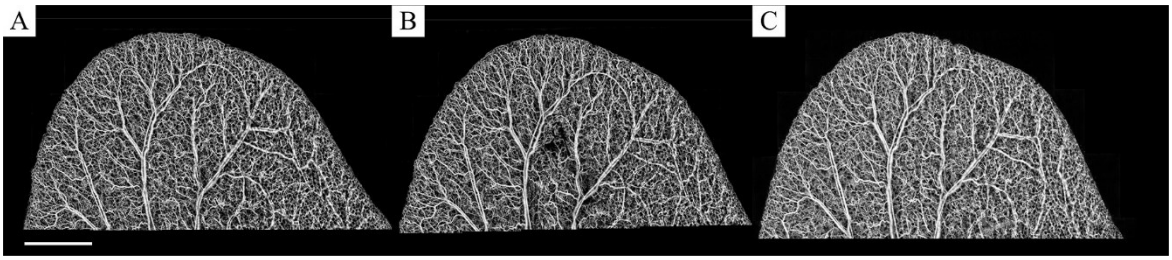

Figure 8-13 Voluma^{TM} soft tissue injection.

Maximum intensity projection maps of microvessels in the injection sample. (A) Baseline image before injection. (B) Same day after injection. (C) One week follow up after injection. Red line = approximate injection site. Scale bar = 1 mm.

Also, from cross-section images overlaid with microvasculature we could not observe any significant blockage of microvessels due external compression caused by Voluma^{TM} fillers. Figure 8-14 shows multiple views of OCT structure cross-sections overlaid with microvessels and the MIP microvessel map after injection and two week follow up in the injection site.

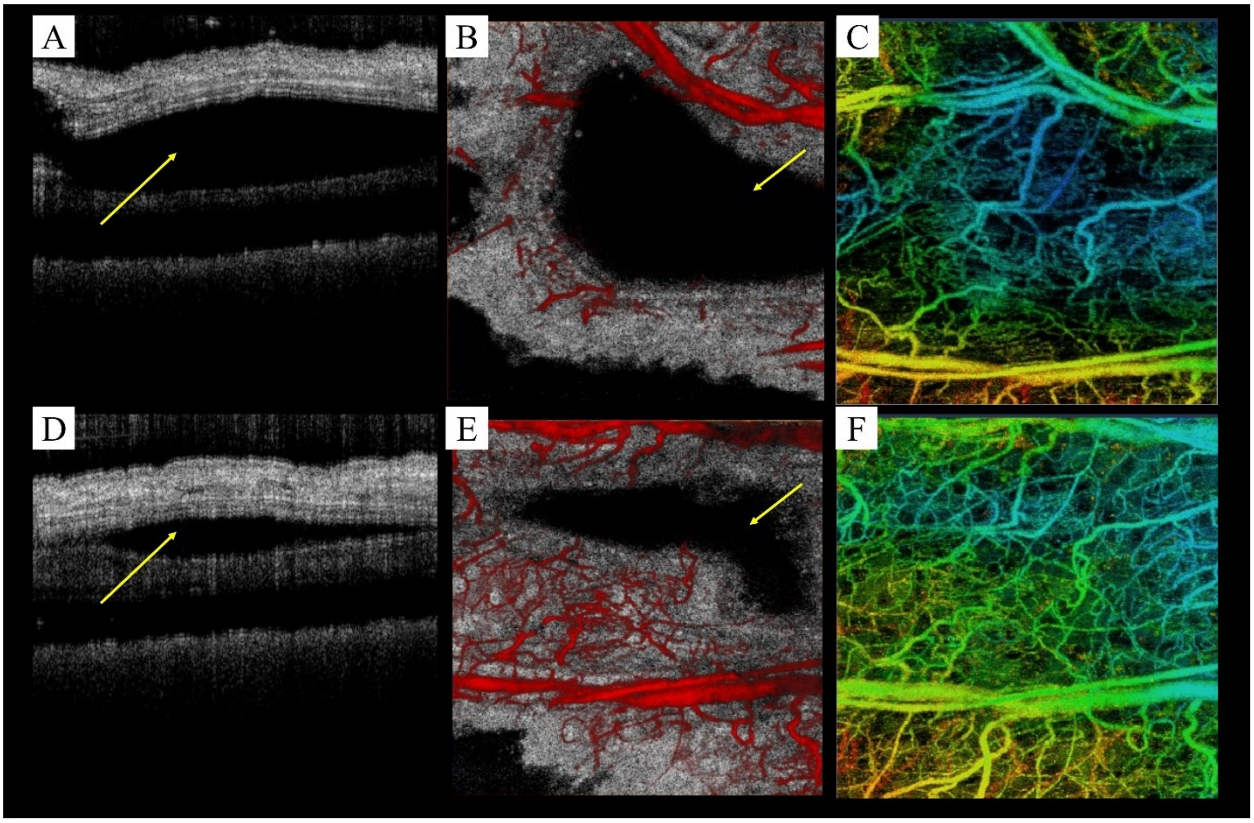

Figure 8-14 Voluma™ soft tissue injection

(A) Cross-section image overlaid with microvessels after injection. (B) Depth-map structure and microvessels overlaid around the injection site. (C) Depth-encoded maximum intensity projection map of microvessels after injection. (D) Cross-section image overlaid with microvessels on two-week follow up. (E) Depth-map cross-section of OCT structure and microvessels overlaid. (F) Depth-encoded maximum intensity projection map of microvessels two weeks after injection. Yellow arrows indicate location of fillers inside the tissue. Field of view is 2x2 mm^2.

We injected ~ 45 µL of Voluma™ diluted at 12.5% using a 34G needle into the external carotid artery and observed the changes in the microcirculation of the ear (Figure 8-15). The reduction of perfusion after the injection was significant and most of the capillaries were no longer perfused after injection. The few remaining vessels had a pattern similar to those of artery-to-artery anastomosis and most of them belong to the ventral part of the ear pinna.

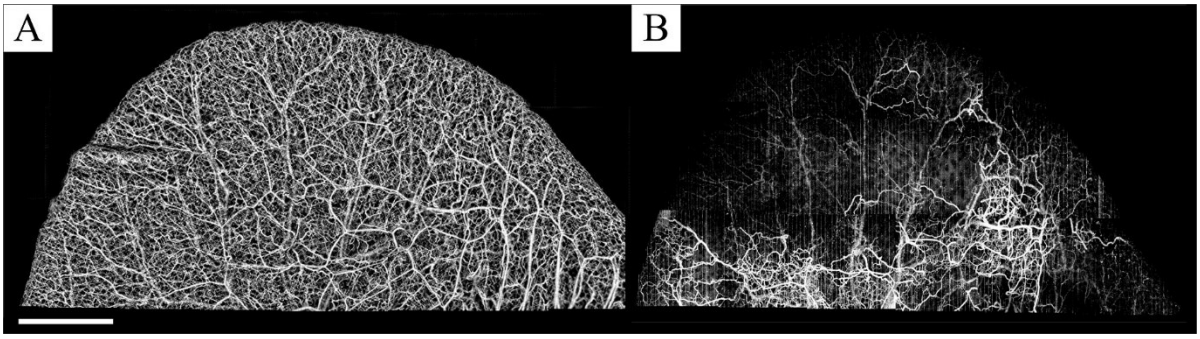

Figure 8-15 Intravascular injection of Voluma™.
(A) Baseline. (B) Occlusion after injection. Scale bar = 1 mm.

8.3.4 Belotero®

Belotero Balance (FDA approved on November 2011 for Merz Pharmaceuticals, LLC) is a sterile, bioresorbable, non-pyrogenic, viscoelastic, clear, colorless, homogenous gel device that is formed by bacterial fermentation of injectable hyaluronic acids. After extraction and purification, HA manufactured from streptococcal cultures is cross-linked with a binding agent (1,4-butanediol diglycidyl ether) in two consecutively executed reactions and reconstituted in a physiologic buffer at $pH = 7$ and concentration of 22.5 mg/mL. Belotero Balance is a monophasic double crosslinked HA gel based on Cohesive Polydensified Matrix (CPM) technology that makes it a low-viscos gel with variable densities of crosslinking in one cohesive structure. The variable zone of crosslinking allows Belotero to integrate into nooks and crannies in the dermis and subcutaneous layers without having to worry as much about lumps and bumps. The main difference between biphasic and monophasic products is in their cross-linking manufacturing method. In biphasic products, crosslinked HA is sieved through a screen to isolate crosslinked HA particles of uniform size [Flynn-2011]. However, monophasic fillers are not sieved and contain a mixture of randomly sized and shaped pieces [Baumann-2002]. Theoretically monophasic products can easily spread throughout the tissue while conventional

HA fillers would not be able to fill the smallest gaps [Kammerer-2005, Taufig-2009, Breithaupt-2012].

Belotero Balance is also marketed as Esthelis® in Europe and other parts of the world and received CE certification clearance in October 2004. The safety of Belotero Balance has been evaluated in three clinical studies and post marketing surveillance. The list of complications associated with the use of the device include allergic reaction including Quincke's edema, tissue necrosis in the glabellar area after injection, inflammation reaction, injection site granuloma, injection site indurations, hematoma after injection, Tyndall effect, Cordon-like effect, bump and pustule at injection site, scarring after injection in the chest, bruising, discoloration, erythema, pain, mild headache and etc. During the clinical studies, only one case was reported with serious adverse event who underwent hip arthroplasty that was not related to treatment with Belotero Balance [Belotero_FDA].

We directly injected 30 μL of Belotero Balance into the mouse ear pinna tissue and observed the changes and dynamics of surrounding microvasculature on the day of injection (Figure 8-16 (B)) and one week after injection (Figure 8-16 (C)). Compared to the baseline image (Figure 8-16 (A)), no obvious change in the microvessels could be observed and tissue was back to normal conditions after the injection.

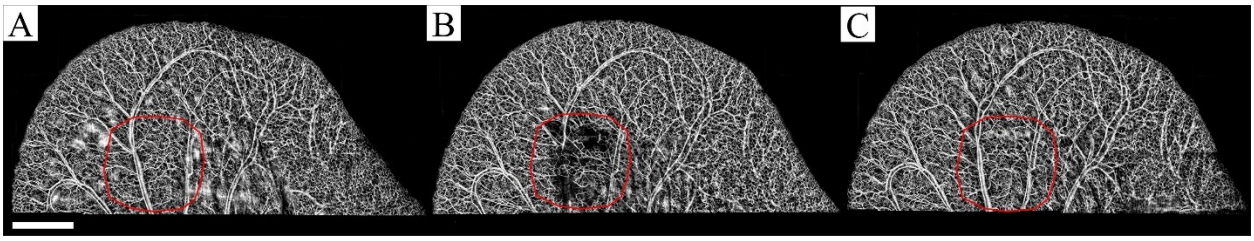

Figure 8-16 Belotero® Balance soft tissue injection.

Maximum intensity projection maps of microvessels in the injection sample (A) Baseline image before injection. (B) Same day after injection. (C) One week follow up after injection. Red line = approximate injection site. Scale bar = 1 mm.

Also, from cross-section images overlaid with microvasculature we could not observe any blockage of microvessels due external compression caused by Belotero Balance fillers. Figure 8-17 shows multiple views of OCT structure cross-sections overlaid with microvessels and the MIP microvessel map after injection and one week follow up in the injection site.

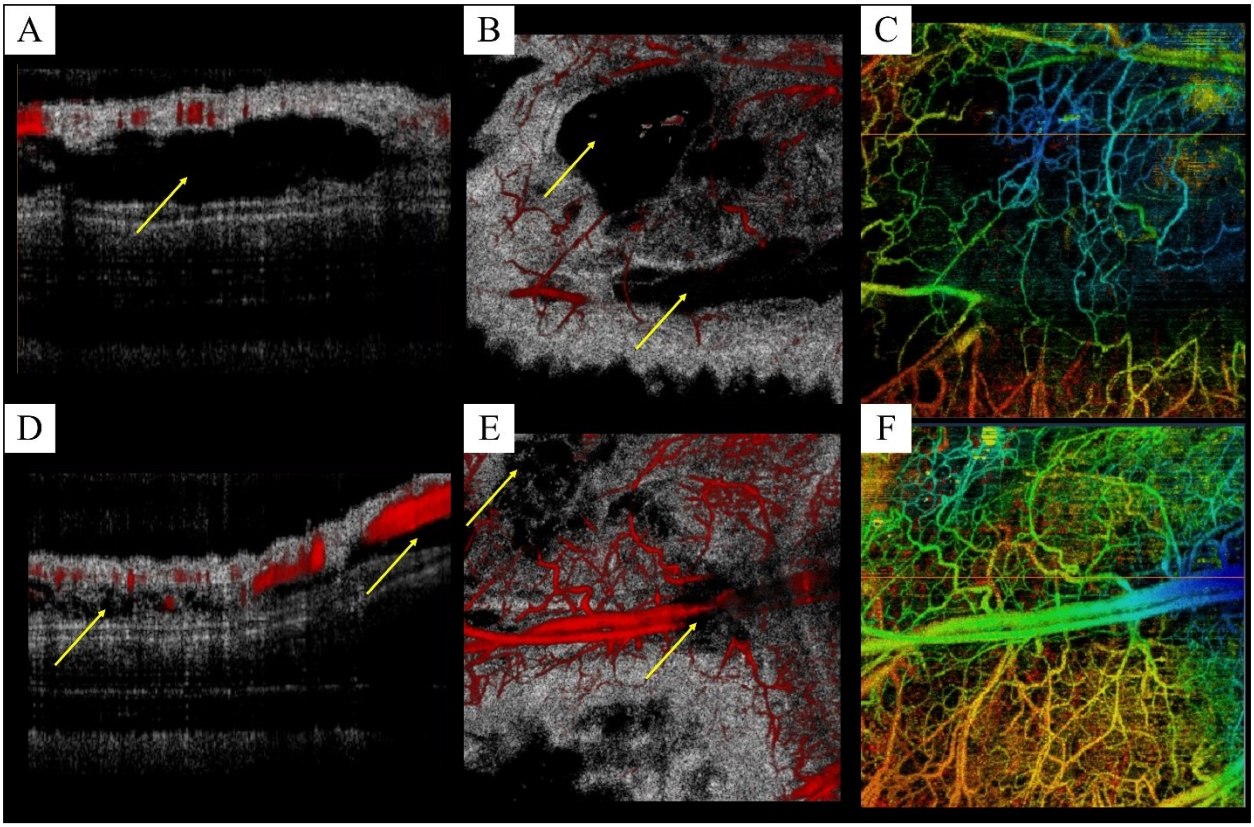

Figure 8-17 Belotero® Balance soft tissue injection

(A) Cross-section image overlaid with microvessels after injection. (B) Depth-map structure and microvessels overlaid around the injection site. (C) Depth-encoded maximum intensity projection map of microvessels after injection. (D) Cross-section image overlaid with microvessels on one-week follow up. (E) Depth-map cross-section of OCT structure and microvessels overlaid. (F) Depth-encoded maximum intensity projection map of microvessels one week after injection. Yellow arrows indicate location of fillers inside the tissue. Field of view is 2x2 mm^2.

In another experiment, 30 μL of diluted (12.5%) Belotero® Balance was directly injected into the external carotid artery and moderate peripheral nonperfusion of the mouse pinna was observed with OCT/OMAG (Figure 8-18). Most of the larger vessels remained patent, but a small reduction of flow was observed at capillary sites. At a distal section of the ear pinna showed significant blood flow reduction while the proximal blood vessels seemed intact. In a side-by-side comparison of sections before and after intra-arterial injection, these changes become very apparent (Figure 8-18). One explanation is that Belotero® consists of particles with different size distribution and a 34G needle have only passed small particles that did not block any major artery but reduced total blood flow in the capillaries. Also, ear tissue consists of many anastomosis and collateral vessels that can partially compensate the flow reduction in the tissue due to filler blockage. In the future, our results have to be confirmed with histopathology to identify the exact location of these blockages and filler accumulations.

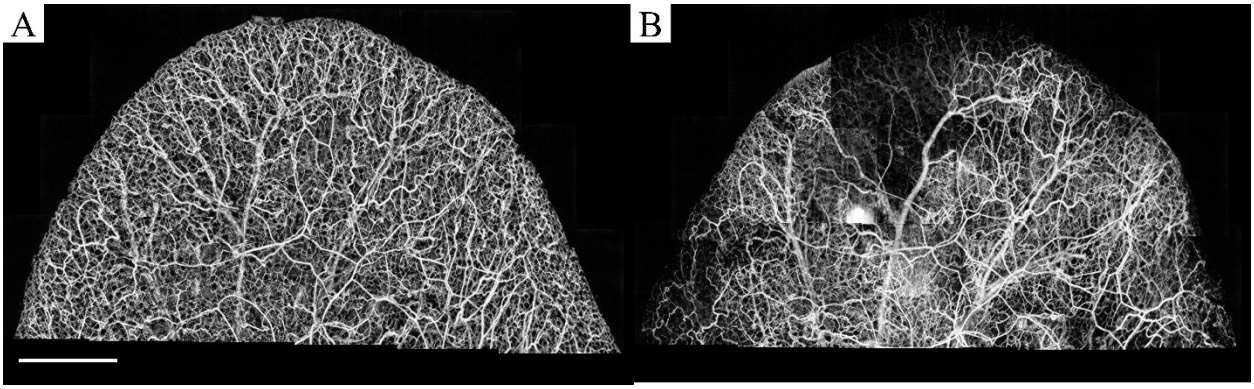

Figure 8-18 Belotero® intravascular injection.

(A) Baseline microvasculature MIP. (B) After intra-arterial injection of Belotero® into the external carotid artery.

8.3.5 Radiesse®

Radiesse® is a sterile, non-pyrogenic, semi-solid, cohesive implant whose principle component is synthetic calcium hydroxylapatite suspended in a gel carrier of sterile water for injection, glycerin and sodium carboxymethylcellulose. The principle durable component of Radiesse® is synthetic calcium hydroxylapatite, a biomaterial with over twenty years of use in orthopedics, neurosurgery, dentistry, otolaryngology and ophthalmology. The range of particles size varies between 25-45 microns and is usually injected with a 25 or 27 gauge needle. Radiesse® is currently marketed in Europe, Canada and South America. During the clinical trials, no adverse effect related to Radiesse® injection was reported. Because the calcium hydroxylapatite contents found in Radiesse® is identical to that found in the matrix of bone, Radiesse® particles are seen on both X-ray and CT scans [Radiesse_FDA]. Radiesse® is typically used for long-lasting correction of deep wrinkles and folds and contouring of facial features such as cheekbones and the nasal dorsum. After injection, the microspheres undergo fibrous encapsulation and provide a network of scaffolding for collagen ingrowth from surrounding tissue. The gel carrier is usually absorbed in the skin in about 2 months while the tissue ingrowth provides long-lasting results until the calcium hydroxylpatite microspheres degrade over several months [Sukhjit-2006].

We directly injected 25 μL of Radiesse® into the mouse ear pinna tissue and observed the changes and dynamics of surrounding microvasculature on the day of injection (Figure 8-19(B)) and one week after injection (Figure 8-19(C)). Compared to the baseline image (Figure 8-19(A)), no obvious change in the microvessels could be observed and tissue was back to normal conditions after the injection.

Figure 8-19 Radiesse® soft tissue injection.

Maximum intensity projection maps of microvessels in the injection sample (A) Baseline image before injection. (B) Same day after injection. (C) One week follow up after injection. Red line indicates the injection site. Scale bar = 1 mm.

Also, from cross-section images overlaid with microvasculature we could not observe any blockage of microvessels due external compression caused by Radiesse® fillers. Figure 8-20 shows multiple views of OCT structure cross-sections overlaid with microvessels and the MIP microvessel map after injection and one week follow up in the injection site.

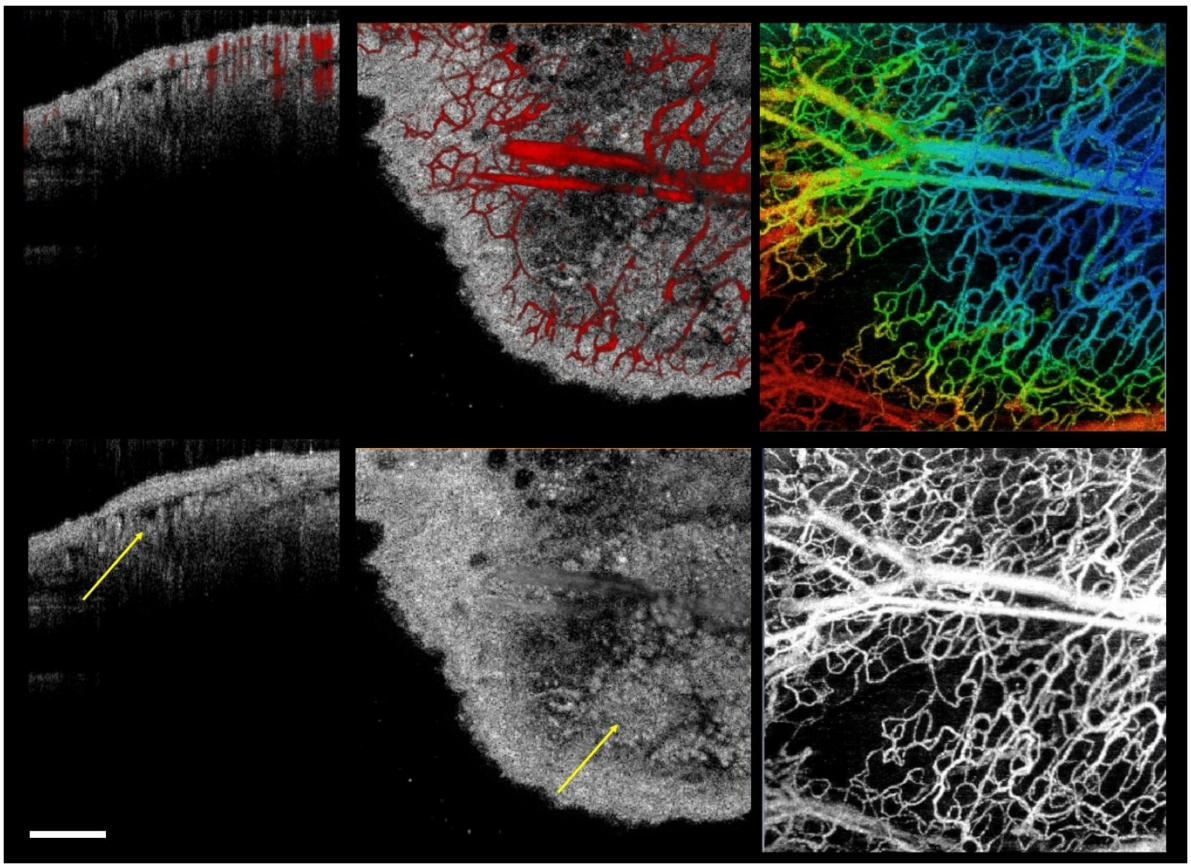

Figure 8-20 Radiesse® soft tissue injection.

(A) Cross-section image overlaid with microvessels after injection. (B) Depth-map structure and microvessels overlaid around the injection site. (C) Depth-encoded maximum intensity projection map of microvessels after injection. (D) Cross-section structure image with an arrow indicating location of Radiesse® particles. (E) Depth-map cross-section of OCT structure with an arrow indicating location of Radiesse® particles. (F) Maximum intensity projection maps of blood vessels at the injection site. Field of view is 2x2 mm^2. Scale bar = 0.5 mm.

8.4 Conclusions and future work

In our mouse pinna model, direct injection of filler material into the soft tissues did not result in significant vascular occlusion, ischemia, or necrosis. Only in one case, the injection accidentally damaged a major vein and the filler blocked that vein. However, intra-arterial injection of HA-based fillers blocked the arteries and we conclude that the vascular occlusion hypothesis is present. In our experiments, we could not observe any capillary damage due to vascular

compression. Part of the reason is that our ear pinna model only consists of a cartilage layer sandwiched by two layers of highly vascularized skin with multiple collateral support. Therefore, partial blockage of one of the major arteries/veins could be easily compensated with the surrounding collateral and choke vessels. However, direct injection of filler into the arteries through the external carotid could eventually block the blood flow and perfusion in the ear that confirmed the intra-vascular blockage hypothesis.

The success rate for intra-arterial injection into external carotid artery followed by imaging was around 50%. Since the mice carotid arteries are relatively smaller than the needles that come along with fillers, we had to utilize a smaller needle and dilute the filler with saline down to 12.5% to make it possible to pass through the 34G needle. After injection of filler into the carotid artery, the needle had to be carefully pulled out to avoid possible damages to the artery and terminal bleeding. We overcame this challenge by utilizing an ultra-strong tissue glue that a few drops were applied while the needle was still in the artery. Although all these cautions were taken, the success rate was still around 50%. Direct injection of cosmetic filler into the carotid artery can partially induce more complications in the mice such as stroke that survival follow-up studies were not possible and animals had to be sacrificed.

In the future, an *in vivo* model with larger arteries should be utilized so that direct intra-arterial injection would be feasible. Models such as rabbit ear could be studied that no vital complication would happen after injection and post-injection follow-up studies be possible to develop therapeutic plans for dermal filler complications. In the future, our samples should be sent to histology for further analysis and finding the exact location of filler aggregation in the tissue.

Chapter 9. SUMMARY AND FUTURE WORK

In this thesis, we development processing techniques for label-free quantification of microcirculatory network *in vivo* using optical coherence tomography (OCT). OCT works very similar to ultrasound, only mechanical pressure waves have been replaced by photons. OCT is currently established as one of the standard imaging modalities in ophthalmology to assess posterior chamber and anterior chamber of the eye. There exist several blinding disease that are irreversible if advanced such as glaucoma, age-related macular degeneration (AMD) and diabetic retinopathy. These diseases have distinct features and characteristics that are detected on OCT scans and patients with symptoms related to these diseases should be monitored with OCT scan on a regular basis. Another major application of OCT in terms of market is in the field of intra-vascular cardiology and assessment of vulnerable plaque. Along intravascular ultrasound (IVUS), intravascular OCT (IV-OCT) has been utilized to assess the inner wall of coronary arteries at micron resolution (order of 10x improvement compared to IVUS). Besides ophthalmology and cardiology, other popular applications of OCT include dermatology, pathology and small animal studies.

Similar to ultrasound Doppler imaging, OCT hemodynamics and microcirculation can be assessed by repeated temporal measurements at the same spatial location. By manipulating scanning mirrors and considering variations in the speckle signal, blood flow perfusion within capillaries can be assessed along tissue structural information.

In chapter 2, we proposed an eigen-regression technique to suppress background and assess blood flow perfusion maps within the tissue structures. Hardware and optics limits the OCT field of view and scanning range. In order to scan a larger field of view, sample tissue or system can

be mechanically translated along the X and Y axis and multiple scans be acquired at adjacent locations. When the imaging is performed at each tile, the probing light is subject to specular reflection at the tissue surface when it shines onto sample. Furthermore, the propagation of light within the tissue suffers from attenuation and scattering which makes the backscattering light collected at the detector non-uniform. These physical limitations can result in local imaging contrast degraded, leading to non-uniform appearance of the micro-angiogram images. In order to overcome these limitations, we proposed an automatic digital histogram equalization to be utilized to create a uniform distribution of intensities and qualitatively improve the contrast of images (chapter 3). This process allowed fixed or adaptive manipulation of the dynamic range such that the results are more informative for human eye.

In order to quantify the blood flow and flux within microcirculatory network *in vivo*, we utilized a super-resolution technique (Multiple Signal Classification or MUSIC) to simultaneously quantify bidirectional RBC flow and flux by spectral estimation of the received OCT signal from moving particles within capillaries and microvessels (chapter 4). We showed the efficiency and performance of the proposed method in simulation and tissue-mimicking flow phantom. Compared to the existing methods that can either quantify flow direction or power, our proposed method allowed simultaneous flow (velocity) direction and power (flux) estimation. Since, a super-resolution estimation technique was utilized, our method did not need a large data set to reconstruct power spectrum of the OCT signal. This method may be utilized to facilitate the evaluation of tissue oxygen/nutrition exchange and consumption by microstructures in biological tissues such as human/animal retina, skin and rodent brain.

The lymphatic system is a part of microcirculatory network that usually develops in parallel to the blood vessels in the skin and in most internal organs and is not present in central nervous

system, bone marrow and avascular structures such as cartilage, epidermis and cornea. Lymphatic system collects interstitial fluid from extracellular spaces and plays an important role in the immune system. Although most of the existing lymphatic imaging techniques require contrast agents, their toxicity and side effects can limit their applications. Since the lymph fluid is clear and transparent, lymphatic vessels appear as reduced scattering (system noise level) vessel-like areas in OCT structure cross-section images. The origin of these reduced-scattering connected tubular structures in the skin has been already confirmed by intra-dermal injection of Evan's blue dye and monitoring the uptake path by surrounding lymph vessels into the SLN. Therefore, these lymph vessels can be visualized by applying a lower threshold on the OCT intensity image. However, the intensity-threshold technique does not take the physical shape of the vessels into account, therefore not robust to intensity variations and noise caused by speckle and light absorption in the structure. In chapter 5, we developed an automatic method for segmenting lymphatic vessel in OCT structure images using filtering technique and vesselness models based on Hessian multi-scale filters. We demonstrate the capability of OCT for non-invasive label-free imaging of lymphatic vessels along with blood flow perfusion within tissue beds and a segmentation method to extract lymphatic vessel lumen. In order to observe the capability of our system and technique, we created a biopsy punch wound on the mouse ear and monitored the dynamics and healing process of lymphatic and blood vessels around the wound. Label-free non-invasive imaging and segmentation of SLNs and lymphatic vessels can be used in different applications such as dermatology, cosmetic and beauty, cancer, wound healing and infectious disease where lymphatic system plays an important role in delivering immune response and draining waste. The observed lymphatic vessels on the OCT structure images are directly related to the resolution of the system. By increasing the system resolution, smaller

lymphatic vessels and capillaries can also be observed and eventually segmented using our proposed method.

In chapter 6, we developed a segmentation method to quantify geometrical and physical parameters of the vessels such as vessel diameter and orientation. We tested the efficiency of our algorithm on angiogenesis wound healing model and quantified the healing process after a biopsy punch. To quantify the accuracy of our segmentation technique, standard dataset with manual segmentation technique from retina fundus images were selected. The segmentation algorithm was compared with the manual segmentation provided by the experts and achieved a reasonably good results compared to the results of other techniques reported on that dataset. Our segmentation technique is not limited to OCT angiograms and can be applied to other imaging techniques with similar vasculature pattern.

After developing quantification and visualization techniques in chapters 2-6, we utilized these tools in two translational applications of OCT and optical micro-angiography (OMAG). In chapter 7, cutaneous wound healing stages in a mouse ear pinna model was investigated. We demonstrated the capability of OMAG to describe in detail the microcirculation response including capillaries, large vessels and lymphatic vessels during wound healing phases. Our results were in agreement with expected behavior of tissue during wound healing stages and we can conclude that OCT/OMAG proves to be a practical tool for tracking wound healing in mouse model. In the future, we would like to generalize our results to human studies to design treatment strategies for burns, chronic skin ulcers and diabetes mellitus.

In chapter 8, we studied complications of injectable cosmetic dermal fillers for skin wrinkle removal. Based on the American Society of Plastic Surgery report in 2012, nearly 2 million cosmetic filler injections were performed in the United States, with the majority of these

injections (1.4 million) being hyaluronic acid (HA) gel fillers. With increased use of injectable fillers, growing reports of filler-induced complications have been reported all around the world. Some complications appear immediately after injections (0-2 days) that include under/overcorrection, implant visibility or Tyndall effect, sensitivity to the injected material, and ischemia with or without necrosis. Other complications such as infection, tissue discoloration, inflammation, nodularity, and angioedema may occur in the early post-procedure period (3-14 days). Also, long term complications (>14 days) such as persistent erythema, telangiectasia, migration, scarring, and granuloma formation have also been reported. There are multiple hypothesis about causes of post-injection tissue necrosis, but the exact mechanism for tissue death is not fully understood. Current theories include arterial or venous compression or obstruction, trauma to the vessel wall, and intravascular (intra-arterial) injection with embolization of the filler material into the capillary bed where oxygen exchange normally occurs. In chapter 8, we utilized OCT and OMAG technologies in the mouse ear pinna model to study the mechanisms of filler-induced tissue necrosis at the capillary level. Two experiments were designed to test mechanisms proposed for tissue necrosis post filler injection. In the first experiment, we directly injected the filler into the soft tissue. This experiment was designed to test the hypothesis whether filler can compress the tissue and hence damage the microvasculature supply. In the second experiment, we directly injected the filler into an artery and observed the changes in the downstream microvasculature. In our mouse pinna model, direct injection of filler material into the soft tissues did not result in significant vascular occlusion, ischemia, or necrosis. Only in one case, the injection accidentally damaged a major vein and the filler blocked that vein. However, intra-arterial injection of HA-based fillers blocked the arteries and we conclude that the vascular occlusion hypothesis is present. In our experiments, we could not

observe any capillary damage due to vascular compression. In the future, a model with larger vessels similar to human arteries should be utilized so that direct intra-arterial injection would be feasible. Also, our results need to be confirmed with histology of tissue samples after injection of dermal fillers.

One of the limitations of our current system is that processing bottleneck that is usually performed offline and might take a few minutes after capturing each 3D dataset to visualize the data. With the recent development of parallel computing units and general purpose graphical processing units (GPUs), CUDA-enabled GPUs can be utilized to perform parallel processing on OCT data to achieve real-time OCT angiography. OCT is an ideal case for parallel processing units because each A-line is independent of the others in a 3D dataset. In that case, the theoretical processing limit will be based on camera speed and scanner limitations. Therefore, processing at a rate higher than that of the acquisition can be the goal of GPU parallel processing.

BIBLIOGRAPHY

[Huang-1991] D. Huang, E.A. Swanson, C.P. Lin, J.S. Schuman et al., "Optical coherence tomography," Science, 254(5035): 1178-1181, 1991.

[Leitgeb-2003] R. Leitgeb, C. Hitzenberger and A.F. Fercher, "Performance of fourier domain vs. time domain optical coherence tomography," *Optics Express,* vol. 11, no. 8, pp. 889-894, 2003.

[Choma-2003] M. Choma, M. Sarunic, C. Yang and J. Izatt, "Sensitivity advantage of swept source and Fourier domain optical coherence tomography," *Optics Express,* vol. 11, no. 18, pp. 2183-2189, 2003.

[An-2010_Full-Range] L. An, H.M. Subhash and R.K. Wang, "Full range complex spectral domain optical coherence tomography for volumetric imaging at 47 000 A-scans per second," *Journal of Optics*, vol. 12, pp. 84003, 2010.

[Wang-2007_FR] R.K. Wang, "*In vivo* full-range complex Fourier domain optical coherence tomography," *Applied Physics Letters,* vol. 90, no. 5, 2007.

[An-2008_Retina-Choroid] L. An and R.K. Wang, "In vivo volumetric imaging of vascular perfusion within human retina and choroids with optical micro-angiography," Optics Express, vol. 16, no. 15, pp. 11438-11452, 2008.

[Li-2006] X. Li and H. Ren, "Clutter rejection filters for optical Doppler tomography," Optics Express, vol. 14, no. 13, pp. 6103-3112, 2006.

[Chen-1997] Z. Chen, T.E. Milner, D. Dave and J.S. Nelson, "Optical Doppler tomographic imaging of fluid flow velocity in highly scattering media," Optics Letters, vol. 22, no. 1, pp. 64-66, 1997.

[Wang-2004] L. Wang, Y. Wang, S. Guo, J. Zhang, M. Bachman, G. P. Li and Z. Chen, "Frequency domain phase-resolved optical Doppler and Doppler variance tomography," Optics Communications, vol. 242, no. 4-6, pp. 345-350, 2004.

[Ding-2002] Z. Ding, Y. Zhao, H. Ren, J. Nelson and Z. Chen, "Real-time phase-resolved optical coherence tomography and optical Doppler tomography," Optics Express, vol. 10, no. 5, pp. 236-245, 2002.

[Kellam-1996] K. Kellam and P. Altmeyer, "Capillary blood cell velocity in human skin capillaries located perpendicularly to the skin surface: measured by a new laser Doppler anemometer," Microvascular Research, vol. 52, pp. 188-192, 1996.

[An-2010_wide] L. An, H.M. Subhash, D. Wilson and R.K. Wang, "High resolution wide field imaging of retinal and choroidal blood perfusion with optical micro-angiography", Journal of Biomedical Optics, 15 (March/April), 026011 (2010).

[Al-Hafeez_2012] D. Al-Hafeez, Derek Nankivil, Theresa Bustamante, Anthony Kuo, and Joseph A. Izatt, "Simultaneous swept source optical coherence tomography of the anterior segment and retina using coherence revival," Optics Letters, Vol. 37, Issue 11, pp. 1883-1885 (2012).

[An-2011_Full-Range] L. An, and R.K. Wang, "Full-range complex ultrahigh sensitive optical microangiography", Optics Letters Vol. 36, Iss. 6, pp. 831–833 (2011)

[Yi-2009] Yi, K., Mujat, M., Sun, W., Burnes et al., “Imaging of optic nerve head drusen: improvements with spectral domain optical coherence tomography,” Journal of glaucoma, 18(5), 373, 2009.
[Regatieri-2012] Regatieri C.V., Branchini L., James G. Fujimoto, and Jay S. Duker. "Choroidal imaging using spectral-domain optical coherence tomography," Retina (Philadelphia, Pa.) 32(5): 865, 2012.
[Li-2011_limbus] P. Li, L. An, R. Reif, T.T. Shen, M. Johnstone, and R.K. Wang, "In vivo microstructural and microvascular imaging of the human corneo-scleral limbus using optical coherence tomography." Biomedical optics express 2(11): 3109-3118, 2011. .
M. Johnstone, E. Martin, and A. Jamil, "Pulsatile flow into the aqueous veins: manifestations in normal and glaucomatous eyes," Experimental Eye Research 92(5): 318-327, 2011.
[Lim-2008] L.S. Lim, T. Han, et al. "Corneal imaging with anterior segment optical coherence tomography for lamellar keratoplasty procedures," American journal of ophthalmology, 145(1): 81-90, 2008.
[Li-2012] P. Li, R. Reif, Z. Zhi, E. Martin, T.T. Shen, M. Johnstone and R.K. Wang, "Phase-sensitive optical coherence tomography characterization of pulse-induced trabecular meshwork displacement in ex vivo nonhuman primate eyes," Journal of Biomedical Optics,17(7): 076026-1, 2012.
[Imai-2001] M. Imai, H. Iijima and N. Hanada, "Optical coherence tomography of tractional macular elevations in eyes with proliferative diabetic retinopathy," American journal of ophthalmology, 132(1): 81-84, 2001.
[Srinivasan-2012] V.J. Srinivasan, H. Radhakrishnan, E.H. Lo, E.T. Mandeville, J.Y. Jiang, S. Barry and A.E. Cable, “OCT methods for capillary velocimetry,” Biomedical Optics Express, 3(3), 612-629, 2012.
[Liu-2012] G. Liu, W. Jia, V. Sun, B. Choi, and Z. Chen, “High-resolution imaging of microvasculature in human skin in vivo with optical coherence tomography,” Opt. Express 20(7), 7694–7705 (2012).
[Zhao-2000_Doppler] Y. Zhao, Z. Chen, C. Saxer, Q. Shen, S. Xiang, J. F. de Boer, and J. S. Nelson, “Doppler standard deviation imaging for clinical monitoring of in vivo human skin blood flow,” Opt. Lett. 25(18), 1358–1360 (2000).
[Barton-2005] J. Barton and S. Stromski, “Flow measurement without phase information in optical coherence tomography images,” Opt. Express 13(14), 5234–5239 (2005).
[Yasuno-2007] Y. Yasuno, Y. Hong, S. Makita, M. Yamanari, M. Akiba, M. Miura, and T. Yatagai, “In vivo high-contrast imaging of deep posterior eye by 1-μm swept source optical coherence tomography and scattering optical coherence angiography,” Opt. Express 15(10), 6121–6139 (2007).
[Jia-2012] Y. Jia, O. Tan, J. Tokayer, B. Potsaid, Y. Wang, J. J. Liu, M. F. Kraus, H. Subhash, J. G. Fujimoto, J. Hornegger, and D. Huang, “Split-spectrum amplitude-decorrelation angiography with optical coherence tomography,” Opt. Express 20(4), 4710–4725 (2012).
[Motaghiannezam-2012] R. Motaghiannezam and S. Fraser, “Logarithmic intensity and speckle-based motion contrast methods for human retinal vasculature visualization using swept source optical coherence tomography,” Biomed. Opt. Express 3(3), 503–521 (2012).
[Tao-2008] Y. K. Tao, A. M. Davis, and J. A. Izatt, “Single-pass volumetric bidirectional blood flow imaging spectral domain optical coherence tomography using a modified Hilbert transform,” Opt. Express 16(16), 12350–12361 (2008).

[Ren-2006] H. Ren, T. Sun, D. J. MacDonald, M. J. Cobb, and X. Li, “Real-time in vivo blood-flow imaging by movingscatterer-sensitive spectral-domain optical Doppler tomography,” Opt. Lett. 31(7), 927–929 (2006).
[Capon-1969] J. Capon, "High-resolution frequency-wavenumber spectrum analysis," Proceedings of the IEEE 57(8): 1408-1418, 1969.
[Burg-1967] J.P. Burg, "Maximum-entropy spectral analysis", 37th Ann. Int. Meet., Soc. Explor. Geophys., Ph.D. thesis, Oklahoma City, Okla., Oct. 31, 1967 (1967)
Shannon, Claude Elwood. "Communication in the presence of noise." Proceedings of the IRE 37.1 (1949): 10-21.
[Wang-2007_3D_OMAG] Wang, Ruikang K. "Three-dimensional optical micro-angiography maps directional blood perfusion deep within microcirculation tissue beds in vivo."Physics in medicine and biology 52, no. 23 (2007): N531.
[Wang-2006] R.K. Wang and Z. Ma, “Real time flow imaging by removing texture pattern artifacts in ultrafast spectral domain optical Doppler tomography”, Optics Letters, 31, 3001-3003, 2006.
[Suri-2002] J.S. Suri, K. Liu, L. Reden and S. Laxminarayan, "A review on MR vascular image processing algorithms: acquisition and prefiltering: part I," *IEEE transactions on information technology in biomedicine: a publication of the IEEE Engineering in Medicine and Biology Society,* 6(4): 324, 2002.
[Lesage-2009] D. Lesage, E.D. Angelini, I. Bloch, and G. Funka-Lea, "A review of 3D vessel lumen segmentation techniques: Models, features and extraction schemes," *Medical Image Analysis,* 13(6): 819-845, 2009.
[Krissian-2000] K. Krissian, G. Malandain, N. Ayache, R. Vaillant, and Y. Trousset, "Model-based detection of tubular structures in 3D images," *Computer vision and image understanding,* 80(2): 130-171, 2000.
[Shaw-2009] T.J. Shaw and P. Martin, “Wound repair at a glance,” *Journal of cell science*, *122*(18): 3209-3213, 2009.
[Baum-2006] C. L. Baum and C.J. Arpey, “Normal cutaneous wound healing: clinical correlation with cellular and molecular events,” *Dermatologic surgery*, *31*(6), 674-686, 2006.
[Rockson-2008] S. G. Rockson, “The lymphatic continuum revisited,” Annals of the New York Academy of Sciences 1131 (2008): ix.
[Leak-1970] L. V. Leak, “Electron microscopic observations on lymphatic capillaries and the structural components of the connective tissue-lymph interface,” Microvasc Res, 2:361–91, 1970.
[PARTSCH-1984] H.A. PARTSCH, A. URBANEK and B. WENZEL-HORA, “The dermal lymphatics in lymphoedema visualized by indirect lymphography,” Br. J. Dermatol. 110: 431–438, 1984.
[SUGA-2003] SUGA, K., N. OGASAWARA, Y. YUAN, et al. 2003. Visualization of breast lymphatic pathways with an indirect computed tomography lymphography using a nonionic monometric contrast medium iopamidol: preliminary results.Invest. Radiol. 38: 73–84.
[YUAN-2006] YUAN, Z., L. CHEN, Q. LUO, et al. 2006. The role of radionuclide lymphoscintigraphy in extremity lymphedema. Ann. Nucl. Med. 20: 341–344.
[MCNEILL-1989] MCNEILL, G.C., M.H. WITTE, C.L. WITTE, et al. 1989.Whole-body lymphangioscintigraphy: preferred method for initial assessment of the peripheral lymphatic system. Radiology 172: 495–502.

[SZUBA-2003] SZUBA, A., W.S. SHIN, H.W. STRAUSS, et al. 2003. The third circulation: radionuclide lymphoscintigraphy in the evaluation of lymphedema. J. Nucl. Med. 44: 43–57.
[CL´EMENT-2004] CL´EMENT, O. & A. LUCIANI. 2004. Imaging the lymphatic system: possibilities and clinical application. Eur. Radiol. 14: 1498–1507.
[MISSELWITZ-2006] MISSELWITZ, B. 2006. MR contrast agents in lymph node imaging. Eur. J. Radiol. 58: 375–382.
[BARRETT-2006] T. BARRETT, P.L.CHOYKE&H.KOBAYASHI, "Imaging of lymphatic system: new horizons," ContrastMedia Mol. Imaging 1: 230–245, 2006.
[FISCHER-1997] M. FISCHER, U. COSTANZO, U. HOFFMAN, et al., "Flow velocity of cutaneous lymphatic capillaries in patients with primary pymphedema," Microcirculation 17: 143–149, 1997.
[MELLOR-2000] R. H. MELLOR, A.W.B. STANTON, P. AZARDO, et al., "Enhanced cutaneous lymphatic network in the forearms of women with postmastectomy oedema," J. Vasc. Res. 37: 501–512, 2000.
[GURFINKEL-2000] M. GURFINKEL, A.B. THOMPSON, W.RALSTON, et al., "Pharmacokinetics of ICG and HPPH-car for the detection of normal and tumor tissue using fluorescence, nearinfrared reflectance imaging: a case study," Photochem. Photobiol. 72: 94–102, 2000.
[BANERJI-1999] BANERJI, S., J.NI, S.-X.WANG, et al., "LYVE-1, a new homologue of CD44 glycoprotein, is a lymph specific receptor for hyaluronan," J. Cell Biol. 144: 789–801, 1999.
[Tammela-2010] Tammela T, Alitalo K (2010) Lymphangiogenesis: Molecular mechanisms and future promise. Cell 140:460–476.
[Alitalo-2005] K. Alitalo, T. Tammela, and T.V. Petrova. "Lymphangiogenesis in development and human disease." Nature 438, no. 7070 : 946-953 (2005).
[Oliver-2004] G. Oliver, "Lymphatic vasculature development." Nature Reviews Immunology 4, no. 1: 35-45 (2004).
[Zgraggen-2013] S. Zgraggen, A. M. Ochsenbein and M. Detma, "An important role of blood and lymphatic vessels in inflammation and allergy," Journal of allergy, 2013.
[Jang-2002] Jang, Ik-Kyung, Brett E. Bouma, Dong-Heon Kang, Seung-Jung Park, Seong-Wook Park, Ki-Bae Seung, Kyu-Bo Choi et al. "Visualization of coronary atherosclerotic plaques in patients using optical coherence tomography: comparison with intravascular ultrasound." Journal of the American College of Cardiology 39, no. 4 (2002): 604-609.
[Bouma-2003] Bouma, B. E., G. J. Tearney, H. Yabushita, M. Shishkov, C. R. Kauffman, D. DeJoseph Gauthier, B. D. MacNeill et al. "Evaluation of intracoronary stenting by intravascular optical coherence tomography." Heart 89, no. 3 (2003): 317-320.
[Kubo-2007] Kubo, Takashi, Toshio Imanishi, Shigeho Takarada, Akio Kuroi, Satoshi Ueno, Takashi Yamano, Takashi Tanimoto et al. "Assessment of Culprit Lesion Morphology in Acute Myocardial InfarctionAbility of Optical Coherence Tomography Compared With Intravascular Ultrasound and Coronary Angioscopy." Journal of the American College of Cardiology 50, no. 10 (2007): 933-939.
[Yabushita-2002] Yabushita, Hiroshi, Brett E. Bouma, Stuart L. Houser, H. Thomas Aretz, Ik-Kyung Jang, Kelly H. Schlendorf, Christopher R. Kauffman et al. "Characterization of human atherosclerosis by optical coherence tomography." Circulation 106, no. 13 (2002): 1640-1645.
[Fujimoto-2003] Fujimoto, James G. "Optical coherence tomography for ultrahigh resolution in vivo imaging." Nature biotechnology 21, no. 11 (2003): 1361-1367.

[Brezinski-2006] Brezinski, Mark E. Optical coherence tomography: principles and applications. Academic press, 2006.
[Wang-2012_ Book] Wang, Lihong V., and Hsin-I. Wu. Biomedical optics: principles and imaging. John Wiley & Sons, 2012.
[Born-1999] Born, Max, and Emil Wolf. Principles of optics: electromagnetic theory of propagation, interference and diffraction of light. CUP Archive, 1999.
[Fercher-1995] Fercher, Adolph F., Ch K. Hitzenberger, G. Kamp, and Sy Y. El-Zaiat. "Measurement of intraocular distances by backscattering spectral interferometry." Optics Communications 117, no. 1 (1995): 43-48.
[Fercher-1979] Fercher, A. F., H. Bartelt, H. Becker, and E. Wiltschko. "Image formation by inversion of scattered field data: experiments and computational simulation." Applied optics 18, no. 14 (1979): 2427-2439.
[Wolf-1969] Wolf, Emil. "Three-dimensional structure determination of semi-transparent objects from holographic data." Optics Communications 1, no. 4 (1969): 153-156.
[Dändliker-1970] Dändliker, R., and K. Weiss. "Reconstruction of the three-dimensional refractive index from scattered waves." Optics communications 1, no. 7 (1970): 323-328.
[Bracewell-2000] Bracewell R N 2000 "The Fourier Transform and its Applications" (Singapore: McGraw-Hill).
[Podoleanu-1999] Podoleanu, Adrian Gh, and David A. Jackson. "Noise analysis of a combined optical coherence tomograph and a confocal scanning ophthalmoscope." Applied Optics 38, no. 10 (1999): 2116-2127.
[Rollins-1999] Rollins, Andrew M., and Joseph A. Izatt. "Optimal interferometer designs for optical coherence tomography." Optics letters 24, no. 21 (1999): 1484-1486.
[Wojtkowski-2004] Wojtkowski, Maciej, Vivek Srinivasan, Tony Ko, James Fujimoto, Andrzej Kowalczyk, and Jay Duker. "Ultrahigh-resolution, high-speed, Fourier domain optical coherence tomography and methods for dispersion compensation." Optics express 12, no. 11 (2004): 2404-2422.
[Wang-2007_OMAG] Wang, Ruikang K., Steven L. Jacques, Zhenhe Ma, Sawan Hurst, Stephen R. Hanson, and Andras Gruber. "Three dimensional optical angiography." Optics Express 15, no. 7 (2007): 4083-4097.
[An-2010_UHS] An, Lin, Jia Qin, and Ruikang K. Wang. "Ultrahigh sensitive optical microangiography for in vivo imaging of microcirculations within human skin tissue beds." Optics express 18, no. 8 (2010): 8220-8228.
[Yousefi-2011] Yousefi, Siavash, Zhongwei Zhi, and Ruikang K. Wang. "Eigendecomposition-based clutter filtering technique for optical microangiography." Biomedical Engineering, IEEE Transactions on 58, no. 8 (2011): 2316-2323.
[An-2011] An, Lin, Tueng T. Shen, and Ruikang K. Wang. "Using ultrahigh sensitive optical microangiography to achieve comprehensive depth resolved microvasculature mapping for human retina." Journal of biomedical optics 16, no. 10 (2011): 106013-106013.
[Qin-2011] Qin, Jia, Jingying Jiang, Lin An, Daniel Gareau, and Ruikang K. Wang. "In vivo volumetric imaging of microcirculation within human skin under psoriatic conditions using optical microangiography." Lasers in surgery and medicine43, no. 2 (2011): 122-129.
[Jia-2011] Jia, Yali, Peng Li, and Ruikang K. Wang. "Optical microangiography provides an ability to monitor responses of cerebral microcirculation to hypoxia and hyperoxia in mice." Journal of Biomedical Optics 16, no. 9 (2011): 096019-096019.

[Zhi-2011] Zhi, Zhongwei, Yeongri Jung, Yali Jia, Lin An, and Ruikang K. Wang. "Highly sensitive imaging of renal microcirculation in vivo using ultrahigh sensitive optical microangiography." Biomedical optics express 2, no. 5 (2011): 1059-1068.
[Subhash-2010] H. M. Subhash, V. Davila, H. Sun, A. T. Nguyen-Huynh, X. Shi, A. L. Nuttall and R. K. Wang, "Volumetric in vivo imaging of microvascular perfusion within the intact cochlea in mice using ultra-high sensitive optical microangiography," *IEEE Transactions on Medical Imaging*, doi: 10.1109/TMI.2010.2072934.
[Vakoc-2005] B. Vakoc, S. Yun, J. de Boer, G. Tearney and B. Bouma, "Phase-resolved optical frequency domain imaging," *Optics Express*, vol. 13, no. 14, pp. 5483-5493, 2005.
[Kruse-2002] D. E. Kruse and K. W. Ferrara, "A new high resolution color flow system using an eigendecomposition-based adaptive filter for clutter rejection," *IEEE Transactions on Ultrasonics, Ferroelectrics and Frequency Control*, vol. 49, no. 10, pp. 1384-1399, 2002.
[Song-2006] F. Song, D. Zhang and X. Gong, "Performance evaluation of eigendecomposition-based adaptive clutter filter for color flow imaging," *Ultrasonics*, vol. 44, pp. e67-71, 2006.
[Marks-2006] J. G. Marks and J. J. Miller, "Lookingbill and Marks' Principles of Dermatology," *Saunders Elsevier*, ISBN 1416031855, 2006.
[Eriksson-1980] E. Eriksson, J. V. Boykin and R. N. Pittman, "*Microvascular Research*, vol. 19, no. 3, pp. 374-379, 1980.
[Lovstakken-2006] L. Lovstakken, S. Bjaerum, K. Kristoffersen, R. Haaverstad and H. Torp, "Real-time adaptive clutter rejection filtering in color flow imaging using power method iterations," *IEEE Transactions on Ultrasonics, Ferroelectrics and Frequency Control* , vol. 53, no. 5, pp. 1597-1608, 2006.
[Misgeld-2006] Misgeld T, Kerschensteiner M. In vivo imaging of the diseased nervous system. Nature Reviews Neuroscience 2006; 7, no. 6: 449-463.
[McDonald-2003] McDonald DM, Choyke P. Imaging of angiogenesis: from microscope to clinic. Nature medicine 2003; 9, no. 6: 713-725.
[Molina-2005] Molina C, Saver J. Extending reperfusion therapy for acute ischemic stroke emerging pharmacological, mechanical, and imaging strategies. *Stroke* 2005; 36, no. 10: 2311-2320.
[Martin-1997] Martin P. Wound healing--aiming for perfect skin regeneration. *Science* 1997; 276, no. 5309: 75-81.
[Wollstein-2005] Wollstein G, Paunescu L, Ko T Fujimoto JG, et al. Ultrahigh-resolution optical coherence tomography in glaucoma. Ophthalmology 2005**;** 112, no. 2: 229-237.
[Hee-1996] Hee M, Baumal C, Puliafito C, et al. Optical coherence tomography of age-related macular degeneration and choroidal neovascularization. *Ophthalmology* 1996; *103*(8), 1260.
[Miles-2012] Miles KA, Lee TY, Goh V, et al. Current status and guidelines for the assessment of tumor vascular support with dynamic contrast-enhanced computed tomography. European radiology 2012; 1-12.
[Tan-2012] Tan TL, Sim KS, Tso CP, Chong AK. Contrast enhancement of computed tomography images by adaptive histogram equalization-application for improved ischemic stroke detection. International Journal of Imaging Systems and Technology. 2012; 22(3), 153-160.
[Pisano-2000] Pisano ED, Cole EB, Hemminger BM, et al. Image Processing Algorithms for Digital Mammography: A Pictorial Essay1. Radiographics 2000; 20(5), 1479-1491.
[Gonzalez-2002] Gonzalez RC, Woods RE. Digital image processing. *Prentice Hall* 2002; 519-532.

[Pizer-1987] Pizer S M, Amburn E P, Austin J D, Cromartie R, Geselowitz A, Greer T, Romeny B, Zimmerman J, Zuiderveld K. Adaptive histogram equalization and its variations. *Computer vision, graphics, and image processing* 1987; 39, no. 3: 355-368.
[Pizer-1990] Pizer SM, Johnston RE, Ericksen JP, Yankaskas BC, Muller KE. Contrast-limited adaptive histogram equalization: speed and effectiveness. Proceedings of First Conference on Visualization in Biomedical Computing, May 1990.
[Zuiderveld-1997] Zuiderveld K. Contrast limited adaptive histogram equalization. In *Graphics gems IV* 1997; (pp. 474-485). Academic Press Professional, Inc.
[Reif-2012] Reif R, Qin J, An L, Zhi Z, Dziennis S, Wang RK. "Quantifying optical microangiography images obtained from a spectral domain optical coherence tomography system." *Journal of Biomedical Imaging* 2012; 9.
[Saleem-2012] Saleem A, Azeddine B, Boualem B. Image fusion-based contrast enhancement. *EURASIP Journal on Image and Video Processing* 2012; no. 1: 10.
[Masters-2004] Masters B R. Fractal analysis of the vascular tree in the human retina. *Annual Review of Biomedical Engineering* 2004; 6: 427-452.
[Kleinfeld-1998] D. Kleinfeld, M. P. Partha, F. Helmchen and W. Denk, "Fluctuations and stimulus-induced changes in blood flow observed in individual capillaries in layers 2 through 4 of rat neocortex." Proc. Nat. Acad. Sci., vol. 95, no. 26, pp. 15741-15746 (1998).
[Hagen-1998] C. E. Hagen, M. R. Daha, J. O. Hermans, K. Andrassy, E. Csernok, G. Gaskin, P. Lesavre et al., "Diagnostic value of standardized assays for anti-neutrophil cytoplasmic antibodies in idiopathic systemic vasculitis," Kidney int. Vol. 53, no. 3, pp. 743-753 (1998).
[Jennette-1997] J. C. Jennette and R. J. Falk, "Small-vessel vasculitis," New England Journal of Medicine, vol. 337, no. 21, pp. 1512-1523 (1997).
[Donaldson-1963] V. H. Donaldson and R. R. Evans, "A biochemical abnormality in hereditary angioneurotic edema: absence of serum inhibitor of C 1-esterase," The American journal of medicine, vol. 35, no. 1, pp. 37-44 (1963).
[Horstmann-1951] P. Horstmann, "The oxygen consumption in diabetes mellitus," Acta. Medica. Scandinavica vol. 139, no. 4 pp. 326-330 (1951).
[Seyfried-2010] T. N. Seyfried and L. M. Shelton, "Cancer as a metabolic disease," Nutr. Metab. (Lond) vol. 7, no. 7 (2010).
[Wang-2011] Z. Wang, E. Klipfell, B. J. Bennett, R. Koeth, B. S. Levison, B. DuGar, A. E. Feldstein et al., "Gut flora metabolism of phosphatidylcholine promotes cardiovascular disease," Natr. Vol. 472, No. 7341, pp. 57-63 (2011).
[Lee-1999] J. M. Lee, G. J. Zipfel and D. W. Choi, "The changing landscape of ischaemic brain injury mechanisms," Natr., vol. 399, pp. A7-A14 (1999).
[Gariano-2005] R. F. Gariano and T. W. Gardner, "Retinal angiogenesis in development and disease," Natr. vol. 438, no. 7070, pp. 960-966 (2005).
[Stern-1975] M. D. Stern, "In vivo evaluation of microcirculation by coherent light scattering," vol 254, pp. 56-58 (1975).
[Herrick-1998] A. L. Herrick and S. Clark, "Quantifying digital vascular disease in patients with primary Raynaud's phenomenon and systemic sclerosis," Annals of the rheumatic diseases, vol. 57, no. 2, pp. 70-78 (1998).
[Murray-2004] A. K. Murray, A. L. Herrick and T. A. King. "Laser Doppler imaging: a developing technique for application in the rheumatic diseases," Rheumatology, vol. 43, no. 10, pp. 1210-1218 (2004).

[Bornmyr-2001] S. Bornmyr, J. Castenfors, E. Evander, G. Olsson, U. Hjortsberg, and P. Wollmer, "Effect of local cold provocation on systolic blood pressure and skin blood flow in the finger," Clinical Physiology, vol. 21, no. 5, pp. 570-575 (2001).
[Niazi-1993] Z. Niazi, T. Essex, R. Papini, D. Scott, N. R. McLean and M. J. M. Black, "New laser Doppler scanner, a valuable adjunct in burn depth assessment," Burns, vol. 19, no. 6, pp. 485-489 (1993).
[Jeng-2006] J. C. Jeng, A. Bridgeman, L. Shivnan, P. M. Thornton, H. Alam, T. J. Clarke, K. A. Jablonski and M. H. Jordan, "Laser Doppler imaging determines need for excision and grafting in advance of clinical judgment: a prospective blinded trial," Burns, vol. 29, no. 7, pp. 665-670 (2003).
[Kloppenberg-2001] F. Kloppenberg, G. Beerthuizen and H. Ten Duis, "Perfusion of burn wounds assessed by laser Doppler imaging is related to burn depth and healing time," Burns, vol. 27, no. 4, pp. 359-363 (2001).
[Harrison-1993] D. K. Harrison, N. C. Abbot, J. Swanson Beck and P. T. McCollum, "A preliminary assessment of laser Doppler perfusion imaging in human skin using the tuberculin reaction as a model," Physiological measurement, vol. 14, no. 3, pp. 241 (1993).
[Clough-1999] G. F. Clough, "Role of nitric oxide in the regulation of microvascular perfusion in human skin in vivo," The Journal of physiology, vol. 516, no. 2, pp. 549-557 (1999).
[Newton-2002] D. J. Newton, F. Khan, J. J. F. Belch, M. R. Mitchell and G. P. Leese, "Blood flow changes in diabetic foot ulcers treated with dermal replacement therapy," The Journal of foot and ankle surgery, vol. 41, no. 4, pp. 233-237 (2002).
[Clark-2003] S. Clark, G. Dunn, T. Moore, M. Jayson, T. A. King and A. L. Herrick, "Comparison of thermography and laser Doppler imaging in the assessment of Raynaud's phenomenon," Microvascular research, vol. 66, no. 1, pp. 73-76 (2003).
[Seifalian-1995] A. M. Seifalian, K. Chaloupka, and S. P. Parbhoo, "Laser Doppler perfusion imaging–a new technique for measuring breast skin blood flowm" Journal of Vascular Research, vol. 15, no. 3, pp. 125-130 (1995).
[Ferrell-2001] W. R. Ferrell, P. V. Balint, C. G. Egan, J. C. Lockhart and R. D. Sturrock, "Metacarpophalangeal Joints in Rheumatoid Arthritis: Laser Doppler Imaging—Initial Experience1," Radiology, vol. 220, no. 1, pp. 257-262 (2001).
[Maslov-2008] K. Maslov, H. F. Zhang, S. Hu and L. V. Wang, "Optical-resolution photoacoustic microscopy for in vivo imaging of single capillaries," Optics letters, vol. 33, no. 9, pp. 929-931 (2008).
[LHWang-2008] L. V. Wang, "Prospects of photoacoustic tomography," Medical physics, vol. 35 pp. 5758 (2008).
[Jiang-2012] Y. Jiang, A. Forbrich, T. Harrison and R. J. Zemp, "Blood oxygen flux estimation with a combined photoacoustic and high-frequency ultrasound microscopy system: a phantom study," Journal of Biomedical Optics, vol. 17, no. 3, pp. 0360121-0360128 (2012).
[Tomlins-2005] P. H. Tomlins and R. K. Wang, "Theory, developments and applications of optical coherence tomography," Journal of Physics D: Applied Physics, vol. 38, no. 15, pp. 2519 (2005).
[Fercher-2003] A. Fercher, W. Drexler, C. K. Hitzenberger and T. Lasser, "Optical coherence tomography-principles and applications," Reports on progress in physics, vol. 66, no. 2 pp. 239 (2003).

[Wang-2007_cerebro] R. K. Wang and S. Hurst, "Mapping of cerebro-vascular blood perfusion in mice with skin and skull intact by Optical Micro-angiography at 1.3 μm wavelength," Opt. Express, 15(18), 11402-11412 (2007).
[Izatt-1997] J. A. Izatt, M. D. Kulkarni, S. Yazdanfar, J. K. Barton, and A. J. Welch, "In vivo bidirectional color Doppler flow imaging of picoliter blood volumes using optical coherence tomography," Opt. Lett. 22(18), 1439–1441 (1997).
[Zhao-2000] Y. Zhao, Z. Chen, C. Saxer, S. Xiang, J. F. de Boer, and J. S. Nelson, "Phase-resolved optical coherence tomography and optical Doppler tomography for imaging blood flow in human skin with fast scanning speed and high velocity sensitivity," Opt. Lett. 25(2), 114–116 (2000).
[Wang-2008_retina] Y. Wang, B. A. Bower, J. A. Izatt, O. Tan and D. Huang, "Retinal blood flow measurement by circumpapillary Fourier domain Doppler optical coherence tomography." Journal of biomedical optics, 13(6), 064003-064003 (2008).
[Wang-2002] R. K. Wang, "Signal degradation by multiple scattering in optical coherence tomography of dense tissue: a Monte Carlo study towards optical clearing of biotissues," Physics in medicine and biology, 47(13), 2281 (2002).
[Szabo-2004] T. L. Szabo, "Diagnostic ultrasound imaging: inside out," Academic Press (2004).
[Srinivasan-2010] V. J. Srinivasan, S. Sakadžić, I. Gorczynska, S. Ruvinskaya, W. Wu, J. G. Fujimoto, and D. A. Boas, "Quantitative cerebral blood flow with optical coherence tomography," Optics express 18(3), 2477 (2010).
[Zhi-2011_volumetric] Z. Zhi, W. Cepurna, E. Johnson, T. Shen, J. Morrison and R. K. Wang, "Volumetric and quantitative imaging of retinal blood flow in rats with optical microangiography," Biomedical optics express, 2(3), 579-591 (2011).
[Zhi-2012_retina] Z. Zhi, X. Yin, S. Dziennis, T. Wietecha, K. L. Hudkins, C. E. Alpers and R. K. Wang, "Optical microangiography of retina and choroid and measurement of total retinal blood flow in mice," Biomedical optics express, 3(11), 2976 (2012).
[Makita-2011] S. Makita, F. Jaillon, M. Yamanari, M. Miura and Y. Yasuno, "Comprehensive in vivo micro-vascular imaging of the human eye by dual-beam-scan Doppler optical coherence angiography," Optics Express 19(2), 1271-1283 (2011).
[Choi-2012] W. J. Choi, B. Baumann, J. J. Liu, A. C. Clermont, E. P. Feener, J. S. Duker and J. G. Fujimoto, "Measurement of pulsatile total blood flow in the human and rat retina with ultrahigh speed spectral/Fourier domain OCT," Biomedical optics express, 3(5), 1047 (2012).
[Rubin-1993] J. M. Rubin and R. S.Alder, "Power Doppler expands standard color capability," Diagnostic imaing, 15(12), 66-9 (1993).
[Babcock-1996] D. S. Babcock, H. Patriquin, M. LaFortune, M Dauzat. "Power Doppler sonography: basic principles and clinical applications in children," Pediatric Radiology 26(2): 109-115 (1996).
[Shung-1992] K. K. Shung, G. Cloutier and C. C. Lim, "The effects of hematocrit, shear rate, and turbulence on ultrasonic Doppler spectrum from blood," IEEE Transactions on Biomedical Engineering, 39(5), 462-469 (1992).
[Huang-2011] C. C. Huang and Y. C. Chang, "Ultrasonic attenuation and backscatter from flowing whole blood are dependent on shear rate and hematocrit between 10 and 50 MHz," IEEE Transactions on Ultrasonics, Ferroelectrics and Frequency Control, 58(2), 357-368 (2011).
[Wang_2010] Y. Wang, and R.K. Wang, "Autocorrelation optical coherence tomography for mapping transverse particle-flow velocity," Optics Letters 35, 3538-3540 (2010).

[Lee-2013] J. Lee, W. Wu, F. Lesage and D. A. Boas, "Multiple-capillary measurement of RBC speed, flux, and density with optical coherence tomography," Journal of Cerebral Blood Flow & Metabolism, 33(11), 1707-1710 (2013).
[Schmidt-1986] R. Schmidt, "Multiple emitter location and signal parameter estimation," Antennas and Propagation, IEEE Transactions on 34 (3), 276-280. (1986).
[Maple-1987] S. L. Maple, Jr., Digital Spectral Analysis with Applications, (Englewood Cliffs, NJ: Prentice-Hall, 1987).
[Castanié-2013] Castanié, F. (Ed.), "Digital spectral analysis: parametric, non-parametric and advanced methods," John Wiley & Sons, (2013).
[Shannon-1949] C.E. Shannon, "Communication in the presence of noise," Proceedings of the IRE 37(1): 10-21 (1949).
[Cobbold-2007] R.S.C. Cobbold, Foundations of Biomedical Ultrasound. Oxford University Press. pp. 422–423 (2007).
[Devor-2012] A. Devor, S. Sakadžić, V. J. Srinivasan, M. A. Yaseen, K. Nizar, P. A. Saisan and D. A. Boas, "Frontiers in optical imaging of cerebral blood flow and metabolism," Journal of Cerebral Blood Flow & Metabolism, 32(7), 1259-1276 (2012).
[Lee-2012] J. Lee, W. Wu, J. Y. Jiang, B. Zhu and D. A. Boas, "Dynamic light scattering optical coherence tomography," Optics Express 20(20): 22262-22277 (2012).
[Unekawa-2010] M. Unekawa, M. Tomita, Y. Tomita, H. Toriumi, K. Miyaki and N. Suzuki, "RBC velocities in single capillaries of mouse and rat brains are the same, despite 10-fold difference in body size," Brain research 1320: 69-73 (2010).
[Nagahara-2011] M. Nagahara, Y. Tamaki, A. Tomidokoro and M. Araie, "In vivo measurement of blood velocity in human major retinal vessels using the laser speckle method," Investigative Ophthalmology & Visual Science 52(1): 87-92 (2011).
[Shi-2013] L. Shi, J. Qin, R. Reif and R. K. Wang, "Wide velocity range Doppler optical microangiography using optimized step-scanning protocol with phase variance mask," Journal of biomedical optics, 18(10): 106015-106015 (2013)
[Serov-2001] A. Serov, W. Steenbergen, and F. F. M. de Mul, "Prediction of the photodetector signal generated by Doppler-induced speckle fluctuations: theory and some validations," J. Opt. Soc. Am. A 18, 622-630 (2001).
[Serov-2005] A. Serov, B. Steinacher and T. Lasser, "Full-field laser Doppler perfusion imaging and monitoring with an intelligent CMOS camera," Optics Express 13(10): 3681-3689 (2005).
[Makita-2006] S. Makita, Y. Hong, M. Yamanari, T. Yatagai, and Y. Yasuno, "Optical coherence angiography," Optics Express, vol, 14(17), 7821, (2006).
[Mariampillai-2008] A. Mariampillai, B. A. Standish, E. H. Moriyama, M. Khurana, N. R. Munce, M. K. Leung and [Yang-2008] V. X. Yang, "Speckle variance detection of microvasculature using swept-source optical coherence tomography," Optics letters, 33(13), 1530-1532, (2008).
[Kim-2011] D. Y. Kim, J. Fingler, J. S. Werner, D. M. Schwartz, S. E. Fraser and R. J. Zawadzki, "In vivo volumetric imaging of human retinal circulation with phase-variance optical coherence tomography," Biomedical optics express 2, no. 6 : 1504-1513, (2011).
J. Fingler, D. Schwartz, C. Yang and S. E. Fraser, "Mobility and transverse flow visualization using phase variance contrast with spectral domain optical coherence tomography," Optics express 15, no. 20: 12636-12653 (2007).
[Akaike-1973] H. Akaike, "Maximum likelihood identification of Gaussian autoregressive moving average models," Biometrika, 60(2), 255-265 (1973).

[Rissanen-1978] J. Rissanen, "Modeling by shortest data description," Automatica, 14(5), 465-471 (1978).
[Schwarz-1978] G. Schwarz, "Estimating the dimension of a model," The annals of statistics, 6(2), 461-46 (1978).
[Kasai-1985] C. Kasai, K. Namekawa, A. Koyano and R. Omoto, “Real-time two-dimensional blood flow imaging using an autocorrelation technique,” IEEE Trans. Sonics Ultrason, 32(3), 458-464 (1985).
[Chan-2013] A. C. Chan, E. Y. Lam and V. J. Srinivasan, “Comparison of kasai autocorrelation and maximum likelihood estimators for Doppler optical coherence tomography,” IEEE transactions on medical imaging, 32(6), 1033 (2013).
[Stoica-1989] P. Stoica, and N. Arye, “MUSIC, maximum likelihood, and Cramer-Rao bound,” Acoustics, Speech and Signal Processing, IEEE Transactions on, 37(5), 720-741 (1989).
[Zhang-2009] W. Zhang, J. J. Iliff, C. J. Campbell, R.K. Wang, P.D. Hurn, N. J. Alkayed, “Role of Soluble Epoxide Hydrolase in the Sex-Specific Vascular Response to Cerebral Ischemia”, Journal of Cerebral Blood Flow & Metabolism, 29, 1475-1481 (2009).
[Kellogg-2006] D. L. Kellogg, “In vivo mechanisms of cutaneous vasodilation and vasoconstriction in humans during thermoregulatory challenges,” J. of Appl. Physiol. **100**(5), 1709-1718 (2006).
[Baun-2012] J. Baun, Vascular ultrasound: physics, instrumentation and hemodynamics, ProSono publishing, December 2012.
[Kinmonth-1952] J.B. Kinmonth, “Lymphangiography in man; a method of outlining lymphatic trunks at operation,” Clinical Science. 11: 13–20 (1952).
[Kinmonth-1955] J. B. Kinmonth, G. W. Taylor and R. K. Harper, Lymphangiography. British Medical Journal, 1(4919), 940, 1955.
[Rabin-2006] O. Rabin, J. Perez, J. Grimm, G. Wojtkiewicz, and R. Weissleder, "An X-ray computed tomography imaging agent based on long-circulating bismuth sulphide nanoparticles," Nature materials, 5(2), 118-122, 2006.
[Lardinois-2003] D. Lardinois, W.Weder, T.F. Hany, et al. “Staging of non–small-cell lung cancer with integrated positronemission tomography and computed tomography,” The New England Journal of Medicine, 348: 2500–2507 (2003).
[Modi-2007] S. Modi, A. W. B. Stanton, P. S. Mortimer, and J. R. Levick. "Clinical assessment of human lymph flow using removal rate constants of interstitial macromolecules: a critical review of lymphoscintigraphy." Lymphatic research and biology 5, no. 3: 183-202, (2007).
[Proulx-2013] S. T. Proulx and M. Detmar. "Molecular mechanisms and imaging of lymphatic metastasis." Experimental Cell Research (2013).
[Vassallo-1992] P. Vassallo, K. Wernecke, N. Roos, PE. Peters, "Differentiation of benign from malignant superficial lymphadenopathy: the role of high-resolution US," Radiology 183: 215–220, 1992.
[Tregnaghi-1997] A. Tregnaghi, A. De Candia, M. Calderone, L. Cellini, C. R. Rossi, E. Talenti, S. Blandamura, S. Borsato, P. C. Muzzio, L. Rubaltelli, "Ultrasonographic evaluation of superficial lymph node metastases in melanoma," European Journal of Radiology, 24: 216–221, 1997.
[Yang-2001] W. T. Yang, C. Metreweli, P. K. Lam, J. Chang, "Benign and malignant breast masses and axillary nodes: evaluation with echo-enhanced color power Doppler US. Radiology," 220: 795–802, 2001

[Choi-2004] S. H. Choi, Y. Kono, J. Corbeil, O. Lucidarme, R. F. Mattrey, "Model to quantify lymph node enhancement on indirect sonographic lymphography", American Journal of Roentgenology, 183: 513–517, 2004.
[Yang-2012] J. M. Yang, C. Favazza, R. Chen, J. Yao, X. Cai, K. Maslov and L. V. Wang, "Simultaneous functional photoacoustic and ultrasonic endoscopy of internal organs in vivo," Nature Medicine, 18(8), 1297-1302, 2012.
[De La Zerda-2008] A. De La Zerda, C. Zavaleta, S. Keren, S. Vaithilingam, S. Bodapati, Z. Liu, J. Levi et al. "Carbon nanotubes as photoacoustic molecular imaging agents in living mice." Nature nanotechnology 3, no. 9: 557-562, 2008.
[Pan-2010] D. Pan, M. Pramanik, A. Senpan, S. Ghosh, S. A. Wickline, L. V. Wang, and G. M. Lanza. "Near infrared photoacoustic detection of sentinel lymph nodes with gold nanobeacons." Biomaterials 31, no. 14: 4088-4093, 2010.
[Kim-2009] J. W. Kim, E. I. Galanzha, E. V. Shashkov, H. M. Moon, and V. P. Zharov. "Golden carbon nanotubes as multimodal photoacoustic and photothermal high-contrast molecular agents." nature nanotechnology 4, no. 10: 688-694, 2009.
[Lucarelli-2009] R. Lucarelli, M. Ogawa, N. Kosaka, B. Turkbey, H. Kobayashi, and Peter L. Choyke. "New approaches to lymphatic imaging." Lymphatic research and biology 7, no. 4: 205-214, 2009.
[Landsman-1976] M. L. Landsman, G. Kwant, G. A. Mook, and W. G. Zijlstra. "Light-absorbing properties, stability, and spectral stabilization of indocyanine green." Journal of applied physiology 40, no. 4: 575-583, 1976.
[Ghoroghchian-2009] P. Ghoroghchian, M. Therien, and D. Hammer. "In vivo fluorescence imaging: a personal perspective." Wiley Interdisciplinary Reviews: Nanomedicine and Nanobiotechnology 1, no. 2: 156-167, 2009.
[Hama-2007] Y. Hama, Y. Koyama, Y. Urano, P. Choyke, and Hisataka Kobayashi. "Two-color lymphatic mapping using Ig-conjugated near infrared optical probes." Journal of Investigative Dermatology 127, no. 10: 2351-2356, 2007.
[Gao-2004] X. Gao, Y. Cui, R. M. Levenson, L. Chung, and S. Nie. "In vivo cancer targeting and imaging with semiconductor quantum dots." Nature biotechnology 22, no. 8: 969-976, 2004.
[Zhang-2011] F. Zhang, G. Niu, G. Lu, and X. Chen. "Preclinical lymphatic imaging." Molecular Imaging and Biology 13, no. 4: 599-612, 2011.
[Kosaka-2009] N. Kosaka, M. Ogawa, N. Sato, P. L. Choyke, and H. Kobayashi. "In vivo real-time, multicolor, quantum dot lymphatic imaging." Journal of Investigative Dermatology 129, no. 12: 2818-2822, 2009.
[Kim-2003] S. Kim, Y. T. Lim, E. G. Soltesz, A. M. De Grand, J. Lee, A. Nakayama, J. A. Parker et al. "Near-infrared fluorescent type II quantum dots for sentinel lymph node mapping." Nature biotechnology 22, no. 1: 93-97, 2003.
[Knapp-2007] D. Knapp, L. G. Adams, A. M. DeGrand, J. D. Niles, J. A. Ramos-Vara, A. B. Weil, M. A. O'Donnell, M. D. Lucroy, and J. V. oni. "Sentinel lymph node mapping of invasive urinary bladder cancer in animal models using invisible light." European urology 52, no. 6: 1700-1709, 2007.
[Ramos-Vara-2005] J. A. Ramos-Vara, "Technical aspects of immunohistochemistry." Veterinary Pathology Online 42, no. 4 (2005): 405-426.
[Mäkinen-2001] T. Mäkinen, T. Veikkola, S. Mustjoki, T. Karpanen, B. Catimel, E. C. Nice, L. Wise et al. "Isolated lymphatic endothelial cells transduce growth, survival and migratory signals via the VEGF-C/D receptor VEGFR-3." The EMBO journal 20, no. 17: 4762-4773, 2001.

[Hong-2002] Y. Hong, N. Harvey, Y. Noh, V. Schacht, S. Hirakawa, M. Detmar and Guillermo Oliver, "Prox1 is a master control gene in the program specifying lymphatic endothelial cell fate," Developmental dynamics 225, no. 3: 351-357, 2002.
[Breiteneder-Geleff-1999] S. Breiteneder-Geleff, A. Soleiman, H. Kowalski, R. Horvat, G. Amann, E. Kriehuber, K. Diem et al. "Angiosarcomas express mixed endothelial phenotypes of blood and lymphatic capillaries: podoplanin as a specific marker for lymphatic endothelium." The American journal of pathology 154, no. 2: 385-394, 1999.
[Jackson-2003] D. Jackson, "The Lymphatics Revisited: New Perspectives from the Hyaluronan Receptor LYVE-1," Trends in Cardiovascular Medicine, Volume 13, Issue 1, Pages 1–7, January 2003.
[Adams-2007] R. Adams and K. Alitalo. "Molecular regulation of angiogenesis and lymphangiogenesis." Nature Reviews Molecular Cell Biology 8, no. 6 : 464-478, 2007.
[Maby-El Hajjami-2008] H. Maby-El Hajjami and T. V. Petrova. "Developmental and pathological lymphangiogenesis: from models to human disease." Histochemistry and cell biology 130, no. 6: 1063-1078, 2008.
[Mäkinen-2005] Mäkinen, Taija, et al. "PDZ interaction site in ephrinB2 is required for the remodeling of lymphatic vasculature." Genes & development 19.3 (2005): 397-410.
[Martínez-Corral-2012] I. Martínez-Corral, D. Olmeda, R. Diéguez-Hurtado, T. Tammela, K. Alitalo and S. Ortega. "In vivo imaging of lymphatic vessels in development, wound healing, inflammation, and tumor metastasis." Proceedings of the National Academy of Sciences 109, no. 16 (2012): 6223-6228.
[Weller-2003] G. Weller, ER, E. Lu, M. Csikari, A. L. Klibanov, D. Fischer, W. R. Wagner, and F. S. Villanueva. "Ultrasound imaging of acute cardiac transplant rejection with microbubbles targeted to intercellular adhesion molecule-1." Circulation 108, no. 2: 218-224, 2003.
[Korpanty-2007] G. Korpanty, J. G. Carbon, P. A. Grayburn, J. B. Fleming, and R. A. Brekken. "Monitoring response to anticancer therapy by targeting microbubbles to tumor vasculature." Clinical Cancer Research 13, no. 1: 323-330, 2007.
[Willmann-2008] J. K. Willmann, R. Paulmurugan, K. Chen, O. Gheysens, M. Rodriguez-Porcel, A. M. Lutz, I. Y. Chen, X. Chen, and S. S. Gambhir. "US Imaging of Tumor Angiogenesis with Microbubbles Targeted to Vascular Endothelial Growth Factor Receptor Type 2 in Mice1." Radiology 246, no. 2: 508-518, 2008.
[Burton-2008] J. B. Burton, M. Johnson, M. Sato, S. Boon S. Koh, D. J. Mulholland, D. Stout, A. F. Chatziioannou, M. E. Phelps, H. Wu, and L. Wu. "Adenovirus-mediated gene expression imaging to directly detect sentinel lymph node metastasis of prostate cancer." Nature medicine 14, no. 8: 882-888, 2008.
[Kalchenko-2012] V. Kalchenko, Y. Kuznetsov, I. Meglinski, and A. Harmelin, "Label free in vivo laser speckle imaging of blood and lymph vessels," Journal of Biomedical Optics 17, no. 5: 0505021-0505023, 2012.
[Wang-2010] R.K. Wang, L. An, P. Francis and D. Wilson, “Depth-resolved imaging of capillary networks in retina and choroid using ultrahigh sensitive optical microangiography”, Optics Letters 35, 1467-1469 (2010).
[Jung-2011] Y. Jung, R. Reif, Y. Zeng, and R. K. Wang. "Three-dimensional high-resolution imaging of gold nanorods uptake in sentinel lymph nodes." Nano letters 11, no. 7: 2938-2943, 2011.

[Jung-2010] Y. Jung, Z. Zhi, and R. K. Wang. "Three-dimensional optical imaging of microvascular networks within intact lymph node in vivo." Journal of biomedical optics 15.5: 050501-050501, 2010.
[Zhi-2012] Z. Zhi, Y. Jung and R. K. Wang. “Label-free 3D imaging of microstructure, blood and lymphatic vessels within tissue beds in vivo”, Optics Letters, Vol 37 (5), 812-814 (2012).
[Vakoc-2009] B. Vakoc, R. M. Lanning, J. A. Tyrrell, et al. "Three-dimensional microscopy of the tumor microenvironment in vivo using optical frequency domain imaging." Nature medicine 15, no. 10: 1219-1223 (2009).
[Frangi-1998] A. Frangi, W. Niessen, K. Vincken, and M. Viergever. "Multiscale vessel enhancement filtering." Medical Image Computing and Computer-Assisted Interventation—MICCAI’98 : 130-137 (1998).
[Yousefi-2013_LymphJBO] S. Yousefi, J. Qin, Z. Zhi and R. K. Wang, “Label-free optical lymphangiography: development of an automatic segmentation method applied to optical coherence tomography to visualize lymphatic vessels using Hessian filters,” Journal of Biomedical Optics, 18(8): 086004-086004, 2013.
[Jung-2013] Y. Jung, S. Dziennis, Z. Zhi, R. Reif, Y. Zheng and R. K. Wang, “Tracking Dynamic Microvascular Changes during Healing after Complete Biopsy Punch on the Mouse Pinna Using Optical Microangiography,” PloS one, 8(2), e57976 (2013).
[Veronesi-1997] P. Veronesi, G. Paganelli, V. Galimberti et al., “Sentinel-node biopsy to avoid axillary dissection in breast cancer with clinically negative lymph-nodes,” Lancet 349, 1864–1867, 1997.
[Krag-1998] D. Krag, D. Weaver, T. Ashikaga et al., “The sentinel node in breast cancer—a multicenter validation study,” N. Engl. J. Med. 339, 941–946, 1998.
[Purushotham-2005] A. D. Purushotham, S. Upponi, M. B. Klevesath, L. Millar, J. Peter Myles, and S. W. Duffy, “Morbidity after sentinel lymph node biopsy in primary breast cancer: results from a randomized controlled trial,” J. Clin. Oncol. 23, 4312–4321 2005.
[Li-2000] X. Li, C. Chudoba, T. Ko, C. Pitris, and J. G. Fujimoto, “Imaging needle for optical coherence tomography,” Opt. Lett. 25, 1520–1522, 2000.
[Singer-1999] Singer A.J. and Clark R.A., ”Cutaneous wound healing," New England J Med, 341(10): 738-746 (1999).
[Barker-1989] Barker J.H., Hammersen F., Bondar I., Uhl E., Galla T J., Menger M.D. and Messmer K., "The hairless mouse ear for in vivo studies of skin microcirculation," Plastic and reconstructive surgery, 83(6), 948-959 (1989).
[Peplow-2010] Peplow P.V., Chung T.Y. and Baxter G.D., "Laser photobiomodulation of wound healing: a review of experimental studies in mouse and rat animal models," Photomedicine and Laser Surgery, 28(3), 291-325 (2010).
[Werner-2003] Werner S. and Grose R., "Regulation of wound healing by growth factors and cytokines," Physiological reviews, 83(3), 835-870 (2003).
[Rege-2012] Rege A., Thakor N.V., Rhie K. and Pathak A.P., "In vivo laser speckle imaging reveals microvascular remodeling and hemodynamic changes during wound healing angiogenesis," Angiogenesis, 15(1), 87-98 (2012)
[Mallett-1992] Mallett S.V. and Cox D.J.A., “Thrombelastography,” British Journal of Anaesthesia, 69(3), 307-313 (1992).
[Raghow-1994] Raghow R., “The role of extracellular matrix in postinflammatory wound healing and fibrosis,” The FASEB journal, 8(11), 823-831 (1994).

[Boyd-1959] Boyd J. F. and Smith A. N., “The effect of histamine and a histamine-releasing agent (compound 48/80) on wound healing,” The Journal of Pathology and Bacteriology, 78(2), 379-388 (1959).
[Gillitzer-2001] Gillitzer R. and Goebeler M., “Chemokines in cutaneous wound healing,” Journal of Leukocyte Biology, 69(4), 513-521 (2001).
[Rappolee-1988] Rappolee D.A., Mark D., Banda M.J. and Werb Z., “Wound macrophages express TGF-alpha and other growth factors in vivo: analysis by mRNA phenotyping,” Science, 241(4866), 708-712 (1988).
[Oladipupo-2011] Oladipupo S., Hu S., Kovalski J., Yao J., Santeford A., Sohn R.E. and Arbeit J. M., "VEGF is essential for hypoxia-inducible factor-mediated neovascularization but dispensable for endothelial sprouting," Proceedings of the National Academy of Sciences, 108(32), 13264-13269 (2011).
[Song-2010] Song G., Nguyen D.T., Pietramaggiori G., Scherer S., Chen B., Zhan Q. and Murphy G. F., "Use of the parabiotic model in studies of cutaneous wound healing to define the participation of circulating cells," Wound Repair and Regeneration, 18(4), 426-432 (2010).
[Tonnesen-2000] Tonnesen M.G., Feng X. and Clark R. A., "Angiogenesis in wound healing," Journal of Investigative Dermatology symposium proceedings, 5(1): 40-46, Nature Publishing Group, (2000).
[Greenhalgh-1998] Greenhalgh D.G., "The role of apoptosis in wound healing," The International Journal of Biochemistry & Cell Biology, 30 (9): 1019–1030, (1998).
[Falanga-2005] Falanga V., "Wound healing and its impairment in the diabetic foot," The Lancet, 366(9498):1736–1743 (2005).
[Ruszczak-2003] Ruszczak Z., "Effect of collagen matrices on dermal wound healing," Advanced Drug Delivery Reviews, 55(12): 1595–1611 (2003).
[Larjava-2012] Larjava H., Häkkinen L. and Koivisto L., "Re-Epithelialization of Wounds," Oral Wound Healing, 81-123 (2012).
[DiPietro-1995] DiPietro L.A., "Wound healing: the role of the macrophage and other immune cells," Shock, 4(4): 233-240, (1995).
[Bartkova-2003] Bartkova J., Grøn B., Dabelsteen E. and Bartek J., "Cell-cycle regulatory proteins in human wound healing," Archives of Oral Biology, 48 (2): 125–32 (2003).
[Son-2005] Son H.J., Bae H.C., Kim, H.J., Lee D.H., Han D.W. and Park J. C., "Effects of β-glucan on proliferation and migration of fibroblasts," Current Applied Physics, 5 (5): 468–71 (2005).
[Eichler-2006] Eichler M.J., Carlson M.A., "Modeling dermal granulation tissue with the linear fibroblast-populated collagen matrix: a comparison with the round matrix model,” Journal of dermatological science 41(2): 97–108, (2006).
[Mirastschijski-2004] Mirastschijski U., Haaksma C.J., Tomasek J.J. and Agren M.S., "Matrix metalloproteinase inhibitor GM 6001 attenuates keratinocyte migration, contraction and myofibroblast formation in skin wounds," Experimental Cell Research, 299(2): 465–475 (2004).
[Hinz-2006] Hinz B., "Masters and servants of the force: the role of matrix adhesions in myofibroblast force perception and transmission," European Journal of Cell Biology, 85(3–4): 175–81 (2006).
[Vanderwee-2007] Vanderwee K., Michael C., Dealey C., Gunningberg L. and Defloor T., "Pressure ulcer prevalence in Europe: a pilot study," Journal of evaluation in clinical practice, 13(2): 227-235 (2007).

[Galiano-2004] Galiano R. D., Michaels V., Dobryansky M., Levine J. P., and Gurtner G.C., "Quantitative and reproducible murine model of excisional wound healing," Wound repair and regeneration, 12(4), 485-492 (2004).
[Sullivan-2001] Sullivan T. P., Eaglstein W. H., Davis S. C. and Mertz P., "The pig as a model for human wound healing," Wound repair and regeneration, 9(2), 66-76, (2001).
[Meyer-1978] Meyer W., Schwarz R. and Neurand K., "The skin of domestic mammals as a model for the human skin with special reference to the domestic pig," Curr. Probl. Derm., 7:39–52 (1978).
[Morris-1990] Morris G.M. and Hopewell J.W., "Epidermal cell kinetics of the pig: a review," Cell Tissue Kinetics, 23:271–82 (1990).
[Montagna-1966] Montagna W. and Yun J.S., "The skin of the domestic pig," J Invest Dermatol, 43:11–21 (1964).
[Winter-1966] Winter G. D. "A study of wound healing in the domestic pig," PhD Thesis, Birbeck College, University of London, (1966).
[Marcarian-1966] Marcarian H. Q. and Calhoun M. L., "Microscopic anatomy of the integument of adult swine," Am. J. Vet. Res., 27:765–72 (1966).
[Forbes-1969] Forbes P. D., "Vascular supply of the skin and hair in swine," Advances in the biology of the skin, 9th ed., New York, NY:Pergamon 419 (1969).
[Rothenberger-2013] Rothenberger J., Held M., Jaminet P., Schiefer J., Petersen W., Schaller H.E. and Rahmanian-[[Schwarz-2013] Schwarz A., "Development of an animal frostbite injury model using the Goettingen-Minipig," Burns, 40(2):268-273, (2013).
[Mortite-1947] Mortite A. R. and Henriques F. C., "Studies of thermal injury II. The relative importance of time and surface temperature in the causation of cutaneous burns," Am. J. Path., 23:695–720 (1947).
[Girard-2011] Girard M., Nicholas G., Strouthidis C., Ethier R. and Mari J. M., "Shadow removal and contrast enhancement in optical coherence tomography images of the human optic nerve head," Investigative ophthalmology & visual science 52(10): 7738-7748, (2011).
[Vermeer-2014] Vermeer K.A., Mo J., Weda J.J.A., Lemij H.G. and de Boer J.F., "Depth-resolved model-based reconstruction of attenuation coefficients in optical coherence tomography," Biomedical Optics Express, 5(1): 322-337 (2014).
[Reif-2012_cochlear] Reif R., Qin J., Shi L., Dziennis S., Zhi Z., Nuttall A.L. and Wang R.K., "Monitoring hypoxia induced changes in cochlear blood flow and hemoglobin concentration using a combined dual-wavelength laser speckle contrast imaging and Doppler optical microangiography system," PloS one, 7(12), e52041 (2012).
[Kuck-2014] Kuck M., Strese H., Alawi S.A., Meinke M. C., Fluhr J. W., Burbach G. J., Krah M., Sterry W. and Lademann J., "Evaluation of optical coherence tomography as a non-invasive diagnostic tool in cutaneous wound healing," Skin Research and Technology, 20(1): 1-7 (2014).
[Greaves-2013] Greaves N.S., Benatar B., Whiteside S., Alonso-Rasgado T., Baguneid M. and Bayat A., "Optical coherence tomography: a reliable alternative to invasive histological assessment of acute wound healing in human skin?," British Journal of Dermatology, (in press), (doi: 10.1111/bjd.12786) (2013).
[Vincent-1993] Vincent, L., "Morphological Grayscale Reconstruction in Image Analysis: Applications and Efficient Algorithms," IEEE Transactions on Image Processing, Vol. 2, No. 2, April, 1993, pp. 176-201.
[Metz-1978] Metz, C.E., "Basic principles of ROC analysis," In Seminars in nuclear medicine, 8(4), 283-298. WB Saunders, 1978.

[Staal-2004] J.J. Staal, M.D. Abramoff, M. Niemeijer, M.A. Viergever, B. van Ginneken, "Ridge based vessel segmentation in color images of the retina", IEEE Transactions on Medical Imaging, 2004, vol. 23, pp. 501-509.
[Niemeijer-2004] M. Niemeijer, J.J. Staal, B. van Ginneken, M. Loog, M.D. Abramoff, "Comparative study of retinal vessel segmentation methods on a new publicly available database", in: SPIE Medical Imaging, Editor(s): J. Michael Fitzpatrick, M. Sonka, SPIE, 2004, vol. 5370, pp. 648-656.
[Hoover-2000] Hoover, A., Kouznetsova, V., & Goldbaum, M., "Locating blood vessels in retinal images by piecewise threshold probing of a matched filter response," Medical Imaging, IEEE Transactions on, 19(3), 203-210 (2000).

[Niemeijer-2004] M. Niemeijer, J.J. Staal, B. van Ginneken, M. Loog, M.D. Abramoff, "Comparative study of retinal vessel segmentation methods on a new publicly available database", in: SPIE Medical Imaging, Editor(s): J. Michael Fitzpatrick, M. Sonka, SPIE, 2004, vol. 5370, pp. 648-656.
[Zana-2001] F. Zana and J. Klein, Segmentation of vessel-like patterns using mathematical morphology and curvature evaluation, IEEE Transactions on Image Processing 10(7), pp. 1010-1019, 2001.
[Jiang-2003] X. Jiang and D. Mojon, Adaptive local thresholding by verification-based multithreshold probing with application to vessel detection in retinal images, IEEE Transactions on Pattern Analysis and Machine Intelligence 25(1), pp. 131-137, 2003.
[Martínez-Pére-1999] M. Martínez-Pérez, A. Hughes, A. Stanton, S. Thom, A. Bharath, and K. Parker, Scale-space analysis for the characterisation of retinal blood vessels, in Medical Image Computing and Computer-Assisted Intervention - MICCAI'99, C. Taylor and A. Colchester, eds., pp. 90-97, 1999.
[Chaudhuri-1989] S. Chaudhuri, S. Chatterjee, N. Katz, M. Nelson, and M. Goldbaum, Detection of blood vessels in retinal images using two-dimensional matched filters, IEEE Transactions on Medical Imaging 8(3), pp. 263-269, 1989.
[Al-Diri-2009] B. Al-Diri, A. Hunter, D. Steel, An Active Contour Model for Segmenting and Measuring Retinal Vessels, IEEE Transactions on Medical Imaging, 28(9), pp. 1488-97, 2009.
[Goldenberg-2013] Goldenberg, D., Shahar, J., Loewenstein, A., & Goldstein, M., "Diameters of Retinal Blood Vessels in A Healthy Cohort As Measured By Spectral Domain Optical Coherence Tomography," RETINA, 33(9), 1888-1894 (2013).
[Pilch-2012] Pilch, M., Wenner, Y., Strohmayr, et al., "Automated segmentation of retinal blood vessels in spectral domain optical coherence tomography scans," Biomedical optics express, 3(7), 1478-1491 (2012).
[Srivastava-2013] Srivastava, S., Sharma, U., Durbin, M. K., & Schmoll, T., U.S. Patent Application 13/781,375 (2013).
[Lee-2014] Lee, J., Jiang, J. Y., Wu, W., Lesage, F., & Boas, D. A., "Statistical intensity variation analysis for rapid volumetric imaging of capillary network flux," Biomedical Optics Express, 5(4), 1160-1172 (2014).
[Poole-2014] Poole, K. M., Patil, C. A., Nelson, C. E. et al., "Longitudinal study of arteriogenesis with swept source optical coherence tomography and hyperspectral imaging," In SPIE BiOS, 89341Z-89341Z, International Society for Optics and Photonics, 2014.
[Kowalski-2014] Kowalski, W. J., Teslovich, N. C., Chen, C. Y., et al., "Simultaneous real-time quantification of blood flow and vascular growth in the chick embryo using optical coherence

tomography," In SPIE BiOS, 895307-895307, International Society for Optics and Photonics, 2014.
[Hachach-Haram-2013] Hachach-Haram N, Gregori M, Kirkpatrick N, Young R, Collier J., "Complications of facial fillers: resource implications for NHS hospitals," BMJ Case Rep. (2013).
[Sclafani-2009] Sclafani AP, Fagien S., "Treatment of injectable soft tissue filler complications," Dermatologic Surgery 35(s2):1672-1680 (2009).
[Bachmann-2009] Bachmann F, Erdmann R, Hartmann V, Wiest L, Rzany B., "The spectrum of adverse reactions after treatment with injectable fillers in the glabellar region: results from the Injectable Filler Safety Study," Dermatologic Surgery, 35(s2):1629-1634 (2009).
[Cohen-2008] Cohen JL., "Understanding, avoiding, and managing dermal filler complications," Dermatologic Surgery, 34(s1): S92-99, (2008).
[Grunebaum-2009] Grunebaum LD, Bogdan Allemann I, Dayan S, Mandy S, Baumann L., "The risk of alar necrosis associated with dermal filler injection," Dermatologic Surgery, 35(s2) :1635-1640 (2009).
[McCracken-2006] McCracken MS, Khan JA, Wulc AE, et al., "Hyaluronic acid gel (Restylane) filler for facial rhytids: lessons learned from American Society of Ophthalmic Plastic and Reconstructive Surgery member treatment of 286 patients," Ophthalmic Plastic & Reconstructive Surgery, 22(3): 188-191 (2006).
[Daines-2013] Daines SM, Williams EF., "Complications associated with injectable soft-tissue fillers: a 5-year retrospective review," JAMA Facial Plastic Surgery, 15(3): 226-231 (2013).
[Friedman-2002] Friedman PM, Mafong EA, Kauvar AN, Geronemus RG., "Safety data of injectable nonanimal stabilized hyaluronic acid gel for soft tissue augmentation," Dermatologic Surgery, 28(6): 491-494 (2002).
[Hanke-1991] Hanke CW, Higley HR, Jolivette DM, Swanson NA, Stegman SJ., "Abscess formation and local necrosis after treatment with Zyderm or Zyplast collagen implant," Journal of American Academy of Dermatology, 25(2 Pt 1): 319-326 (1991).
[Narins-2006] Narins RS, Jewell M, Rubin M, Cohen J, Strobos J., "Clinical conference: management of rare events following dermal fillers--focal necrosis and angry red bumps," Dermatologic Surgery, 32(3): 426-434 (2006).
[Schanz-2002] Schanz S, Schippert W, Ulmer A, Rassner G, Fierlbeck G., "Arterial embolization caused by injection of hyaluronic acid (Restylane)," British Journal of Dermatology, 146(5): 928-929 (2002).
[Salles-2008] Salles AG, Lotierzo PH, Gemperli R, et al., "Complications after polymethylmethacrylate injections: report of 32 cases," Plastic and Reconstructive Surgery, 121(5): 1811-1820 (2008).
[Gladstone-2007] Gladstone HB and Cohen JL., "Adverse effects when injecting facial fillers," Seminars in Cutaneous Medicine and Surgery, 26(1): 34-39 (2007).
[Cox-2011] Cox SE and Adigun CG., "Complications of injectable fillers and neurotoxins," Dermatologic Therapy, 24(6): 524-536 (2011).
[Glaich-2006] Glaich AS, Cohen JL, Goldberg LH., "Injection necrosis of the glabella: protocol for prevention and treatment after use of dermal fillers," Dermatologic Surgery, 32(2): 276-281 (2006).
[Hirsch-2007] Hirsch RJ, Brody HJ, Carruthers JD., "Hyaluronidase in the office: a necessity for every dermasurgeon that injects hyaluronic acid," Journal of Cosmetic and Laser Therapy, 9(3):182-185 (2007).

[Bailey-2011] Bailey SH, Cohen JL, Kenkel JM., "Etiology, prevention, and treatment of dermal filler complications," Aesthetic Surgery Journal, 31(1):110-121 (2011).
[Kim-2011_filler] Kim YJ, Kim SS, Song WK, Lee SY, Yoon JS., "Ocular ischemia with hypotony after injection of hyaluronic acid gel," Ophthalmic Plastic and Reconstructive Surgery, 27(6):e152-155 (2011).
[Kim_DW-2011] Kim DW, Yoon ES, Ji YH, Park SH, Lee BI, Dhong ES., "Vascular complications of hyaluronic acid fillers and the role of hyaluronidase in management," Journal of Plastic, Reconstructive and Aesthetic Surgery, 64(12): 1590-1595, (2011).
[Lazzeri-2012] Lazzeri D, Agostini T, Figus M, Nardi M, Pantaloni M, Lazzeri S., "Blindness following cosmetic injections of the face," Plastic Reconstructive Surgery, 129(4): 995-1012 (2012).
[Silva-2004] Silva MT, Curi AL. "Blindness and total ophthalmoplegia after aesthetic polymethylmethacrylate injection: case report," Arquivos de neuro-psiquiatria, 62(3B): 873-874 (2004).
[Kassir-2011] Kassir R, Kolluru A, Kassir M., "Extensive necrosis after injection of hyaluronic acid filler: case report and review of the literature," Journal of Cosmetic Dermatology, 10(3): 224-231 (2011).
[Kleydman-2012] Kleydman K, Cohen JL, Marmur E., "Nitroglycerin: a review of its use in the treatment of vascular occlusion after soft tissue augmentation," Dermatologic Surgery, 38(12):1889-1897 (2012).
[Kwon-2012] Kwon SG, Hong JW, Roh TS, Kim YS, Rah DK, Kim SS., "Ischemic Oculomotor Nerve Palsy and Skin Necrosis Caused by Vascular Embolization After Hyaluronic Acid Filler Injection: A Case Report," Annals of Plastic Surgery, 71(4): 333-3334, (2012).
[Inoue-2008] Inoue K, Sato K, Matsumoto D, Gonda K, Yoshimura K., "Arterial embolization and skin necrosis of the nasal ala following injection of dermal fillers," Plastic Reconstructive Surgery, 121(3) :127e-128e (2008).
[Kablik-2009] Kablik J, Monheit GD, Yu L, Chang G, Gershkovich J., "Comparative physical properties of hyaluronic acid dermal fillers," Dermatol Surg., 35 Suppl 1:302-312, 2009.
[Bogdan-2008] Bogdan Allemann I, Baumann L., "Hyaluronic acid gel (Juvéderm) preparations in the treatment of facial wrinkles and folds," Clin Interv Aging, 3(4):629-634, 2008.
[Johns-1996] Johns C, Gavras I, Handy DE, Salomao A, Gavras H., "Models of experimental hypertension in mice," Hypertension, 28(6):1064-1069, 1996.
[Bowman-2005] Bowman PH, Narins RS, "Hylans and soft tissue augmentation Carruthers J, Carruthers A (eds) Procedures in cosmetic dermatology: soft tissue augmentation," Elsevier Saunders, Philadelphia, p-34 (2005).
[Allemann-2008] Allemann IB, Baumann L, "Hyaluronic acid gel (Juvederm) preparations in the treatment of facial wrinkles and folds," Clin Interv Aging 3(4):629–634 (2008).
[Shiffman-2013] Shiffman M.A., Di Giuseppe A., "Cosmetic Surgery, Art and Techniques," Springer 2012.
[Sukhjit-2006] Sukhjit JS, Burgett RA, "Dermal fi ller agents: a practical review," Curr Opin Ophthalmol 17(5):471–479 (2006).
[Flynn-2011] Flynn TC, Sarazin D, Bezzola A, et al., "Comparative histology of intradermal implantation of mono and biphasic hyaluronic acid fillers [published online ahead of print January 27, 2011]. Dermatol Surg. 2011;37:637-643
[Baumann-2002] Baumann, Blyumin M, Sogol S., "Dermal fillers In Cosmetic Dermatology: Principles and Practice," 1st ed. New York, NY: McGraw-Hill; 2002.

[Kammerer-2005] Kammerer S., "Belotero: a CPM-technology based HA-filler. easy handling, smooth spreading in the tissues," Dermatology News, 11:2-3, 2005.
[Taufig-2009] Taufig AZ, Szoke A, Kuhnel W., "A new strategy to detect intradermal reactions after injection of resorbable dermal fillers," J Asthetisch Chirurgie, 2:29-36, (2009).
[Breithaupt-2012] Breithaupt A.D., Custis T. and Beddingfield F., "Next-generation dermal fillers and volumizers. Cosmetic Dermatology," 25(4), 184, 2012.
[Sundaram-2010] Sundaram, H., Voigts, B., Beer, K., & Meland, M., "Comparison of the rheological properties of viscosity and elasticity in two categories of soft tissue fillers: calcium hydroxylapatite and hyaluronic acid," Dermatologic Surgery, 36(s3), 1859-1865 (2010).
[Santoro-2011] Santoro, S., Russo, L., Argenzio, V., & Borzacchiello, A., "Rheological properties of cross-linked hyaluronic acid dermal fillers," Journal of Applied Biomaterials & Biomechanics, 9(2), 2011.
[FDA_Restylane] Executive Summary Restylane Injectable Gel P040024/S051, U.S. Food and Drug Administration, Public Advisory Committee Meeting, April 27, 2011, Available at: http://www.fda.gov/downloads/AdvisoryCommittees/CommitteesMeetingMaterials/MedicalDevices/MedicalDevicesAdvisoryCommittee/GeneralandPlasticSurgeryDevicesPanel/UCM252494.pdf.
[Juvederm_FDA] Juvéderm Gel Implants – P050047, Device approval and clearance overview, U.S. Food and Drug Administration, June 2, 2006.
[Belotero_FDA] Belotero Balance – P090016, Device approval and clearance overview, U.S. Food and Drug Administration, November 14, 2011.
[Voluma_FDA] Juvederm Voluma XC – P110033, Device approval and clearance overview, U.S. Food and Drug Administration, October 22, 2013.
http://www.accessdata.fda.gov/scripts/cdrh/cfdocs/cftopic/pma/pma.cfm?num=P110033
[Sculptra_FDA] Sculptra Aesthetic – P030050/S002, Device approval and clearance overview, U.S. Food and Drug Administration, July 28, 2009.
http://www.accessdata.fda.gov/scripts/cdrh/cfdocs/cfTopic/pma/pma.cfm?num=P030050S002
[Radiesse_FDA] Radiesse 1.cc and 0.3cc – P050052, Device approval and clearance overview, U.S. Food and Drug Administration, December 22, 2006.
http://www.accessdata.fda.gov/scripts/cdrh/cfdocs/cftopic/pma/pma.cfm?num=p050052